Sustainable and Degradable Epoxy Resins Containing Multifunctional Biobased Components

by
Minjie Shen

A dissertation submitted to the Department of Chemical & Biomolecular Engineering,
College of Engineering
in partial fulfillment of the requirements for the degree of

Doctor of Philosophy

in Chemical Engineering

Chair of Committee: Megan L. Robertson

Committee Member: Alamgir Karim

Committee Member: Jeffrey D. Rimer

Committee Member: Eva M. Harth

Committee Member: Venkatesh Balan

University of Houston
August 2021

ACKNOWLEDGMENTS

Firstly, I would like to express my sincere gratitude to my advisor, Prof. Megan L. Robertson for her great guidance and encouragement during my 5-year Ph.D. career. She always encourages me and provides me with opportunities to attend conferences and workshops to develop networking and presentation skills. She also offers great help with my paper writing and presentation slides all the time. She has also provided me with lots of insightful discussion and advice on my research. I truly appreciate her patience, enthusiasm and guidance.

Secondly, I would also thank Prof. Alamgir Karim, Prof. Jeffrey D. Rimer, Prof. Eva Harth and Prof. Venkatesh Balan for serving as my committee members. I appreciate their time and effort on my dissertation and defense. I would specially thank Prof. Alamgir Karim, Prof. Jeffrey D. Rimer, who have also been my committee members for my qualification exam and proposal defense. Their useful comments and beneficial discussion in this study have helped me a lot throughout my PhD study.

I would also like to express my deep thanks to Dr. Ramanan Krishnamoorti, Dr. Jacinta Conrad, Dr. Scott K. Smith and Dr. Eva M. Harth for their assistance in experiments. I would also like to express my sincere appreciation to Navjot Singh Randhawa for access and training on the scanning electron microscope and gold sputter. I also thank the Rice University Shared Equipment Authority for access to the Bruker MicroToF ESI LC-MS system.

I would also like to thank my former and current group members in our lab for their assistance and encouragement over the years: Dr. Vivek Yadav, Dr. Brian Rohde, Dr.

Wenyue Ding, Dr. Tyler Cooksey, Dr. Jialin Qiu, Dr. Xuejian Chen, Dr. Hongda Cao, Dr. Vijjamarri Srikanth, Dr. Fahimeh Khakzad, Dr. Yanchun Tang, Dr. Mohammad Tuhin, Tzu-Han Li, Josiah Hanson, Rosalie Berg, Stephanie Sontgerath and Ronard Herrera. I am so grateful that I have had so wonderful lab mates and I cherish our friendship. I also want to express special thanks to Dr. Guozhen Yang, Rawan Almallahi, Zeshan Rizvi, Eliud Gonzalez-Martinez for guiding me into this study. I would also appreciate my undergraduate students Cristian Oviedo, Yu-Ming Sheu, Ricky Ortiz, Natalia Butler, Adarius Cannon and Mohammad Daniyal for their great help on polymer synthesis and characterization.

Last but not the least, I would like to express my deepest appreciation to my family for their support and encouragement. I thank my parents, Xuhong Shen and Xuemei Liu, as they have always been there for me. My deepest thanks go to my girlfriend Simei Wang, who have been accompanying and supporting me through the recent three years. I am so beloved to have them in my life.

ABSTRACT

Epoxy resins were synthesized from a variety of biorenewable feedstocks, including epoxidized vanillic acid (EVA) and epoxidized 4-hydroxy benzoic acid (E4HBA), derived from lignin, epoxidized salicylic acid (ESA, a plant-based phenolic acid), and epoxidized soybean oil (ESO). The epoxy monomers were cured with an anhydride curing agent, and the curing behavior was studied using Fourier transform infrared (FTIR) spectroscopy and differential scanning calorimetry to ensure high conversion of functional groups to form the epoxy network. Evolution of viscoelastic behavior of the EVA-based epoxy resin was monitored through in situ rheology and compared to a conventional epoxy resin derived from the diglycidyl ether of bisphenol A (DGEBA). The EVA-based epoxy resin exhibited faster curing kinetics as compared to the DGEBA-based epoxy resin, and the storage (G') and loss (G") moduli of the EVA-based epoxy resin were higher than that of the DGEBA-based epoxy resin after gelation was achieved. The complex viscosity of the EVA-based epoxy resin was consistently higher than that of the DGEBA-based epoxy resin throughout the curing process. Both resins exhibited similar volume change during curing. The resulting EVA-based epoxy showed promising thermal and mechanical properties and can serve as a suitable replacement for the conventional DGEBA-based epoxy resin in applications.

The accelerated hydrolytic degradation behaviors of the epoxy resins were monitored in basic solution at 80 °C. All biobased epoxy resins underwent rapid degradation in a basic solution as compared to the conventional DGEBA-based epoxy resin. ESO- and ESA-based epoxy resins exhibited the fastest degradation rates, whereas

E4HBA- and EVA-based epoxy resins exhibited more moderate degradation rates. The degradation profiles, observed as the mass loss as a function of exposure time in the basic solution, showed good agreement with predictions from a solid-state kinetic model. Mass spectrometry and scanning electron microscopy analyses confirmed the epoxy resins underwent hydrolytic degradation, through a surface erosion mechanism in basic solutions. The impacts of various factors on the degradation rate were explored. including differences in the epoxy monomer structures; crosslink and ester densities, degree of hydrophilicity, and glass transition temperature of the resin; as well as solubility of degradation products.

The accelerated hydrolytic degradation behaviors of EVA- and ESO-based epoxy resins were also investigated in acidic solutions. The epoxy resins exhibited sigmoidal degradation kinetics in acidic solutions, consistent with bulk erosion mechanisms observed in linear polyesters. A solid-state reaction order model with autocatalysis was utilized to predict the mass fraction remaining as a function of exposure time in acidic solution and the data and model were in good agreement. Mass spectrometry and FTIR analyses confirmed the degradation mechanism as cleavage of ester groups in the crosslinked structures. The influences of solvent composition and temperature on degradation kinetics were also explored.

These combined results demonstrate biobased, ester-containing epoxy resins undergo rapid hydrolysis in both basic and acidic solutions, providing a route for end-of-life management of thermoset waste.

TABLE OF CONTENTS

LIST OF TABLES

LIST OF FIGURES

Chapter 1 Introduction

1.1 Importance of Epoxy Resins and Challenges of Commercial Epoxy Resins

Polymers are one of most important and enormously used materials in our daily life. Due to their wide range of properties, polymers are ubiquitous materials used in countless commercial products. Thermoset polymers are highly crosslinked materials, accounting for around 15% of polymers production in the United States, and used in diverse applications due to their high degree of durability and stability. Epoxy resins are an important class of thermoset polymer, with wide ranging applications in coatings, adhesives, aircraft parts, automobile parts, insulation, building materials and wind turbine blades, among others [1]. Furthermore, epoxy resins are a dominant class of thermoset polymer used in polymer composite materials, which have attractive features of high modulus, strength, and desirable thermal, electrical, and mechanical properties [2]. Currently, commercial epoxy resins are derived from the diglycidyl ether of bisphenol A (DGEBA), an industrial petrochemical which is controversial for its health effects and environmental issues. Unfortunately, limited options are available for processing thermosets, such as epoxy resins, at the end of their useful lifetime, and most thermoset waste eventually resides in landfills. Due to their highly crosslinked structures, conventional recycling processes cannot be applied to thermoset polymers, though new approaches are being developed for creating recyclable thermosets. In the next two sections, we will go through the strategies to overcome these challenges of commercial epoxy resins.

1.2 Epoxy Resins Developed from Renewable Resources

Continuous depletion of nonrenewable oil and gas, and also environmental and sustainability concerns drive researchers to derive polymeric materials from renewable,

non-toxic raw materials. Many renewable sources have been used to create epoxy resins, such as vegetable oils, including soybean oil, linseed oil, castor oil and palm oil, sugar-derived molecules, and lignin. Epoxidized soybean oil (ESO), made from soybean oil, has been widely studied as a replacement for traditional epoxide-containing molecules to form epoxy resins. However, ESO-based epoxy resins exhibit inferior thermal properties and mechanical behavior when compared to traditional epoxy resins. More recently, research has focused on synthesizing epoxy resins from biorenewable monomers which provide attractive mechanical properties to the epoxy resins. Zhao et al. used 2-methoxy-4-propylphenol derived from bamboo to synthesize epoxy resins. Mimicking the structure of the commercially used DGEBA, Aouf et al. converted gallic acid found in gallotannins to epoxy resins which contain two glycidyl ether groups linked to two aromatic rings. Xie et al. also extracted liquefied bagasse and cured it along with DGEBA; the resulting epoxy resins presented higher adhesive shear strength and better thermal stability.

Lignin is an abundant source from waste of plants. After pyrolysis or chemical treatments such as exposure to basic solutions, lignin can be depolymerized to many byproducts containing useful functionalities such as hydroxyl groups, aromatic rings or unsaturated bonds. A variety of methods have been explored to incorporate lignin in epoxy resins [3]. In one approach, lignin is directly blended with the epoxy monomer and curing agent and subsequently cured, however the resulting epoxy resins typically exhibit poor mechanical properties as the unmodified lignin has low reactivity with the curing agent [4-6]. Alternatively, a variety of lignin depolymerization processes (such as acid treatment, basic treatment, and pyrolysis) have been first applied to break the lignin down to a distribution of smaller molecules, which is then functionalized and cured to form an epoxy

resin. However, this method normally produces epoxy resins with poor properties and due to the mixture of small molecules, the structure-property relationships are difficult to investigate.

While the above approaches directly utilize lignin (or its depolymerization products) to form epoxy resins, which is advantageous from the standpoint of utilizing fully the lignin resource for the application, there are key limitations. The variability of the lignin resources and diversity of the degradation product distributions can lead to significant variability in monomer feedstock and resulting epoxy resin properties. Furthermore, such variability hinders identification of structure-property relationships in lignin-based epoxy systems. Therefore, a number of studies have identified key components of lignin depolymerization, and use the model compounds to form epoxy resins. Among these model compounds, vanillin is a very important and promising one. Vanillin is produced on a scale of more than 10 thousand tons per year and 15% of the produced vanillin is from lignin [7]. These model compounds including vanillin (and its derivative vanillic acid) [8, 9], 4-hydroxybenzoic acid and vanillyl alcohol, among others. These small molecules can be easily functionalized with epoxide groups and contain aromatic groups, mimicking the structure of DGEBA. Epoxy resins derived from model lignin compounds usually exhibit comparable thermal and mechanical properties to commercial epoxy resins [10-12].

Though the synthesis and thermomechanical properties of epoxy resins derived from lignin have been explored, little attention has been given to other properties which are critical for use of these materials in applications. Notably, evolution of viscoelastic properties of the epoxy monomer and curing agent mixture prior to gelation, and identification of the gelation point, which are critical properties for manufacturing

components using the epoxy resins (such as in infusion of fibers for composites, or application of adhesives) [13-15], have been underexplored in these systems. Such properties are well understood in conventional epoxy resins [16-18], and expanding on this knowledge for biobased systems would help bridge the gap from research prototype to manufacturing and use in applications.

1.3 End-of-Life Strategies for Epoxy Resin Waste

Epoxy resins, like other thermoset polymers, are non-recyclable through traditional recycling methods and thus create waste in landfills. An alternative approach is the chemical, bio-, or thermal degradation of the polymer to form small molecule byproducts, which can subsequently be reused (i.e. chemical recycling).

Polymer degradation under mild conditions is a topic of much interest in polymer science [19-21]. Aliphatic polyesters readily undergo hydrolytic degradation [22-30], and extensive experimental studies have been undertaken and models developed to describe their degradation behavior [31-36]. By contrast, the degradation behavior of thermoset polymers has been significantly underexplored. Pyrolysis, also known as thermal degradation, can degrade both DGEBA-based [37-40] and biobased [41-45] epoxy resins, typically requiring temperatures above 400 °C to fully degrade the polymers, and producing low molecular weight byproducts (with little decomposition of the bisphenol A moiety in the case of DGEBA-based resins [37]). Though pyrolysis is an effective way to break down a network polymer, it is also quite energy intensive. Solvolysis can also be employed, in which a chemical reagent reacts with functional groups on the network to decompose it into smaller molecules. DGEBA-based epoxy resins have been depolymerized using nitric acid [46], tetralin and decalin [47], CO_2-expanded water [48],

ethanol with $ZnCl_2$ [49], phosphotungstic acid with ethanol [50], supercritical isopropanol with KOH [51], alcohol/catalyst systems [52-56], and near critical water [57]. However, these approaches typically require either chemicals which are not environmentally friendly or high temperatures that are energy intensive. Strategies such as changing the curing agent or incorporating a comonomer can be utilized to minimize the energy needed [58-60]. Photodegradation is generally not a viable option due to its slow kinetics [61, 62].

Thermoset polymers that undergo hydrolysis and solvolysis under benign conditions typically contain degradable chemical groups: a variety of thermosets containing esters [63-65], acetals [12, 66, 67], carbonates [68], sulfur moieties [69-71], Schiff bases [72], and furans and maleimides linkages [73-75] have been reported. The hydrolysis and solvolysis of linear polyesters have been explored extensively over the last 20 years. Linear polyesters undergo ester hydrolysis and solvolysis under benign conditions, at low temperatures, and often assisted by the presence of catalysts. Throughout these decades of research, insight has been gained into degradation mechanisms. Burkersroda et al. first introduced a theoretical model that includes a critical device dimension to predict the erosion mechanism of water-insoluble biodegradable polymer matrices, which depends on not only the hydrolysis or solvolysis reaction but also diffusion of water (or solvent) into the specimen. The authors proposed that all degradable polymers can undergo either surface or bulk erosion, depending on the degradation conditions, which induce disparate behaviors. In surface erosion, in which bond cleavage is faster than water diffusion into the specimen, hydrolysis/solvolysis occurs mainly in the region of the sample near the surface. By contrast, in bulk erosion, in which water diffusion into the specimen is more rapid than bond cleavage, hydrolysis/solvolysis occurs throughout the entire

specimen simultaneously at a constant velocity throughout the erosion process. Polyesters such as polylactide and poly(lactide-*co*-glycolide) were shown to degrade differently in basic and acidic solutions. In basic solution, the degradation process commenced as soon as the samples were introduced to the solution, and the mass reduced linearly with degradation time, characteristic of surface erosion. In acidic solution, the samples exhibited little mass loss for a period of time while the solution infiltrated them, after which an abrupt loss of sample mass was observed, characteristic of bulk erosion.

More recently, the focus is turning to degradation mechanisms in crosslinked polyester thermosets. Two routes are possible for the preparation of thermosets containing degradable ester bonds. In some cases, monomers are used that contain ester functionality. Alternatively, the curing process itself may generate esters as in the case of anhydride curing of an epoxy monomer. Zhang et al. demonstrated that ester-containing epoxy resins exhibit very similar mass loss behavior to that of linear polyesters in basic and acidic solutions. In basic solution, the degradation behavior was consistent with surface erosion and in acidic solution, the degradation behavior was consistent with bulk erosion.

1.4 Factors Affect Hydrolysis or Solvolysis Rates in Epoxy Resins

1.4.1 Effect of pH

Solution pH plays an important role in controlling degradation mechanisms and rates. Acid or base may act as catalysts to promote hydrolysis or solvolysis reactions. Epoxy resins bearing aromatic imine bonds exhibited accelerated degradation rates in a variety of solvents with the addition of 0.17 M HCl [76]. The degradation time of an acetal-containing vanillin-based epoxy resin decreased from 19 to 10 min as the concentration of HCl was increased from 0.1 to 0.5 M, and then further decreased to 8 min at 1.0 M HCl

[12]. The degradation rate increased for ester-containing isosorbide-based and sucrose soyate-based epoxy resins when the sodium hydroxide (NaOH) concentration increased from 0.1 to 10 M [64, 77]. These studies demonstrate the acceleration of degradation rates in the presence of acid or base; however, increasing the acid or base concentration can also have the effect of reducing the solubility of the degradation products. In this case, the degradation rate may decrease, as shown in the case of a carbon fiber-reinforced epoxy resin containing imine groups for which the degradation time increased from 300 to 718 min when the HCl concentration increased from 0.1 to 1.0 M [78].

As discussed in last section, the degradation mechanisms in basic and acidic solutions are quite different from one another: degradation proceeds as surface erosion in basic solution and bulk erosion in acidic solution. Additionally, the degradation rates can be quite different under basic and acidic conditions. The degradation of ester-containing sugar-derived epoxy resins completed within hours in 1 M NaOH and within 50-70 days in 1 M HCl [79]. Similarly, ester-containing epoxy resins derived from trehalose, epoxidized soybean and β-cyclodextrin could be degraded within several hours in basic solution, whereas no degradation occurred in neutral water or acidic solution [80]. Ester-containing isosorbide and sucrose soyate-based epoxy resins degraded within 12 min in 1 M NaOH and took 48 h to degrade in 1 M HCl [64, 77]. An isosorbide diferulate-based epoxy resin degraded fully within 40 h in an NaOH solution, and exhibited relatively slow degradation in HCl [81]. The acid strength can also play a role in determining degradation rate: a diepoxy monomer containing bicyclo diacetal could be fully degraded within 40 min in 1 M HCl and the degradation time increased to 70 min in 1 M sulfuric acid (H_2SO_4) and 480 min in phosphoric acid (H_3PO_4). In the hydrolysis of acetals, both the oxocarbonium

formation and hemiacetal cleavage require sufficient H^+ concentration; however, the medium-strong acid H_3PO_4 could only protonate partially compared to fully protonated HCl and H_2SO_4 at same solution concentrations [82].

1.4.2 Effect of temperature

The degradation temperature is an important factor that will determine energy costs associated with disposing of thermosets through hydrolysis or solvolysis. There is much demand for the ability to degrade thermoset polymers at relatively low temperatures. Citric acid based epoxy resins containing esters cured with an anhydride curing agent lost 46.4% of their mass at 50 °C in H_2O_2/DMF, and this was increased to a mass loss of 99.9% at 90 °C [65]. Similarly, the hydrolysis rate of a vanillin-based epoxy resin containing acetal groups increased by a factor of 10 in an acetone/water solution when the temperature was increased from room temperature to 50 °C [12]. An epoxy thermoset bearing aromatic imine bonds degraded more rapidly at 65 °C relative to 25 °C [76]. An anhydride–cured DGEBA-based epoxy resin, depolymerized by selective ester bond cleavage in a TBD (triazabicyclodecene)/alcohol solution, showed a factor of 5 increase in degradation rate as the temperature was raised from 150 to 180 °C [55, 56].

Biobased epoxy resins which contain cleavable bonds (esters, acetals, imines) typically require significantly lower hydrolysis or solvolysis temperatures than that of commercial DGEBA (or other bisphenol monomer) epoxy resins. Commercial epoxy resins usually require temperatures around 300 °C, combined with high pressure, for hydrolysis or solvolysis to proceed [83, 84]. By contrast, there are many examples in the literature of biobased epoxy resins which can degrade at room temperature or slightly elevated temperatures. Imine-containing biobased epoxy resins underwent hydrolysis at

room temperature in 0.1 M HCl and fully degraded within 4 h [78]. Similarly, a soybean oil-based epoxy resin degraded fully at room temperature in 1 M NaOH within 1 h [80]. An acetal-containing biobased epoxy resin degraded within 1 h at 50 °C in 0.1 M HCl in DMF [82].

1.4.3 Effect of catalyst

Developing an efficient catalyst or optimizing the appropriate amount of catalyst is crucial to identifying degradation protocols that operate at lower temperatures, and thus lower energy cost, as well as utilize more benign conditions (reducing acid or base concentration and avoiding toxic solvents). A citric acid based epoxy resin containing ester groups, cured with anhydride curing agent, could be fully degraded within 2 h at 90 °C in DMF when H_2O_2 was present, which produces free radicals and promotes decomposition [65]. The presence of CO_2 in water and an acetone/water (80/20) solution enhanced resin degradation under conditions of high temperature and high pressure, where CO_2 acted as a catalyst in the presence of the phenol produced by the resin degradation [48]. The degradation of carbon fiber reinforced amine-cured epoxy resins occurred in water at supercritical or near critical conditions: only 79.3 wt% of the sample mass was degraded in supercritical water conditions and this increased to 95.3 wt% with the addition of KOH as an alkali catalyst [85]. In the degradation of anhydride-cured DGEBA-based epoxy resins, TBD acted as a strongly basic catalyst and promoted cleavage of ester groups [55, 56]. A weak Lewis acid (zinc chloride, magnesium chloride and aluminium chloride) promoted degradation of a carbon fiber reinforced amine-cured epoxy resin in acetone/water by reducing the reaction activation energy [83]. The addition of KOH

reduced the initial decomposition temperature of an amine-cured epoxy resin by 10 to 30 °C and promoted the formation of complex alcohols [51].

1.4.4 Effect of solvent composition

Changing the solvent system has a large impact on degradation. An important effect of the choice of solvent is the solubility of degradation products; degradation rates are inhibited when degradation products are insoluble. Vanillin-based epoxy resins were degraded in a variety of solvents containing HCl; degradation proceeded much more slowly in ethanol as compared to that in methanol, acetone, THF and DMF, attributed to the significantly worse solubility of the degradation products in ethanol [78]. Similarly, in another study, a vanillin-based epoxy resin containing an imine group showed very slow hydrolysis rates in toluene and benzene due to the poor solubility of degradation products in these two solvents [78]. In the degradation of an amine-cured commercial epoxy resin, it was discovered the optimal degradation conditions occurred in acetone/water (80/20) for which the solubility of degradation products was greatest [48]. Similarly, in an acetal-containing epoxy resin, acetone/water (90/10) was the most effective solvent [82].

The affinity of thermoset polymers to the solvents also plays an important role in controlling solvolysis rates, as increased wettability of the thermoset surface to the solvent enhances the degradation rate. An imine-containing epoxy resin showed a decrease in solvolysis rate as the polarity of the solvent and affinity of thermoset to the solvent decreased (water > dimethyl sulfoxide > DMF > ethanol > THF > benzene) [76]. An acetal-containing epoxy resin degraded more rapidly when the solvent polarity increased [12, 82]. Ethylene glycol monobutyl ether degraded an anhydride-cured DGEBA epoxy resin faster than other alcohols due to the higher affinity of the solvent to the epoxy resin

[55, 56]. Finally, adding THF or acetone to water improved the hydrolysis rate of an amine-cured commercial epoxy resin [86].

1.4.5 Effect of type and concentration of monomer and curing agent

Varying the monomer type can have a larger impact on the degradation rate. In comparison of various biobased epoxy resins derived from vanillic acid, biobased phenolic acids, and soybean oil, increasing the number of esters per epoxy monomer and increasing the epoxy resin hydrophilicity was found to increase the degradation rate [87]. An isosorbide diferulate-based epoxy resin which contained esters could be fully degraded in HCl solution within 40 h, while a syringaresinol-based epoxy resin which didn't contain any cleavable groups degraded much more slowly [81]. Choice of curing agent may also influence degradation rate: the degradation rate increased for sulfide-containing epoxy resins in 2-mercaptoethanol when the concertation of disulfide bonds in the curing agent increased [88].When epoxidized soybean oil (ESO) was cured with trehalose, a more hydrophillic resin was produced as compared to curing with β-cyclodextrin, and the trehalose-cured resin degraded more rapidly [80].

Varying the ratio of epoxy monomer to curing agent can also tune the degradation rate of an epoxy resin. In sucrose soyate-based epoxy resins, as the ratio of the monomer to curing agent increased, the degradation rate increased [64, 77]. ESO-based epoxy resins cured with trehalose and β-cyclodextrin degraded more rapidly when the ESO content was reduced, due to the high ester content in the curing agents [80].

1.5 Overview of the thesis

In the following chapters, the dissertation is organized as outlined below.

Chapter 2 describes the experimental methods used in this study. Detailed information on matetrials used, synthesis procedures and characterization methods will be discussed.

Chapter 3 discusses the synthesis and thermal and mechanical properties of biobased epoxy resins. This chapter also investigates the curing behavior of EVA-based epoxy resins in FTIR and rheometer, and reveals the comparable thermal and mechanical properties to commerical epoxy resins.

Chapter 4 investigates the synthesis of biobased epoxy resins containing ester linkages and discusses the accelerated degradation behavior of biobased epoxy resins in basic conditions. The degradation mechanism in basic conditions is further discussed and a kinetic model is utilized to predict the degradation behavior in basic conditions. Various factors that affect the degradations in basic conditions are also discussed.

Chapter 5 discusses the accelerated degradation of biobased epoxy resins in acidic conditions. The degradation mechanism in acidic conditions is further investigated and a kinetic model is proposed to predict the degradation behavior in mild acidic conditions. Various factors that affect the degradations in acidic conditions are also discussed.

Chapter 6 presents a different project focusing on developing degradable and thermally stable spiro polycycloacetals from renewable resources. The degradation behavior of this class of spiro polycycloacetals is investigated. Introduction, materials used and experimental methods will be discussed seperately in chapter 6 for this project.

Chapter 7 gives a summary of this research and future work is also discussed.

Chapter 2: Experimental Methods

This chapter describes synthesis and characterization methods for the development of sustainable and degradable epoxy resins, as well as the methods to measure the degradation rates of the resulting epoxy resins.

2.1. Materials

All chemicals were purchased from Sigma-Aldrich unless otherwise noted and were used as received: ESO was kindly supplied free of charge by Arkema, Inc. (trade name Vikoflex 7170; contains an average of 4.27 epoxide groups per triglyceride molecule following nuclear magnetic resonance, NMR, analysis), vanillic acid (4-hydroxy-3-methoxybenzoic acid, ≥97%), salicylic acid (SA, ≥99%, FG/Halal/Kosher), 4-hydroxybenzoic acid (4HBA, 99%, ReagentPlus), methylhexahydrophthalic anhydride (MHHPA, Huntsman, Aradur HY 1102, ≥99%), 1- methyl-imidazole (1-MI, Huntsman, Accelerator DY 070), N,N-dimethylformamide (DMF, BDH, ≥99.8%, ACS reagent), potassium carbonate (K_2CO_3, ≥99.0%, ACS reagent), allyl bromide (97%), ethyl acetate (BDH, ≥99.5%, ACS grade), magnesium sulfate ($MgSO_4$, BDH, ≥99.0%, anhydrous reagent grade), meta-chloroperoxybenzoic acid (mCPBA, ≤77%), sodium sulfite (Na_2SO_3, AMRESCO, 98.0%, ACS grade), sodium bicarbonate ($NaHCO_3$, ACS reagent, 99.7-100.3%), hexane (BDH, ≥60%, ACS grade), chloroform (Macron, ACS grade), and silica gel (Macron, grade 62, 60-200 Mesh), and hydrogen chloride solution (32 wt% HCl in H_2O).

2.2. Epoxy resin synthesis

2.2.1 Preparation of biobased epoxy monomers

Vanillic acid was allylated with the following procedures. Vanillic acid (10.0g, 59.5 mmol) was dissolved into 340 mL of DMF in a 1000 mL round-bottom flask with a

magnetic stir bar, sealed with a rubber septum, and cooled to 0 °C using an ice bath. K_2CO_3 (18.1g, 131 mmol) was then added to the flask. After three minutes of stirring, allyl bromide (131 mmol) was added dropwise with a syringe (the molar ratio of ally bromide to vanillic acid was 2.20 to 1, to achieve higher conversion). After adding the allyl bromide, the reaction was allowed to warm to room temperature and the reaction proceeded for 48 h. Distilled water (340 ml) was added to the reactants and the product was extracted by ethyl acetate (three times) in a separatory funnel, by gently shaking the solution for 5 minutes and then allowing it to sit for 1 min; (the product was found in the top layer which was the organic phase). The organic phase was washed with an equivalent volume of saturated brine and dried over $MgSO_4$. Ethyl acetate was removed from the product using a rotary evaporator, and the product was dried in a vacuum oven at 50 °C for 24 h, or until DMF was not observed through NMR analysis.

AVA was converted to epoxidized vanillic acid (EVA) through the following procedures. AVA (5.00g, 20.1 mmol) was dissolved into 500 mL chloroform in a 1000 mL glass round bottom flask with a magnetic stir bar sealed with a rubber septum. mCPBA (27.8g, 161 mmol) was added to the flask (at a molar ratio of allylated vanillic acid : mCPBA of 8 : 1). The solution was stirred at 40 °C for 24 hours. After 24 hours, the solution was washed with an equivalent volume of a 10%wt Na_2SO_3 aqueous solution and separated using a separatory funnel. The organic phase (bottom layer) was then washed with an equivalent volume of a saturated $NaHCO_3$ solution and separated using a separatory funnel. Finally, the organic phase (bottom layer) was washed with an equivalent volume of saturated brine and separated using a separatory funnel. The chloroform was then removed from the product using a rotary evaporator. The EVA product was purified by silica gel

chromatography using hexane/ethyl acetate (40/60). The organic solvent was removed using a rotary evaporator and the product was dried in a vacuum oven at 60 °C overnight.

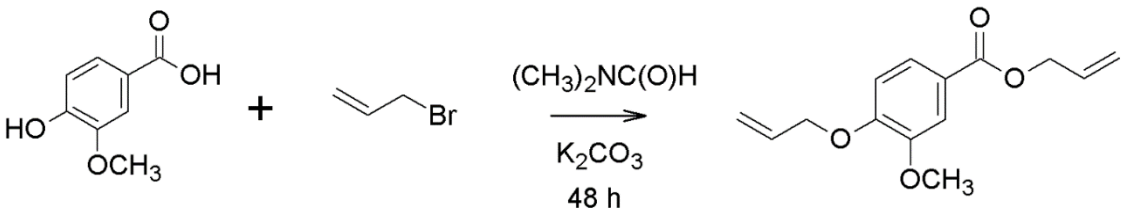

Scheme 2. 1: Allylation of vanillic acid

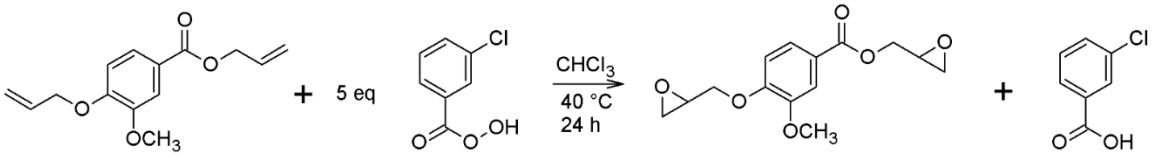

Scheme 2. 2: Epoxidation of AVA

Epoxidized salicylic acid (ESA) and epoxidized 4-hydroxybenzoic acid (E4HBA) were synthesized following previously reported procedures.

2.2.2 Preparation of epoxy resins

EVA was melted at 94 °C prior to use (the other epoxy monomers were liquids at room temperature). The epoxy monomer (DGEBA, ESO, EVA, ESA, or E4HBA) was mixed with MHHPA (stoichiometry based on equal molar epoxide and anhydride groups) and 3 phr (parts per hundred parts by weight of resin) 1-MI at 50 °C in a 20 mL scintillation vial using magnetic stirring for 10 minutes. The mixture was placed in the following sample holders appropriate for each characterization experiment: (a) in a preweighed Tzero aluminum pan for differential scanning calorimetry, (b) in a pan for thermogravimetric analysis, and (c) in an aluminum mold for hydrolysis degradation analysis. The sample was

then transferred to a convection oven and cured. The following curing schedule was used for EVA, ESA, E4HBA, and DGEBA-based epoxy resins: 70 °C for 2 hours, then 170 °C for 2 hours. ESO required a longer first curing stage (as the reaction kinetics were significantly slower), with the following curing schedule: 70 °C for 24 hours, then 170 °C for 2 hours. Table 2.1 shows the amount of epoxy monomer, curing agent, and catalyst used for each sample.

Table 2. 1**:** Amounts of epoxy monomer, curing agent and catalyst used in epoxy resin Synthesis

Epoxy Monomer	Epoxy Monomer Mass (g)	Curing agent Mass (g)	Catalyst Mass (g)
DGEBA	1	0.97	0.03
ESO	1	0.75	0.03
EVA	1	1.20	0.03
ESA	1	1.35	0.03
E4HBA	1	1.35	0.03

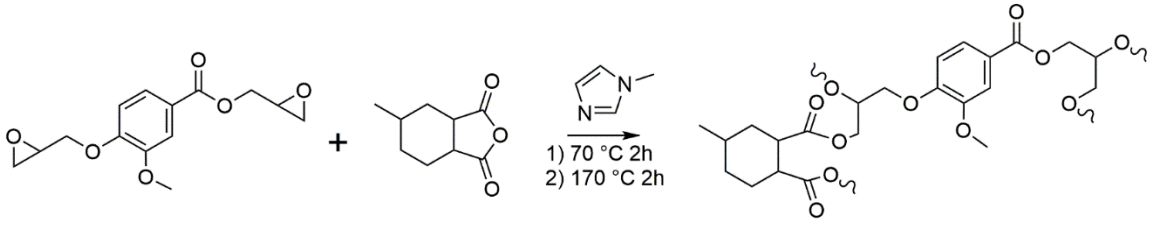

Scheme 2. 3: Anhydride curing of EVA

2.3. Epoxy resin characterization

2.3.1 Nuclear Magnetic Resonance

^{1}H NMR (400, 500, 600 MHz) and ^{13}C NMR (100 MHz) experiments were conducted using a JEOL ECA-400 instrument with deuterated chloroform (Cambridge

Isotope Laboratories, Inc., 99.8 atom % D) as the solvent. Chemical shifts were referenced to the solvent proton resonance (7.26 ppm for ^{1}H NMR, 77.2 ppm for ^{13}C NMR).

2.3.2 Differential Scanning Calorimetry

Differential scanning calorimetry (DSC) was conducted with a TA Instruments Q2000 differential scanning calorimeter, under 50 ml/min nitrogen flow, and calibrated with an indium standard. Samples were encapsulated in a Tzero aluminum pan, equilibrated at 40 °C, and subjected to a heat-cool-heat cycle from 40 –200 °C at a rate of 10 °C/min. The glass transition (T_g) was identified as the inflection point in the second heating cycle.

2.3.3 Thermogravimetric Analysis

Thermogravimetric analysis (TGA) experiments were conducted using a TA Instruments Q500 analyzer. The samples were heated from 25 °C to 550 °C at a rate of 10 °C/min in an argon environment.

2.3.4 Optical Microscopy

Optical microscopy was performed on a Leica DM2500 M microscope with a HCX PL FLUOTAR 20X/0.50 BD objective in bright field mode using a mercury lamp. Optical microscopy slides were prepared by taking a drop of reactive monomer mixture, sandwiching it between a glass slide and a glass coverslip, and curing the epoxy resin following the protocol described previously. For optical micrographs which showed dispersed particles, the micrographs were converted to binary images, and processed with ImageJ to identify the pixel area for each particle. With knowledge of the microns/pixel of the micrograph, each particle area in micron^2 was characterized. Assuming a circular particle, the circle diameter was calculated ($D_i = 2(A_i/\pi)^{1/2}$). We did not account for the

potential underestimation of D_i due to the two dimensional projection of the sphere. Additionally, particles of a size too small to be observed at the magnification chosen have been neglected. The Sauter mean diameter (D_m) was calculated for the population of oil droplets in the micrograph as

$$D_m = \frac{\sum_i^n {D_i}^3}{\sum_i^n {D_i}^2}, \qquad \text{(eqn. 2.1)}$$

where D_i is the diameter of one particle and n is the number of particles in 1 micrograph. The standard deviation was calculated based on the population of particles examined within the same image. In the case where co-continuous morphologies were observed, optical micrographs were processed using the ImageJ Fast Fourier transform (FFT) function. The average domain size (d) was taken to be that at the peak maximum in the intensity versus wavevector ($q=2\pi/d$). The error was quantified by calculating the peak width at half maximum.

2.3.5 Scanning Electron Microscopy

The surface structures of the neat and degraded samples were imaged using a Jeol JSM-6010LA field emission scanning electron microscope at a voltage of 15kV. The surface was etched with ionized argon gas and subsequently coated with gold using a Denton Vacuum Desk V sputter coater for 1.5 minutes. The gold thickness was approximately 10 nm.

2.3.6 Mass Spectrometry

In Chapter 4, mass Spectrometry experiments were conducted using a Bruker MicroToF ESI LC-MS System. This MicroToF instrument is equipped with an ESI source and is interfaced with an Agilent 1200 HPLC system. The mobile phase was a mixture of

50% water and 50% ethanol. The epoxy resin degradation products were dissolved in acetonitrile and the concentration of the solution was 10 µg/ml prior to injection into the MicroToF.

In Chapter 5, mass spectrometry experiments were carried out using a Thermo Exactive mass spectrometer. It was operated in positive ionization mode, with a spray voltage of 1.5kV. This high-resolution Orbitrap MS is equipped with a TriVersa NanoMate nano-electrospray (nESI) source. The epoxy resin degradation products were dissolved in water at a concentration of 10 µg/ml, and 5 µL of each sample was continuously infused by an Advion TriVersa NanoMate. Applied voltages were 62.5 V for the ion transfer capillary and 100 V for the tube lens, respectively. The ion transfer capillary was set at 250 °C and the m/z range was 150-1000 (normal mass range) in profile mode.

2.3.7 Fourier Transform Infrared Spectroscopy-Attenuated Total Reflectance (FTIR-ATR)

FTIR spectra were obtained on a Thermo Scientific Nicolet 4700 spectrometer in transmission mode. The OMNIC Series software was used to follow selected peaks at 1.928 cm^{-1} resolution using 32 scans. FTIR-ATR was performed on the samples before degradation and at various stages of the degradation process.

2.3.8 Dynamic Mechanical Analysis (DMA)

DMA experiments were performed on a TA instrument (DMA Q800) at a heating rate of 3 °C/min, from room temperature to 250 °C (for the EVA-based epoxy resin) and 160 °C (for the ESO-based epoxy resin), at a frequency of 1 Hz using three-point bending

mode. Prior to the measurement, epoxy resin samples were cured in an aluminum mold (25 mm × 6 mm ×1 mm).

2.3.9 Contact Angle Measurements

Water contact angles were measured using an OCA 15EC video-based optical contact angle measuring instrument at ambient temperature. The SCA 20 software was used to record the water contact images. 1µL DI water droplets were deposited onto 5 different positions on polished surfaces of the epoxy resins. 1500 grit sandpaper was used to polish the sample surfaces and dust was removed using compressed nitrogen.

2.3.10 Rheological Property Measurements

The curing behavior of EVA-based epoxy resins was evaluated using a TA instruments DHR-2 rheometer with 40 mm diameter parallel plates, and a sample thickness of 2 mm. The stage was pre-heated to 70 °C before loading the mixture (epoxy monomer, curing agent and catalyst) and was kept isothermally at 70 °C throughout the experiments. Time sweep experiments, in which the storage (G') and loss (G") moduli and complex viscosity (η*) were measured as a function at time at fixed strain and frequency, were conducted with strain of 1% and frequency of 1 Hz [89]. Strain sweep experiments were also conducted at different time points, in which strain was varied (0.1-100%) at fixed frequency (1 Hz) to identify the linear region. Subsequently, frequency sweep experiments were conducted at different time points, in which the strain was fixed (in the identified linear region) and frequency varied from 0.16-16 Hz. Experiments were also conducted at 70 °C to measure the normal force (F_n) with fixed gap of 2 mm, as well as to measure the change in gap at constant normal force of 0 N.

2.3.11 Tensile Testing

Tensile testing was conducted using an Instron 5966 universal testing system containing a load cell with maximum force of 2 kN. Dog-bone shaped testing bars (ASTM D638, bar type 5, thickness 1.5 mm) were prepared following the curing protocol described above. Pneumatic grips (maximum force 2 kN) were used to affix the sample in the testing frame with a compressed air pressure of 60 psi. The elongation rate of test specimens was set as 10 mm/min. The engineering stress was calculated using the measured force and known cross-sectional area of the sample. The strain was calculated based on the travel distance of the grips. Each tensile measurement was repeated with 5 test specimens that broke in the gauge region and did not contain a visible macroscopic defect (voids, bubbles, etc.) at the point of fracture.

2.3.12 Hydrolytic Degradation Experiments in Basic Solution

Epoxy resin samples (10 mm × 5 mm ×3 mm) were degraded in basic solutions following literature procedures [90, 91]. The initial sample weight was recorded, and the sample was placed in 10 mL of 3 wt% NaOH solution at 80 °C for a specified time period (0.04 wt% sodium azide was also added to the solution to prevent microbial growth). The sample was then rinsed with deionized (DI) water, rinsed with a 1 wt% HCl solution to neutralize the solution, rinsed with DI water again, and finally dried in a vacuum oven at 50 °C overnight. The sample weight was recorded, and then the sample was placed back in the NaOH solution for additional time. This process was repeated until the whole sample degraded.

2.3.13 Hydrolytic Degradation Experiments in Acidic Solutions

Epoxy resin samples were cured in an aluminum mold (10 mm × 5 mm ×3 mm) and the initial sample weight was recorded for each sample. Degradation solutions were prepared by adding concentrated HCl (32 wt% in water) to various solvents (water, THF, acetone, and DMF), to prepare solutions at a final concentration of 10 wt% HCl. Specifically, 100 g concentrated HCl (32 g HCl and 68 g water) was added to 220 g of the diluting solvent (water, THF, acetone or DMF). Detailed degradation solution compositions are listed in Table A3.1 in the *Appendix 3*. 0.04 wt% sodium azide was also added to the solution to prevent microbial growth.

Each epoxy resin sample was placed in 10 mL of 10 wt% HCl and maintained at 25 or 80 °C for a specified time period. The sample was then removed from the solution, rinsed with deionized (DI) water, rinsed with 3 wt% NaOH solution for neutralization, and finally dried in a vacuum oven at 50 °C overnight. The final weight was then recorded and compared to the initial weight. The samples were not reused for subsequent degradation experiments (fresh samples were prepared for every time point). Each time point shown on degradation plots represents average measurements taken over three individual samples.

Chapter 3: Vanillin-based epoxy resins with excellent processability and thermomechanical behavior

This chapter discusses the processing behavior of epoxidized vanillic acid (EVA)-based epoxy resins, derived from lignin. The EVA-based epoxy resin was synthesized using both conventional and green chemistry methods. The curing behavior was studied using Fourier transform infrared (FTIR) spectroscopy to ensure high conversion of functional groups. The resulting EVA-based epoxy resin showed promising thermal and mechanical properties as compared to a conventional diglycidyl ether of bisphenol A (DGEBA)-based epoxy resin. The EVA-based epoxy resin required less time to achieve gelation under the same curing conditions, facilitating more rapid manufacturing. The EVA-based epoxy resin exhibited higher storage and loss moduli and complex viscosity during the curing process as compared to the DGEBA-based epoxy resin.

3.1 Epoxy monomer synthesis and curing of epoxy resins

We have employed a two-step epoxidation protocol in order to avoid the use of epichlorohydrin due to its toxicity. Vanillic acid, derived from lignin, was first converted to allylated vanillic acid (AVA) and AVA was subsequently reacted with mCPBA to form EVA following our previously reported procedures (Scheme 3.1) [87]. We additionally explored a more environmentally friendly chemo-enzymatic protocol for epoxidation of the allyl groups on AVA [92], which used hydrogen peroxide, caprylic acid, and immobilized lipase B from Candida antarctica (Novozyme 435) as the catalyst (Scheme 3.1) in toluene. The mechanism of the reaction was previously reported to be epoxidation of double bonds by percaprylic acid formed through reaction of C8 and H_2O_2[92]. Table A1.1 and Figure A1.1 summarize the impact of the AVA:C8: H_2O_2 molar ratio and reaction

time and temperature on the resulting conversion of double bonds to epoxide groups (in the range of 30-60% conversion), with a more extensive discussion provided in the *Appendix 1*. As the chemo-enzymatic route did not achieve as high conversion as the chemical route employing mCPBA (previously reported as 70% conversion [87]), we proceeded further with our study employing the mCPBA route to synthesize large quantities of EVA for subsequent curing and physical property testing.

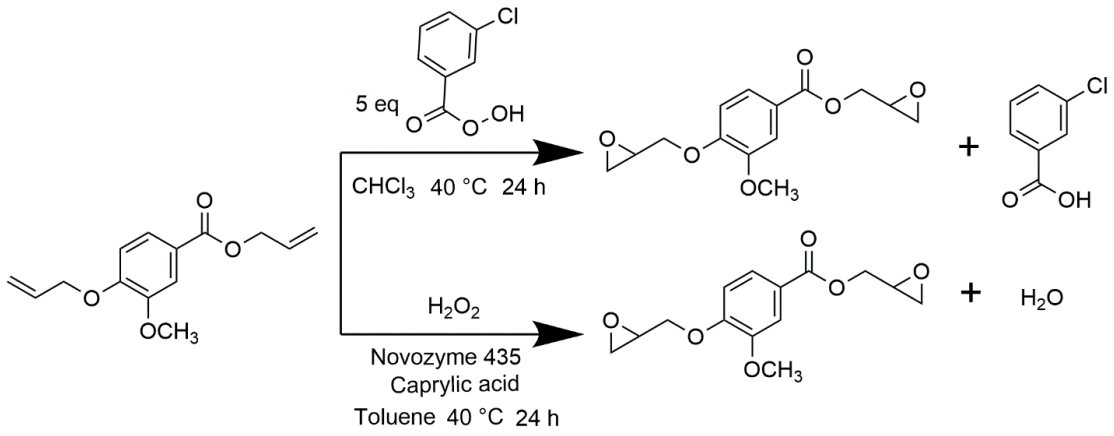

Scheme 3. 1: Epoxidation of AVA using conventional (top) and chemo-enzymatic (bottom) methods.

^{1}H NMR analysis identified the structures of EVA synthesized by the mCPBA route (previously reported in ref. [87]) and through chemo-enzymatic epoxidation of AVA (Figure 3.1). The peaks observed in the region of 2.5-3.5 ppm are associated with formation of epoxide groups and no peaks were found in the region of 5-6 ppm (associate with allyl groups), confirming the recovery of EVA monomer following purification (Figure 3.1a). The appearance of carbon peaks at 45 and 50 ppm also confirmed the formation of epoxide groups (Figure 3.1b). The pure EVA monomer was then utilized for the curing reaction.

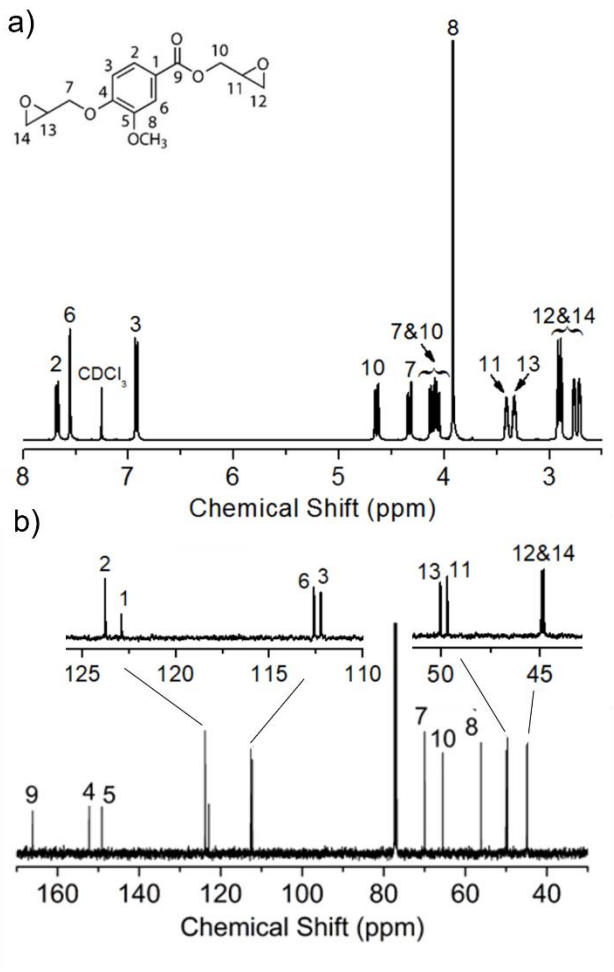

Figure 3. 1 a) ^{1}H NMR and b) ^{13}C spectra of EVA in *d*-chloroform.

EVA was cured to form an epoxy resin through a two-step curing protocol (70 °C for 2 h and 170 °C for 2 h), where a lower temperature stage was first employed to cure the resin without significant loss of monomer, and a second, higher temperature stage was then used to achieve high conversion of monomer (reported in our prior studies [87, 93]). The conversion of the curing reaction between EVA monomer and curing agent MHHPA (in the presence of catalyst 1-MI) was directly monitored through *in situ* FTIR (Figure 3.2a). During the first stage of the reaction (solid curves in Figure 3.2a), in which the temperature was held at 70 °C for 2 h, systematic decreases of intensities of the anhydride group peaks

at 1788 and 1857 cm^{-1} (C=O stretching) were monitored. Similarly, systematic decreases in peak intensities in the range of 900-1007 cm^{-1} associated with the epoxide ring (anhydride C-O and C-O-C stretching), as well as peaks at 915 cm^{-1} (epoxide C-O stretching) and 845 cm^{-1} (epoxide C-O-C stretching) were observed. Additionally, a systematic increase in intensity was observed for ester group peaks at 1736 cm^{-1} (C=O stretching), confirming formation of the epoxy network. Once the reaction temperature was increased to 170 °C for the second stage of the reaction (dashed curves in Figure 3.2a), further decrease of peak intensities of the anhydride group at 1788 and 1857 cm^{-1} (C=O stretching) and epoxide ring in the range of 900-1007 cm^{-1} (anhydride C-O and C-O-C stretching), at 915 cm^{-1} (epoxide C-O stretching), and at 845 cm^{-1} (epoxide C-O-C stretching) were observed, indicating further curing took place. Meanwhile, an increase in intensity was observed for ester group peaks at 1736 cm^{-1} (C=O stretching), confirming further formation of the epoxy network. The conversion of anhydride groups was quantified using the change in peak intensity for the peaks at 1788 and 1857 cm^{-1} (C=O stretching). During the first stage (2h at 70 °C), low conversion of anhydride groups was achieved (30-50%) (Figure 3.2b). After 2 h, the temperature was raised to 170 °C. After 0.5 h of curing at 170 °C, the conversion of anhydride groups increased to 80-90%. Ultimately, the reaction conversion reached 95% after 1-2 h of second stage curing at 170 °C. We also monitored the glass transition temperature (T_g) of the samples at different second stage curing times using DSC (Figure 3.2c). While the T_g initially increased after 2 h of second stage curing (T_g = 146 °C), it then decreased with further second stage curing, possibly due to thermal degradation when held at high temperatures for an extended period.

We therefore used 2 h of second stage curing to maximize the T_g (and resulting crosslink density) of the epoxy resin.

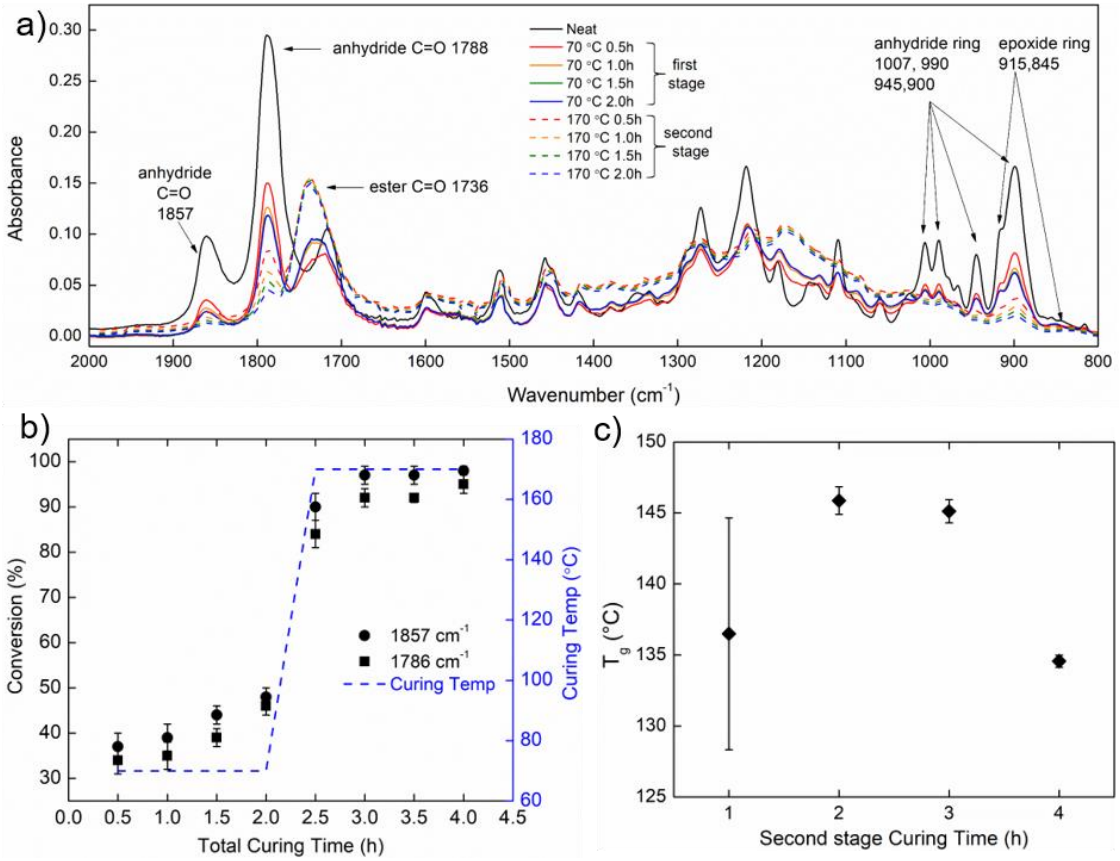

Figure 3. 2**:** a) Curing of EVA with MHHPA (catalyzed with 1-MI) monitored through *in situ* FTIR. b) Conversion of anhydride groups (data points) quantified through analysis of FTIR data in a). c) T_g of cured specimens following different second stage curing times (at 170 °C).

3.2 Evolution of viscoelastic properties of EVA-based epoxy resins during curing

Gelation is one of the most important phenomena occurring during the curing reaction of epoxy resins [94, 95]. At the gel point, the viscous liquid (epoxy monomer, curing agent and catalyst) transforms into an elastic gel and a network material is achieved [96]. Thus, determining the gel point is critical for processing of epoxy resins [97]. Furthermore, the viscoelastic properties of the materials as it transforms from a liquid to

solid govern its processing requirements for applications such as composites and adhesives. Importantly, in order for a biobased monomer such as EVA to replace more conventional epoxy monomers such as DGEBA, the viscoelastic properties during curing must be characterized.

We have observed physical changes in the EVA-based epoxy resin during first stage of curing (2 h at 70 °C), in which the viscous liquid (epoxy monomer, curing agent and catalyst) solidifies to a soft solid. We therefore measured the storage (G') and loss (G") moduli, as well as complex viscosity (η*) as a function of curing time at 70 °C, in order to compare the gel point and viscoelastic properties of the EVA-based epoxy resin to a more conventional DGEBA-based epoxy resin.

A commonly used criterion to determine the gel point of a thermoset is the crossover of G' and G" [98, 99]. An isothermal time sweep was first conducted (Figure 3.3a), during which G' and G" both increased with curing time until their values were equal to one another (at the crossover point), occurring at around 70 min of curing, which was thus identified as the curing time at which an infinite network has formed (the "gel"). Before the gel point, G" was higher than G', indicating the mixture was a liquid. After the gel point, G' was higher than G", which is characteristic of a solid, and G' and G" reached plateau values of 1.3 and 0.6 MPa, respectively, at around 87 min. The complex viscosity (η*) of the mixture was also monitored (Figure 3.3b). η* increased with curing time and a sharp change in slope was observed at 62 min (indicating proximity to the gel point); it reached a plateau value of 3×10^5 Pa·s by around 81 min. We compare the behavior of the EVA-based epoxy resin to that of a DGEBA-based epoxy resins that was cured using the same protocol (Figures 3.3a and 3.3b). The DGEBA-based epoxy resin exhibited slower

curing kinetics, with the crossover of G' and G" obtained at 130 min. Following gelation, the DGEBA-based epoxy resin reached plateau values (after 134 min) of 0.7 and 0.3 MPa for G' and G", respectively, which is lower than that observed in the EVA-based system, indicating higher stiffness of the EVA network. η* (Figure 3.3b) also increased, a sharp change in slope was observed at 130 min, and it reached a plateau value of 1 x 10^5 Pa·s by around 133 min. η* of the EVA-based epoxy resin was around 3 times higher than that of DGEBA-based epoxy resin.

A more accurate criterion to determine the gel point is identification of the time at which tan δ (G"/G') becomes independent of frequency (ω) [16, 95]. tan δ vs. time was plotted at various ω in Figure 3.3c for the EVA-based epoxy resin. At early curing times, tan δ decreased with ω. At around 63 min, tan δ was independent of ω, indicating the gel point was reached. Similarly, for the DGEBA-based epoxy resins, the ω-independent tan δ was observed at 128 min (Figure 3.3d), indicating the gel point was higher than that of the EVA-based epoxy resin.

The volume change or shrinkage during curing is also important from a manufacturing point of view. We therefore further investigated the curing behavior through measuring changes in normal force at constant gap (fixed distance between parallel plates), and alternatively through measuring the needed sample gap to keep the normal force near 0 N during curing (Figure 3.3e). It is anticipated that the sample will undergo shrinkage during curing, leading to decrease in either measured normal force (measured at constant gap [96]) or sample gap (measured at constant normal force [98]). When the experiment was conducted at constant gap, the normal force was initially constant. After 70 min of curing the EVA-based epoxy resin, the force began to decrease and reached a minimum

value around 96 min, identifying gelation was taking place. After the normal force decreased to a certain point, it then began to increase. Similarly, when the experiment was conducted at constant normal force, the gap initially was constant and then began to decrease at around 50 min, reaching a minimum value at around 60 min (in the vicinity of the gel point as quantified above), and subsequently increased. We attributed the increase in either normal force or gap after gelation to relaxation of the material, as the measured T_g of the sample at this stage of curing was 63 °C, which is below the curing temperature of 70 °C. In the case of the DGEBA-based epoxy resin, the force reached a minimum value at around 131 min (at constant gap), and the gap reached a minimum value at around 112 min (at constant force). We calculated the volume of the sample during curing (Figure 3.3f**),** and the EVA-based epoxy resin showed an 0.4% change in volume upon curing, whereas the DGEBA-based epoxy resin showed an 0.3% change, indicating similar degree of shrinkage for both resins upon gelation.

Table 2 summarizes the viscoelastic properties and gel points (from various methods) of both the EVA- and DGEBA-based epoxy resins. Regardless of the criterion used for determining the gel point, the EVA-based epoxy resin required less time to achieve gelation as compared to the DGEBA-based epoxy resin, which is an advantageous property for manufacturing. After gelation, the EVA-based epoxy showed significantly higher moduli (G' and G'') and η* as compared to the DGEBA-based epoxy resins. The resins exhibited similar volume change during curing.

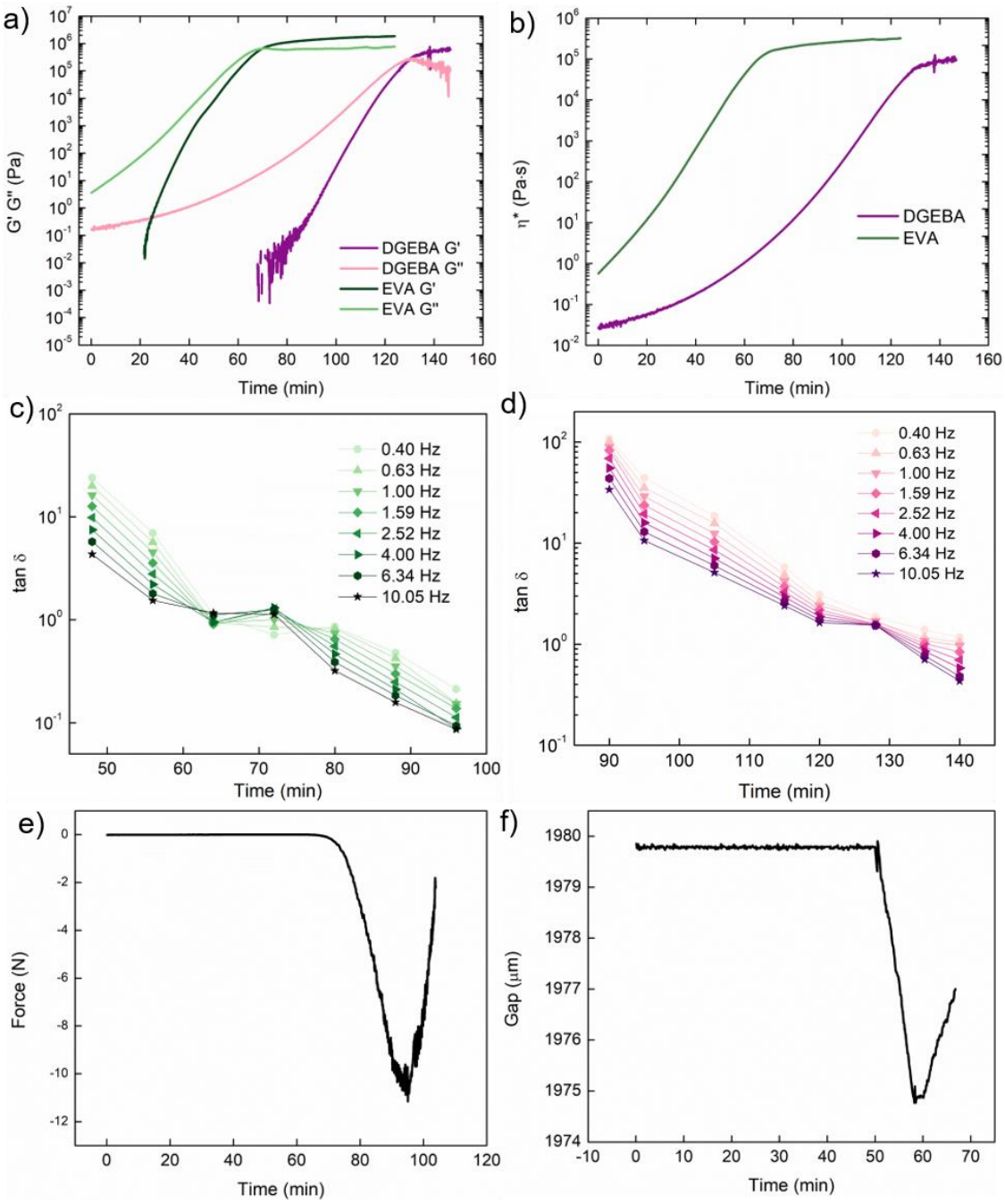

Figure 3. 3: Monitoring the viscoelastic properties of the EVA- and DGEBA-based epoxy resin during the first stage of the curing reaction at 70 °C: a) storage (G') and loss (G") moduli, b) complex viscosity η*, c) tan δ of EVA-based epoxy resin, d) tan δ of DGEBA-based epoxy resin e) measured normal force (at constant sample gap), and f) sample gap (at constant normal force) as a function of curing time (at frequency 1 Hz and strain 10%).

Table 3. 1: Rheological properties and gel point of epoxy resins

Monomer	G' (Pa)[a]	G" (Pa)[a]	η* (Pa-s)[a]	Gel point (min) from G' / G" crossover	Gel point (min) from tan δ	Gel point from change in η*
EVA	$1*10^6$	$6*10^5$	$2*10^5$	70	63	62
DGEBA	$3*10^5$	$8*10^5$	$2*10^4$	130	128	130

[a] Measured after 80 min curing at 70 °C for the EVA-based epoxy resin and after 2 h curing at 70 °C for the DGEBA-based epoxy resin (when each reached the plateau values), at frequency of 1 Hz and strain of 10 %.

3.3 Mechanical properties of EVA-based epoxy resins

We have previously reported that the T_g of the EVA-based epoxy resin is slightly higher than that of the DGEBA-based epoxy resin (Table 3.2) [87, 100]. It is unsurprising that the EVA-based epoxy resin can achieve the high T_g of the more traditional DGEBA-based resin, as the crosslink density of the two resins are comparable to one another (Table 3.2). Here, we focus on quantiifation of the tensile properties ands fracture mechanisms of the EVA-based epoxy resins, benchmarked to that of the DGEBA-based epoxy resin.

To measure the mechanical properties of EVA-based epoxy resins, tensile tests were conducted on multiple specimens (Figure A1.5), with average values of tensile strength, modulus and strain at break listed in Table 3.2. Representative data obtained from EVA-based and DGEBA-based epoxy resins are shown in Figure 3.4. We observed that

EVA-based and DGEBA-based epoxy resins had similar moduli (around 2.5 GPa) and the EVA-based epoxy resins exibited a slightly higher tensile strength (85 MPa) compared to that of the DGEBA-based epoxy resin (80 MPa). Both resins are brittle, with the strain at break of the EVA-based epoxy resin (5%) slightly lower than that of the DGEBA-based epoxy resin (8%). These results confirmed that EVA-based epoxy resin exhibits appropriate tensile behavior to function as a suitable replacement for the DGEBA-based epoxy resin in many applications. We attribute the high T_g, high crosslink density, and desirable tensile properties of the EVA-based epoxy resin to the presence of rigid aromatic rings in the monomer structure, which mimics that of DGEBA. The T_g of the tensile testing specimens were measured (Figure A1.6), and the resultig T_g values were comprable to that previously reported for the EVA-based epoxy resin [87].

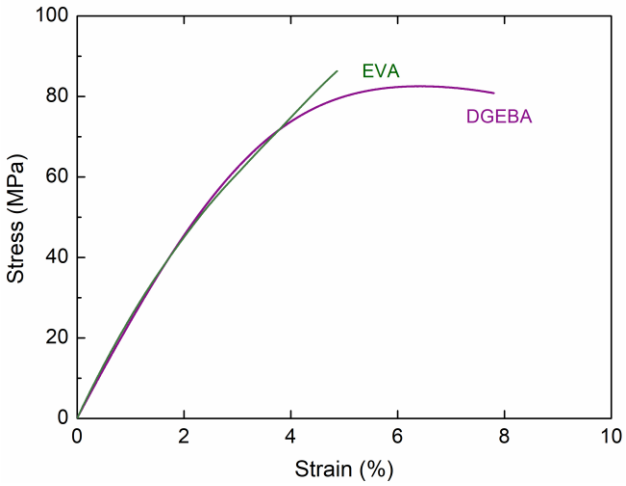

Figure 3. 4**:** Tensile testing data obtained from EVA- and DGEBA-based epoxy resins

Table 3. 2: Properties of EVA and DGEBA-based epoxy resins

Monomer	Tensile strength (MPa)	Modulus (GPa)	Strain at break (%)	T_g (°C)	E' (MPa) at T_g + 60 °C	Crosslink density (mmol/cm^3)[a]
EVA	85 ± 3	2.5 ± 0.4	5 ± 1	146 ± 2[a]	40 ± 4[a]	3.4 ± 0.3[a]
DGEBA	80 ± 2	2.5 ± 0.2	8 ± 2	140.1 ± 0.4[b]	36 ± 2[a]	3.5 ± 0.2[c]

[a] Reported in ref. [87]
[b] Reported in ref. [100]
[c] Provided in *Appendix 1*

3.4 Conclusions

Sustainable and degradable epoxy resin, EVA-based epoxy resin, was synthesized using green chemistry method. An optimized curing protocol was proposed to achieve high conversion of curing reaction between EVA monomer and MHHPA anhydride curing agent. The resulting EVA-based epoxy resins showed desirable thermal and mechanical properties compared to commercial DGEBA-based epoxy resins, mainly due to the rigid aromatic structures in the epoxy network. Additionally, EVA-based epoxy resins showed less gelation time under same curing temperature compared to DGEBA-based epoxy resins, indicating easier manufacturing in application field. EVA-based epoxy resins also exhibited higher moduli and complex viscosity compared to DGEBA-based epoxy resins. To summarize, lignin-derived EVA-based epoxy resin with desirable thermal, mechanical and degradable properties is good candidate for replacement of DGEBA-based epoxy resins.

Chapter 4: Accelerated hydrolytic degradation of ester-containing biobased epoxy resins

In this chapter, we investigated the accelerated hydrolytic degradation of epoxy resins in a basic solution at 80 °C, including a new epoxy resin derived from vanillic acid (a lignin-derived molecule), as well as epoxy resins derived from plant-based phenolic acids, soybean oil, and bisphenol A (the conventional epoxy monomer source). All biobased epoxy resins underwent rapid degradation in a basic solution as compared to the conventional DGEBA-based epoxy resin. ESO- and ESA-based epoxy resins exhibited the fastest degradation rates, whereas E4HBA- and EVA-based epoxy resins exhibited more moderate degradation rates. Variations in degradation rate are attributed to differences in epoxide content, monomer structure, degree of hydrophilicity, crosslink density, and proximity to glass transition temperature. The degradation profiles, mass loss as a function of exposure time in the basic solution, showed good agreement with predictions from a solid-state kinetic model. Mass spectrometry and scanning electron microscopy analyses confirmed the epoxy resins underwent hydrolytic degradation, through a surface erosion mechanism.

4.1 Epoxy monomer synthesis and epoxy resin curing protocol

A variety of biobased epoxy monomers, which contain ester groups, were prepared (Figure 4.1). Vanillic acid, derived from lignin [101, 102], was converted to epoxidized vanillic acid (EVA). Plant-based phenolic acids, salicylic acid and 4-hydroxybenzoic acid, were converted to epoxidized salicylic acid (ESA) and epoxidized 4-hydroxybenzoic acid (E4HBA), respectively. Epoxidized soybean oil (ESO) was obtained from a commercial source.

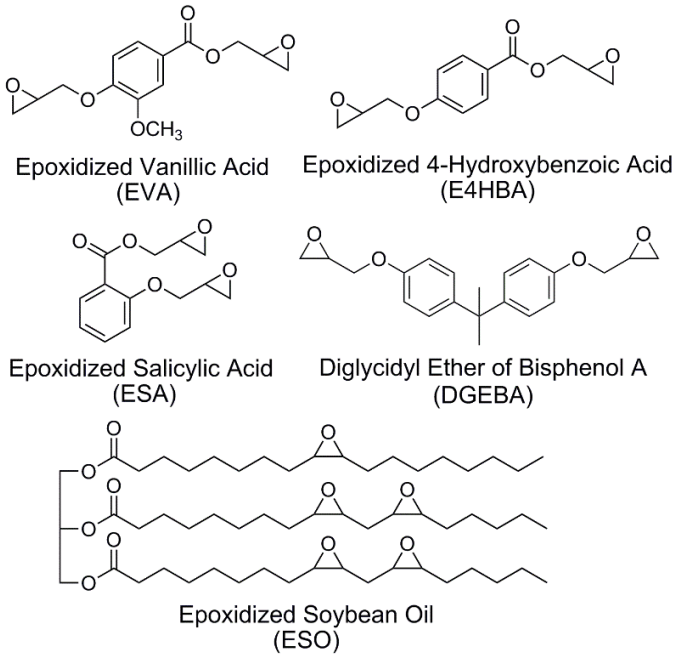

Figure 4. 1**:** Chemical structures of epoxidized vanillic acid (EVA), epoxidized salicylic acid (ESA), epoxidized 4-hydroxybenzoic acid (E4HBA), epoxidized soybean oil (ESO), and diglycidyl ether of bisphenol A (DGEBA), used in this study.

A two-step procedure was employed for the synthesis of EVA (Scheme 4.1). This procedure, based on literature [103], was previously reported by our group for the synthesis of ESA and E4HBA, and avoids the toxicity concerns of the use of epichlorohydrin. Briefly, vanillic acid was reacted with allyl bromide to form allylated vanillic acid (AVA), which was subsequently reacted with mCPBA to form EVA (Scheme 4.1). An alternative one-step synthetic protocol for the preparation of EVA has been previously reported [101].

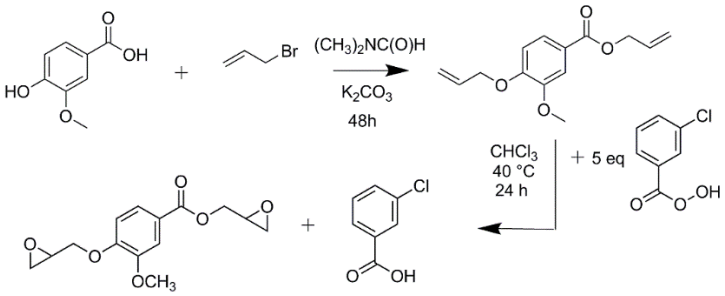

Scheme 4. 1**:** Synthesis of EVA.

^{1}H NMR analysis identified the structures of AVA and EVA (Figure 4.2; vanillic acid spectra shown in Figure A2.1 for reference). The peaks in the region of 5-6 ppm are associated with the allyl groups in AVA. The disappearance of the allyl group peaks at 5-6 ppm, and presence of epoxide peaks in the region of 2.5-3.5 ppm, confirmed the conversion of allyl groups to epoxide groups in EVA. The AVA and EVA structures were further confirmed with ^{13}C NMR analysis (Figure A2.2).

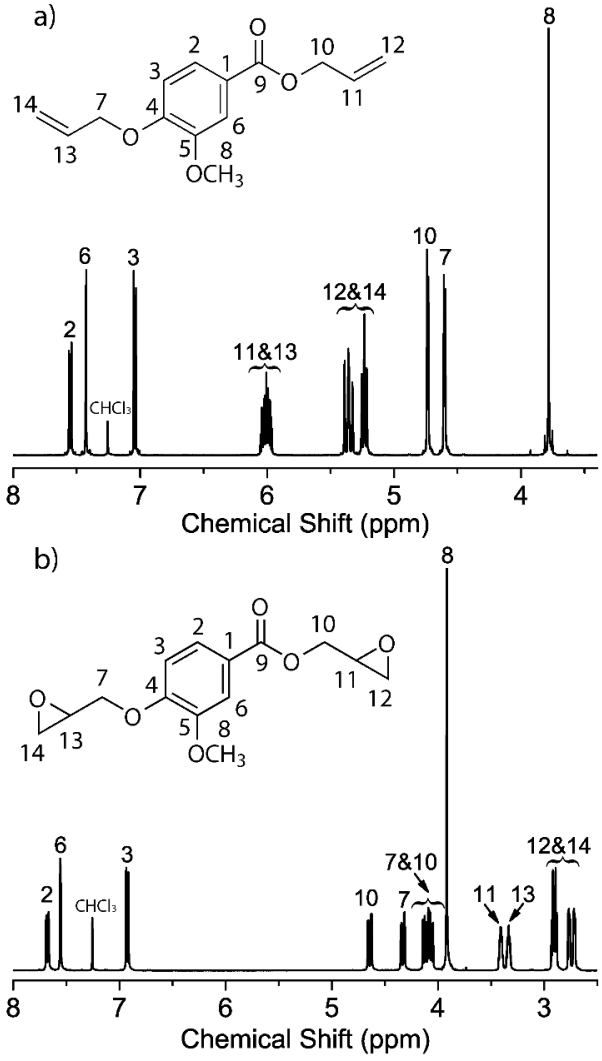

Figure 4. 2**:** ^{1}H NMR spectra of a) AVA and b) EVA. The conversion and yield of the allylation of vanillic acid to form AVA were 99% and 98%, respectively. The conversion and yield of the epoxidation of AVA to form EVA were 70% and 32%, respectively.

The epoxy monomers (EVA, ESA, E4HBA, ESO and DGEBA) were cured with a curing agent to form highly crosslinked epoxy resin thermosets. Following our prior work on the preparation of epoxy resins from ESA and E4HBA, we employed an anhydride curing agent (MHHPA) along with a catalyst (1-MI), shown in Figure 4.3. Previously, we demonstrated this curing agent produced biobased epoxy resins (using ESA and E4HBA monomers) with desirable thermal and mechanical properties.

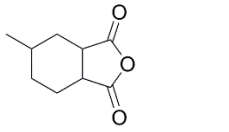

Methylhexahydrophthalic anhydride (MHHPA)

1-Methylimidazole (1-MI)

Figure 4. 3**:** Curing agent and catalyst used in this study.

The curing of the epoxy monomers with MHHPA/1-MI (Schemes A2.1-A2.5) was investigated with *in situ* DSC analysis. EVA was melted first at 94 °C (as its onset melting temperature was 91 °C, Figure A2.3) before adding the stoichiometric amount of curing agent and 1-MI catalyst and mixing them at 50 °C. The ESA, E4HBA, ESO, and DGEBA monomers were mixed with stoichiometric amounts of curing agent and 1-MI catalyst at 50 °C. The mixtures of epoxy monomer/MHHPA/1-MI were then sealed in DSC pans and monitored with DSC while heating at a constant rate of 10 ° C/min. The resulting DSC data are shown in Figure 4.4. While EVA, ESA, and E4HBA exhibited similar curing temperatures under constant heating rate to that of DGEBA, the ESO monomer required significantly higher temperature for complete curing. The higher curing temperature of the ESO-based epoxy resin is attributed to the presence of less accessible internal epoxide

groups; in contrast, DGEBA, EVA, ESA, E4HBA contain terminal epoxy groups [104, 105].

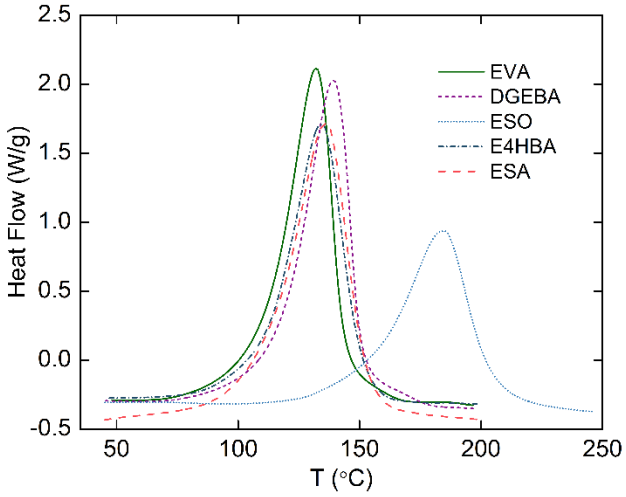

Figure 4. 4**:** *In situ* DSC data obtained upon curing EVA, ESA, E4HBA, ESO, and DGEBA monomers with MHHPA (catalyzed with 1-MI). (Data for ESA and E4HBA monomers were obtained from ref. [100]).

We employed a two-stage curing protocol for all of the epoxy resins, following our prior work. The first, lower temperature, curing stage was used to promote curing without evaporation of monomer or curing agent. The second, higher temperature, curing stage was selected well above the T_g of the cured resin to avoid vitrification and maximize reaction conversion. The onset evaporation temperatures for the epoxy monomers were identified from TGA as 275 °C (EVA), 90 °C (ESA), and 97 °C (E4HBA), and that of the MHHPA curing agent was 95 °C (Figures A2.3-A2.4). To avoid monomer evaporation, the first curing stage was conducted at 70 °C. After mixing the reactants and stirring at 50 °C for 10 minutes until the solution became transparent, the mixture was placed in a convection oven at 70 °C for various time periods until the mixture visually solidified (requiring 2 h of curing at 70 °C for EVA, ESA, E4HBA, and DGEBA, and 24 h of curing at 70 °C for

ESO). The temperature of the second curing stage was set at 170 °C, well above the T_g of the cured epoxy resins. To identify the time of the second curing stage, T_g was monitored as a function of second stage curing time (Figure A2.5). For all epoxy resins, an optimal second stage curing time was determined to be 2 h, allowing for maximum conversion, providing consistently high T_g values (with little deviation), and avoiding thermal degradation (Figure A2.5). The resulting EVA-based epoxy resin exhibited a high T_g (146 ± 2 °C), comparable to that of the traditional DGEBA-based epoxy resin (140.1 ± 0.4 °C) and slightly higher than that of the ESA- and E4HBA-based epoxy resins (131 ± 3 °C and 136 ± 5 °C, respectively). The ESO-based epoxy resin exhibited a significantly lower T_g (69 ± 7 °C).

4.2 Thermal properties and phase behavior of epoxy resins prepared from mixtures of ESO and DGEBA.

Mixtures of DGEBA and ESO monomers, with contents varying from 0-100 wt% ESO (of the total ESO and DGEBA content), were cured with a stoichiometric amount of MHHPA (catalyzed with 1-MI). The resulting epoxy resin T_g as a function of ESO content is shown in Table 4.2. Increasing the ESO content resulted in a substantial decrease in T_g. In addition, epoxy resins with higher ESO content exhibited larger deviations in the T_g. Optical microscopy was used to test the phase homogeneity of the epoxy resins (Figures 4.5 and A2.6). The background subtracted images indicated that the epoxy resins containing 40, 60 and 80% ESO (relative to the total amount of ESO and DGEBA) were macroscopically phase separated into ESO-rich and DGEBA-rich domains (both prior to and after the second curing stage), whereas the epoxy resin with 20 wt% ESO was homogeneous throughout the curing process. As DGEBA and ESO have disparate curing

kinetics (Figure 4.4), it is likely that the more rapid curing of the DGEBA monomer promotes phase separation of the DGEBA-rich domains from the unreacted ESO. The epoxy resin containing 40 wt% ESO exhibited a submicron average particle size of 0.6 μm (Table 4.1). A drastic increase in particle size was observed for the epoxy resins with 60 and 80 wt% ESO (9.4 and 9.8 μm, respectively). The morphology was also distinct for the three epoxy resins: the sample with 40 wt% ESO exhibited a co-continuous morphology whereas the 60 and 80 wt% samples exhibited dispersed particle morphologies, in which the particles aggregated into strands in the 80 wt% sample.

Table 4. 1**:** T_g and domain size for epoxy resins prepared from mixtures of ESO and DGEBA cured with MHHPA/1-MI.

Monomer[a]	T_g (°C)	Domain size (μm)
0% ESO	140.1 ± 0.4	NA[b]
20% ESO	120 + 2	NA[b]
40% ESO	117 ± 2	0.6 ± 0.1[c]
60% ESO	103 ± 1	9.4 ± 0.4[d]
80% ESO	90 ± 6	9.8 ± 0.4[d]
100% ESO	69 ± 7	NA[b]

[a] wt% ESO indicates ESO content relative to total amount of ESO and DGEBA
[b] Homogeneous samples
[c] Characterized from FFT of the optical micrograph (domain size = $2\pi/q$)
[d] Sauter-mean diameter of the dispersed particles (Equation 2.1). Particle size distributions shown in Figure A2.7.

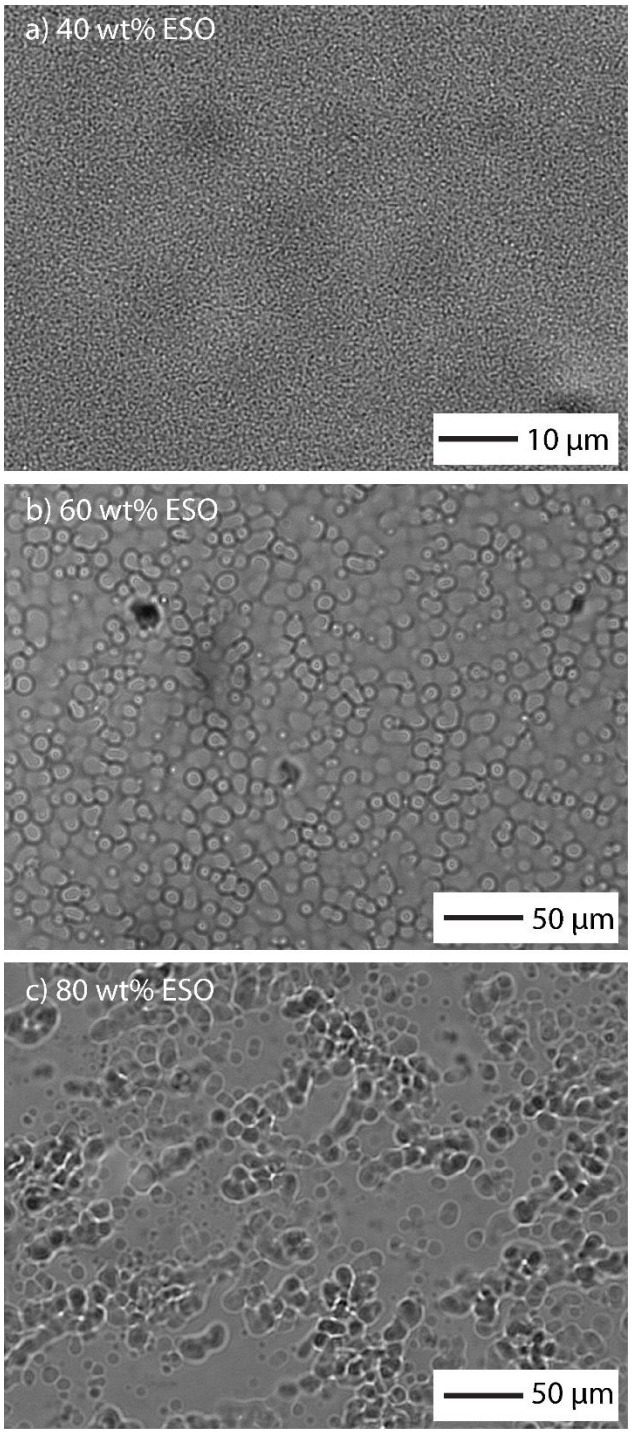

Figure 4. 5**:** Optical microscopy images of epoxy resins with differing ESO content (wt% ESO is the ESO content relative to the total amount of ESO and DGEBA).

4.3 Degradation behavior of biobased epoxy resins in basic solutions

The hydrolytic degradation behavior of the epoxy resins was characterized by placing the samples in 3 wt% NaOH solution at 80 °C and monitoring their mass as a function of exposure time in the basic solution (Figure 4.6). All biobased epoxy resins, in which the epoxy monomers contain ester groups, exhibited significantly more rapid degradation rates relative to the DGEBA-based epoxy resin (Figure 4.6a). The anhydride-cured ESO-based epoxy resin exhibited the fastest degradation rate (disappearing within 4-5 days, Figure 4.6a). While the curing of an epoxy monomer with an anhydride curing agent produces a small concentration of esters throughout the epoxy network, amine-curing does not have this affect. The anhydride-cured ESO-based epoxy resin exhibited a slightly faster degradation rate than that of the amine-cured ESO-based epoxy resin reported previously by our group. The rapid degradation behavior of the ESO-based epoxy resin is in stark contrast to the behavior of the DGEBA-based epoxy resin: with anhydride-curing, the DGEBA-based epoxy resin showed a slow degradation rate (Figure 4.6), and with amine-curing, it did not exhibit any noticeable mass loss in the basic solution, for up to 3 months.[90] The ESA-based epoxy resin also rapidly degraded, at a rate slightly slower than that of the ESO-based epoxy resin. E4HBA- and EVA-based epoxy resins exhibited more moderate degradation rates (Figure 4.6a). We also probed the degradation behavior of epoxy resins synthesized from mixtures of ESO and DGEBA monomers, in which the degradation rate was tunable based upon the relative concentration of ESO in the epoxy resin. The degradation rate systemically increased with increasing ESO content in the epoxy resin (Figures 4.6b and 4.6c). Camera images of the epoxy resins at different degradation times are shown in Figure 4.7.

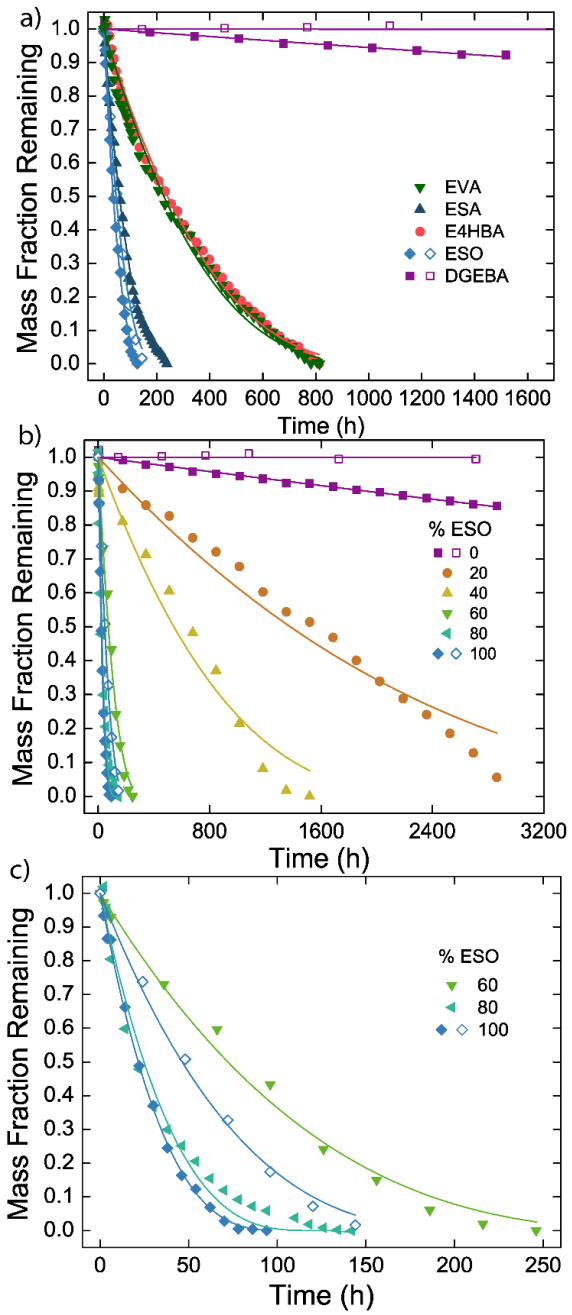

Figure 4. 6**:** Fraction of mass remaining of epoxy resins as a function of exposure time in a 3 wt% NaOH solution at 80 °C for: a) EVA, ESA, E4HBA, ESO and DGEBA-based epoxy resins; and b) c) epoxy resins prepared from mixtures of ESO/DGEBA with varying ESO content (relative to total amount of ESO and DGEBA).

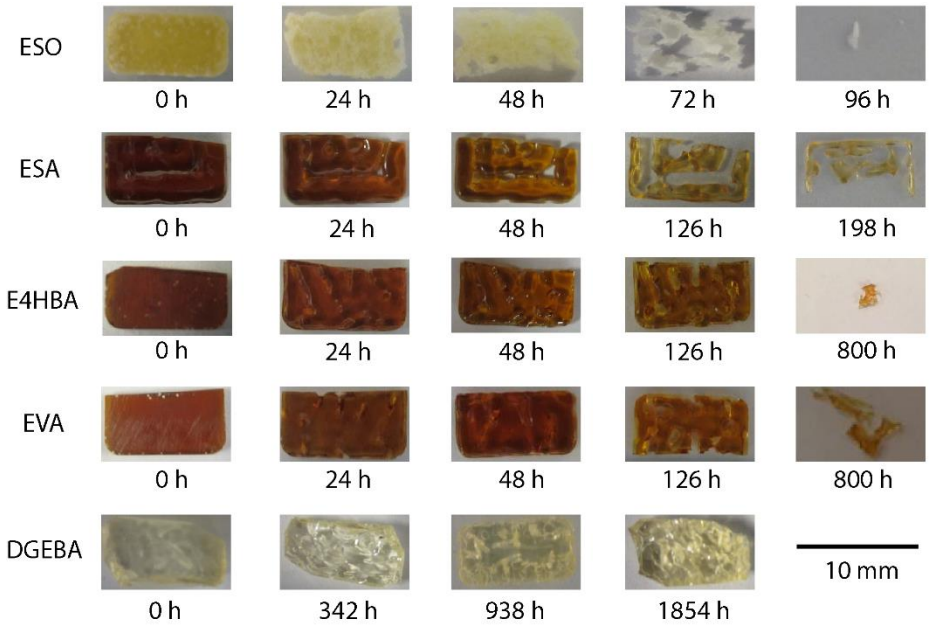

Figure 4. 7**:** Camera images of epoxy resin specimens following exposure to a 3 wt% NaOH solution at 80 °C.

4.4 Exploration of a model for ester-containing thermoset degradation

It is well established that linear polyesters undergo significantly different degradation behaviors in basic and acidic solutions [28, 106]. Polyesters degrade through two primary mechanisms: bulk and surface erosion, which occur in acidic and basic solutions, respectively [22, 23]. In bulk erosion, hydrolysis occurs throughout the entire specimen simultaneously, whereas in surface erosion, hydrolysis mainly occurs in the region near the surface. The hydrolysis mechanisms of linear polyesters such as polylactide and poly(lactide-*co*-glycolide) have been described with well-established models [107-109], but few studies have examined the degradation behavior of crosslinked thermosets containing ester groups. We therefore hypothesized that epoxy thermosets containing ester groups would also follow the surface erosion mechanism in basic solutions.

The contracting volume model describes the dissolution of a cubic solid governed by contraction of the sample volume as the solid-liquid interface moves toward the specimen center. In application of this model, the rate limiting step in the erosion of the sample is assumed to be contraction of the solid-liquid interface, rather than nucleation, diffusion, or even the chemical reaction which occurs at the surface. A prior literature study has successfully applied this model to the catalyzed solvolysis of a DGEBA-based epoxy resin at elevated temperatures. We have extended this model to the rectangular cuboid-shaped degradation samples employed in this study (described in the *Appendix 2*),

$$1 - (1 - \alpha)^{1/3} = kt \qquad \text{(eqn. 4.1)}$$

where α is the mass fraction of the sample remaining at time t, and k is the degradation rate constant.

The contracting volume model was applied to mass loss data obtained from the biobased epoxy resins in 3 wt% NaOH solution at 80 °C (solid curves in Figure 4.6). The model described the degradation profile well for all the neat epoxy resins (with R^2 values of 0.985 to 0.998 (Figure 4.6a)). We considered other solid-state kinetic models, such as n^{th} order reaction models, diffusion-based models, and nucleation-based models, but these models provided a worse fit to the data (Figure A2.10 and Table A2.2). There were larger deviations between the model and data for epoxy resins synthesized from mixtures of ESO and DGEBA with lower ESO content (20-40 wt% ESO, with R^2 values ranging from 0.950 to 0.958). There may be some influence of the presence of macroscopically phase separated ESO-rich and DGEBA-rich domains on the degradation rate. Additionally, the ESO segments of the network may not be uniformly distributed throughout the network, which could influence the observed degradation rate.

The fitted rate constants (k) for all the epoxy resins are listed in Tables 4.2 and 4.3. The ESO-based epoxy resin (with the highest concentration of esters in the epoxy network - 3 esters per ESO monomer) exhibited the largest degradation rate constant k, followed by the ESA-based epoxy resin. Interestingly, though the ESA and E4HBA monomers contain the same number of ester groups (1 per monomer), and differ only in the placement of the ester groups along the aromatic ring (*ortho* vs. *para* placement, respectively), the E4HBA-based epoxy resin showed a more moderate degradation rate constant than that of the ESA-based epoxy resin. EVA- and E4HBA-based epoxy resins, which contain the same *para* placement of ester groups on the epoxy monomer and differ only in the addition of a methoxy group to the EVA monomer, exhibited indistinguishable degradation rate constants. Finally, the DGEGA-based epoxy resin, for which the DGEBA monomer does not contain any ester groups, exhibited a significantly smaller degradation rate constant as compared to all biobased epoxy resins. The rate constant for epoxy resins synthesized from mixtures of DGEBA and ESO increased systematically with increasing ESO content in the resin (Table 4.3).

Table 4. 2**:** Degradation rate constant, k (in a 3 wt% NaOH solution at 80 °C) and physical properties of epoxy resins cured with MHHPA/1-MI.

Monomer	k ($\times 10^{-3}$ mm^{-1} hr^{-1})	T_g (°C)	Water Contact Angle (°)	# of esters in epoxy monomer	Crosslink Density (mmol/ cm^3)	Ester Density (mmol/ cm^3)
ESO	8.4 ± 0.9	69 ± 7	53 ± 2	3	1.4 ± 0.2	5.6 ± 0.8
ESA	2.9 ± 0.6	131 ± 3	59 ± 1	1	2.4 ± 0.2	7.2 ± 0.6
E4HBA	0.8 ± 0.3	136 ± 5	61 ± 2	1	3.3 ± 0.3	9.9 ± 0.9
EVA	0.8 ± 0.1	146 ± 2	58 ± 3	1	3.4 ± 0.3	10.2 ± 0.9
DGEBA	0.02 ± 0.01	140.1 ± 0.4	65 ± 1	0	3.5 ± 0.2	3.5 ± 0.2

Table 4. 3**:** Degradation rate constant, k (in a 3 wt% NaOH solution at 80 °C) for epoxy resins prepared from mixtures of ESO and DGEBA cured with MHHPA/1-MI.

Monomer[a]	k ($\times 10^{-3}$ mm^{-1} hr^{-1})
0% ESO	0.02 ± 0.01
20% ESO	0.17 ± 0.02
40% ESO	0.44 ± 0.02
60% ESO	2.9 ± 0.1
80% ESO	9.0 ± 0.7
100% ESO	8.4 ± 0.9

[a] wt% ESO indicates ESO content relative to total amount of ESO and DGEBA

4.5 Investigation of the degradation mechanisms in ester-containing thermosets

SEM was used to further confirm the surface erosion mechanism of the epoxy resins in basic solutions. The surfaces of neat ESO and DGEBA-based epoxy resins, as well as those degraded in basic solutions for 6 and 50 h, were observed with SEM (Figure 4.8). Both neat samples had homogeneous and flat surfaces. After 6 h in basic solution, the ESO-based epoxy resin exhibited various-sized crevices in the surface, whereas the DGEBA-based epoxy resin exhibited only minor scratches. As the degradation time increased, both the crevices on the ESO-based epoxy resin and the scratches on the DGEBA-based epoxy resin surfaces grew, an indication of surface erosion. The crevices on the surface of the ESO-based epoxy resin likely provided pathways for more regions of the sample to be exposed to the solution.

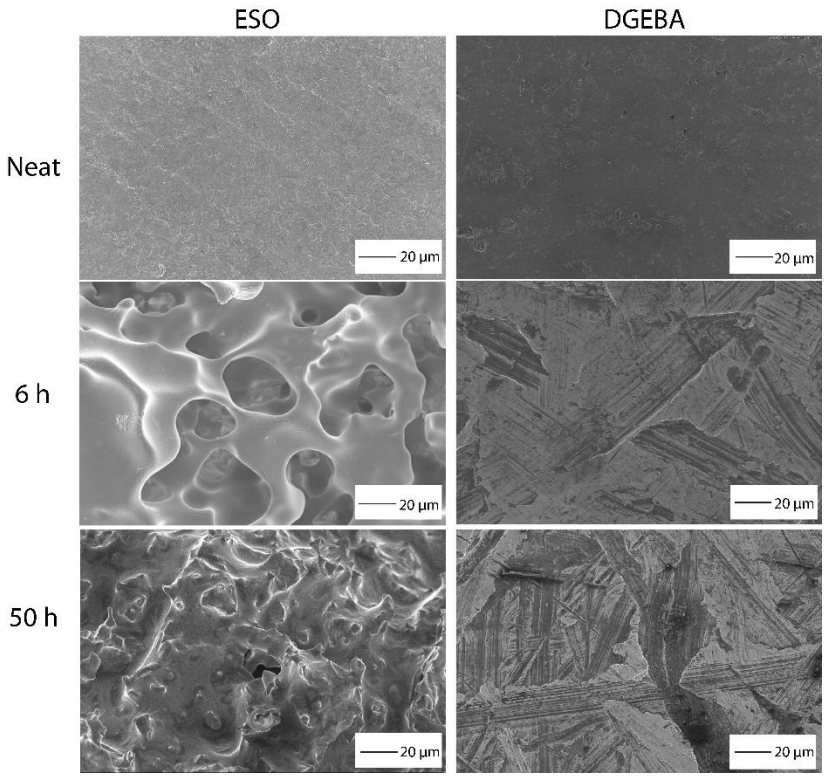

Figure 4. 8**:** SEM images of the surfaces of ESO-based and DGEBA-based epoxy resins, showing surface changes after soaking in a 3wt% NaOH solution at 80 °C for 6 and 50 h. (Lower magnification images are shown in Figure A2.8).

Mass spectrometry was used to investigate the degradation mechanism (Figures 4.9 and A2.9). We fully degraded the ESO-based epoxy resin and removed all the solvent. The degradation products were then dissolved in acetonitrile, at a concentration of 10 µg/ml. Soybean oil is comprised of a mixture of fatty acids,[110] mainly oleic acid, linoleic acid, linolenic acid, and smaller contents of stearic acid and palmitic acid. Therefore, the ESO monomer may contain any combination of these fatty acids, in which unsaturated carbon-carbon double bonds have been converted to epoxide groups. We considered all possibilities for the ESO monomer chemical structure (detailed description in the *Appendix 2*). We also considered that in addition to the esters present on the ESO monomer, anhydride curing may result in ester formation. The spacing of isotope peaks on the mass

spectrum indicated that all molecules had single charges. With this information, we calculated the m/z values of each of the possible chemical fragments that could remain after cleavage of the ester groups on the epoxy resin network through ester hydrolysis (Scheme 4.2). We also considered the presence of either H^+ or Na^+ ions, and the possibility of exchange between H and Na within the molecules (Na was likely present due to the use of NaOH for the degradation process). Mass spectrometry peaks with intensities below 500 were neglected, as this is commensurate with the background intensity.

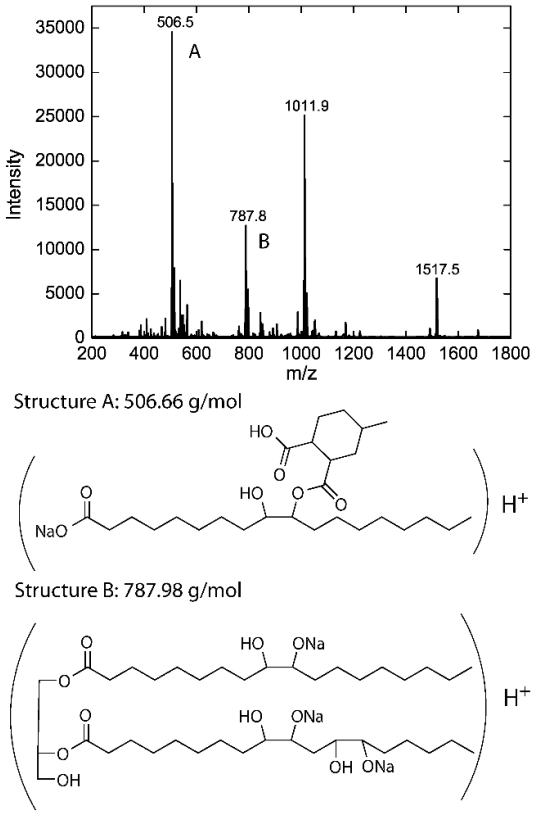

Figure 4. 9**:** Mass spectrometry analysis of degradation products of the ESO-based epoxy resin. The peaks labeled A and B are associated with the structures indicated below the data.

There were four main components in the degradation products, whose m/z values were 506.5, 787.8, 1011.9 and 1517.5. The peaks located at 506.5 and 787.8 are consistent

with the two degradation products whose molecular structures are shown as A and B in Figure 4.9. Aggregates of two or three molecules with structure A are consistent with the peaks observed at 1011.9 and 1517.5 m/z, respectively. The presence of these major degradation products further confirmed that mechanism of the degradation was the hydrolysis of the ester groups. Other minor peaks present in the spectrum were also investigated and the structures are shown in Table A2.2.

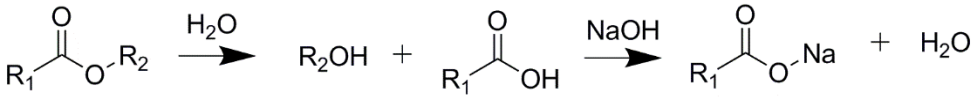

Scheme 4. 2: Epoxy resin degradation through ester hydrolysis (with neutralization reaction).

4.6. Additional factors influencing epoxy resin degradation in basic solutions

Many factors may potentially influence the degradation rates of epoxy resins in basic solution (Table 4.2). We anticipate that the hydrophilicity of the epoxy resin surface plays an important role in the surface erosion process.[77, 111, 112] We measured the water contact angle on the epoxy resin surfaces, and found that the ESO-based epoxy resin was the most hydrophilic, whereas the DGEBA-based epoxy resin was the most hydrophobic (Table 4.2). Additionally, we may consider proximity to the T_g and crosslink density as factors that may influence the degradation rate[77, 111, 112]. The ESO-based epoxy resin exhibited a significantly reduced T_g as compared to the other epoxy resins (Table 4.2) We used DMA to calculate the crosslink density of all the epoxy resins (detailed information will be discussed in Chapter 5 for the EVA-, DGEBA-, and ESO-based epoxy resins and DMA data and analyses for the ESA- and E4HBA-based epoxy resins are provided in Figure 2.11 of Appendix 2), and the crosslink densities of all resins are provided in Table 4.2. The low T_g

(below the temperature at which sample degradation was conducted) and reduced crosslink density may have accelerated the degradation rate of the ESO-based epoxy resin. By contrast, two of the biobased epoxy resins containing aromatic groups (E4HBA, and EVA) both exhibited similar T_g's, and similar crosslink densities, as compared to the DGEBA-based epoxy resin (Table 4.2). ESA-based epoxy resins, however, had lower crosslink density compared to other aromatic-containing epoxy resins. This may be due to the *ortho* position of two epoxy groups in ESA monomer, creating limited space for further crosslinking reaction. On the other hand, the E4HBA and EVA-based epoxy resins had very similar crosslinking density to the DGEBA-based epoxy resin, likely due to the similar *para* position of the two epoxy groups. The addition of the methoxy group in the aromatic structure of the EVA monomer had little impact on the degradation rates as the EVA- and E4HBA-based epoxy resins showed very similar degradation behaviors. As degradation proceeds as hydrolysis of ester groups, the ester density should have a large influence on the degradation rate. We calculated the ester density from the crosslink density and ester groups per epoxy monomer (Table 4.2). We noticed that EVA- and E4HBA-based epoxy resins with similar and highest ester density, also showed very similar degradation rates. ESO- and ESA-based epoxy resins that have lower ester density than other biobased epoxy resins showed faster degradation rates, which we attribute to their lower crosslink density and higher degree of hydrophilicity. The DGEBA-based epoxy resin that exhibited the slowest degradation rate also had the lowest ester density. Thus, the accelerated degradation rates of these biobased epoxy resins as compared to the DGEBA-based epoxy resin is likely due to their increased ester content, higher degree of hydrophilicity, and in the case of ESO- and ESA-based epoxy resins, lower crosslink density of the network. All the factors including crosslink density,

ester density and degree of hydrophilicity showed a combined impact on the observed degradation rates.

4.7 Conclusions:

We investigated the accelerated hydrolytic degradation of epoxy resins in a basic solution at 80 °C, including a new epoxy resin derived from vanillic acid (a lignin-derived molecule), as well as epoxy resins derived from plant-based phenolic acids, soybean oil, and bisphenol A (the conventional epoxy monomer source). The biobased epoxy resins (excluding the vegetable oil- based resins) exhibited glass transition temperatures comparable to that of the conventional epoxy resin. The biobased epoxy resins all exhibited more rapid hydrolytic degradation behavior due to higher ester content and higher degree of hydrophilicity, in contrast to the conventional DGEBA-based epoxy resin. The degradation rate of the ESO-based epoxy resin was further enhanced by reduced glass transition temperature and crosslink density. A solid-state kinetic model was used to model the degradation behavior, which was in good agreement with experimental data for the neat epoxy resins. The ESO-based epoxy resin (containing 3 esters per monomer) exhibited the largest degradation rate constant k, followed by the ESA-based epoxy resin (1 ester per monomer, *ortho* placement of ester groups). EVA- and E4HBA-based epoxy resins (1 ester per monomer, *para* placement of ester groups, and similarly high ester density) exhibited more moderate, and indistinguishable, degradation rate constants. Finally, the DGEBA-based epoxy resin (with the lowest ester density) exhibited a significantly smaller degradation rate constant as compared to all biobased epoxy resins. Epoxy resins derived from mixtures of ESO and DGEBA showed tunable degradation rate constants, systematically increasing as the ESO wt% constant was increased. The degradation

mechanism was explored and confirmed as surface erosion. Mass spectrometry analysis verified degradation proceeded through hydrolysis of ester groups. These results demonstrate biobased epoxy resins with higher ester contents and higher degree of hydrophilicity can be hydrolytically degraded more rapidly than conventional epoxy resins, and under mild conditions (low temperatures, and in aqueous solutions), which could be leveraged for the creation of biodegradable thermoset polymers.

This chapter extends the existing knowledge of thermoset degradation behavior, showing biobased epoxy resins with higher ester contents undergo rapid degradation under mild conditions (low temperatures and thus low energy requirements, and in aqueous solutions). As hydrolytic degradation is an important aspect of polymer biodegradation, these results may be extended to create biodegradable thermoset polymers, which can be processed at the end of their life in a compost environment, providing new thermoset waste treatment options.

Chapter 5: Degradation behavior of biobased epoxy resins in mild acidic media

In this chapter, the accelerated hydrolytic degradation of biobased epoxy resins, prepared through anhydride curing of epoxidized vanillic acid (EVA, a product of lignin depolymerization) and epoxidized soybean oil (ESO) was investigated in acidic solutions. The biobased epoxy resins exhibited sigmoidal degradation kinetics in acidic solutions, consistent with bulk erosion mechanisms observed in linear polyesters. By contrast, earlier work reported surface erosion behavior of these biobased epoxy resins in basic solution. A solid-state reaction order model with autocatalysis was utilized to predict the mass fraction remaining as a function of exposure time in acidic solution and the data and model were in good agreement. Mass spectrometry and Fourier-transform Infrared Spectroscopy analyses confirmed the degradation mechanism as cleavage of ester groups in the crosslinked structures. The influences of solvent composition and temperature on degradation kinetics were also explored. These results demonstrate ester-containing epoxy resins undergo hydrolysis in acidic solutions, providing a route for end-of-life management of thermoset waste.

5.1 Epoxy Resin Synthesis and Characterization

Vanillic acid, a byproduct of lignin depolymerization, was converted to EVA following our previously reported procedures. We avoided the use of epichlorohydrin, a known chemical with high toxicity. Instead, we employed a two-step procedure: allylation (vanillic acid was reacted with allyl bromide) followed by epoxidation (through reaction with mCPBA) to form EVA. The resulting product was analyzed with ^{1}H NMR and ^{13}C NMR, confirming the presence of EVA (Figure A3.1 in the *Appendix 3*). ESO was purchased from a commercial source. EVA and ESO were cured through reaction with the

anhydride curing agent MHHPA (catalyst 1-MI was also added into the reaction mixture). The development of the curing protocol was discussed in our previous work. For EVA/MHHPA, the resin was cured at 70 °C for 2 h and 170 °C for 2 h. For ESO/MHHPA, the resin was cured at 70 °C for 24 h and 170 °C for 2 h. Using these protocols, the conversion of functional groups during curing was 98% and 79% for EVA- and ESO-based epoxy resins, respectively. Figure 5.1 illustrates the chemical structures of the epoxy monomers, curing agent, and catalyst.

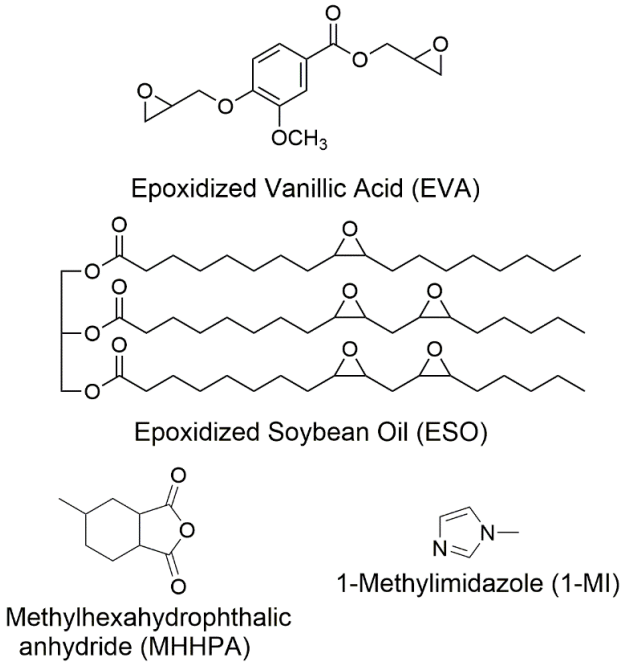

Figure 5. 1**:** Chemical structures of epoxidized vanillic acid (EVA), epoxidized soybean oil (ESO), as well as the curing agent (methylhexahydrophthalic anhydride) and catalyst (1-methylimidazole).

The storage modulus (E') of each epoxy resin was measured using DMA (Figure 5.2). The rubbery plateau occurred at around 170 ℃ and 110 °C for EVA- and ESO-based epoxy resins, respectively. The crosslink density (ν_e) was calculated using the theory of rubber elasticity:

$$\nu_e = \frac{E'}{3RT} \qquad \text{(eqn. 5.1)}$$

where R is the gas constant and T is the absolute temperature. For the determination of ν_e, E' was quantified at a temperature T = T_g + 60 °C, chosen following literature precedence, where T_g is the glass transition temperature. T_g of each epoxy resin is summarized in Table 5.1). ν_e of the EVA-based epoxy resin was appropriately 2.4 times higher than that of the ESO-based epoxy resin (Table 5.1). The more flexible structure of ESO created a lower density epoxy network, with lower T_g as compared to the EVA-based epoxy resin. The density of ester groups in the network (ν_{ester}) was also calculated, using knowledge of the theoretical network structure and ester content of each strand, and measured ν_e. This calculation is described in detail in the *Appendix 3* (Figures A3.2 and A3.3 and Schemes A3.1 and A3.2) and the ester density is summarized in Table 5.1. Though the ESO monomer has 3 ester groups, whereas the EVA monomer has only 1, the more compact structure of the EVA monomer, and resulting significantly higher crosslink density, led to the higher ester concentration of the EVA-based epoxy resin as compared to the ESO-based epoxy resin (Table 5.1).

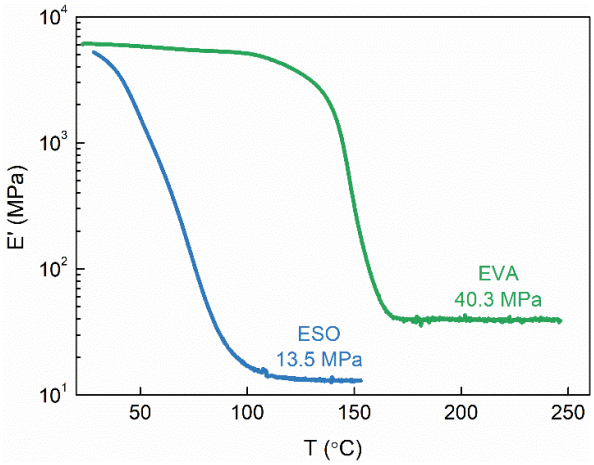

Figure 5. 2: Storage modulus of EVA- and ESO-based epoxy resins measured by DMA.

Table 5. 1**:** Characteristics of EVA- and ESO-based epoxy resins

Epoxy Monomer[a]	T_g (°C)[b]	E' (MPa)[c] at T_g + 60 °C	ν_e (mmol/cm^3)[c]	ν_{ester} (mmol/cm^3)[d]	θ (°)[e] Acetone/H_2O	θ (°)[e] THF/H_2O	θ (°)[e] DMF/H_2O	θ (°)[e] H_2O
EVA	146 ± 2	40 ± 4	3.4 ± 0.3	10.2 ± 0.9	51 ± 1	54 ± 3	59 ± 2	58 ± 3
ESO	69 ± 7	13.5 ± 0.2	1.4 ± 0.2	5.6 ± 0.8	45 ± 3	46 ± 3	56 ± 2	53 ± 2

[a] Cured with MHHPA / 1-MI
[b] Glass transition temperature (T_g) measured with differential scanning calorimetry.
[c] Storage modulus (E') and crosslink density (ν_e) measured with DMA
[d] Ester density (ν_{ester}) in the network, calculated in the *Appendix 3*
[e] Contact angles (θ) of epoxy resins using various solvent mixtures at 25 °C. The solvent compositions were equivalent to that used in degradation experiments. 100 g concentrated HCl (32 g HCl and 68 g water) was added to 220 g of the diluting solvent (water, THF, acetone or DMF).

The contact angles of various solvent systems (acetone/H_2O, THF/ H_2O, DMF/ H_2O, pure H_2O) were measured for both ESO- and EVA-based epoxy resins, and the results are summarized in Table 5.1. The contact angle for the ESO-based epoxy resin was consistently lower than that of the EVA-based epoxy resin, for the various solvent systems studied. For both resins, the contact angle was lower for acetone/H_2O and THF/water, and higher for DMF/water and pure water.

5.2 Quantifying Degradation Rates and Identifying Erosion Mechanisms of Biobased Epoxy Resins in Acidic Aqueous Solutions

Both EVA- and ESO-based epoxy resins were degraded in a 10 wt% HCl aqueous solution. The ESO-based epoxy resin degraded more rapidly (disappearing within 296 h) as compared to the EVA-based epoxy resin (disappearing within 1,584 h) (Figure 5.3). This trend is similar to that previously observed in basic solution, in which the ESO-based

epoxy resin exhibited faster degradation. There are many factors which impact the hydrolytic degradation rate of the epoxy resins in both acidic and basic solutions. The ester density is higher for the EVA-based epoxy resin, yet the ESO-based epoxy resin is slightly more hydrophilic (Table 5.1). Importantly, the ESO-based epoxy resin has a more open network structure, with lower ν_e and T_g (the degradation experiments in acidic water were conducted at 80 °C, which is above the T_g of the ESO-based epoxy resin).

The degradation profiles in acidic and basic solutions are contrasted in Figure 5.3. In basic solution, the epoxy resin mass loss began immediately after immersion in the medium, and mass continuously reduced linearly with time, characteristic of surface erosion where bond cleavage is faster than solvent diffusion. This behavior has been observed previously for linear polyesters in basic solutions, such as polylactic acid (PLA) and poly(lactic acid-*co*-glycolic acid) (PLGA). By contrast, in acidic solution, both the EVA- and ESO-based epoxy resins exhibited a delay period during which mass loss did not commence after immersion in the acidic medium. After this delay, mass loss occurred dramatically (Figure 5.3). At longer times, both epoxy resins exhibited deceleration during the final stages of the degradation process. The degradation profiles in acidic solution are thus consistent with a sigmoidal curve. These trends correspond well with literature on degradation behavior of linear polyesters in acidic solutions, in which bulk erosion occurs. During bulk erosion of linear polyesters, it takes some time for the solution to immerse into the polymer matrix, after which the polymer matrix degrades rapidly.

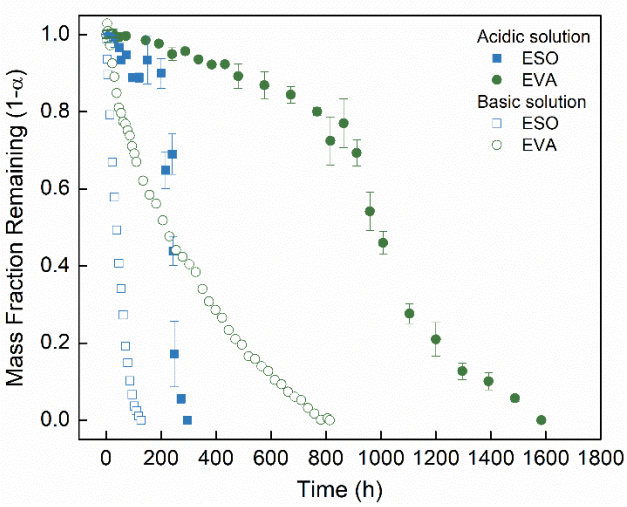

Figure 5. 3**:** Mass fraction remaining of ESO- and EVA-based epoxy resins in 10 wt% HCl aqueous solution at 80 °C (closed symbols) and 3 wt% NaOH aqueous solution at 80 °C (open symbols).

We observed slight swelling of the samples in acidic solution at early times (the mass increased by 0.3% within the first 8 h for the ESO-based epoxy resin and by 0.4% within the first 24 h for the EVA-based epoxy resin). This swelling behavior is attributed to absorption of the acidic solution into the samples, consistent with the bulk erosion mechanism. The relatively longer swelling time of EVA-based epoxy resins is attributed to the more hydrophobic surface and higher glass transition temperature of EVA-based epoxy resins compared to ESO-based epoxy resins (Table 5.1).

5.3 Models for Predicting Degradation of Epoxy Resins in Acidic Media

Few studies have examined models to predict the degradation behavior of crosslinked thermoset polymers. In our prior study, we demonstrated that EVA- and ESO-based epoxy resins underwent surface erosion in basic solution (3 wt% NaOH aqueous solution) and a contracting volume model was utilized to predict the degradation behavior. Here, we evaluate solid-state kinetic models for predicting degradation behavior of epoxy resins in acidic solution. The mass remaining as a function of exposure time in the acidic

solution was consistent with a sigmoidal curve for both ESO- and EVA-based epoxy resins (Figure 5.3). We considered the use of various solid state reaction models: reaction order models, diffusion-based models, nucleation-based models, and the contracting volume model that we used previously for degradation in basic solutions (model fitting shown in Figures A3.5-A3.7 in the *Appendix 3*). Two solid state kinetic models were able to capture the sigmoidal behavior observed in Figure 5.3: a reaction order model with autocatalysis, and the nucleation model. As reaction order models with autocatalysis have been previously applied to linear polyesters, it is therefore reasonable to expect that the ester-containing thermosets would undergo hydrolysis through a similar mechanism. We will therefore focus our discussion on the application of the reaction order model with autocatalysis to the degradation data (and the application of the nucleation model is discussed in the *Appendix 3*).

The hydrolysis of ester bonds under acidic conditions forms molecules containing carboxylic acid end-groups (Scheme 5.1), which can further catalyze hydrolysis. This phenomenon is called autocatalysis. Many studies have demonstrated that autocatalysis is of great importance in accelerating hydrolysis of ester groups.

The general form for an autocatalyzed reaction is

$$\frac{d\alpha}{dt} = (k_1 + k_2\alpha^m)(1-\alpha)^n \qquad \text{(eqn.5.2)}$$

where $\propto$ is the mass fraction degraded at time t

$$\propto = \frac{m_0 - m}{m_0} \qquad \text{(eqn.5.3)}$$

and m_0 is the initial mass at $t = 0$, m is the mass at time t, k_1 is the catalyzed rate constant (in this study, hydrolysis is acid-catalyzed), k_2 is the autocatalyzed rate constant, and m and n are reaction orders.

In the hydrolysis of linear polyesters, degradation kinetics were assumed to be first order in acidic conditions, indicating the reaction rate is only related to the concentration of ester groups in the system. Thus, we treat $n = 1$ in eqn. 5.2. We also consider that the autocatalytic effect is primarily related to the concentration of carboxylic acid groups produced by hydrolysis, and thus $m = 1$ in eqn.5. 2. Therefore, eqn. 5.2 can be simplified as

$$\frac{d\alpha}{dt} = (k_1 + k_2\alpha)(1 - \alpha) \qquad \text{(eqn.5.4)}$$

, with the integration of eqn. 5.4 we obtained

$$\ln\frac{k_1 + k_2\alpha}{1-\alpha} = (k_1 + k_2)t + C \qquad \text{(eqn.5.5)}$$

, and with application of the boundary condition that at $t = 0$, $\alpha = 0$:

$$C = lnk_1 \qquad \text{(eqn.5.6)}$$

The mass fraction remaining is therefore

$$1 - \alpha = \frac{k_1 + k_2}{\exp[(k_1 + k_2)t + \ln k_1] + k_2} \qquad \text{(eqn.5.7)}$$

Application of the reaction order model with autocatalysis (eqn. 5.7) to the degradation data obtained in acidic media is shown in Figure 5.4. The degradation behavior is well-predicted by the reaction order model with autocatalysis for both ESO- and EVA-

based epoxy resins (R^2 was 0.935 and 0.988 for ESO- and EVA-based epoxy resins, respectively). The obtained rate constants were k_1 = 8.41x10^{-8} h^{-1}, k_2 = 5.67x10^{-2} h^{-1}, and k_1 = 1.71x10^{-5} h^{-1}, k_2 = 5.88x10^{-3} h^{-1} for ESO- and EVA-based epoxy resins, respectively. The reaction order model with autocatalysis captured the observed sigmoidal mass loss trend exhibiting three stages: 1) an initial time period of little mass loss, 2) a time period of rapid mass loss, and 3) deceleration at the latest stages of degradation. We note the mass loss rate was under-predicted at early times by the model in Figure 5.4, which may be due to the presence of surface erosion, *i.e.,* cleavage of ester groups at the surface when the epoxy resin was immersed into the solvent. For both ESO- and EVA- based epoxy resins, the rate constant associated with autocatalysis (k_2) was greater than the rate constant associated with the reaction order model (k_1). Thus, autocatalysis had a significant impact on the observed degradation behavior. k_2 of the ESO-based epoxy resin was an order of magnitude greater than that of the EVA-based epoxy resin. We normalized the observed rate constants to the ester density in each network (Table 5.1), which resulted in k_2/ν_{ester} = 1.01x10^{-2} and 5.76x10^{-4} cm^3 mmol^{-1} h^{-1} for the ESO- and EVA-based epoxy resins, respectively. Though the EVA-based epoxy resin had a higher ester density in the network, the normalized k_2/ν_{ester} for the ESO-based epoxy resin was two orders of magnitude greater than that of the EVA-based epoxy resin. Important factors governing the higher degradation rate of the ESO-based epoxy resin are likely the higher hydrophilicity and lower crosslink density (Table 5.1), as discussed previously.

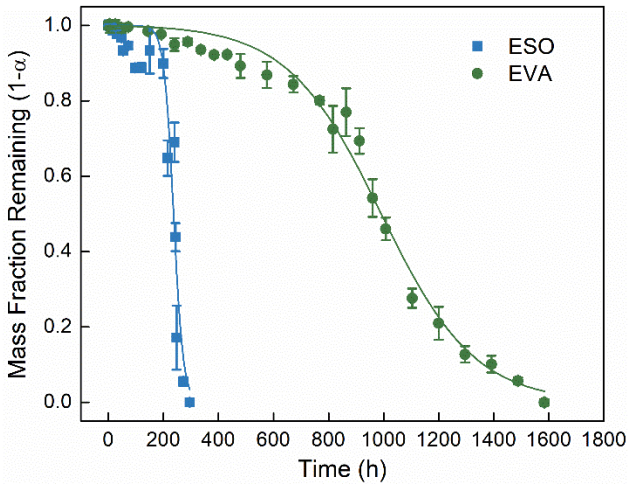

Figure 5. 4**:** Mass fraction remaining $(1-\propto)$ of ESO- and EVA-based epoxy resins in 10 wt% HCl aqueous solution at 80 °C. Averages are shown over three independent measurements with error bars representing the standard deviation.

5.4 Analysis of Degradation Products and Degradation Sample Surface Composition

The degradation products of EVA-based epoxy resins in 10 wt% HCl aqueous solution were analyzed using mass spectrometry (Figure 5.5a). There were six main peaks observed in the mass spectrum and the assigned chemical structures are listed in Figure 5.5b. In the event of complete hydrolysis of all esters within the network structure, only the structures at 187.1 and 243.0 g/mol should be observed (associated with the curing agent MHHPA and epoxy monomer, respectively). Both were major degradation products observed in Figure 5.5. In the case of incomplete degradation, with some esters remaining intact, a variety of degradation product structures can be considered. The remaining peaks were assigned to those structures, with major peaks described in Figure 5.5b and minor peaks described in Figures A3.8 in the *Appendix 3.* In all cases, the observed degradation products were consistent with hydrolysis of ester groups (Scheme 5.1). Similar analyses were conducted on the ESO-based epoxy resin (Figures A3.9 and A3.10 in the *Appendix*

3). As soybean oil contains diverse molecules with differing fatty acid compositions, we considered the average composition of soybean oil in this analysis (following our prior work on the degradation products of ESO-based epoxy resins in basic solutions). In the ESO-based epoxy resin degradation products, the fragment at 187.1 g/mol was also observed in high concentration, associated with the curing agent. Other major and minor peaks are identified in Figures A3.9-A3.10 in the *Appendix 3*. The ESO-based epoxy resin degradation products are also consistent with the proposed hydrolysis mechanism in Scheme 5.1.

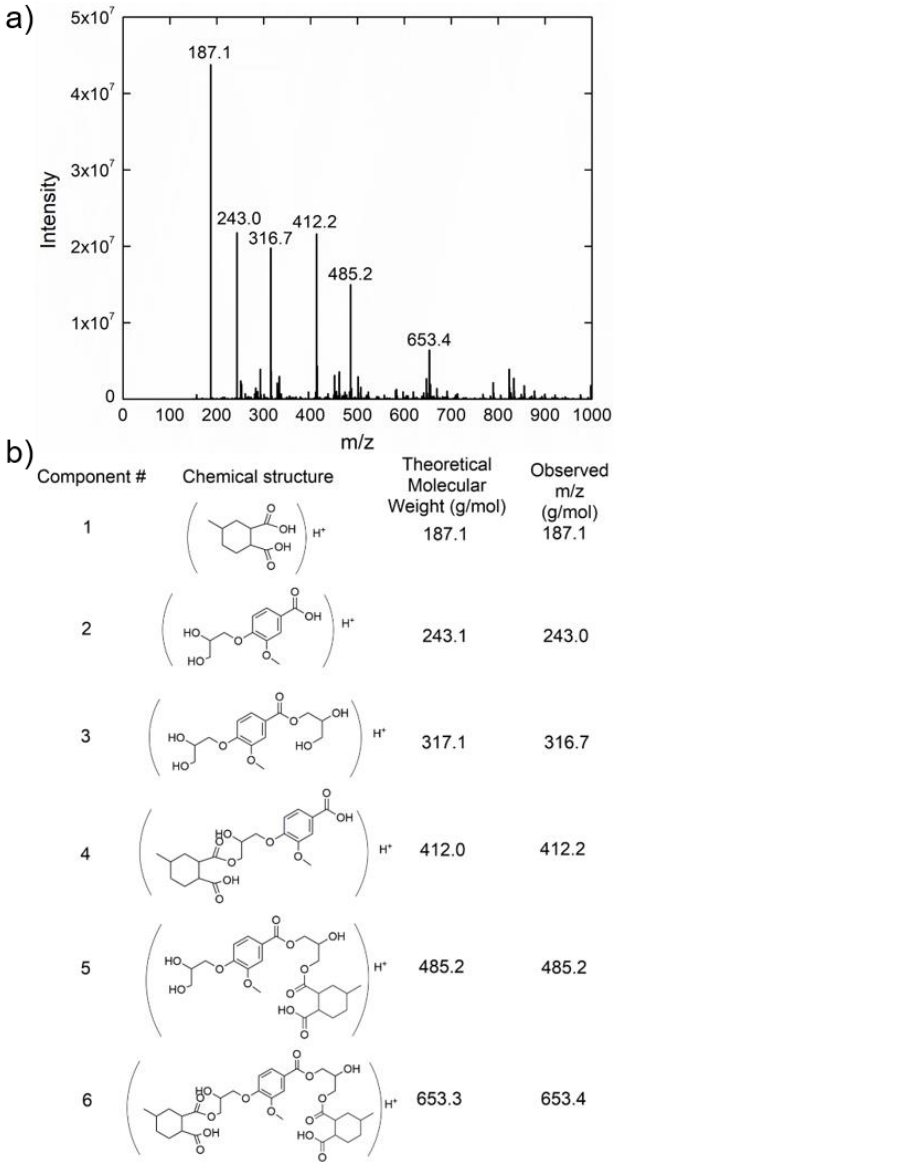

Figure 5. 5**:** (a) Mass spectrum obtained from products of the degradation of the EVA-based epoxy resin in 10 wt% HCl aqueous solution at 80 °C. (b) Proposed chemical structures and theoretical molecular weights for major peaks observed in (a)

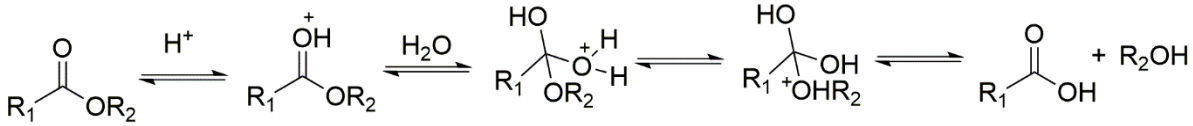

Scheme 5. 1: Epoxy resin degradation through ester hydrolysis in acidic conditions

The presence of relevant chemical moieties in the EVA-based epoxy resins before and after immersion in 10 wt% HCl aqueous solution (Figure 5.6) was evaluated with FTIR-ATR. The broad band observed in the 3500-3200 cm^{-1} region, corresponding to hydroxyl groups (OH bending), greatly increased in intensity after immersion in the acidic solution and is attributed to the cleavage of ester groups. A significant difference in the spectra obtained before and after immersion in the acidic medium was the appearance of peaks around 1700 cm^{-1} region, consistent with the presence of carboxylic acid groups (COOH bending) after degradation. These data provide further support for the cleavage of ester groups during degradation, thus producing an increased concentration of –OH and –COOH groups in the degradation products. No other significant changes were observed in the FTIR-ATR spectrum.

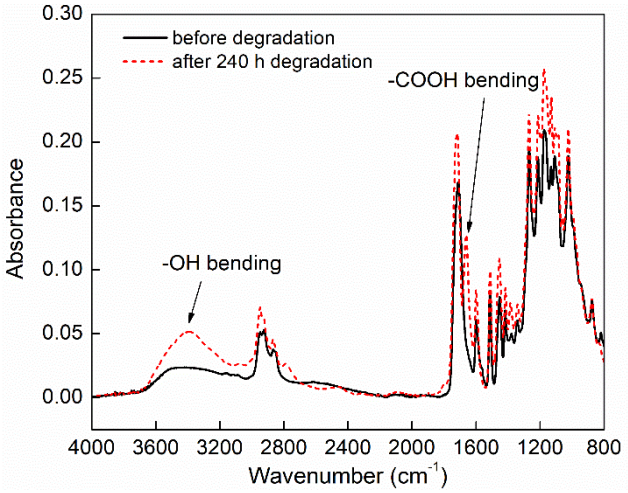

Figure 5. 6**:** FTIR-ATR spectra obtained from EVA-based epoxy resins before (black solid curve) and after immersion in 10 wt% HCl aqueous solution for 240 h (red dashed curve).

5.6 Effect of Solvent Composition and Temperature on Degradation Rate

We examined the impact of solvent composition and temperature on the degradation behavior of the EVA- and ESO-based epoxy resins (Figure 5.7), employing organic solvents such as DMF, acetone and THF, along with water. Degradation of both the EVA- and ESO-based epoxy resins occurred most rapidly at 25 °C in the solvent system acetone/H_2O, followed by THF/H_2O and then DMF/H_2O. At 80 °C, degradation occurred more rapidly in DMF/H_2O as compared to pure water. For the DMF/H_2O solvent system, a significant increase in degradation rate was observed at 80 °C compared to 25 °C. The mass loss behavior (Figure 5.7) was fit to the reaction order model with autocatalysis (eqn. 5.7) and the degradation rate constants are summarized in Table 5.2. A reasonable quality of fit was observed for the data taken in all solvent conditions. Two important factors must be evaluated when considering the impact of the solvent composition and temperature: the degradation product solubility, and wettability of the thermoset surface to the solvent. We have already presented the contact angles of the epoxy resins using the same solvent systems which were employed during the degradation experiments, summarized in Table 5.1. The contact angles of acetone/H_2O and THF/H_2O were lowest for both ESO- and EVA-based epoxy resins (Table 5.1), and degradation proceeded most rapidly in these solvents (Figure 5.7). The wettability of the resin to the solvent therefore likely has an important role in governing degradation rate.

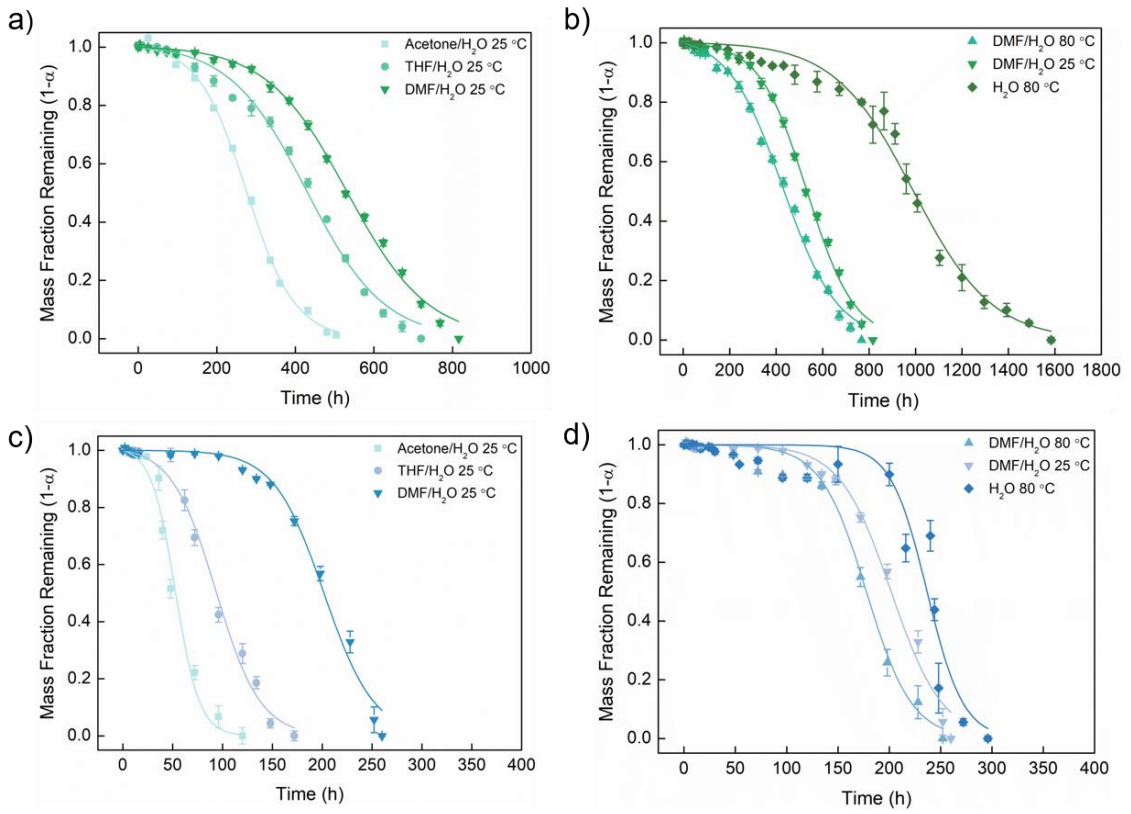

Figure 5. 7**:** Mass fraction remaining $(1-\propto)$ of a) b) EVA-based epoxy resins and c) d) ESO-based epoxy resin in 10 wt% HCl solution using different solvent systems (DMF/H_2O, acetone/H_2O, THF/H_2O, H_2O) and temperatures (25 and 80 °C).

Table 5. 2**:** Degradation rate constants k_1, k_2 of EVA- and ESO-based epoxy resins in various solvents[a]

Solvent Mixture[b]	T (ºC)	EVA-based epoxy resin k_1 (h^{-1})	EVA-based epoxy resin k_2 (h^{-1})	ESO-based epoxy resin k_1 (h^{-1})	ESO-based epoxy resin k_2 (h^{-1})
Acetone/H_2O	25	$1.87x10^{-4}$	$1.60x10^{-2}$	$1.04x10^{-3}$	$8.17x10^{-2}$
THF/H_2O	25	$1.27x10^{-4}$	$1.01x10^{-2}$	$6.61x10^{-4}$	$4.44x10^{-2}$
DMF/H_2O	25	$5.36x10^{-5}$	$9.72x10^{-3}$	$1.27x10^{-5}$	$3.99x10^{-2}$
DMF/H_2O	80	$2.16x10^{-4}$	$8.29x10^{-3}$	$1.50x10^{-5}$	$4.51x10^{-2}$
H_2O	80	$1.71x10^{-5}$	$5.88x10^{-3}$	$8.41x10^{-8}$	$5.67x10^{-2}$

[a] Obtained through fitting the solid-state reaction order model with autocatalysis to the mass loss data in Figures 5.4 and 5.7

[b] 100 g concentrated HCl (32 g HCl and 68 g water) was added to 220 g of the diluting solvent (water, THF, acetone or DMF).

In order to evaluate the affinity of the epoxy resin degradation products to the solvents, we applied group contribution methods to calculate the Hansen solubility parameters (δ) of the major epoxy resin degradation products (the chemical structures of degradation products are provided in Figure 5.5 and Figures A3.9 and A3.10 of the *Appendix 3*), and the results are summarized in Table 5.3. δ of each major degradation product and solvent are listed in Table A3.3 and the calculation procedure is discussed in the *Appendix 3*. δ of the EVA-based epoxy resin degradation product mixture (using the 6 main degradation products) was calculated using the volume fraction of each component i (ϕ_i)

$$\delta_{mixture} = \sum_i \delta_i \phi_i \qquad \text{(eqn.5.8)}$$

and $\delta_{mixture}$ was calculated using the solvent composition in Table A3.1. The mixture of the 6 main EVA-based epoxy resin degradation products had the largest affinity for the DMF/H_2O solvent mixture, followed by THF/H_2O, and then acetone/H_2O. δ of DMF/H_2O, THF/H_2O and acetone/H_2O were all within a reasonable range of δ of the degradation product mixture, indicating the degradation products would likely have reasonable solubility in these solvents. However, δ of the degradation product mixture significantly differed from that of pure water, indicating poor solubility (Table 5.3), which is a likely explanation for the slow degradation kinetics in water. In the case of the ESO-based epoxy resin, the degradation products contained a higher concentration of hydroxyl groups, and δ of the degradation product mixture was much closer to that of pure water (Table 5.3), indicating better solubility in water. The ESO-based epoxy resin degradation product

mixture is expected to have the greatest solubility in pure water, followed by DMF/H_2O, and then THF/H_2O and acetone/H_2O. In both EVA- and ESO-based epoxy resins, we did not observe a direct correlation between degradation product solubility (Table 5.3) and degradation rate constant (Table 5.2). Therefore, the effect of solvent conditions (solvent choice and temperature) is likely governed by competing effects of degradation product solubility and affinity of the epoxy resin to the solvent (quantified as contact angle in Table 5.1). In the case of the EVA-based epoxy resins, the fastest degradation kinetics occurred in the acetone/water system, for which the contact angle of the epoxy resin was lowest (Table 5.1), and the solubility parameter predictions indicate likely solubility of the degradation product mixture in the bulk solvent. In the case the ESO-based epoxy resin, fastest degradation also occurred in the acetone/water system, and the contact angle of the ESO-based epoxy resin was lowest in acetone/water, while the degradation product solubility was predicted to be significantly worse (Table 5.1) as compared to that in pure water.

Table 5. 3**:** Hansen solubility parameter (δ) of epoxy resin degradation product mixtures and solvent mixtures

Mixture of degradation products or solvents	δ ($MPa^{1/2}$)	$(\delta_1 - \delta_2)^2$ (MPa) EVA[a]	$(\delta_1 - \delta_2)^2$ (MPa) ESO[b]
EVA-based epoxy resin degradation product mixture	30.4	NA	NA
ESO-based epoxy resin degradation product mixture	40.3	NA	NA
acetone/H_2O	26.3	16.8	196.0
THF/H_2O	27.1	10.9	174.2
DMF/H_2O	30.9	0.3	88.4
H_2O	47.8	302.8	56.3

[a] Square of difference of solubility parameters of EVA-based epoxy resin degradation product mixture and solvent mixture.

[b] Square of difference of solubility parameters of ESO-based epoxy resin degradation product mixture and solvent mixture.

5.6 Conclusions

We investigated the accelerated hydrolytic degradation of ESO- and EVA-based epoxy resins in acidic solutions. Even though the EVA-based epoxy resin had a higher density of ester groups within the epoxy network, the ESO-based epoxy resin degraded more rapidly than the EVA-based epoxy resin in acidic aqueous solution, attributed to the more hydrophilic nature and lower crosslink density and glass transition temperature of the ESO-based epoxy resin. A solid-state reaction order model with autocatalysis was used to predict the sigmoidal trend of the degradation profile, and was in good agreement with the experimental data for both ESO and EVA-based epoxy resins in acidic solutions. The degradation mechanism of the biobased epoxy resins in acidic solution was identified as bulk erosion, which is quite different from surface erosion behavior observed in basic solution. Mass spectrometry and FTIR-ATR confirmed that degradation proceeded as hydrolysis of ester groups. The impacts of solvent composition and temperature on degradation kinetics were also examined, related to the epoxy resin affinity to the solvent and solubility of degradation products. The EVA-based and ESO-based epoxy resins degraded most rapidly in the acetone/H_2O solvent system, for which the contact angle was lowest for both resins. The degradation product mixture was also predicted to be soluble in acetone/water for the EVA-based epoxy resin. By contrast, the degradation product mixture solubility was predicted to be greatest in pure water for the ESO-based epoxy resin, and yet degradation proceeded most slowly in this solvent. These results provide further knowledge on degradation behavior of biobased epoxy resins in acidic solutions, enhancing

our understanding of the degradation mechanism of ester-containing epoxy resins. This study demonstrates that ester-containing biobased epoxy resins can be degraded in mild acidic conditions, which could be a future consideration for the development of sustainable and degradable biobased epoxy resins to replace conventional petroleum-based thermosets.

Chapter 6: Degradability, thermal stability, and high thermal properties in spiro polycycloacetals partially derived from lignin

In this chapter, a series of partially bio-based spiro polycycloacetals were synthesized using bio-renewable feedstocks, vanillin and its derivative syringaldehyde, along with pentaerythritol and commercially available co-monomers including 4,4′-difluorobenzophenone (DFP) and bis(4-fluorophenyl) sulfone (DFS). These spiro polycycloacetals displayed high thermal stabilities (degradation temperatures in the range of 343 – 370 °C, as quantified by 5% mass loss) and high glass transition temperatures (in the range of 179 – 243 °C). While DFS-containing polymers were amorphous, DFP-containing polymers were semi-crystalline with high melting temperatures (in the range of 244 – 262 °C). The hydrolytic degradation behavior of one spiro polycycloacetal, derived from vanillin and DFP, was investigated. Importantly, the spiro polycycloacetal was rapidly degraded to small molecules and oligomeric byproducts under acid-catalyzed conditions. This class of spiro polycycloacetals is therefore an important contributor to the development of more easily degradable polymers which also retain sufficiently high thermal properties and thermal stability.

6.1 Introduction

The derivation of polymers from renewable resources has been of great interest in academia and industry due to their significant applications as eco-friendly materials. Utilization of biobased sources for plastics production minimizes the consumption of petro-chemical reservoirs, limiting industrial dependence on depleting fossil fuel feedstocks [113-121]. The fate of materials in the environment is one of the key considerations in evaluation of the life cycle of polymers [122, 123]. Incorporating labile functional groups

into the polymer backbone offers a solution for addressing plastic waste through hydrolytic degradation to small molecule byproducts, which can be subsequently re-used to make new materials [93, 124-129]. In this regard, an increasing effort has been dedicated to providing biomass-derived chemical building blocks to synthesize hydrolytically degradable polymers including polyesters, polyamides, poly(silyl ether)s, polyurethanes, among others [93, 125, 126, 128-131].

Among the numerous biobased polymers reported, polyacetals are an important class of polymer with remarkable degradation properties and significant potential applications [116, 132, 133]. The presence of a cleavable acetal unit in the polymer backbone permits rapid degradation under acid-catalyzed hydrolysis[132-137]. Polyacetals have been synthesized from renewable feedstocks, such as starch [138] and cellulose[139]. Among these renewable feedstocks, vanillin, a lignin-derived compound, and its derivative, syringaldehyde, have gained much popularity recently [7, 12, 114, 140, 141]. The presence of hydroxyl and aldehyde functional groups, as well as highly aromatic structures, on these lignin-based molecules make them prime candidates as chemical feedstocks for high performance, biobased polyacetals [12, 114, 141].

The thermal stabilities and thermal transitions of synthetic polymers are major criteria to determine their potential applications [142]. Polymers such as poly(arylene ether)s, poly(ether ether ketone), and polyphenylsulfones are used in super engineering plastics due to their high glass transition temperatures (T_g), which are typically greater than 150 °C [143-145]. However, the majority of these high T_g super engineering plastics are non-degradable and synthesized from petrochemical feedstocks [146, 147]. It is therefore of much interest to synthesize high-T_g polymers from biobased feedstocks with enhanced

degradation properties. In the case of polyacetals, the majority of literature studies have involved linear polyacetals, which exhibited low thermal degradation temperatures, low T_g, and poor chemical resistance, which limits their engineering applications [138, 148-151]. To overcome these limitations, researchers have been focusing on the design of polyacetals with structurally rigid backbones. In this regard, incorporation of cycloacetal and spiro cycloacetal units into the polymer backbone has gained much interest in the literature [12, 141, 152-154]. The structural rigidity in the polymer backbone increased the T_g relative to non-cyclic polyacetals, though the thermal degradation temperatures were not greatly enhanced [12, 141, 153, 154]. Thus, designing and developing polyacetals with inherent degradability, high T_g, and superior thermal stability is a challenging but extremely significant problem.

Herein we describe the synthesis and characterization of spiro polycycloacetals utilizing bioaromatic hydroxyaldehydes, polyols, and aromatic sulfonates or benzophenone. Notably, the incorporation of aromatic sulfonates or benzophenone into the polymer backbone, along with bioaromatic aldehydes, increased the aromaticity and rigidity of polymer backbone, which further improved the polymer thermal stability as well as T_g [145]. To our knowledge, these are the first examples of bioaromatic-based spiro polycycloacetals with T_g values up to 243°C, melting points up to 262°C, and thermal degradation temperatures (quantified as 5% mass loss) up to 370 °C. We also demonstrate their rapid hydrolytic degradation in acidic media. The hydrolytic degradation behavior of one spiro polycycloacetal, derived from vanillin and 4,4′-difluorobenzophenone (DFP), was quantified in various acidic solvents; the polymer showed the fastest degradation

behavior in acidic acetone and degraded completely to small molecule and oligomeric byproducts within 10 h.

6.2 Experimental Methods

6.2.1 Materials

All chemicals were purchased from Sigma-Aldrich unless otherwise noted and were used as received: *p*-hydroxybenzaldehyde (vanillin, ≥97%, FG), 3,5-dimethoxy-4-hydroxybenzaldehyde (syringaldehyde**,** ≥98%, FG), difluorobenzophenone (DFP, 99%), bis(4-fluorophenyl) sulfone (DFS, 99%), 2,2-bis(hydroxymethyl)-1,3-propanediol (pentaerythritol, 99%), *p*-toluene sulfonic acid monohydrate (*p*-TSA.H_2O, ACS reagent, ≥98.5%), N,N-dimethylformamide (DMF, anhydrous, 99.8%), sodium bicarbonate ($NaHCO_3$, ACS reagent, ≥99.7%), potassium carbonate (K_2CO3, 9.995% trace metals basis), 18-crown-6 (≥99.0%), dimethyl sulfoxide-d_6 (*d*-DMSO, 99.9 atom % D, purchased from Cambridge Isotope Laboratories), deuterium oxide (D_2O, 99.9 atom % D), acetone-d_6 (99.9 atom % D), dimethylsulfoxide (DMSO, anhydrous, ≥99.9%), petroleum ether (ACS reagent), methanol (HPLC, ≥99.9%), acetone (ACS reagent, ≥99.5%), ethyl acetate (ACS reagent, ≥99.5%), and 1,2,4,5-tetramethylbenzene (ACS reagent, ≥98%), acetonitrile (HPLC, ≥99.9%).

6.2.2 Monomer Synthesis

Synthesis of 4,4'-(2,4,8,10-tetraoxaspiro[5.5]undecane3,9-diyl)bis(2-methoxyphenol) (VPA): The synthesis of VPA followed previously reported protocols.[12] Two eqv. of vanillin (40.0 g) and 1 eqv. of pentaerythritol (18.0 g) were added to a dry 500 mL round bottom flask equipped with a mechanical stir bar and a Dean–Stark trap, followed by the addition of a catalyst, *p*-TSA.H_2O (1.12 g, 2 wt% of the total weight of

vanillin and pentaerythritol), at room temperature. DMF (165 mL) was then added as the solvent and petroleum ether (180 mL) as the water-removing solvent (in which the petroleum ether was boiled continuously to remove produced water, and subsequently condensed back into the reaction flask). The reaction flask was connected to a reflux condenser and then heated at 90 °C overnight (18-20 h). After the reaction, the flask was cooled to room temperature and the reaction mixture was transferred into a 1 L $NaHCO_3$ aqueous solution (3 wt. %) and filtered using a Büchner funnel (equipped with filter paper) attached to a 1 L vacuum flask. The resulting product was washed with 100 mL of distilled water 4-5 times. The purified VPA monomer was dried at 80 °C overnight (18-20 h). 36 g of product was obtained as a white solid (yield: 67.8%).

Synthesis of 4,4'-(2,4,8,10-tetraoxaspiro[5.5]undecane3,9-diyl)bis(2,6-dimethoxyphenol) (SPA): The synthesis and purification of SPA followed the same procedures as that of VPA. Syringaldehyde (48.0 g) was used in place of vanillin. 39 g of SPA monomer was obtained as a white solid (yield: 63.8%).

6.2.3 Polymer Synthesis

Synthesis of VPA-DFP: VPA (8.08 g, 20 mmol) and DFP (4.36 g, 20 mmol) monomers were added to a dry single-neck round bottom flask, equipped with a mechanical stir bar and a Dean–Stark apparatus, followed by 25.70 mmol of K_2CO_3 (3.45 g). Next, 1.02 mmol (0.27 g) of 18-crown-6 (0.05 molar equivalent to diol, i.e., VPA) was added to the flask, followed by the addition of 100 mL of DMSO under nitrogen flow. The reaction mixture was heated for 24 h at 155 °C under nitrogen.[145] The round bottom flask was then cooled to room temperature and precipitated into a 1 L H_2O/methanol mixture (50/50 by volume). The precipitated polymer was filtered using a Büchner funnel (equipped with

filter paper) attached to a 1 L vacuum flask and slowly washed with 100 mL of distilled water followed by methanol (15 mL), acetone (15 mL), and ethyl acetate (15 mL). The extracted polymer was dried under vacuum at 80 °C overnight (20-24 h). 9.5 g of VPA-DFP was obtained as the final product (yield: 77.6%).

Synthesis of SPA-DFP: Polymer synthesis and purification procedures followed that described above for VPA-DFP, with the exception that the following monomers were used: SPA (9.3 g, 20 mmol) and DFP (4.37 g, 20 mmol). 9.2 g of SPA-DFP was obtained as the final product (yield: 68.4%).

Synthesis of VPA-DFS: Polymer synthesis and purification procedures followed that described above for VPA-DFP, with the exception that the following monomers were used: VPA (8.08 g, 20 mmol) and DFS (5.09 g, 20 mmol). 10.5 g of VPA-DFS was obtained as the final product (yield: 80.9%).

Synthesis of SPA-DFS: Polymer synthesis and purification procedures followed that described above for VPA-DFP, with the exception that the following monomers were used: SPA (9.3 g, 20 mmol) and DFS (5.09 g, 20 mmol). 11.2 g of SPA-DFS was obtained as the final product (yield: 79.1%).

6.2.4 Monomer and Polymer Characterization

Nuclear magnetic resonance (NMR): ^{1}H NMR (400, 500, 600 MHz), ^{13}C NMR (600 MHz), DEPT (600 MHz), COSY (600 MHz) and HMQC (600 MHz) experiments were conducted using a JEOL ECA-400 spectrometer with deuterated solvents. For analysis of synthesized monomers and polymers, *d*-DMSO was used. For analysis of polymer degradation products, *d*-acetone, *d*-DMSO, and D_2O were used. Chemical shifts

were referenced to the residual protonated solvent resonance (^{1}H NMR: 2.50 ppm for DMSO, 4.80 ppm for H_2O, and 2.04 ppm for acetone. ^{13} C NMR: 39.5 ppm for DMSO and 29.8 ppm for acetone).

Liquid chromatography-mass spectrometry (LC-MS): LC-MS measurements were conducted using an Agilent 6545 QTOF/LC-MS System. The instrument was equipped with a Dual AJS ESI source. The mass range was 60-1,700 m/z. The mobile phase was a mixture of 95% methanol / 5% water, containing 0.1% formic acid, and the flow rate is 0.2 ml/min. The degradation products were dissolved in acetonitrile and the concentration of the solution was 10 μg ml^{-1} prior to injection into the QTOF/LC-MS. The injection volume was 5 μL.

Gel permeation chromatography (GPC): GPC measurements were performed using a Tosoh high performance GPC system (HLC-8320), equipped with an auto injector, a dual differential refractive index (RI) detector, and TSKgel HHR columns connected in series (7.8x300mm G5000HHR, G4000HHR, and G3000HHR), using DMF (Fisher Scientific, Alfa Aesar, HPLC grade, >99.7%, containing 1 g/L LiBr) as the eluent at a flow rate of 1.0 mL/min at 60 °C. Samples were run in triplicate with 100 μL injection volume. Number-average and weight-average molecular weights (M_n and M_w, respectively) and dispersity ($Đ$) were calculated using polystyrene standards with molecular weights ranging from 0.5 to 2.9×10^3 kg/mol provided by Tosoh Science.

Differential scanning calorimetry (DSC): DSC thermograms were collected using a TA Instruments Q2000 differential scanning calorimeter, under 50 mL/min nitrogen flow, and the instrument was calibrated using an indium standard. Samples were encapsulated in hermetic pans, equilibrated at -50 °C, and subjected to a heat – cool – heat cycles from -50

to 300 °C at a rate of 10 °C/min. Melting temperature (T_m) was determined from the peak minimum in the first heating cycle and T_g was identified as the inflection point in the second heating cycle.

Thermogravimetric analysis (TGA): TGA experiments were performed using a TA Instruments Q500 analyzer with alumina sample cups. The samples were heated from 25 – 800 °C at a rate of 10 °C min^{-1} under nitrogen environment. Advantage software was used to analyze the TGA data.

Contact angle measurements: VPA-DFP was coated on silicon wafer using flow coating at 3 cm/s. The silicon wafer was cleaned using a chemical wash and UV-treated for 2 h to remove any contaminants prior to polymer coating. For each silicon wafer, 10 μL solution (5 wt% VPA-DFP in DMSO) was added for flow coating. The silicon wafer was preheated to 90 ºC for better evaporation of DMSO and coating efficiency. Then, contact angles were measured using an OCA 15EC video-based optical contact angle measuring instrument at ambient temperature. The SCA 20 software was used to record the water contact images. 5 μL of the solutions used in degradation experiments (acidic *d*-acetone, *d*-DMSO or D_2O) were deposited onto 3 different positions on the silicon wafer coated with VPA-DFP polymer.

Polymer degradation experiments: Degradation studies were performed in NMR tubes at room temperature. A clean and dry NMR tube was loaded with 10 mg of VPA-DFP and 2.24 mg of 1,2,4,5-tetramethylbenzene (internal standard, for quantitative analysis), followed by the addition of 0.6 mL of deuterated solvent (*d*-acetone, *d*-DMSO or D_2O). The molar ratio of polymer and internal standard used in the degradation study was 1:1. The concentration of the internal standard was 0.0279 mol/L. A homogeneous

mixture was formed when *d*-DMSO was added to the polymer, as it is soluble in DMSO. A non-homogeneous mixture was formed when *d*-acetone and D_2O were added to the polymer, as the polymer is not soluble in these solvents. The NMR tube was then charged with 5 µL of HCl solution in H_2O (35 wt%) to promote acid-catalyzed hydrolysis, with a final acid concentration of 0.1 M. ^{1}H NMR data were obtained at different time intervals in all three solvents and GPC data were obtained at different time intervals in acidic *d*-acetone. At 24 h of total degradation time in acidic *d*-acetone, additional characterization experiments were performed: ^{13}C and 2D NMR, GPC, and LC-MS.

To prepare the samples for GPC measurements, the solvent (*d*-acetone) was removed using a rotary evaporator, and the collected degradation products were dissolved in hexane, followed by extraction using DMF to remove remaining acid and salts prior to injecting in the GPC column. To prepare the samples for LC-MS measurements, the solvent (*d*-acetone) was removed using a rotary evaporator, and the collected degradation products were dissolved in hexane, followed by extraction using acetonitrile to remove remaining acid and salts prior to injecting in the LC-MS column.

6.3 Synthesis of Spiro Acetal Diol Monomers and Spiro Polycycloacetals

The synthesis of spiro polycycloacetals followed a two-step process, including synthesis of bifunctional spiro acetal diol monomers and step-growth polymerization. Bifunctional spiro acetal diol monomers, VPA and SPA, were synthesized using the biogenic hydroxyaldehydes vanillin and syringaldehyde, respectively, along with pentaerythritol and *p*-TSA.H_2O as the catalyst (Scheme 6.1). Although the synthesis of VPA was previously reported and utilized to prepare polycycloacetals [12], to our knowledge the synthesis of SPA has not been demonstrated. These monomers were

characterized using ^{1}H and ^{13}C NMR (Figures 6.1, A4.1, and A4.2). Disappearance of a characteristic aldehyde (-CHO) peak observed in the starting material (vanillin or syringaldehyde) at 9.92-9.98 ppm and appearance of a characteristic -CH peak of the spirocycloacetal unit at 5.34-5.37 ppm in ^{1}H NMR confirmed the formation of the monomers VPA and SPA (Figure 6.1a and A4.1a).

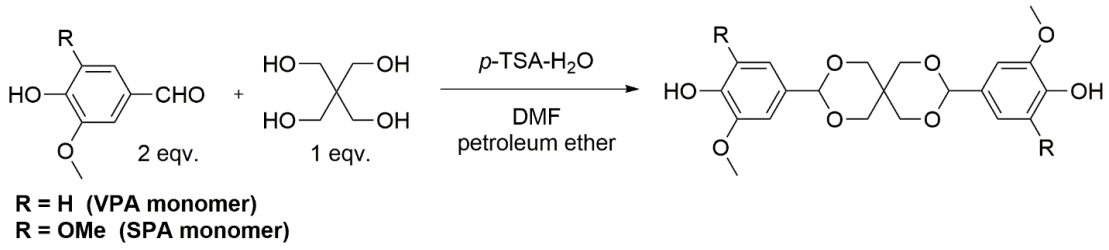

Scheme 6. 1: Synthesis of spiro acetal monomers.

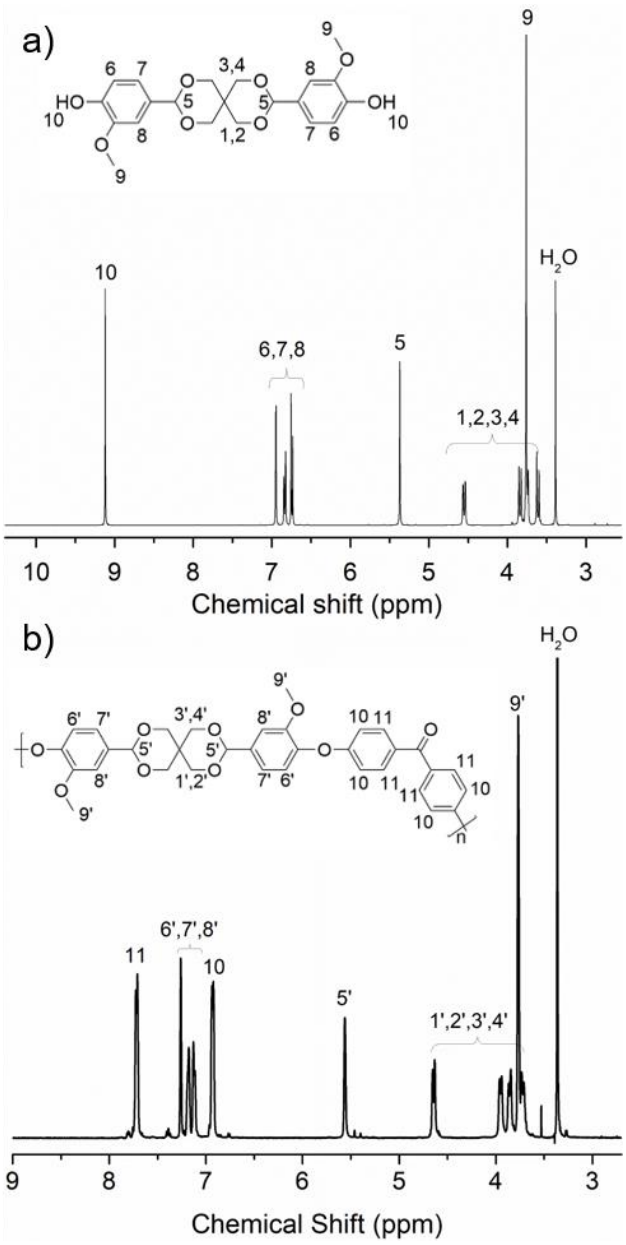

Figure 6. 1: ^{1}H NMR of (a) VPA monomer and (b) VPA-DFP polymer (in *d*-DMSO). Additional ^{1}H and ^{13}C spectra are provided in Figures A4.1 and A4.2.

Spiro polycycloacetals were synthesized using monomers VPA or SPA with a co-monomer (either DFP or DFS) through step-growth polymerization in DMSO at 155 °C, employing K_2CO_3 as the catalyst (Scheme 6.2). The reaction progress was monitored using ^{1}H NMR (Figure 6.1b). As the polymerization proceeded, disappearance of peaks

associated with hydroxyl groups in the VPA monomer at 9.12 ppm (peak 10 in Figure 6.1a) and shifting of the characteristic -CH peak from 5.37 ppm in VPA monomer (peak 9 in Figure 6.1a) to 5.56 ppm in VPA-DFP (peak 9' in Figure 6.1b), as well as shifting of peaks associated with aromatic hydrogens from 6.75-6.95 ppm in the VPA monomer (peaks 6-8 in Figure 6.1a) to 7.11-7.26 ppm in VPA-DFP (peaks 6'-8' in Figure 6.1b) confirmed the depletion of VPA monomer and formation of VPA-DFP polymer. In addition, appearance of peaks associated with the phenyl group in the co-monomer (DFP or DFS) in the aromatic region (at 6.94 and 7.72 ppm) confirmed the incorporation of co-monomer into the polymer chain. The formation of other spiro polycycloacetals (VPA-DFS, SPA-DFP, and SPA-DFS) were also confirmed based on the NMR analysis and the detailed ^{1}H and ^{13}C NMR data are presented in Figures A4.1 and A4.2.

GPC data quantified the number-average molecular weight (M_n) in the range of 4-16 kg/mol and dispersities (Đ) in the range of 1.8-2.8 (Table 6.1), with GPC chromatographs shown in Figure 6.2. Interestingly, VPA-derived polymers showed higher molecular weights than corresponding SPA-derived polymers (Table 6.1), when synthesized under the same conditions. These results suggest that the structurally more rigid syringaldehyde-derived monomer (SPA) exhibited less reactivity than the less rigid vanillin-derived monomer (VPA). Comparatively, polymers synthesized from the DFS co-monomer exhibited higher molecular weights than corresponding polymers synthesized from the DFP co-monomer (Table 6.1).

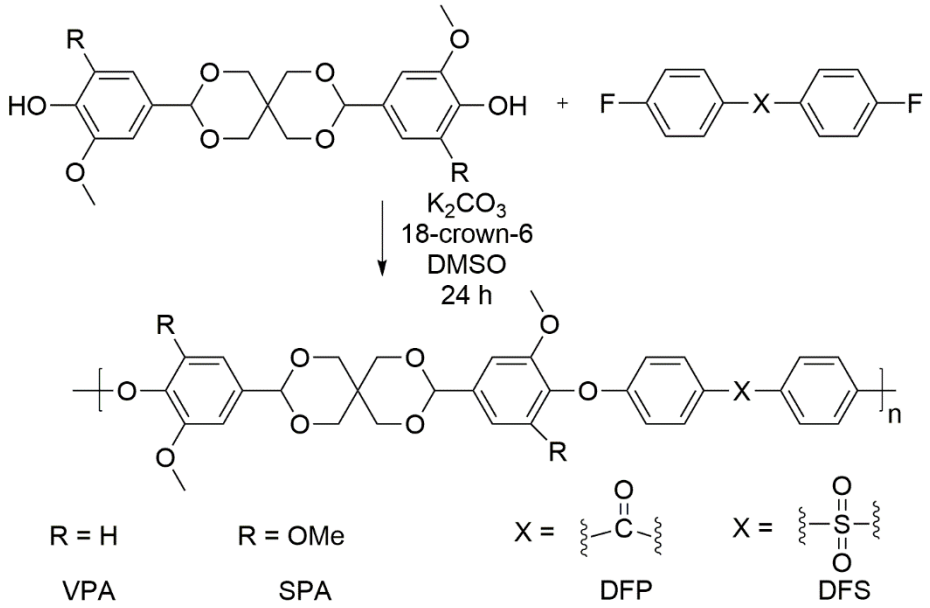

Scheme 6. 2: Synthesis of spiro polycycloacetals.

Table 6. 1: Polymer characteristics[a]

Polymer	M_n **(kg/mol)**	M_w **(kg/mol)**	**Đ**
VPA-DFP	7.3	12.8	1.76
VPA-DFS	16.1	44.7	2.78
SPA-DFP	3.7	7.8	2.12
SPA-DFS	8.9	22.0	2.47

[a]Determined with GPC using polystyrene standards.

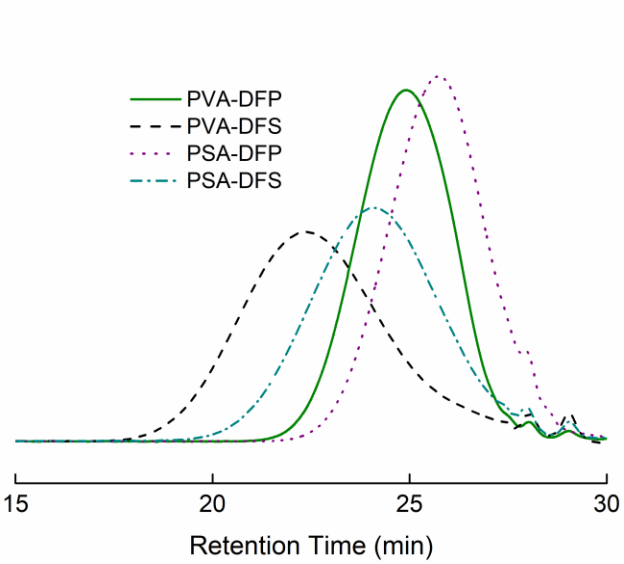

Figure 6. 2**:** GPC chromatographs of polycycloacetals.

6.4 Elevated Thermal Transitions and Stability of Spiro Polycycloacetals

The thermal degradation temperatures of spiro polycycloacetals were evaluated using TGA, conducted from 25 – 800 °C under an inert (Argon) atmosphere. Irrespective of the molecular weight and polymer backbone, all polymers displayed a multi-stage decomposition profile (Figure 6.3). The polymers exhibited $T_{-5\%}$ (the temperature at which 5% weight loss was observed) in the range of 343 – 370 °C, $T_{-50\%}$ (the temperature at which 50% weight loss was observed) in the range of 460 – 506 °C, and T_{max} (the temperature at which the derivative weight % was maximum) in the range of 425 – 537 °C (Table 6.2), which are significantly higher than that previously reported for other cyclic and spiro polycycloacetals (e.g., $T_{-5\%}$ was previously reported in the range of 210 – 349 °C) [141, 153, 154].

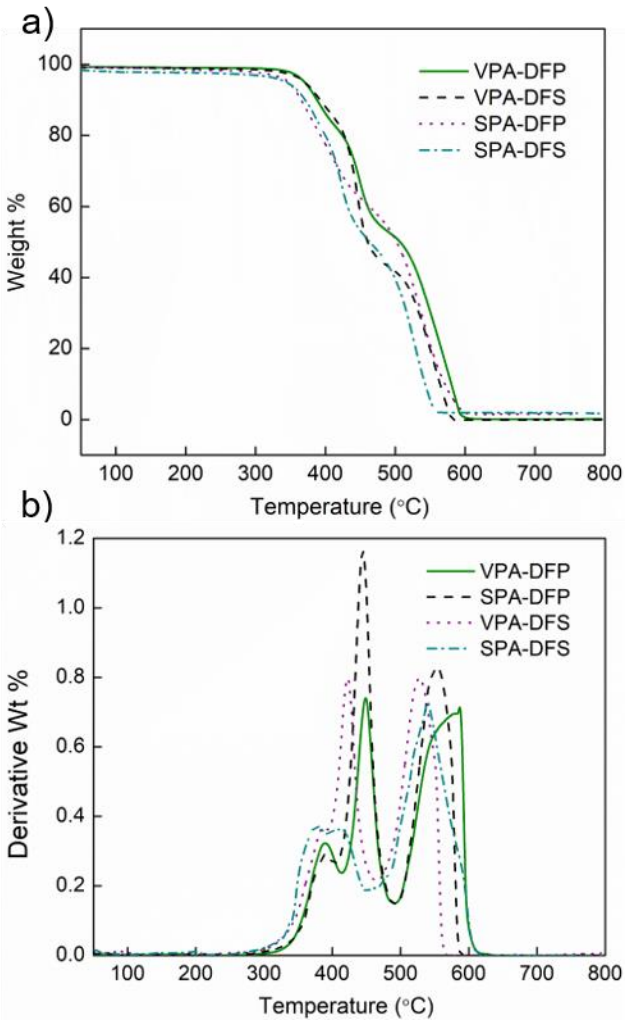

Figure 6. 3**:** (a) Weight % and (b) derivative weight % as a function of temperature obtained from spiro polycyclocacetals using TGA.

Table 6. 2**:** Thermal properties of spiro polycycloacetals

Polymer	T_g **(°C)**	T_m **(°C)**	$T_{-5\%}$ **(°C)**	$T_{-50\%}$ **(°C)**	T_{max} **(°C)**	**Final residual %**
VPA-DFP	179	262	370	506	448	1.5
VPA-DFS	217	NA[a]	347	501	445	0
SPA-DFP	193	244	370	461	425	1.6
SPA-DFS	243	NA[a]	343	460	537	1.7

[a] Not applicable (NA): melting was not observed in these polymers.

DSC thermograms obtained from the first and second heating cycles for VPA-DFP are shown in Figure 6.4 and that of the other polymers are shown in Figure A4.3. The thermal properties (T_g, T_m) of all of the polymers are listed in Table 6.2. The T_g values of these polymers were in the range of 179-243 °C, significantly higher than that reported previously for spiro polycycloacetals (in the range of 57 – 159 °C) [141, 153, 154]. Interestingly, a T_m was observed for the two spiro polycycloacetals synthesized with the DFP comonomer (VPA-DFP and SPA-DFP), but crystallization was not observed during the cooling cycle; these combined results suggest these are semi-crystalline polymers with relatively slow crystallization rates. Polymers synthesized with the DFS comonomer (VPA-DFS and SPA-DFS) did not exhibit crystallization or melting.

As noted above, these polymers exhibited higher T_g values than that of other cyclic and spiro polycycloacetals reported in literature [141, 153, 154]. Incorporating the sterically hindered aromatic co-monomer, DFP or DFS, into the polyacetal backbone thus increased the T_g, which is similar to behavior observed in other super engineering plastics[145]. Since SPA is more structurally rigid than VPA due to the presence of an additional methoxy group, the T_g's of SPA-based polymers were greater than that of the corresponding VPA-based polymers (Table 6.2). Similarly, polymers synthesized using the DFS co-monomer displayed higher T_g's than the corresponding polymers synthesized from the DFP co-monomer, due to the higher rigidity of DFS (Table 6.2).

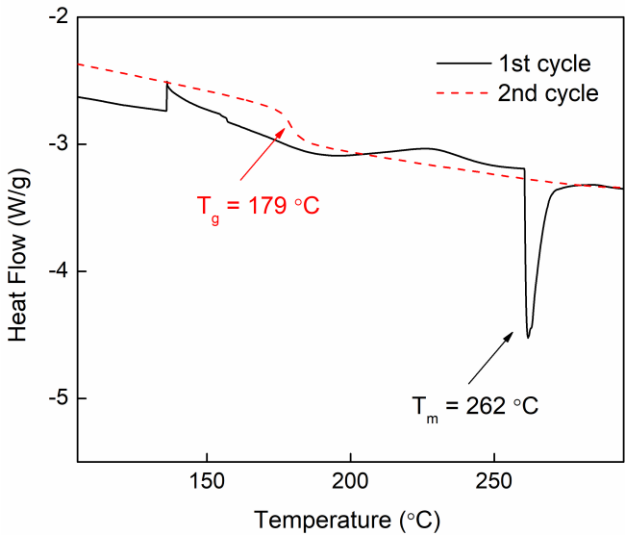

Figure 6. 4**:** Heat flow vs. temperature obtained for VPA-DFP using DSC, shown for the first and second heating cycles.

6.5 Identifying Hydrolytic Degradation Products of VPA and VPA-DFP in Acidic d-Acetone

We performed degradation studies on VPA and VPA-DFP in acidic *d*-acetone (at 0.1 M HCl; 0.6 mL *d*-acetone containing 5 µL of 35 wt% aqueous HCl solution) and monitored the degradation progress using NMR, LC-MS, and GPC. Here we first discuss the identification of degradation products at the end of the degradation process (after 24 h in acidic *d*-acetone for VPA-DFP and 1 h in acidic *d*-acetone for VPA monomer). In the subsequent section, we will present data which track the formation of degradation products over time.

We begin with the degradation behavior of the VPA monomer. Since VPA is soluble in acetone, an initial NMR spectrum was taken before degradation and compared with that obtained after 1 h degradation time (Figure A4.4 and Scheme A4.1). The VPA monomer was completely degraded in acidic *d*-acetone in less than 1 h and produced

vanillin as the major degradation product. The characteristic -CH peak observed in VPA at 5.40 ppm ^{1}H NMR (labeled peak 5 in Figure A4.4a) disappeared after 1 h, accompanied by the appearance of peaks associated with vanillin including the -CHO peak at 9.81 ppm, two sets of aromatic proton peaks at 6.98 and 7.45 ppm, and an -OCH_3 peak at 3.90 ppm (labeled peaks 1, 2/3/4, and 5 in Figure A4.4b, respectively), confirming cleavage of acetal groups of VPA under acidic conditions. In addition, appearance of the -CH_2 peak of pentaerythritol, a byproduct, at 3.75 ppm (labeled peak 7 in Figure A4.4b) confirms the cleavage of acetal groups in the VPA monomer. The appearance of peaks related to vanillin and pentaerythritol clearly suggest that acetal groups are cleavable under acidic conditions. These results led us to perform degradation experiments of VPA-DFP under acidic conditions.

We now discuss the polymer degradation behavior in acidic *d*-acetone. A full discussion of 2D NMR analyses (Figures A4.5-A4.11) is provided in the *Appendix 4*. VPA-DFP is not soluble in acetone and thus only the presence of degradation products and oligomers small enough to be solubilized could be monitored with ^{1}H NMR. We consider the proposed small molecule degradation products which could be formed through acid-catalyzed cleavage of acetal groups summarized in Scheme 6.3. Two neighboring repeat units are highlighted in Scheme 6.3. If both spiro acetals groups fully hydrolyze, the degradation product labeled DP-1 will be formed. If both spiro acetal groups only partially hydrolyze, the degradation product labeled DP-3 will be formed. Finally, if one spiro acetal group fully hydrolyzes and one spiro acetal group partially hydrolyzes, the degradation product labeled DP-2 will be formed. Additionally, full hydrolysis of spiro acetal groups

will produce pentaerythritol as a byproduct. We note that if there are unhydrolyzed segments of the polymer, oligomers may be formed with these end-group structures.

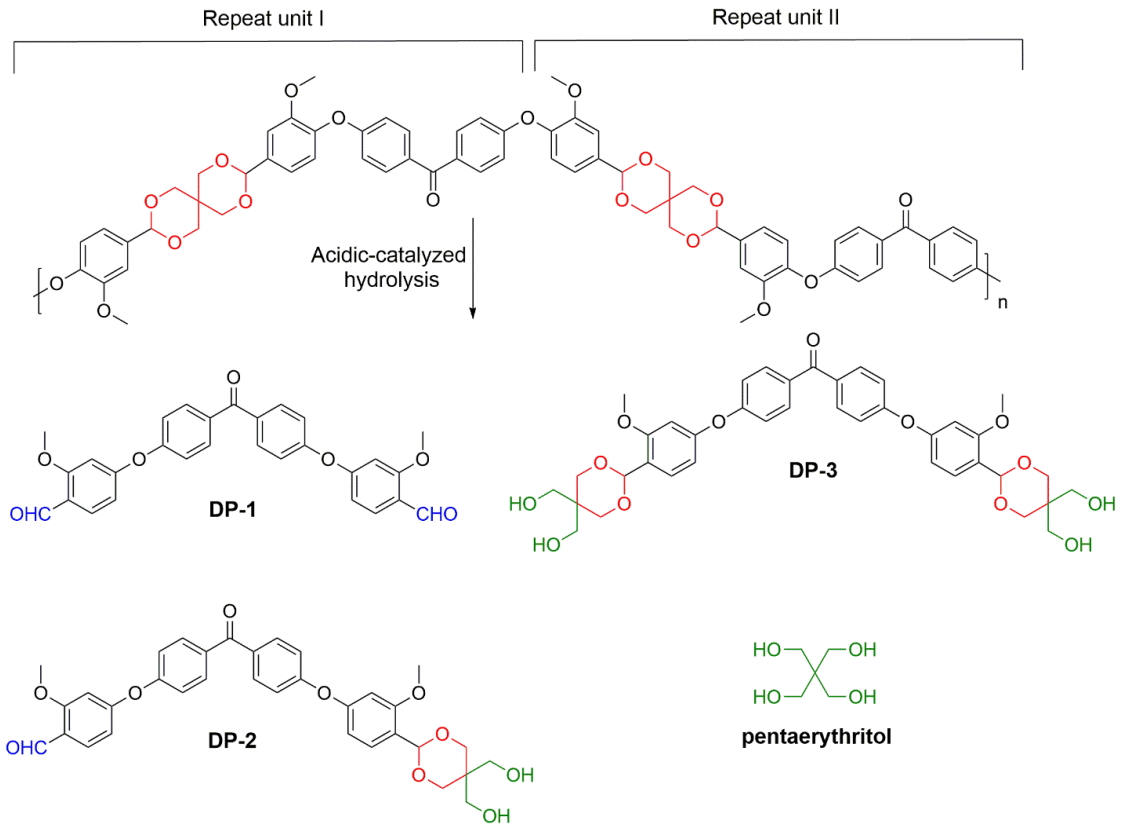

Scheme 6. 3**:** Proposed degradation pathway of the spiro polycycloacetal VPA-DFP in an acidic medium, including probable degradation products. DP: degradation product.

In order to confirm the presence of the four proposed degradation products in Scheme 6.3, ^{1}H, ^{13}C and 2D NMR data were obtained for VPA-DFP after 24 h in acidic *d*-acetone (Figures 6.5 and A4.5 – A4.11). Refer to the discussion in the *Appendix 4* for more details on the peak assignments, obtained through 2D NMR analyses. The presence of fully hydrolyzed acetal groups (found on DP-1 and DP-2 in Scheme 6.3) was identified through the appearance of the -CHO peak at 10.01 ppm in ^{1}H NMR and 191.7 ppm in ^{13}C NMR (labeled peak 2 in Figures 6.5 and A4.7, respectively). The partially hydrolyzed acetal

groups (on DP-2 and DP-3 in Scheme 6.3) are observed through appearance of the -CH groups at 5.48 and 5.58 ppm in ^{1}H NMR and 102 ppm in ^{13}C NMR (labeled peak 10 in Figures 6.5 and A4.7, respectively), as well as -OH groups at 4.7 ppm in ^{1}H NMR (labeled peak 12 in Figure 6.5). We note that the -CH peaks on DP-2 and DP-3 (peak 10 in Figure 6.5) are not expected to be distinguishable; we hypothesize that two peaks are observed in this region due to the presence of H-D exchange, thus shifting the peak slightly. The presence of pentaerythritol is observed through the appearance of the -CH_2 peak at 3.5 ppm in ^{1}H NMR (labeled peak 11 in Figure 6.5) and 32 ppm in ^{13}C NMR (labeled peak 18 in Figure A4.7). Some peaks associated with aromatic protons (labeled as 6-7 and 6'-7'observed in the region of 6.9 – 7.8 ppm in Figure 6.5), are not distinguishable among the three degradation product structures (DP-1, DP-2, and DP-3). However, other aromatic protons (labeled as 3', 4', 5' in Figure 6.5) are shifted due to proximity to the partially hydrolyzed acetal structure. The detailed NMR analyses (discussed further in the *Appendix 4*) therefore support the conclusion that the acid-catalyzed hydrolysis of VPA-DFP resulted in the four degradation products shown in Scheme 6.3, potentially accompanied by oligomers with the same functionalities.

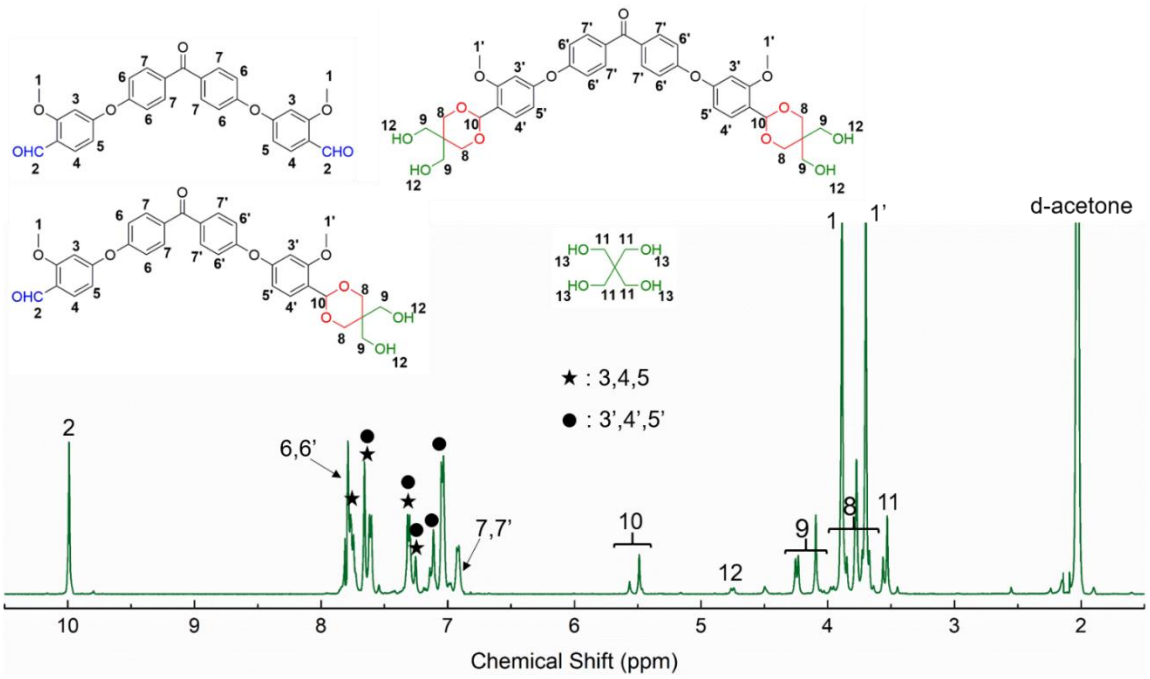

Figure 6. 5: ^{1}H NMR data obtained from the acid-catalyzed hydrolysis of VPA-DFP in *d*-acetone/HCl (0.1 M HCl, pH ~1) at room temperature after 24 h. Degradation experiments were conducted in 0.6 mL *d*-acetone containing 5 µL of 35 wt% aqueous HCl solution.

We used LC-MS to further confirm the identification of degradation products (Figure 6.6). Peaks were observed at m/z of 483 (Figure 6.6a), 601 (Figure 6.6b), 719 (Figure 6.6c), and 137 (Figure 6.6d), confirming the presence of DP-1, DP-2, DP-3, and pentaerythritol, respectively, as the degradation products (products were bound with H^+ and/or Na^+ ions as described in Table 6.3). The respective peak intensities showed that the majority degradation products were DP-1 and pentaerythritol, and only a small amount of DP-2 and DP-3 existed in the degradation product mixture after 24 h. The presence of oligomeric species could not be detected as their size would be outside the accessible range of m/z values for this LC-MS instrument.

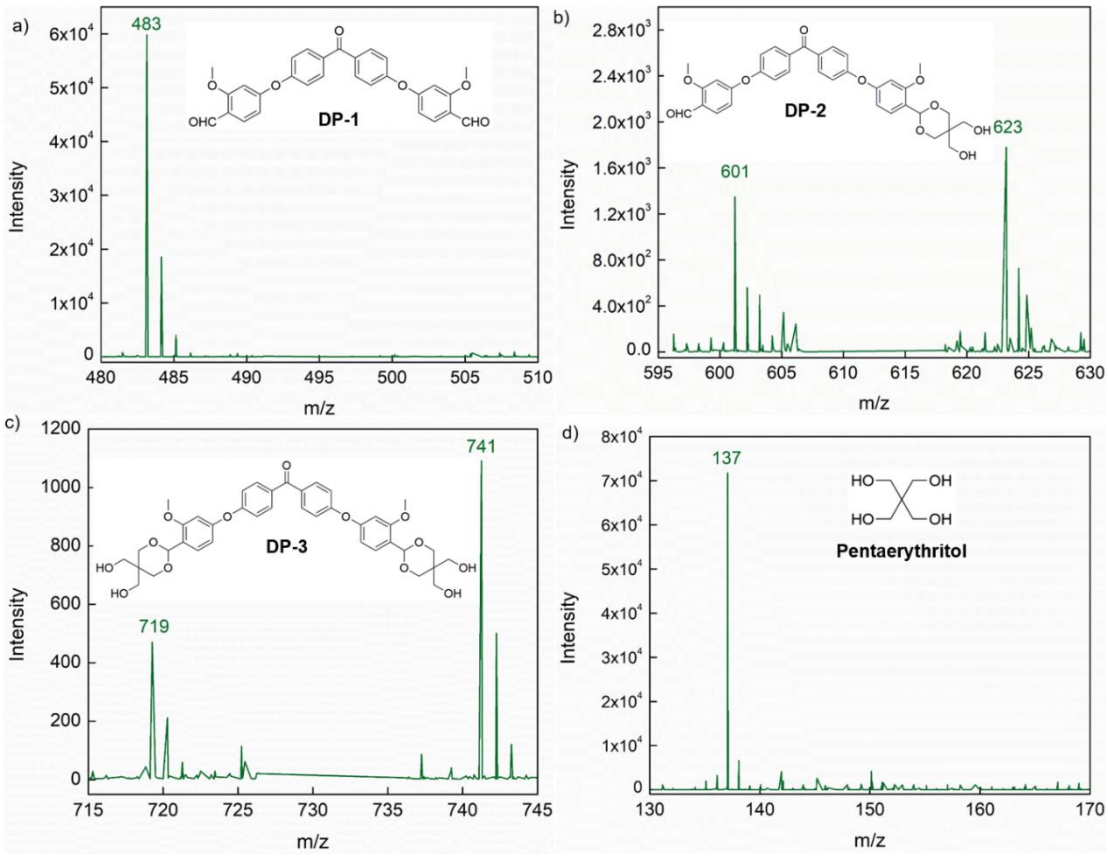

Figure 6. 6**:** LC-MS data obtained from degradation products of VPA-DFP in *d*-acetone/HCl (0.1 M HCl, pH ~1) at room temperature after 24 h degradation time: (a) DP-1, (b) DP-2, (c) DP-3, and (d) pentaerythritol.

Table 6. 3 Molecular weight of degradation products, with bound H^+ and Na^+, and m/z observed in LC-MS.

Degradation Product	Molecular Weight (g/mol)	Molecular Weight with bound H^+ (g/mol)	Molecular Weight with bound Na^+ (g/mol)	m/z observed in LC-MS (g/mol)
DP-1	482.1	483.1	505.1	483.1
DP-2	600.2	601.2	623.2	601.2/623.2
DP-3	718.3	719.3	741.3	719.3/741.3
Pentaerythritol	136.1	137.1	159.1	137.1

6.6 Monitoring Time-Evolution of Degradation Product Compositions of VPA-DFP in Acidic d-Acetone

The time-evolution of the degradation product composition was monitored for VPA-DFP in acidic *d*-acetone, using ^{1}H NMR and GPC. As VPA-DFP is not soluble in *d*-acetone, no peaks were observed for the non-degraded polymer and thus observed peaks are associated with the small molecule degradation products (DP-1, DP-2, DP-3, and pentaerythritol), as well as possibly oligomers small enough to be solubilized. As degradation proceeded, peaks associated with the degradation products appeared in the spectra: -CHO (10.01 ppm) of fully hydrolyzed acetals on DP-1 and DP-2, protons of partially hydrolyzed acetals on DP-2 and DP-3 (-CH at 5.48 and 5.58 ppm and -CH_2 in the range of 3.8 ppm to 4.2 ppm), and aromatic protons found on DP-1, DP-2 and DP-3 (6.9-7.8 ppm) (Figure 6.7). The intensities of these peaks increased over the first 10 h and subsequently no further changes were observed, even up to 96 h.

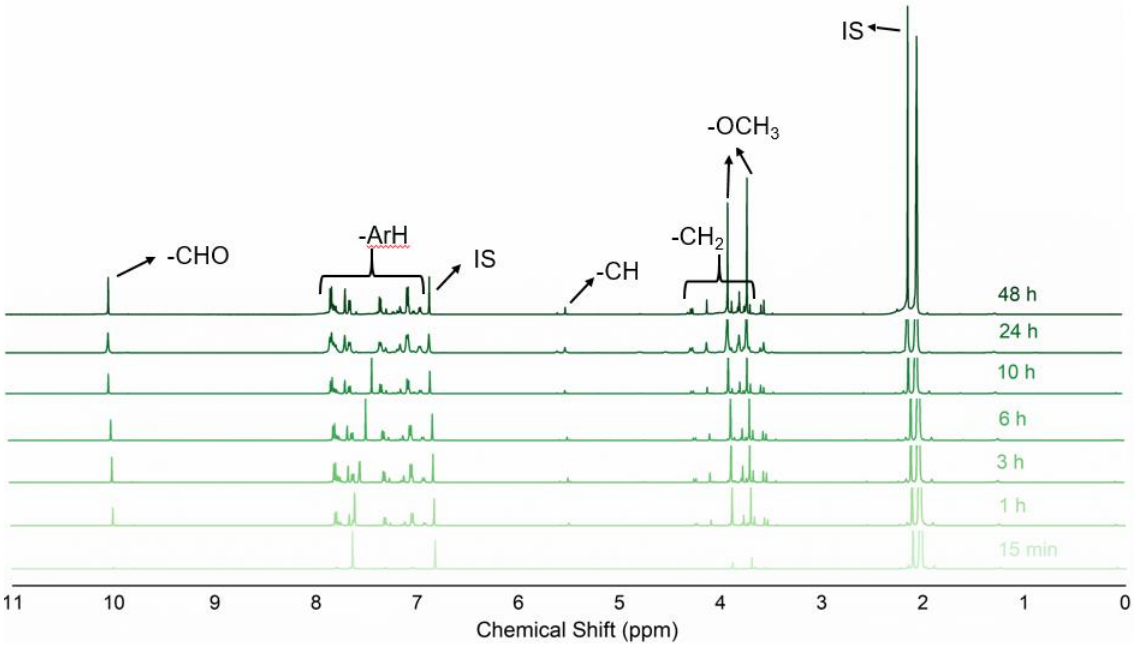

Figure 6. 7**:** ^{1}H NMR data obtained from the acid-catalyzed hydrolysis of VPA-DFP in *d*-acetone/HCl (0.1 M HCl, pH ~1) at room temperature at different time points.

At early times (i.e. 15 min and beyond), both -CHO (10.01 ppm) and -CH peaks (5.48 and 5.58 ppm) peaks are observed, indicating that both fully and partially hydrolyzed structures are present as soon as the degradation process commences. As the degradation process proceeded, the intensity of the -CHO peak increased drastically, suggesting more acetals were fully hydrolyzed. However, even at long times, when changes in the NMR spectra were no longer observed (i.e. longer than 10 hours), -CH peaks are still observed associated with the partially hydrolyzed acetals. Though the degradation process was not complete, no further changes were observed in the spectra upon continued exposure to the acidic solution. Thus, we suggest that degradation products DP-1, DP-2, and DP-3 were present at all times during the process, though the majority of the final degradation product mixture was composed of DP-1 (and possibly oligomers with the same end-functionality) and pentaerythritol.

In order to quantify the degradation process further, we monitored changes in concentration of characteristic chemical groups over time with the use of an internal standard (Figure 6.8): -CHO (10.01 ppm, associated with DP-1 and DP-2), cycloacetal -CH (5.48 and 5.58 ppm, associated with DP-2 and DP-3), and aromatic protons (6.9-7.8 ppm, associated with DP-1, DP-2, and DP-3). As oligomers may be present with the same functional end-groups as DP-1, DP-2, and DP-3, we do not attempt to quantify the concentration of each small molecule degradation product, but rather quantify concentrations of each of the relevant functional groups. The concentration of -CHO groups increased rapidly in the first 10 h of degradation time and then exhibited a plateau after 10 h (Figure 6.8a). If all of the polymer was converted to DP-1, the concentration of -CHO would be 0.0279 mol/L under the conditions used in this experiment. However, the

plateau concentration of -CHO group was slightly lower, 0.0210 mol/L, due to the presence of partially degraded products DP-2 and DP-3. Similarly, the concentration of -CH groups increased during the first 10 h of degradation time, and then exhibited a relatively constant value of 0.00474 mol/L thereafter, indicating a persistent and unchanging presence of the partially hydrolyzed DP-2 and DP-3 at long times as minority components of the degradation product mixture. Additionally, we monitored the change in concentration of aromatic protons over time (Figure 6.8b). Initially, the polymer was not soluble in acetone and aromatic protons were not observed. However, as the polymer degraded to smaller (possibly oligomeric) molecules, their solubility likely increased. Degradation products DP-1, DP-2 and DP-3 are all fully soluble in acetone and contain the same aromatic protons as the polymer repeat unit structure (Scheme 6.3). If the polymer degraded completely to fully soluble species (DP-1, DP-2, DP-3, and even oligomers), the final concentration of aromatic protons would have been 0.195 mol/L. We observed an increase in aromatic proton concentration within 10 hours of degradation time, and a plateau value of 0.194 mol/L, consistent with our expectation.

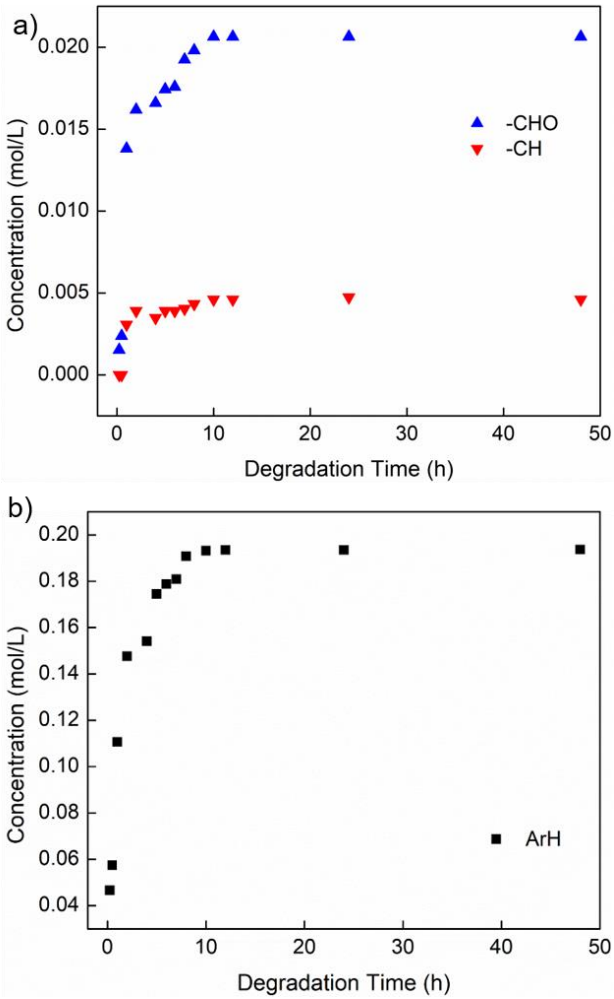

Figure 6. 8**:** Concentration of (a) -CHO (10.01 ppm) and -CH (5.48 and 5.58 ppm) groups and (b) aromatic protons (6.9-7.8) observed at different time points during VPA-DFP degradation in *d*-acetone/HCl at room temperature, quantified from data in Figure 6.7.

To further confirm the existence of DP-1, DP-2, DP-3 and oligomeric degradation products, we used GPC to analyze the molecular weight distribution of degradation products at different degradation times (Figure 6.9a, Table A4.1). The M_n of VPA-DFP prior to degradation was characterized to be 7.3 kg/mol. After 0.5 h of degradation, the polymer peak shifted substantially to the right, consistent with a molecular weight of around 3 kg/mol. This may be due to the formation of oligomeric degradation products.

VPA-DFP is a glassy, semi-crystalline polymer and therefore visually is a white, rigid solid. After 0.5 h of degradation time, it transitioned to a light yellow, soft solid, observed as oligomeric species by GPC. We also noticed the appearance of several lower molecular weight peaks (around 27.2, 27.7, 28.8 and 30.1 min retention time), confirming the presence of smaller degradation products. The molecular weights of smaller species were reasonably consistent with that of DP-3, DP-2, DP-1 and pentaerythritol, respectively (Table A4.1; note that polystyrene standards were used in GPC analyses and therefore only a relative comparison of molecular weights can be made). As the intensities of the peaks associated with the small degradation products increased over time, that of the oligomeric species decreased, indicating further break down of oligomers to DP-1, DP-2, DP-3 and pentaerythritol. We note that at 24 h of degradation time, a small fraction of oligomers still remained. We then varied the molarity of HCl (0.1 – 1 M) at 24 h of degradation time, to explore further degradation of the oligomers at higher acid concentration (Figure 6.9b). We observed the further disappearance of oligomers as the acid concentration was increased, as well as decrease in concentrations of DP-2 and DP-3 and increase in concentration of DP-1 (the fully hydrolyzed byproduct). We did not observed an increase in pentaerythritol concentration as the acid molarity was increased, but we attribute this to the limited solubility of pentaerythritol in DMF (the solvent for GPC experiments).

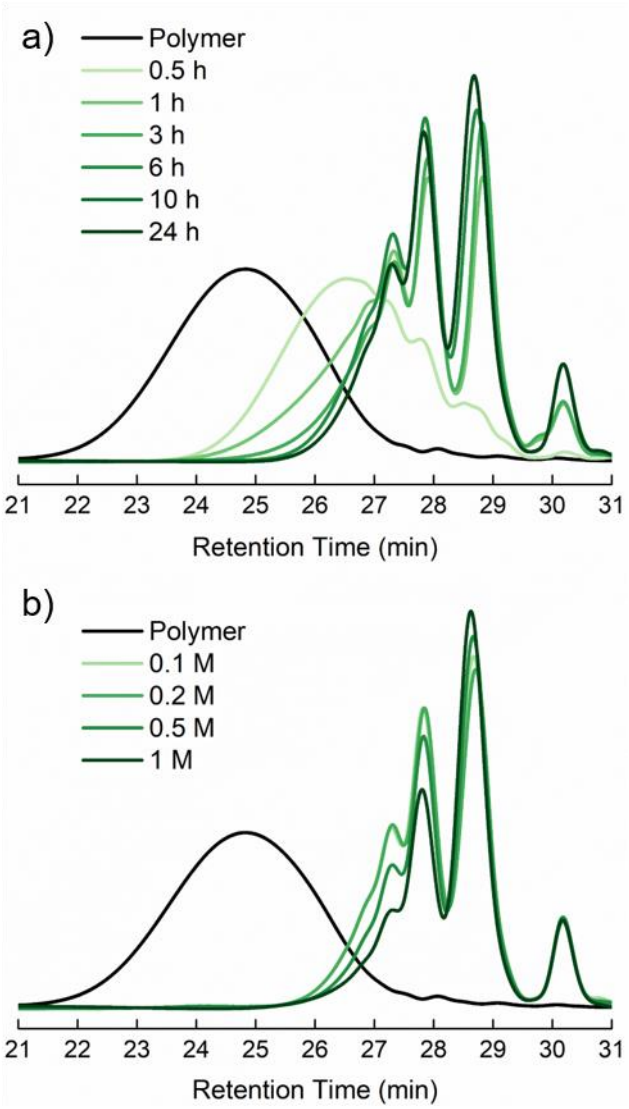

Figure 6. 9**:** GPC data obtained from degradation products of the acid-catalyzed hydrolysis at room temperature of VPA-DFP in *d*-acetone/HCl: a) 0.1 M HCl (pH ~1 at different degradation times and b) varying molarity of acid at 24 h degradation time.

6.7 Impact on Solvent Type on VPA-DFP Degradation Rate

We also compared the degradation rates of VPA-DFP in other solvent systems (acidic *d*-DMSO and D_2O, Figure 6.10). We monitored the change of concentration of -CHO group and we found there was little degradation in D_2O observed up to 168 h, and significantly slower degradation in acidic *d*-DMSO as compared to that observed in in

acidic *d*-acetone. Interestingly, while VPA-DFP is insoluble in acetone and water, it is fully soluble in DMSO.

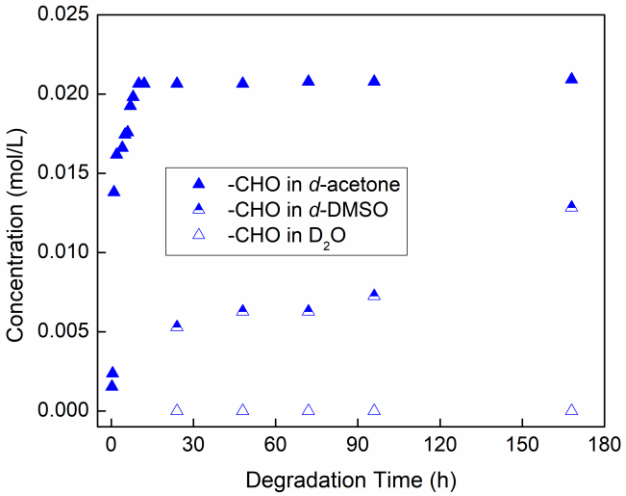

Figure 6. 10**:** Concentration of -CHO (10.01 ppm) group observed at different time points during VPA-DFP degradation in various solvent systems (*d*-acetone/HCl, *d*-DMSO/HCl and D_2O/HCl, containing 0.1 M HCl).

Variation of the solvent composition impacts two important factors which influence the hydrolysis rate:[128] the affinity of the polymer to the solvent and the solubility of the degradation products. We measured the contact angles of a VPA-DFP coated silicon wafer in various solvents (acidic *d*-acetone, acidic *d*-DMSO, and acidic D_2O) and they are summarized in Table 6.4. VPA-DFP exhibited the lowest contact angle in acidic *d*-acetone, followed by acidic *d*-DMSO, and the highest contact angle in D_2O. The rate of hydrolysis therefore appears correlated with the solvent affinity of the polymer.

We also calculated the Hansen Solubility Parameters (δ) of the four degradation products (described in *Appendix 4* and summarized in Table 6.5). We found that δ of DP-1 is very similar to that of *d*-DMSO, and δ of DP-3 and pentaerythritol were very similar to that of D_2O, which should be an indicator of the most favorable conditions for solubility.

δ of DP-2 was not close to any one solvent, indicating conditions were not particularly favorable for solubility. Importantly, δ of all four degradation products were most dissimilar to that of acidic acetone, indicating the worse conditions for solubility in this solvent. Therefore, we observe no correlations between the predicted degradation product solubilities and observed rates of hydrolysis, indicating the solvent affinity of the polymer is likely a more important factor governing the rate of hydrolysis.

Table 6. 4**:** Contact angles of VPA-DFP in various solvent systems

Solvent[a]	Contact Angle (°)
Acidic *d*- acetone	9.5 ± 2.7
Acidic *d*-DMSO	14.7 ± 1.6
Acidic D_2O	69.7 ± 0.8

[a] Acidic solvent compositions were identical to that used in degradation experiments

Table 6. 5: Hansen Solubility Parameter (δ) of VPA-DFP degradation products and solvents

Degradation Product or Solvent	δ ($MPa^{1/2}$)
DP-1	27.5
DP-2	36.3
DP-3	48.1
Pentaerythritol	41.2
Acetone	19.9
DMSO	24.4
H_2O	47.8

6.8 Conclusions

Degradable, thermally stable, and high T_g and T_m polymers were synthesized from bioaromatics, including vanillin and its derivative syringaldehyde, employing difluoro aromatic co-monomers. Incorporation of spiro cycloacetal units, along with aromatic groups, into the polymer backbone resulted in high thermal degradation temperatures, as well as high T_g and T_m. The presence of labile spiro cycloacetal units provided a mechanism for degradation under acid-catalyzed hydrolysis. Degradation studies indicated these spiro

cycloacetal units were relatively stable in an acidic aqueous medium (pH ~ 1), but could be degraded in acidic organic solvents (DMSO and acetone). Among the various solvents, degradation occurred most rapidly in acidic acetone. Four small molecule degradation products, along with solubilized oligomers, were detected in the degradation solution, produced through the acid-catalyzed cleavage of acetal groups. The solvent affinity of the polymer was identified to be a more important factor governing the rate of hydrolysis than the predicted degradation product solubilities.

Chapter 7

7.1 Summary

Firstly, we synthesized a lignin-derived epoxidized vanillic acid (EVA)-based epoxy resin using conventional and green enzyme-based methods. The curing behavior was studied with FTIR to ensure high conversion of functional groups. The resulting EVA-based epoxy resin showed promising thermal and mechanical properties as compared to a conventional diglycidyl ether of bisphenol A (DGEBA)-based epoxy resin. The EVA-based epoxy resin required less time to achieve gelation under the same curing conditions as compared to the DGEBA-based epoxy resin, facilitating more rapid manufacturing. The EVA-based epoxy resin exhibited higher storage and loss moduli and complex viscosity during the curing process as compared to the DGEBA-based epoxy resin. Both resins exhibited similar volume change upon curing.

Secondly, we examined the hydrolytic degradation behavior of ester-containing biobased epoxy resins in basic solutions, and probed their hydrolytic degradation mechanisms. We explored the degradation behavior of biobased epoxy resins containing high ester content than traditional epoxy resins. Importantly, we characterized degradation products following exposure of the resins to basic solutions, identified the degradation mechanism as surface erosion, and quantified degradation rate constants through utilization of a solid-state kinetic model, the contracting volume model.

Thirdly, we examined the hydrolytic degradation behavior of ester-containing biobased epoxy resins in acidic solutions. We characterized the degradation products and remaining sample surface compositions and probed the degradation mechanisms in acidic solutions as bulk erosion. We quantified degradation rate constants through application of

a solid-state reaction order model with autocatalysis to predict the degradation behavior. We also discussed the influence of various factors such as presence of functional groups, network crosslink density and glass transition temperature, and solvent composition and temperature, on degradation behavior.

Finally, we described the synthesis and characterization of spiro polycycloacetals utilizing bioaromatic hydroxyaldehydes, polyols, and aromatic sulfonates or benzophenone. Notably, the incorporation of aromatic sulfonates or benzophenone into the polymer backbone, along with bioaromatic aldehydes, increased the aromaticity and rigidity of polymer backbone, which further improved the polymer thermal stability as well as T_g. We also demonstrated their rapid hydrolytic degradation in acidic media. The hydrolytic degradation behavior of one spiro polycycloacetal, derived from vanillin and 4,4′-difluorobenzophenone was quantified in various acidic solvents; the polymer showed the fastest degradation behavior in acidic acetone and degraded completely to small molecule and oligomeric byproducts within 10 h.

7.2 Future Work

7.2.1 Investigating other ester-containing epoxy monomers from lignin

Vanillic acid is a byproduct of the pyrolysis of lignin. Other viable monomer precursors are produced from different treatments of lignin. Two promising options are ferulic acid and coumaric acid (chemical structures are in Figure 7.1) which can be produced in large amounts by chemical treatments of lignin. Ferulic acid, one of the phenolic compounds in lignin which is released after basic solution treatment of lignin, can be further utilized for many industrial purposes. Ferulic acid and coumaric acid have very similar structures as vanillic acid, and thus may result in epoxy resins with competitive

properties However, no studies to date have investigated ferulic acid or coumaric acid as sources for epoxy resins. The routes of ferulic acid to ferulic acid-based epoxy resin could also vary based on the saturation of carbon carbon double bond in the structure (Scheme 7.1). We could first saturate the double bond and then proceed with epoxidation, which would possibly avoid any side reactions from the unstable double bond. We could also leave the double bond in place and go ahead with the epoxidation step, which could result in epoxy monomers with three epoxide groups. Thus, this method could produce epoxy resins with higher crosslink density due to more epoxide groups per monomer.

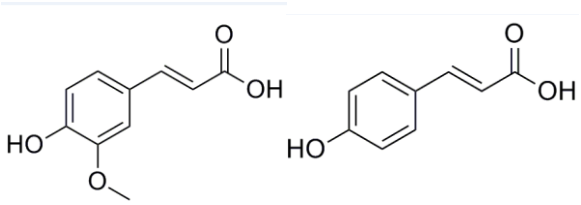

Figure 7. 1: Structures of ferulic acid (left) and coumaric acid (right).

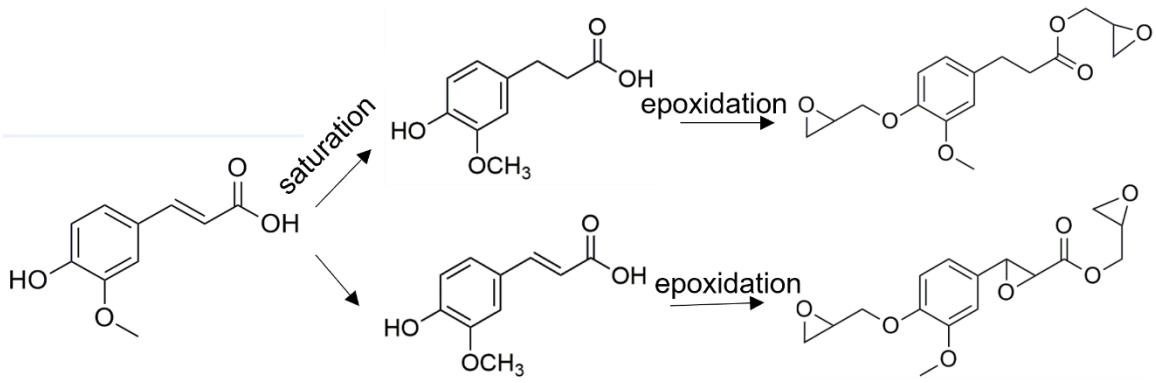

Scheme 7. 1: Different proposed routes to synthesize ferulic acid-based epoxy monomer using ferulic acid.

7.2.2 Creation of imine-containing fully sustainable epoxy resins

There are also other cleavable functional groups that can be utilized in the epoxy resin systems to create desirable mechanical and thermal properties, as well as degradation properties. The imine group is a promising functional group which was recently studied

and can be cleaved in acidic media rapidly [72]. Imine groups could be formed due to the reaction of the aldehyde group in the epoxy monomer and the amine curing agent. Here, I am proposing a new synthesis route that could create fully sustainable epoxy resins with imine functionality using vanillin, amino acid and citric acid. Vanillin is an abundant source after treatment of lignin. Vanillin can then react with amino acid to create imine groups. Recently, researchers have also examined other biobased curing agents including citric acid to create fully biobased epoxy resins. In Scheme 7.2, an example is provided of a fully sustainable epoxy resin that can be synthesized to contain imine groups. With the incorporation of imine groups, the resulting epoxy resins should have recyclable properties, as well as potentially desirable thermal and mechanical properties.

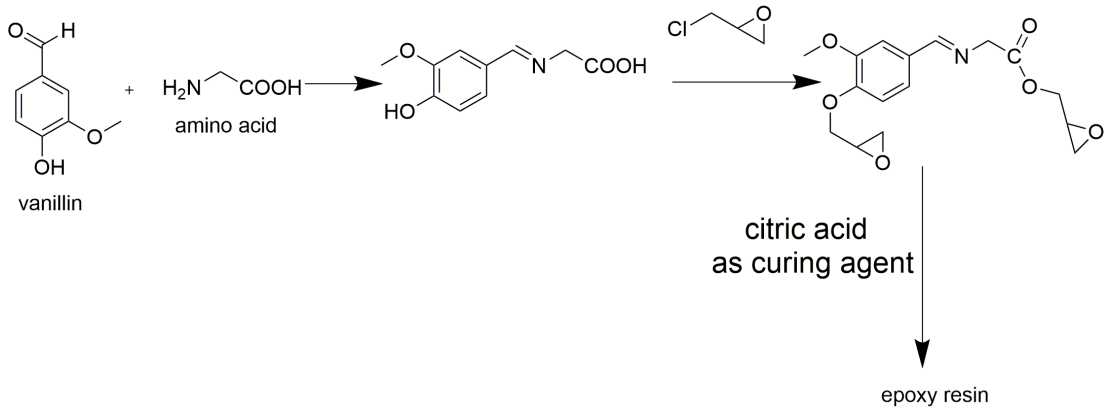

Scheme 7. 2**:** Synthesis scheme of fully sustainable epoxy resins containing imine group

References

1. Bagheri, R., B.T. Marouf, and R.A. Pearson, *Rubber-Toughened Epoxies: A Critical Review.* Polymer Reviews, 2009. **49**(3): p. 201-225.
2. Hussain, F., M. Hojjati, M. Okamoto, and R.E. Gorga, *Review article: Polymer-matrix nanocomposites, processing, manufacturing, and application: An overview.* Journal of Composite Materials, 2006. **40**(17): p. 1511-1575.
3. Upton, B.M. and A.M. Kasko, *Strategies for the Conversion of Lignin to High-Value Polymeric Materials: Review and Perspective.* Chemical Reviews, 2016. **116**(4): p. 2275-2306.
4. Feldman, D., D. Banu, A. Natansohn, and J. Wang, *Structure–properties relations of thermally cured epoxy–lignin polyblends.* Journal of Applied Polymer Science, 1991. **42**(6): p. 1537-1550.
5. Simionescu, C.I., V. Rusan, M.M. Macoveanu, G. Cazacu, R. Lipsa, C. Vasile, A. Stoleriu, and A. Ioanid, *Lignin/epoxy composites.* Composites Science and Technology, 1993. **48**(1): p. 317-323.
6. Delmas, G.-H., B. Benjelloun-Mlayah, Y.L. Bigot, and M. Delmas, *Biolignin™ based epoxy resins.* Journal of Applied Polymer Science, 2013. **127**(3): p. 1863-1872.
7. Fache, M., E. Darroman, V. Besse, R. Auvergne, S. Caillol, and B. Boutevin, *Vanillin, a promising biobased building-block for monomer synthesis.* Green Chemistry, 2014. **16**(4): p. 1987-1998.
8. Memon, H., Y. Wei, L. Zhang, Q. Jiang, and W. Liu, *An imine-containing epoxy vitrimer with versatile recyclability and its application in fully recyclable carbon*

fiber reinforced composites. Composites Science and Technology, 2020. **199**: p. 108314.

9. Desnoes, E., L. Toubal, A.H. Bouazza, and D. Montplaisir, *Biosourced vanillin Schiff base platform monomers as substitutes for DGEBA in thermoset epoxy.* Polymer Engineering & Science, 2020. **60**(10): p. 2593-2605.
10. Su, X., Z. Zhou, J. Liu, J. Luo, and R. Liu, *A recyclable vanillin-based epoxy resin with high-performance that can compete with DGEBA.* European Polymer Journal, 2020. **140**: p. 110053.
11. Wang, S., S. Ma, C. Xu, Y. Liu, J. Dai, Z. Wang, X. Liu, J. Chen, X. Shen, J. Wei, and J. Zhu, *Vanillin-Derived High-Performance Flame Retardant Epoxy Resins: Facile Synthesis and Properties.* Macromolecules, 2017. **50**(5): p. 1892-1901.
12. Ma, S., J. Wei, Z. Jia, T. Yu, W. Yuan, Q. Li, S. Wang, S. You, R. Liu, and J. Zhu, *Readily recyclable, high-performance thermosetting materials based on a lignin-derived spiro diacetal trigger.* Journal of Materials Chemistry A, 2019. **7**(3): p. 1233-1243.
13. Winter, H.H., *Can the gel point of a cross-linking polymer be detected by the G′ – G″ crossover?* Polymer Engineering & Science, 1987. **27**(22): p. 1698-1702.
14. Cadenato, A., J.M. Salla, X. Ramis, J.M. Morancho, L.M. Marroyo, and J.L. Martin, *Determination of gel and vitrification times of thermoset curing process by means of TMA, DMTA and DSC techniques.* Journal of thermal analysis, 1997. **49**(1): p. 269-279.
15. Halley, P.J. and M.E. Mackay, *Chemorheology of thermosets—an overview.* Polymer Engineering & Science, 1996. **36**(5): p. 593-609.

16. Lange, J., N. Altmann, C.T. Kelly, and P.J. Halley, *Understanding vitrification during cure of epoxy resins using dynamic scanning calorimetry and rheological techniques.* Polymer, 2000. **41**(15): p. 5949-5955.

17. Tanaka, Y., J.L. Stanford, and R. Stepto, *Interpretation of Gel Points of an Epoxy–Amine System Including Ring Formation and Unequal Reactivity: Reaction Scheme and Gel-Point Prediction.* Macromolecules, 2012. **45**(17): p. 7186-7196.

18. Matějka, L., *Rheology of epoxy networks near the gel point.* Polymer Bulletin, 1991. **26**(1): p. 109-116.

19. Miller-Chou, B.A. and J.L. Koenig, *A review of polymer dissolution.* Progress in Polymer Science, 2003. **28**(8): p. 1223-1270.

20. Narasimhan, B., *Mathematical models describing polymer dissolution: consequences for drug delivery.* Advanced Drug Delivery Reviews, 2001. **48**(2): p. 195-210.

21. Pappa, G., C. Boukouvalas, C. Giannaris, N. Ntaras, V. Zografos, K. Magoulas, A. Lygeros, and D. Tassios, *The selective dissolution/precipitation technique for polymer recycling: a pilot unit application.* Resources, Conservation and Recycling, 2001. **34**(1): p. 33-44.

22. Busatto, C., E. Berkenwald, N. Mariano, N. Casis, J. Luna, and D. Estenoz, *Homogeneous hydrolytic degradation of poly(lactic-co-glycolic acid) microspheres: Mathematical modeling.* Polymer Degradation and Stability, 2016. **125**: p. 12-20.

23. Busatto, C., J. Pesoa, I. Helbling, J. Luna, and D. Estenoz, *Heterogeneous hydrolytic degradation of poly(lactic-co-glycolic acid) microspheres:*

Mathematical modeling. Journal of Applied Polymer Science, 2017. **134**(43): p. 45464.

24. Iñiguez-Franco, F., R. Auras, G. Burgess, D. Holmes, X. Fang, M. Rubino, and H. Soto-Valdez, *Concurrent solvent induced crystallization and hydrolytic degradation of PLA by water-ethanol solutions.* Polymer, 2016. **99**: p. 315-323.

25. Khanlou, H.M., P. Woodfield, J. Summerscales, G. Francucci, B. King, S. Talebian, J. Foroughi, and W. Hall, *Estimation of mechanical property degradation of poly(lactic acid) and flax fibre reinforced poly(lactic acid) bio-composites during thermal processing.* Measurement, 2018. **116**: p. 367-372.

26. Marten, E., R.-J. Müller, and W.-D. Deckwer, *Studies on the enzymatic hydrolysis of polyesters I. Low molecular mass model esters and aliphatic polyesters.* Polymer Degradation and Stability, 2003. **80**(3): p. 485-501.

27. Polyák, P., E. Urbán, G.N. Nagy, B.G. Vértessy, and B. Pukánszky, *The role of enzyme adsorption in the enzymatic degradation of an aliphatic polyester.* Enzyme and Microbial Technology, 2019. **120**: p. 110-116.

28. Sevim, K. and J. Pan, *A model for hydrolytic degradation and erosion of biodegradable polymers.* Acta Biomaterialia, 2018. **66**: p. 192-199.

29. Shine, R., R. Neghabat Shirazi, W. Ronan, C.A. Sweeney, N. Kelly, Y.A. Rochev, and P.E. McHugh, *Modeling of Biodegradable Polyesters With Applications to Coronary Stents.* Journal of Medical Devices, 2017. **11**(2): p. 021007-021007-12.

30. Weir, N.A., F.J. Buchanan, J.F. Orr, D.F. Farrar, and G.R. Dickson, *Degradation of poly-L-lactide. Part 2: Increased temperature accelerated degradation.*

Proceedings of the Institution of Mechanical Engineers, Part H: Journal of Engineering in Medicine, 2004. **218**(5): p. 321-330.

31. Antheunis, H., J.-C. van der Meer, M. de Geus, A. Heise, and C.E. Koning, *Autocatalytic Equation Describing the Change in Molecular Weight during Hydrolytic Degradation of Aliphatic Polyesters.* Biomacromolecules, 2010. **11**(4): p. 1118-1124.
32. Batycky, R.P., J. Hanes, R. Langer, and D.A. Edwards, *A Theoretical Model of Erosion and Macromolecular Drug Release from Biodegrading Microspheres.* Journal of Pharmaceutical Sciences, 1997. **86**(12): p. 1464-1477.
33. Göpferich, A., *Mechanisms of polymer degradation and erosion.* Biomaterials, 1996. **17**(2): p. 103-114.
34. Göpferich, A., *Polymer Bulk Erosion.* Macromolecules, 1997. **30**(9): p. 2598-2604.
35. Gopferich, A. and R. Langer, *Modeling of polymer erosion.* Macromolecules, 1993. **26**(16): p. 4105-4112.
36. Tamada, J.A. and R. Langer, *Erosion kinetics of hydrolytically degradable polymers.* Proceedings of the National Academy of Sciences of the United States of America, 1993. **90**(2): p. 552-556.
37. Grassie, N., M.I. Guy, and N.H. Tennent, *Degradation of epoxy polymers: Part 4—Thermal degradation of bisphenol-A diglycidyl ether cured with ethylene diamine.* Polymer Degradation and Stability, 1986. **14**(2): p. 125-137.
38. Tudorachi, N. and F. Mustata, *Curing and thermal degradation of diglycidyl ether of bisphenol A epoxy resin crosslinked with natural hydroxy acids as environmentally friendly hardeners.* Arabian Journal of Chemistry, 2017.

39. Patel, R.D., R.G. Patel, and V.S. Patel, *Kinetics of thermal degradation of cured epoxy resins based on triglycidyl-p-aminophenol.* Thermochimica Acta, 1988. **128**: p. 149-156.

40. Barral, L., J. Cano, A.J. López, J. Lopez, P. Nógueira, and C. Ramírez, *Thermal degradation of a diglycidyl ether of bisphenol A/1,3-bisaminomethylcyclohexane (DGEBA/1,3-BAC) epoxy resin system.* Thermochimica Acta, 1995. **269-270**: p. 253-259.

41. Kuo, P.-Y., L. de Assis Barros, Y.-C. Sheen, M. Sain, J.S.Y. Tjong, and N. Yan, *Thermal degradation of extractive-based bio-epoxy monomer and network: Kinetics and mechanism.* Journal of Analytical and Applied Pyrolysis, 2016. **117**: p. 199-213.

42. Natarajan, M. and S.C. Murugavel, *Thermal stability and thermal degradation kinetics of bio-based epoxy resins derived from cardanol by thermogravimetric analysis.* Polymer Bulletin, 2017. **74**(8): p. 3319-3340.

43. Shogren, R.L., Z. Petrovic, Z. Liu, and S.Z. Erhan, *Biodegradation Behavior of Some Vegetable Oil-Based Polymers.* Journal of Polymers and the Environment, 2004. **12**(3): p. 173-178.

44. Tarzia, A., J. Montanaro, M. Casiello, C. Annese, A. Nacci, and A. Maffezzoli, *Synthesis, Curing, and Properties of an Epoxy Resin Derived from Gallic Acid*. 2017. Vol. 13. 2017.

45. Xin, J., P. Zhang, K. Huang, and J. Zhang, *Study of green epoxy resins derived from renewable cinnamic acid and dipentene: synthesis, curing and properties.* RSC Advances, 2014. **4**(17): p. 8525-8532.

46. Dang, W., M. Kubouchi, S. Yamamoto, H. Sembokuya, and K. Tsuda, *An approach to chemical recycling of epoxy resin cured with amine using nitric acid.* Polymer, 2002. **43**(10): p. 2953-2958.

47. Sato, Y., Y. Kondo, K. Tsujita, and N. Kawai, *Degradation behaviour and recovery of bisphenol-A from epoxy resin and polycarbonate resin by liquid-phase chemical recycling.* Polymer Degradation and Stability, 2005. **89**(2): p. 317-326.

48. Oliveux, G., L.O. Dandy, and G.A. Leeke, *Degradation of a model epoxy resin by solvolysis routes.* Polymer Degradation and Stability, 2015. **118**: p. 96-103.

49. Liu, T., M. Zhang, X. Guo, C. Liu, T. Liu, J. Xin, and J. Zhang, *Mild chemical recycling of aerospace fiber/epoxy composite wastes and utilization of the decomposed resin.* Polymer Degradation and Stability, 2017. **139**: p. 20-27.

50. Liu, T., X. Guo, W. Liu, C. Hao, L. Wang, W.C. Hiscox, C. Liu, C. Jin, J. Xin, and J. Zhang, *Selective cleavage of ester linkages of anhydride-cured epoxy using a benign method and reuse of the decomposed polymer in new epoxy preparation.* Green Chemistry, 2017. **19**(18): p. 4364-4372.

51. Jiang, G., S.J. Pickering, E.H. Lester, and N.A. Warrior, *Decomposition of Epoxy Resin in Supercritical Isopropanol.* Industrial & Engineering Chemistry Research, 2010. **49**(10): p. 4535-4541.

52. Destais-Orvoën, N., G. Durand, and G. Tersac, *Glycolysis of epoxide–amine hardened networks II—aminoether model compound.* Polymer, 2004. **45**(16): p. 5473-5482.

53. El Gersifi, K., N. Destais-Orvoën, G. Durand, and G. Tersac, *Glycolysis of epoxide-amine hardened networks. I. Diglycidylether/aliphatic amines model networks.* Polymer, 2003. **44**(14): p. 3795-3801.

54. El Gersifi, K., G. Durand, and G. Tersac, *Solvolysis of bisphenol A diglycidyl ether/anhydride model networks.* Polymer Degradation and Stability, 2006. **91**(4): p. 690-702.

55. Kuang, X., Q. Shi, Y. Zhou, Z. Zhao, T. Wang, and H.J. Qi, *Dissolution of epoxy thermosets via mild alcoholysis: the mechanism and kinetics study.* RSC Advances, 2018. **8**(3): p. 1493-1502.

56. Kuang, X., Y. Zhou, Q. Shi, T. Wang, and H.J. Qi, *Recycling of Epoxy Thermoset and Composites via Good Solvent Assisted and Small Molecules Participated Exchange Reactions.* ACS Sustainable Chemistry & Engineering, 2018. **6**(7): p. 9189-9197.

57. Gong, X., H. Kang, Y. Liu, and S. Wu, *Decomposition mechanisms and kinetics of amine/anhydride-cured DGEBA epoxy resin in near-critical water.* RSC Advances, 2015. **5**(50): p. 40269-40282.

58. Ma, Y. and S. Nutt, *Chemical treatment for recycling of amine/epoxy composites at atmospheric pressure.* Polymer Degradation and Stability, 2018. **153**: p. 307-317.

59. Okajima, I., M. Hiramatsu, Y. Shimamura, T. Awaya, and T. Sako, *Chemical recycling of carbon fiber reinforced plastic using supercritical methanol.* The Journal of Supercritical Fluids, 2014. **91**: p. 68-76.

60. You, S., S. Ma, J. Dai, Z. Jia, X. Liu, and J. Zhu, *Hexahydro-s-triazine: A Trial for Acid-Degradable Epoxy Resins with High Performance.* ACS Sustainable Chemistry & Engineering, 2017. **5**(6): p. 4683-4689.

61. Grassie, N., M.I. Guy, and N.H. Tennent, *Degradation of epoxy polymers. Part 5—Photo-degradation of bisphenol-A diglycidyl ether cured with ethylene diamine.* Polymer Degradation and Stability, 1986. **14**(3): p. 209-216.

62. Dupuis, A., F.-X. Perrin, A. Ulloa Torres, J.-P. Habas, L. Belec, and J.-F. Chailan, *Photo-oxidative degradation behavior of linseed oil based epoxy resin.* Polymer Degradation and Stability, 2017. **135**: p. 73-84.

63. Liu, T., C. Hao, L. Wang, Y. Li, W. Liu, J. Xin, and J. Zhang, *Eugenol-Derived Biobased Epoxy: Shape Memory, Repairing, and Recyclability.* Macromolecules, 2017. **50**(21): p. 8588-8597.

64. Ma, S., D.C. Webster, and F. Jabeen, *Hard and Flexible, Degradable Thermosets from Renewable Bioresources with the Assistance of Water and Ethanol.* Macromolecules, 2016. **49**(10): p. 3780-3788.

65. Yu, C., Z. Xu, Y. Wang, S. Chen, M. Miao, and D. Zhang, *Synthesis and Degradation Mechanism of Self-Cured Hyperbranched Epoxy Resins from Natural Citric Acid.* ACS omega, 2018. **3**(7): p. 8141-8148.

66. Hashimoto, T., H. Meiji, M. Urushisaki, T. Sakaguchi, K. Kawabe, C. Tsuchida, and K. Kondo, *Degradable and chemically recyclable epoxy resins containing acetal linkages: Synthesis, properties, and application for carbon fiber-reinforced plastics.* Journal of Polymer Science Part A: Polymer Chemistry, 2012. **50**(17): p. 3674-3681.

67. Yamaguchi, A., T. Hashimoto, Y. Kakichi, M. Urushisaki, T. Sakaguchi, K. Kawabe, K. Kondo, and H. Iyo, *Recyclable carbon fiber-reinforced plastics (CFRP) containing degradable acetal linkages: Synthesis, properties, and chemical recycling.* Journal of Polymer Science Part A: Polymer Chemistry, 2015. **53**(8): p. 1052-1059.

68. Huh, G., K.-O. Kwon, S.-H. Cha, S.-W. Yoon, M.Y. Lee, and J.-C. Lee, *Synthesis of a photo-patternable cross-linked epoxy system containing photodegradable carbonate units for deep UV lithography.* Journal of Applied Polymer Science, 2009. **114**(4): p. 2093-2100.

69. Zhao, L., Y. Liu, Z. Wang, J. Li, W. Liu, and Z. Chen, *Synthesis and degradable property of novel sulfite-containing cycloaliphatic epoxy resins.* Polymer Degradation and Stability, 2013. **98**(11): p. 2125-2130.

70. Canadell, J., H. Goossens, and B. Klumperman, *Self-Healing Materials Based on Disulfide Links.* Macromolecules, 2011. **44**(8): p. 2536-2541.

71. Rekondo, A., R. Martin, A. Ruiz de Luzuriaga, G. Cabañero, H.J. Grande, and I. Odriozola, *Catalyst-free room-temperature self-healing elastomers based on aromatic disulfide metathesis.* Materials Horizons, 2014. **1**(2): p. 237-240.

72. Harada, M., J. Ando, M. Yamaki, and M. Ochi, *Synthesis, characterization, and mechanical properties of a novel terphenyl liquid crystalline epoxy resin.* Journal of Applied Polymer Science, 2015. **132**(1).

73. Bai, N., K. Saito, and G.P. Simon, *Synthesis of a diamine cross-linker containing Diels–Alder adducts to produce self-healing thermosetting epoxy polymer from a widely used epoxy monomer.* Polymer Chemistry, 2013. **4**(3): p. 724-730.

74. Bai, J., H. Li, Z. Shi, and J. Yin, *An Eco-Friendly Scheme for the Cross-Linked Polybutadiene Elastomer via Thiol–Ene and Diels–Alder Click Chemistry.* Macromolecules, 2015. **48**(11): p. 3539-3546.

75. Gandini, A., *The furan/maleimide Diels–Alder reaction: A versatile click–unclick tool in macromolecular synthesis.* Progress in Polymer Science, 2013. **38**(1): p. 1-29.

76. Zhao, S. and M.M. Abu-Omar, *Recyclable and Malleable Epoxy Thermoset Bearing Aromatic Imine Bonds.* Macromolecules, 2018. **51**(23): p. 9816-9824.

77. Ma, S. and D.C. Webster, *Naturally Occurring Acids as Cross-Linkers To Yield VOC-Free, High-Performance, Fully Bio-Based, Degradable Thermosets.* Macromolecules, 2015. **48**(19): p. 7127-7137.

78. Wang, S., S. Ma, Q. Li, X. Xu, B. Wang, W. Yuan, S. Zhou, S. You, and J. Zhu, *Facile in situ preparation of high-performance epoxy vitrimer from renewable resources and its application in nondestructive recyclable carbon fiber composite.* Green Chemistry, 2019. **21**(6): p. 1484-1497.

79. Zhang, Q., M. Molenda, and T.M. Reineke, *Epoxy Resin Thermosets Derived from Trehalose and β-Cyclodextrin.* Macromolecules, 2016. **49**(22): p. 8397-8406.

80. Zhang, Q., H.R. Phillips, A. Purchel, J.K. Hexum, and T.M. Reineke, *Sustainable and Degradable Epoxy Resins from Trehalose, Cyclodextrin, and Soybean Oil Yield Tunable Mechanical Performance and Cell Adhesion.* ACS Sustainable Chemistry & Engineering, 2018. **6**(11): p. 14967-14978.

81. Janvier, M., L. Hollande, A.S. Jaufurally, M. Pernes, R. Ménard, M. Grimaldi, J. Beaugrand, P. Balaguer, P.-H. Ducrot, and F. Allais, *Syringaresinol: A Renewable*

and Safer Alternative to Bisphenol A for Epoxy-Amine Resins. ChemSusChem, 2017. **10**(4): p. 738-746.

82. Yuan, W., S. Ma, S. Wang, Q. Li, B. Wang, X. Xu, K. Huang, J. Chen, S. You, and J. Zhu, *Synthesis of fully bio-based diepoxy monomer with dicyclo diacetal for high-performance, readily degradable thermosets.* European Polymer Journal, 2019. **117**: p. 200-207.

83. Keith, M.J., G.A. Leeke, P. Khan, and A. Ingram, *Catalytic degradation of a carbon fibre reinforced polymer for recycling applications.* Polymer Degradation and Stability, 2019. **166**: p. 188-201.

84. Deng, T., Y. Liu, X. Cui, Y. Yang, S. Jia, Y. Wang, C. Lu, D. Li, R. Cai, and X. Hou, *Cleavage of C–N bonds in carbon fiber/epoxy resin composites.* Green Chemistry, 2015. **17**(4): p. 2141-2145.

85. Piñero-Hernanz, R., C. Dodds, J. Hyde, J. García-Serna, M. Poliakoff, E. Lester, M.J. Cocero, S. Kingman, S. Pickering, and K.H. Wong, *Chemical recycling of carbon fibre reinforced composites in nearcritical and supercritical water.* Composites Part A: Applied Science and Manufacturing, 2008. **39**(3): p. 454-461.

86. Yuan, Y., Y. Sun, S. Yan, J. Zhao, S. Liu, M. Zhang, X. Zheng, and L. Jia, *Multiply fully recyclable carbon fibre reinforced heat-resistant covalent thermosetting advanced composites.* Nature Communications, 2017. **8**(1): p. 14657.

87. Shen, M., R. Almallahi, Z. Rizvi, E. Gonzalez-Martinez, G. Yang, and M.L. Robertson, *Accelerated hydrolytic degradation of ester-containing biobased epoxy resins.* Polymer Chemistry, 2019. **10**(23): p. 3217-3229.

88. Johnson, L.M., E. Ledet, N.D. Huffman, S.L. Swarner, S.D. Shepherd, P.G. Durham, and G.D. Rothrock, *Controlled degradation of disulfide-based epoxy thermosets for extreme environments.* Polymer, 2015. **64**: p. 84-92.

89. Zhang, Y., Q. Ling, X. Lu, Q. Fang, and F. Sun, *Rheology, morphological evolution, thermal, and mechanical properties of epoxy modified with polysulfone and cellulose nanofibers.* Journal of Applied Polymer Science, 2020. **137**(18): p. 48628.

90. Yang, G., B.J. Rohde, and M.L. Robertson, *Hydrolytic degradation and thermal properties of epoxy resins derived from soybean oil.* Green Materials, 2013. **1**(2): p. 125-134.

91. Umare, S.S. and A.S. Chandure, *Synthesis, characterization and biodegradation studies of poly(ester urethane)s.* Chemical Engineering Journal, 2008. **142**(1): p. 65-77.

92. Aouf, C., J. Lecomte, P. Villeneuve, E. Dubreucq, and H. Fulcrand, *Chemo-enzymatic functionalization of gallic and vanillic acids: synthesis of bio-based epoxy resins prepolymers.* Green Chemistry, 2012. **14**(8): p. 2328-2336.

93. Shen, M. and M.L. Robertson, *Degradation Behavior of Biobased Epoxy Resins in Mild Acidic Media.* ACS Sustainable Chemistry & Engineering, 2021. **9**(1): p. 438-447.

94. Djabourov, M., *Gelation—A review.* Polymer International, 1991. **25**(3): p. 135-143.

95. Raghavan, S.R., L.A. Chen, C. McDowell, S.A. Khan, R. Hwang, and S. White, *Rheological study of crosslinking and gelation in chlorobutyl elastomer systems.* Polymer, 1996. **37**(26): p. 5869-5875.

96. Harsch, M., F. Herzog, and J. Karger-Kocsis, *Cure-induced Normal Force Development in Unfilled and Filled Epoxy Resins.* Journal of Composite Materials, 2008. **42**(21): p. 2299-2309.

97. Martínez-Miranda, M.R., V. García-Martínez, and M.R. Gude, *Gel point determination of a thermoset prepreg by means of rheology.* Polymer Testing, 2019. **78**: p. 105950.

98. Shah, D.U. and P.J. Schubel, *Evaluation of cure shrinkage measurement techniques for thermosetting resins.* Polymer Testing, 2010. **29**(6): p. 629-639.

99. Boonlert-Uthai, T., K. Taki, and A. Somwangthanaroj, *Curing Behavior, Rheological, and Thermal Properties of DGEBA Modified with Synthesized BPA/PEG Hyperbranched Epoxy after Their Photo-Initiated Cationic Polymerization.* Polymers, 2020. **12**(10): p. 2240.

100. Yang, G., B.J. Rohde, H. Tesefay, and M.L. Robertson, *Biorenewable Epoxy Resins Derived from Plant-Based Phenolic Acids.* ACS Sustainable Chemistry & Engineering, 2016. **4**(12): p. 6524-6533.

101. Fache, M., R. Auvergne, B. Boutevin, and S. Caillol, *New vanillin-derived diepoxy monomers for the synthesis of biobased thermosets.* European Polymer Journal, 2015. **67**: p. 527-538.

102. Ghaffar, S.H. and M. Fan, *Lignin in straw and its applications as an adhesive.* International Journal of Adhesion and Adhesives, 2014. **48**: p. 92-101.

103. Aouf, C., H. Nouailhas, M. Fache, S. Caillol, B. Boutevin, and H. Fulcrand, *Multi-functionalization of gallic acid. Synthesis of a novel bio-based epoxy resin.* European Polymer Journal, 2013. **49**(6): p. 1185-1195.

104. Espinoza-Perez, J.D., B.A. Nerenz, D.M. Haagenson, Z. Chen, C.A. Ulven, and D.P. Wiesenborn, *Comparison of curing agents for epoxidized vegetable oils applied to composites.* Polymer Composites, 2011. **32**(11): p. 1806-1816.

105. Mustata, F., N. Tudorachi, and D. Rosu, *Curing and thermal behavior of resin matrix for composites based on epoxidized soybean oil/diglycidyl ether of bisphenol A.* Composites Part B: Engineering, 2011. **42**(7): p. 1803-1812.

106. Burkersroda, F.v., L. Schedl, and A. Göpferich, *Why degradable polymers undergo surface erosion or bulk erosion.* Biomaterials, 2002. **23**(21): p. 4221-4231.

107. Antheunis, H., J.-C. van der Meer, M. de Geus, W. Kingma, and C.E. Koning, *Improved Mathematical Model for the Hydrolytic Degradation of Aliphatic Polyesters.* Macromolecules, 2009. **42**(7): p. 2462-2471.

108. Walter, T., J. Augusta, R.-J. Müller, H. Widdecke, and J. Klein, *Enzymatic degradation of a model polyester by lipase from Rhizopus delemar.* Enzyme and Microbial Technology, 1995. **17**(3): p. 218-224.

109. Zhu, X. and R.D. Braatz, *A mechanistic model for drug release in PLGA biodegradable stent coatings coupled with polymer degradation and erosion.* Journal of biomedical materials research. Part A, 2015. **103**(7): p. 2269-2279.

110. Xia, Y. and R.C. Larock, *Vegetable oil-based polymeric materials: synthesis, properties, and applications.* Green Chemistry, 2010. **12**(11): p. 1893-1909.

111. Ruiz de Luzuriaga, A., R. Martin, N. Markaide, A. Rekondo, G. Cabañero, J. Rodríguez, and I. Odriozola, *Epoxy resin with exchangeable disulfide crosslinks to obtain reprocessable, repairable and recyclable fiber-reinforced thermoset composites.* Materials Horizons, 2016. **3**(3): p. 241-247.

112. Liu, Q., L. Jiang, R. Shi, and L. Zhang, *Synthesis, preparation, in vitro degradation, and application of novel degradable bioelastomers—A review.* Progress in Polymer Science, 2012. **37**(5): p. 715-765.

113. Hillmyer, M.A., *The promise of plastics from plants.* Science, 2017. **358**(6365): p. 868-870.

114. Hufendiek, A., S. Lingier, and F.E. Du Prez, *Thermoplastic polyacetals: chemistry from the past for a sustainable future?* Polymer Chemistry, 2019. **10**(1): p. 9-33.

115. Wang, Z., L. Yuan, and C. Tang, *Sustainable Elastomers from Renewable Biomass.* Accounts of Chemical Research, 2017. **50**(7): p. 1762-1773.

116. Miller, S.A., *Sustainable Polymers: Opportunities for the Next Decade.* ACS Macro Letters, 2013. **2**(6): p. 550-554.

117. Zhu, Y., C. Romain, and C.K. Williams, *Sustainable polymers from renewable resources.* Nature, 2016. **540**(7633): p. 354-362.

118. Cao, H. and P.A. Rupar, *Recent Advances in Conjugated Furans.* Chemistry – A European Journal, 2017. **23**(59): p. 14670-14675.

119. Gandini, A., T.M. Lacerda, A.J.F. Carvalho, and E. Trovatti, *Progress of Polymers from Renewable Resources: Furans, Vegetable Oils, and Polysaccharides.* Chemical Reviews, 2016. **116**(3): p. 1637-1669.

120. Sheldon, R.A., *Green and sustainable manufacture of chemicals from biomass: state of the art.* Green Chemistry, 2014. **16**(3): p. 950-963.

121. Llevot, A., P.-K. Dannecker, M. von Czapiewski, L.C. Over, Z. Söyler, and M.A.R. Meier, *Renewability is not Enough: Recent Advances in the Sustainable Synthesis*

of Biomass-Derived Monomers and Polymers. Chemistry – A European Journal, 2016. **22**(33): p. 11510-11521.

122. Jambeck, J.R., R. Geyer, C. Wilcox, T.R. Siegler, M. Perryman, A. Andrady, R. Narayan, and K.L. Law, *Plastic waste inputs from land into the ocean.* Science, 2015. **347**(6223): p. 768.

123. Geyer, R., J.R. Jambeck, and K.L. Law, *Production, use, and fate of all plastics ever made.* Science Advances, 2017. **3**(7): p. e1700782.

124. Albertsson, A.-C. and M. Hakkarainen, *Designed to degrade.* Science, 2017. **358**(6365): p. 872.

125. Hillmyer, M.A. and W.B. Tolman, *Aliphatic Polyester Block Polymers: Renewable, Degradable, and Sustainable.* Accounts of Chemical Research, 2014. **47**(8): p. 2390-2396.

126. Lavilla, C., A. Alla, A. Martínez de Ilarduya, E. Benito, M.G. García-Martín, J.A. Galbis, and S. Muñoz-Guerra, *Biodegradable aromatic copolyesters made from bicyclic acetalized galactaric acid.* Journal of Polymer Science Part A: Polymer Chemistry, 2012. **50**(16): p. 3393-3406.

127. Ying, H. and J. Cheng, *Hydrolyzable Polyureas Bearing Hindered Urea Bonds.* Journal of the American Chemical Society, 2014. **136**(49): p. 16974-16977.

128. Shen, M., H. Cao, and M.L. Robertson, *Hydrolysis and Solvolysis as Benign Routes for the End-of-Life Management of Thermoset Polymer Waste.* Annual Review of Chemical and Biomolecular Engineering, 2020. **11**(1): p. 183-201.

129. Vijjamarri, S., M. Hull, E. Kolodka, and G. Du, *Renewable Isohexide-Based, Hydrolytically Degradable Poly(silyl ether)s with High Thermal Stability*. ChemSusChem, 2018. **11**(17): p. 2881-2888.

130. Tschan, M.J.L., E. Brulé, P. Haquette, and C.M. Thomas, *Synthesis of biodegradable polymers from renewable resources*. Polymer Chemistry, 2012. **3**(4): p. 836-851.

131. Nakajima, H., P. Dijkstra, and K. Loos, *The Recent Developments in Biobased Polymers toward General and Engineering Applications: Polymers that are Upgraded from Biodegradable Polymers, Analogous to Petroleum-Derived Polymers, and Newly Developed.* Polymers, 2017. **9**(10): p. 523.

132. Pemba, A.G., J.A. Flores, and S.A. Miller, *Acetal metathesis polymerization (AMP): A method for synthesizing biorenewable polyacetals.* Green Chemistry, 2013. **15**(2): p. 325-329.

133. Samanta, S., D.R. Bogdanowicz, H.H. Lu, and J.T. Koberstein, *Polyacetals: Water-Soluble, pH-Degradable Polymers with Extraordinary Temperature Response.* Macromolecules, 2016. **49**(5): p. 1858-1864.

134. Andrade-Gagnon, B., M. Bélanger-Bouliga, P. Trang Nguyen, T.H.D. Nguyen, S. Bourgault, and A. Nazemi, *Degradable Spirocyclic Polyacetal-Based Core-Amphiphilic Assemblies for Encapsulation and Release of Hydrophobic Cargo.* Nanomaterials, 2021. **11**(1): p. 161.

135. Elling, B.R., J.K. Su, and Y. Xia, *Degradable Polyacetals/Ketals from Alternating Ring-Opening Metathesis Polymerization.* ACS Macro Letters, 2020. **9**(2): p. 180-184.

136. Moreno, A., G. Lligadas, J.C. Ronda, M. Galià, and V. Cádiz, *Orthogonally functionalizable polyacetals: a versatile platform for the design of acid sensitive amphiphilic copolymers.* Polymer Chemistry, 2019. **10**(38): p. 5215-5227.

137. Paramonov, S.E., E.M. Bachelder, T.T. Beaudette, S.M. Standley, C.C. Lee, J. Dashe, and J.M.J. Fréchet, *Fully Acid-Degradable Biocompatible Polyacetal Microparticles for Drug Delivery*. Bioconjugate Chemistry, 2008. **19**(4): p. 911-919.

138. Rajput, B.S., S.R. Gaikwad, S.K. Menon, and S.H. Chikkali, *Sustainable polyacetals from isohexides.* Green Chemistry, 2014. **16**(8): p. 3810-3818.

139. Debsharma, T., Y. Yagci, and H. Schlaad, *Cellulose-Derived Functional Polyacetal by Cationic Ring-Opening Polymerization of Levoglucosenyl Methyl Ether.* Angewandte Chemie International Edition, 2019. **58**(51): p. 18492-18495.

140. Fache, M., B. Boutevin, and S. Caillol, *Vanillin, a key-intermediate of biobased polymers.* European Polymer Journal, 2015. **68**: p. 488-502.

141. Pemba, A.G., M. Rostagno, T.A. Lee, and S.A. Miller, *Cyclic and spirocyclic polyacetal ethers from lignin-based aromatics.* Polymer Chemistry, 2014. **5**(9): p. 3214-3221.

142. Nguyen, H.T.H., P. Qi, M. Rostagno, A. Feteha, and S.A. Miller, *The quest for high glass transition temperature bioplastics.* Journal of Materials Chemistry A, 2018. **6**(20): p. 9298-9331.

143. Labadie, J.W., J.L. Hedrick, and M. Ueda, *Poly(aryl ether) Synthesis*, in *Step-Growth Polymers for High-Performance Materials*. 1996, American Chemical Society. p. 210-225.

144. Lindström, A. and M. Hakkarainen, *Designed Chain Architecture for Enhanced Migration Resistance and Property Preservation in Poly(vinyl chloride)/Polyester Blends.* Biomacromolecules, 2007. **8**(4): p. 1187-1194.

145. Park, S.-A., H. Jeon, H. Kim, S.-H. Shin, S. Choy, D.S. Hwang, J.M. Koo, J. Jegal, S.Y. Hwang, J. Park, and D.X. Oh, *Sustainable and recyclable super engineering thermoplastic from biorenewable monomer.* Nature Communications, 2019. **10**(1): p. 2601.

146. Chung, I.S. and S.Y. Kim, *Meta-Activated Nucleophilic Aromatic Substitution Reaction: Poly(biphenylene oxide)s with Trifluoromethyl Pendent Groups via Nitro Displacement.* Journal of the American Chemical Society, 2001. **123**(44): p. 11071-11072.

147. Jedeon, K., M. De la Dure-Molla, S.J. Brookes, S. Loiodice, C. Marciano, J. Kirkham, M.-C. Canivenc-Lavier, S. Boudalia, R. Bergès, H. Harada, A. Berdal, and S. Babajko, *Enamel Defects Reflect Perinatal Exposure to Bisphenol A.* The American Journal of Pathology, 2013. **183**(1): p. 108-118.

148. Klein, R., C. Schüll, E. Berger-Nicoletti, M. Haubs, K. Kurz, and H. Frey, *ABA Triblock Copolymers Based on Linear Poly(oxymethylene) and Hyperbranched Poly(glycerol): Combining Polyacetals and Polyethers.* Macromolecules, 2013. **46**(22): p. 8845-8852.

149. Hammami, N., M. Majdoub, and J.-P. Habas, *Structure-properties relationships in isosorbide-based polyacetals: Influence of linear or cyclic architecture on polymer physicochemical properties.* European Polymer Journal, 2017. **93**: p. 795-804.

150. Chikkali, S., F. Stempfle, and S. Mecking, *Long-Chain Polyacetals From Plant Oils.* Macromolecular Rapid Communications, 2012. **33**(13): p. 1126-1129.

151. Ortmann, P., I. Heckler, and S. Mecking, *Physical properties and hydrolytic degradability of polyethylene-like polyacetals and polycarbonates.* Green Chemistry, 2014. **16**(4): p. 1816-1827.

152. Law, A.C., D.S. Stankowski, B.H. Bomann, S. Suhail, K.H. Salmon, S.W. Paulson, M.J. Carney, and N.J. Robertson, *Synthesis and material properties of elastomeric high molecular weight polycycloacetals derived from diglycerol and meso-erythritol.* Journal of Applied Polymer Science, 2020. **137**(23): p. 48780.

153. Rostagno, M., E.J. Price, A.G. Pemba, I. Ghiriviga, K.A. Abboud, and S.A. Miller, *Sustainable polyacetals from erythritol and bioaromatics.* Journal of Applied Polymer Science, 2016. **133**(45).

154. Sonmez, H.B., F.G. Kuloglu, K. Karadag, and F. Wudl, *Terephthalaldehyde- and isophthalaldehyde-based polyspiroacetals.* Polymer Journal, 2012. **44**(3): p. 217-223.

155. Orellana-Coca, C., J.M. Billakanti, B. Mattiasson, and R. Hatti-Kaul, *Lipase mediated simultaneous esterification and epoxidation of oleic acid for the production of alkylepoxystearates.* Journal of Molecular Catalysis B: Enzymatic, 2007. **44**(3): p. 133-137.

156. Orellana-Coca, C., D. Adlercreutz, M.M. Andersson, B. Mattiasson, and R. Hatti-Kaul, *Analysis of fatty acid epoxidation by high performance liquid chromatography coupled with evaporative light scattering detection and mass spectrometry.* Chemistry and physics of lipids, 2005. **135**(2): p. 189-199.

157. Hill, L.W., *Calculation of crosslink density in short chain networks.* Progress in Organic Coatings, 1997. **31**(3): p. 235-243.

158. Jabłoński, M. and A. Przepiera, *Kinetic Model For The Reaction of Ilmenite With Sulphuric Acid.* Journal of Thermal Analysis and Calorimetry, 2001. **65**(2): p. 583-590.

159. Khawam, A. and D.R. Flanagan, *Solid-State Kinetic Models: Basics and Mathematical Fundamentals.* The Journal of Physical Chemistry B, 2006. **110**(35): p. 17315-17328.

160. Khawam, A. and D.R. Flanagan, *Basics and Applications of Solid-State Kinetics: A Pharmaceutical Perspective**The authors dedicate this review to the memory of Dr. David J.W. Grant who passed away on December 9, 2005. Dr. Grant was an internationally known authority at the University of Minnesota on the solid-state properties of drugs. He will be remembered as a kind, humble, and brilliant scholar.* Journal of Pharmaceutical Sciences, 2006. **95**(3): p. 472-498.

161. Graetz, J. and J.J. Reilly, *Decomposition Kinetics of the AlH3 Polymorphs.* The Journal of Physical Chemistry B, 2005. **109**(47): p. 22181-22185.

162. Hromadová, M., R. Sokolová, L. Pospíšil, and N. Fanelli, *Surface Interactions of s-Triazine-Type Pesticides. An Electrochemical Impedance Study.* The Journal of Physical Chemistry B, 2006. **110**(10): p. 4869-4874.

163. Wu, C., P. Wang, X. Yao, C. Liu, D. Chen, G.Q. Lu, and H. Cheng, *Effects of SWNT and Metallic Catalyst on Hydrogen Absorption/Desorption Performance of MgH2.* The Journal of Physical Chemistry B, 2005. **109**(47): p. 22217-22221.

164. Peterson, V.K., D.A. Neumann, and R.A. Livingston, *Hydration of Tricalcium and Dicalcium Silicate Mixtures Studied Using Quasielastic Neutron Scattering.* The Journal of Physical Chemistry B, 2005. **109**(30): p. 14449-14453.

165. Khawam, A. and D.R. Flanagan, *Complementary Use of Model-Free and Modelistic Methods in the Analysis of Solid-State Kinetics.* The Journal of Physical Chemistry B, 2005. **109**(20): p. 10073-10080.

166. Avrami, M., *Kinetics of Phase Change. I General Theory.* The Journal of Chemical Physics, 1939. **7**(12): p. 1103-1112.

167. Stefanis, E. and C. Panayiotou, *Prediction of Hansen Solubility Parameters with a New Group-Contribution Method.* International Journal of Thermophysics, 2008. **29**(2): p. 568-585.

168. Hansen, C.M., *Hansen Solubility Parameters: A User's Handbook, 2nd edn*. 2007, Boca Raton, Florida: CRC Press, Taylor and Francis Group, .

Appendix 1: Supporting Information for Chapter 3

Chemo-Enzymatic Epoxidation of ALA to form EVA

There are many experimental parameters that could affect the conversion of chemo-enzymatic epoxidation reaction and reaction rate, such as the relative concentrations of caprylic acid (C8), H_2O_2, and C=C double bonds on AVA, reaction time, and reaction temperature [92]. We conducted a series of reaction in which these parameters were varied and resulting conversion of allyl groups to epoxide groups reported (Table A1.1). All reactions were conducted in the presence of Novozyme 435 (at a concentration of 20 wt% relative to the weight of AVA).

First, we chose the ratio C8 : C=C as 1:1 and H_2O_2 : C=C as 2:1. Each AVA molecule has two C=C bonds, so the reactant molar ratio used in entry 1 of Table A1.1 was AVA : C8 : H_2O_2 = 1 : 2 : 4, with reaction time and temperature of 24 h and 40 ºC, respectively. For comparison purposes, comparable reactions with longer reaction time (48 h) and higher temperature (60 ºC) were performed in entries 2 and 3, respectively. However, no improvement on conversion was observed in increasing reaction time or temperature, as all the three reactions showed similar conversion of around 29%. Even higher temperature (above 60 ºC) was not explored due to the rapid loss of enzyme activity at elevated temperatures.

Next, we increased the concentration of C8 and H_2O_2 relative to that of AVA. In entry 4, the reactant ratio was AVA : C8 : H_2O_2 = 1 : 2.4 : 4. In entry 5, the reactant ratio was AVA : C8 : H_2O_2 = 1 : 2 : 4.8. In both cases, the conversion was slightly higher than entries 1-3, around 34%. When we doubled the amount of H_2O_2 (AVA : C8 : H_2O_2 = 1 : 2 : 8 in entry 6), the conversion went to 0%. This is possibly because the enzyme cannot

survive this high concentration of H_2O_2 [155, 156]. We therefore kept the H_2O_2 concentration below this level. When we increased the H2O2 concentration within a more moderate range (Figure A1.1), we observed an increase in conversion, from around 34% to 60% (Figure A1.1, Table A1.1).

Table A1.1: Results of chemo-enzymatic epoxidation of AVA using different amounts of caprylic acid (C8) and H_2O_2.

Entry	Mole ratio (AVA:C8:H_2O_2)	Time (h)	Temp (ºC)	Conversion (%)
1	1 : 2 : 4	24	40	28.7
2	1 : 2 : 4	48	40	29.2
3	1 : 2 : 4	24	60	29.8
4	1 : 2.4 : 4	24	40	34.2
5	1 : 2 : 4.8	24	40	32.0
6	1 : 2 : 8	24	40	0
7	1 : 2.4 : 4.8	24	40	47.1
8	1 : 2.4 : 5.2	24	40	49.2
9	1 : 2.4 : 6	24	40	59.5
10	1 : 2.4 : 6.8	24	40	59.6

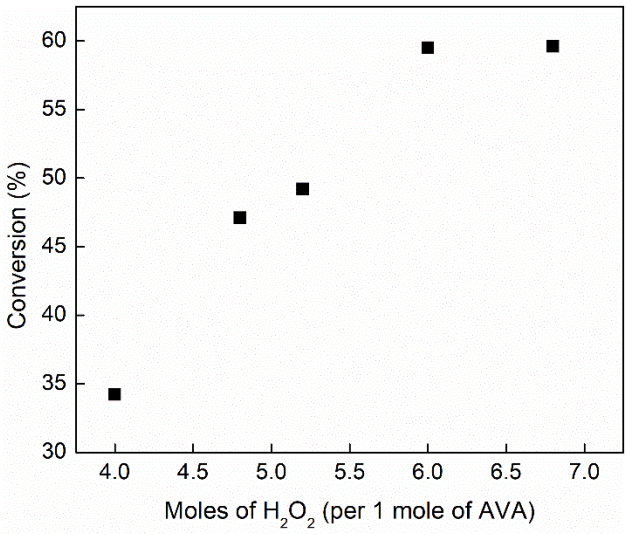

Figure A1.2: Conversion of AVA to EVA with varying molar ratio of H_2O_2 : AVA (with fixed ratio of C8 : AVA at 2.4 : 1, reaction temperature of 40 °C, and reaction time of 24 h).

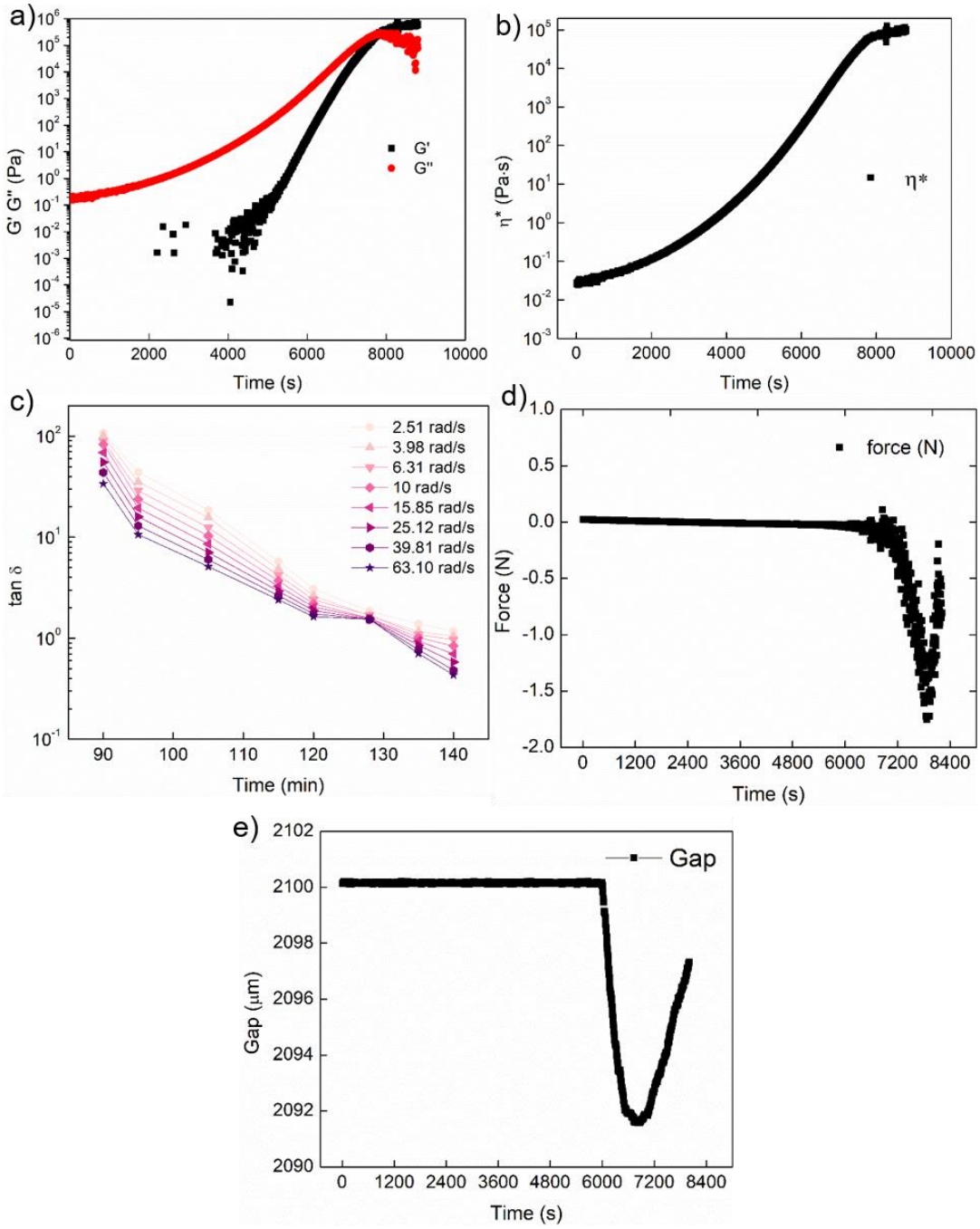

Figure A1.3: Isothermal curing experiments of DGEBA-based epoxy resins at 70 ºC in rheometer. a) Plots of G', G'' and b) complex viscosity change against time of EVA-based epoxy resins at 70 ºC. c) tan δ curves at various frequencies. d) Force change. e) Gap change

Thermomechanical Properties of EVA-based Epoxy Resins

The storage modulus (E') of the EVA-based epoxy resin was previously measured and is compared to that of DGEBA-based epoxy resin in **Figure A1.5**. E' decreased with temperature until reaching the rubbery plateau at around 171 ºC and 162 ºC for EVA-based and DGEBA-based epoxy resins, respectively. The cross-link density (ν_e) was calculated from the plateau E' (quantified at $T = T_g + 60$ ºC):[157]

$$\nu_e = \frac{E'}{3RT} \qquad \text{(eqn. A1.1)}$$

where R is the gas constant and T is the absolute temperature.

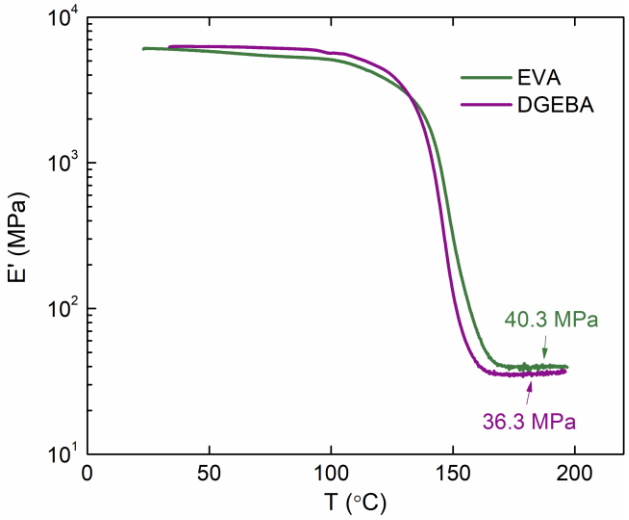

Figure A1.4: Storage modulus (E') of EVA- and DGEBA-based epoxy resins measured by DMA.

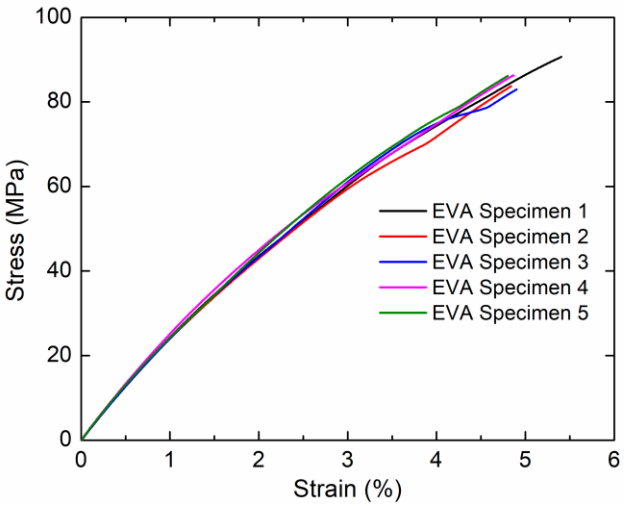

Figure A1.5: Tensile testing data obtained from the EVA-based epoxy resin.

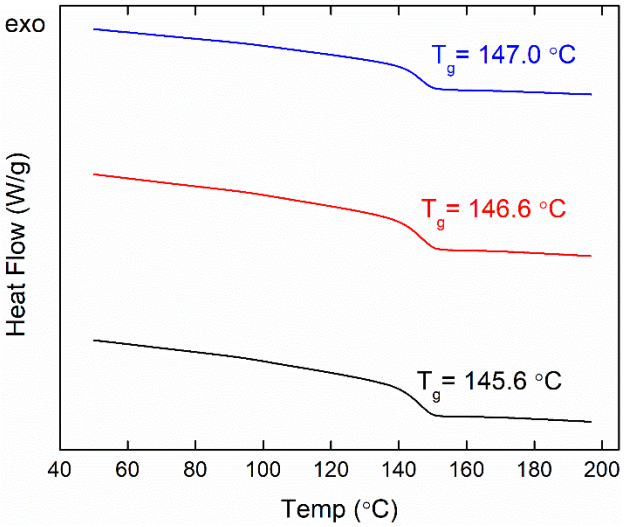

Figure A1.6: T_g measured in the grip region of fractured tensile bars. The color of each curve corresponds to the tensile testing data shown in Figure A1.6: the black curve was obtained from Specimen 1, the red curve was obtained from Specimen 2, and the blue curve was obtained from Specimen 3.

Appendix 2: Supporting Information for Chapter 4

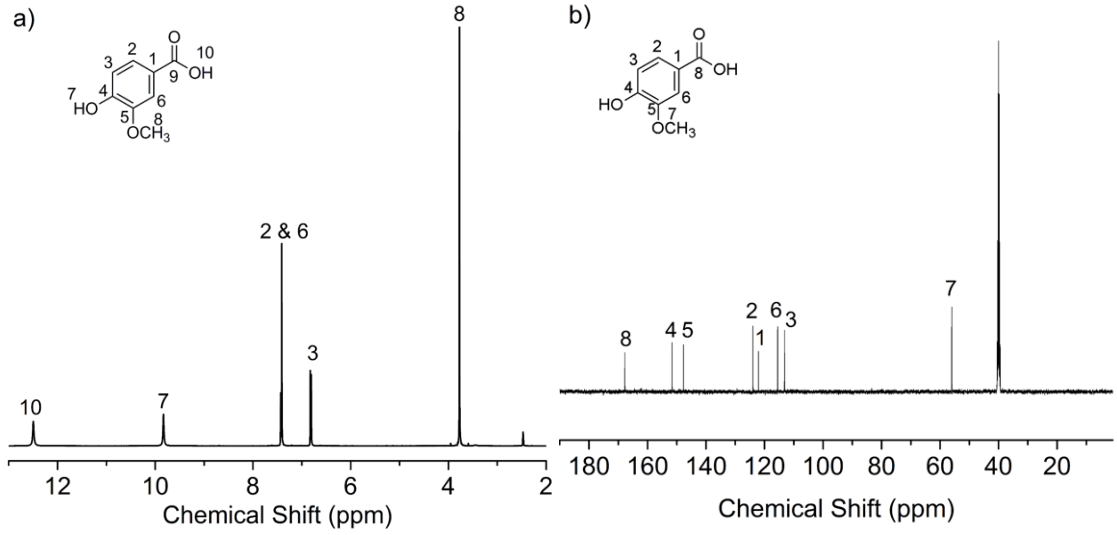

Figure A2.1: a) ^{1}H NMR and b) ^{13}C NMR data obtained from VA.

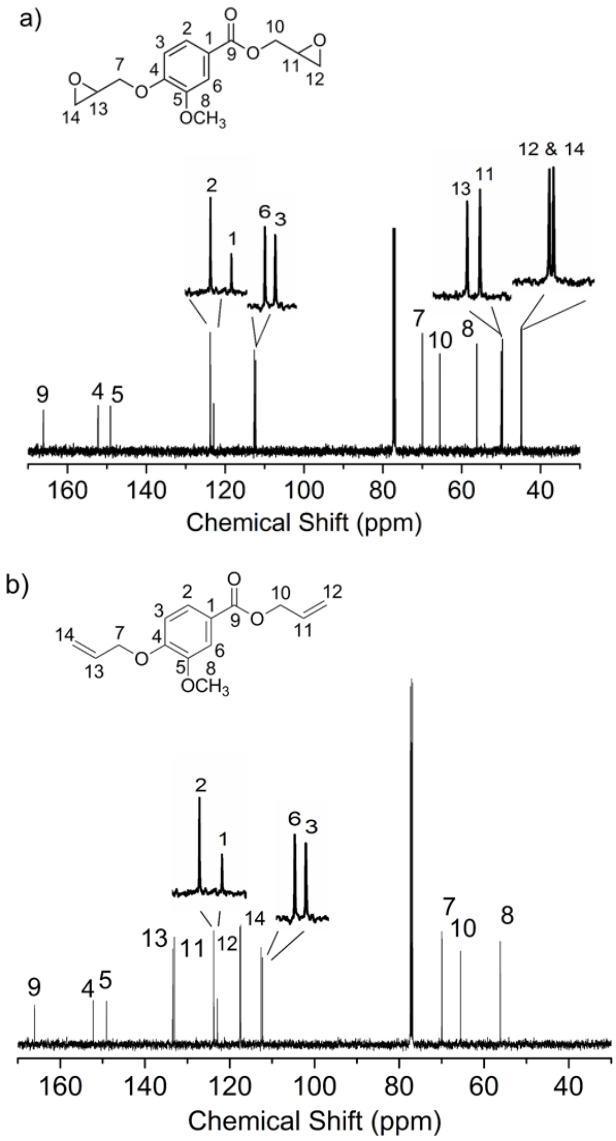

Figure A2.2: ^{13}C NMR data obtained from a) EVA and b) AVA.

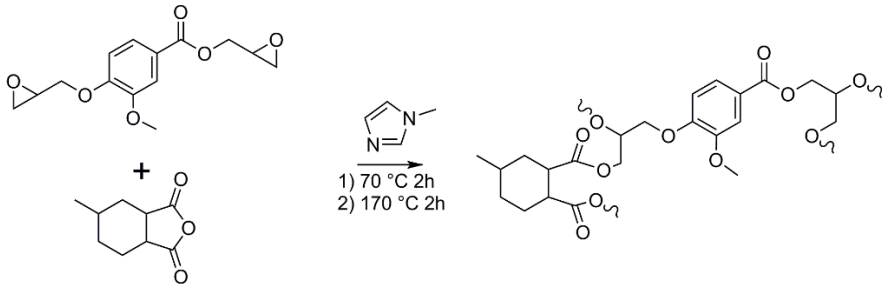

Scheme A2.1: Curing of EVA with MHHPA (catalyzed by 1-MI) to form an epoxy resin.

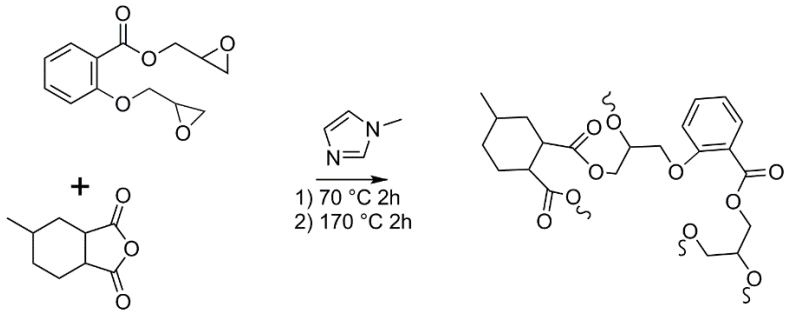

Scheme A2.2: Curing of ESA with MHHPA (catalyzed by 1-MI) to form an epoxy resin.

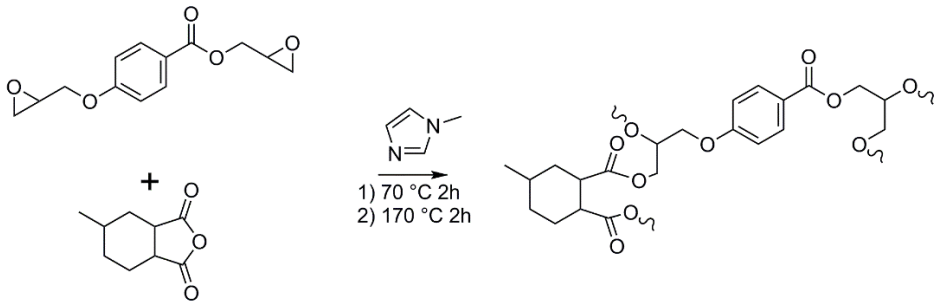

Scheme A2.3: Curing of E4HBA with MHHPA (catalyzed by 1-MI) to form an epoxy resin.

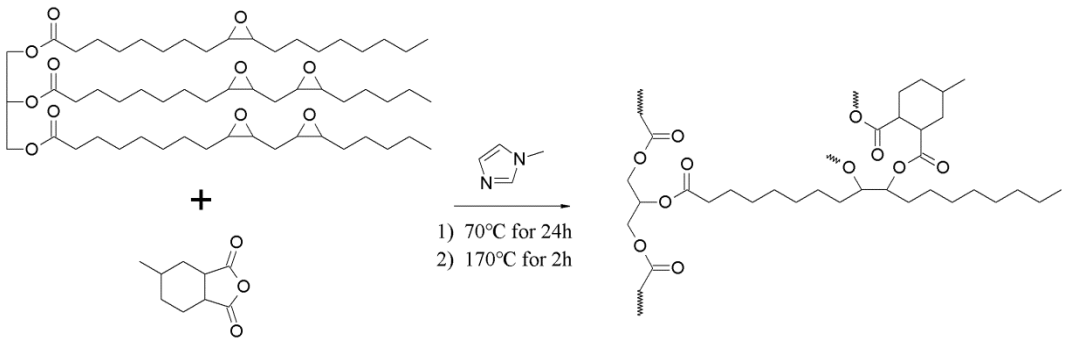

Scheme A2.4: Curing of ESO with MHHPA (catalyzed by 1-MI) to form an epoxy resin.

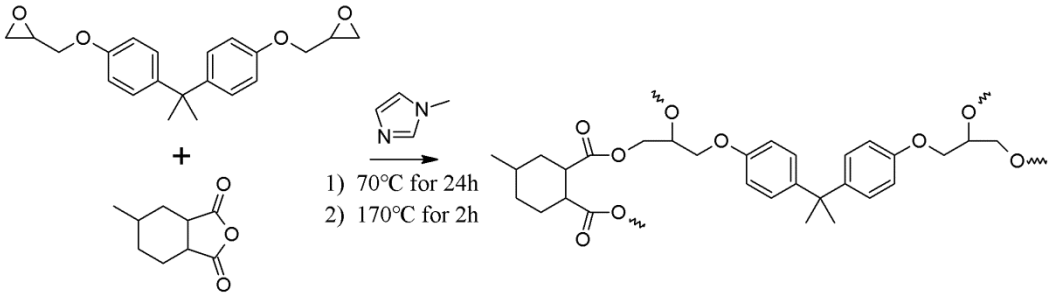

Scheme A2.5: Curing of DGEBA with MHHPA (catalyzed by 1-MI) to form an epoxy resin.

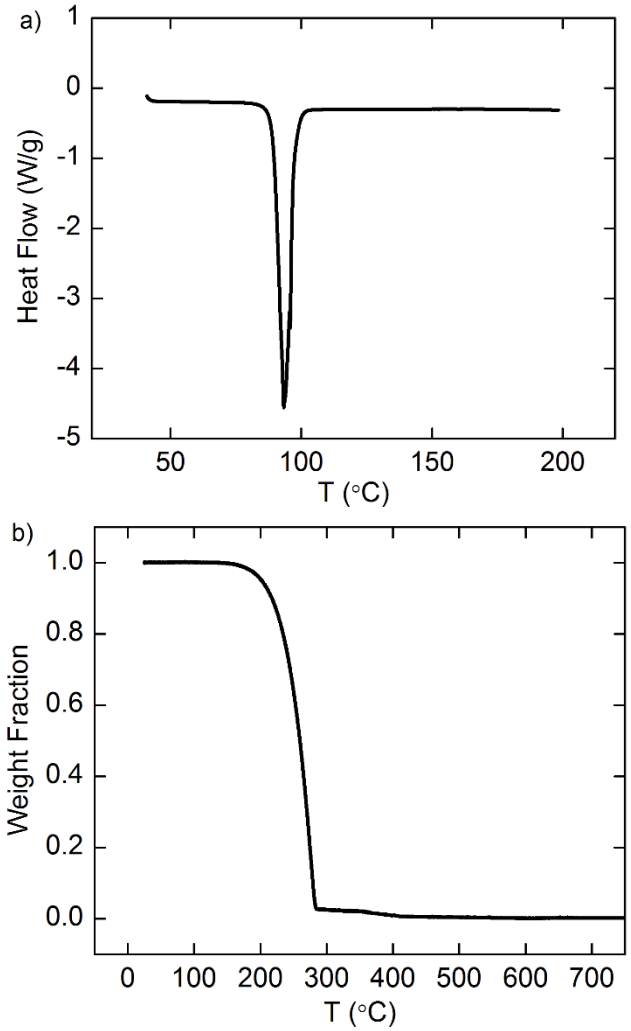

Figure A2.3: a) DSC data and b) TGA data obtained from the EVA monomer.

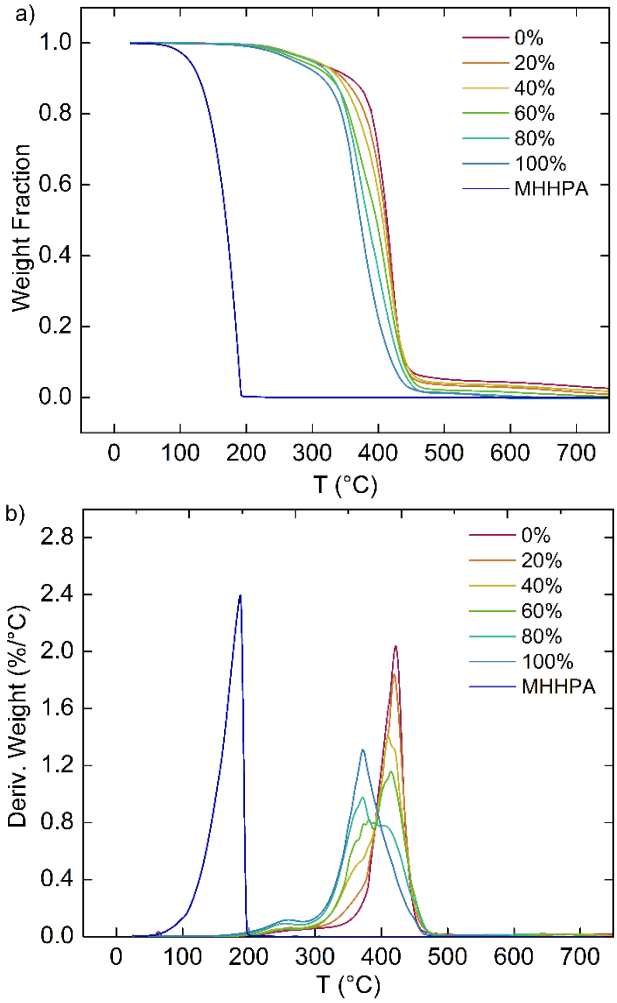

Figure A2.4: Weight loss and derivative weight loss as functions of temperature, from TGA, for epoxy resins containing different ESO and DGEBA contents (% ESO is the % relative to total amount of ESO and DGEBA). MHHPA curing agent is included for comparison purposes.

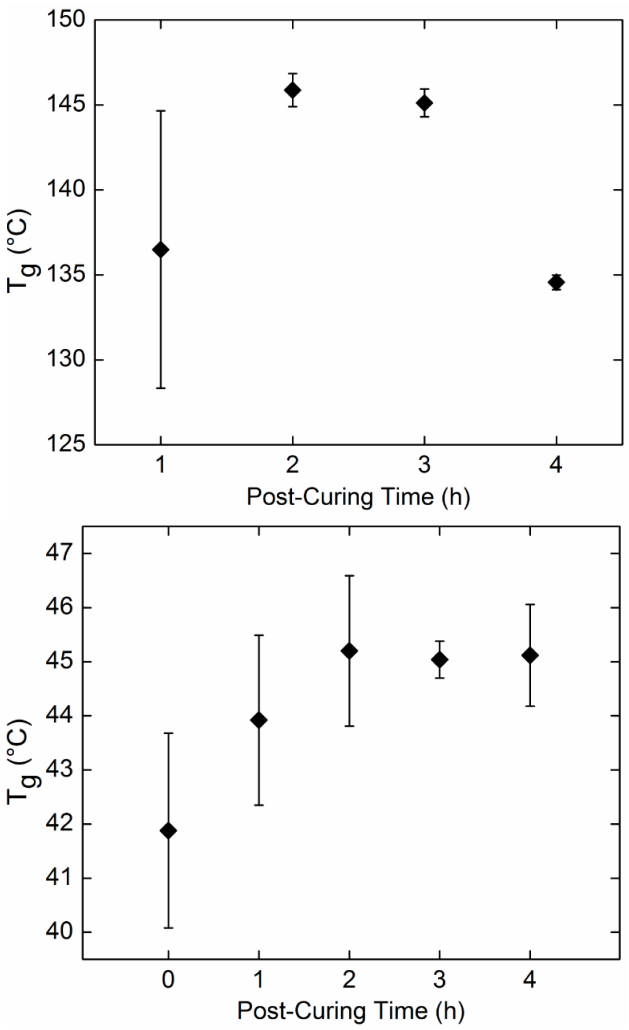

Figure A2.5: Glass transition temperature (T_g) as a function of post-curing time at 170 °C for a) EVA- and b) ESO-based epoxy resins.

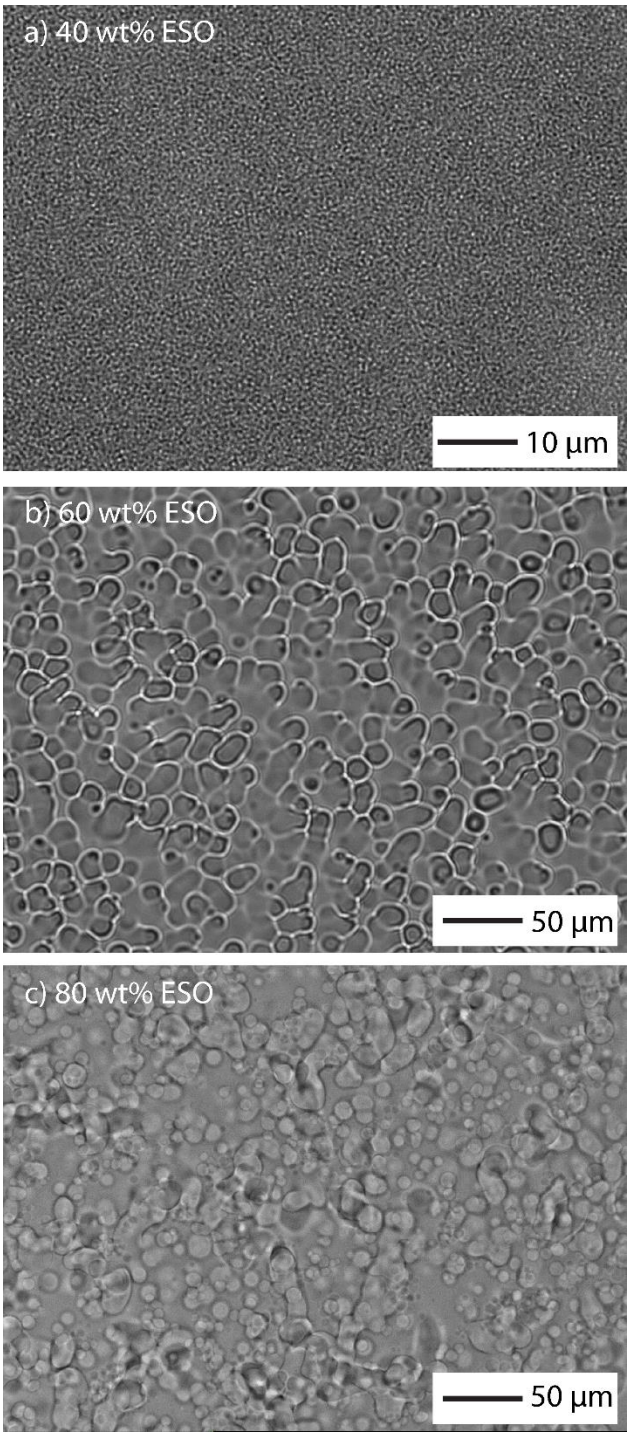

Figure A2.6: Optical microscopy images of epoxy resins after first-stage curing with differing ESO content (wt% ESO is the ESO content relative to the total amount of ESO and DGEBA).

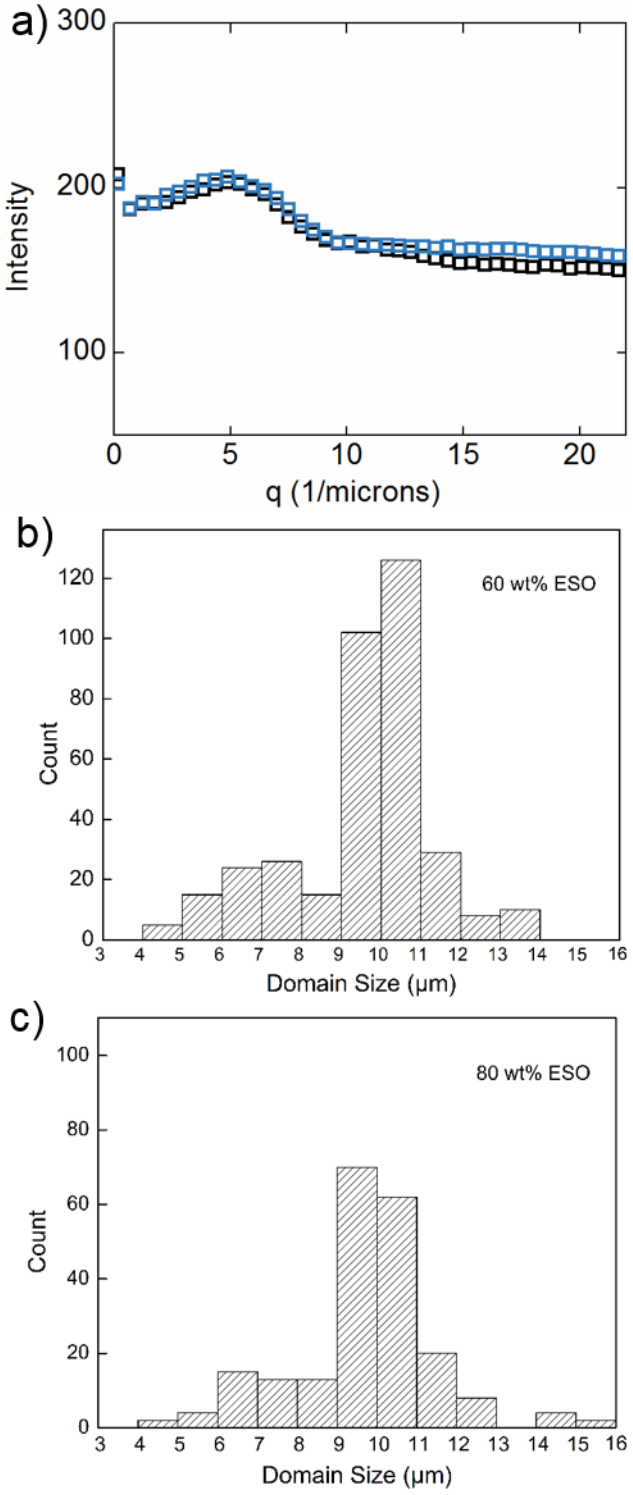

Figure A2.7: a) Intensity vs. q, obtained through the fast Fourier transform (FFT) of optical micrographs obtained from an epoxy resin containing 40 wt% ESO (of the total ESO and DGEBA monomer), prior to curing (black squares) and following curing with MHHPA/1-MI (blue squares). b, c) Particle size distributions obtained through image analysis of optical micrographs.

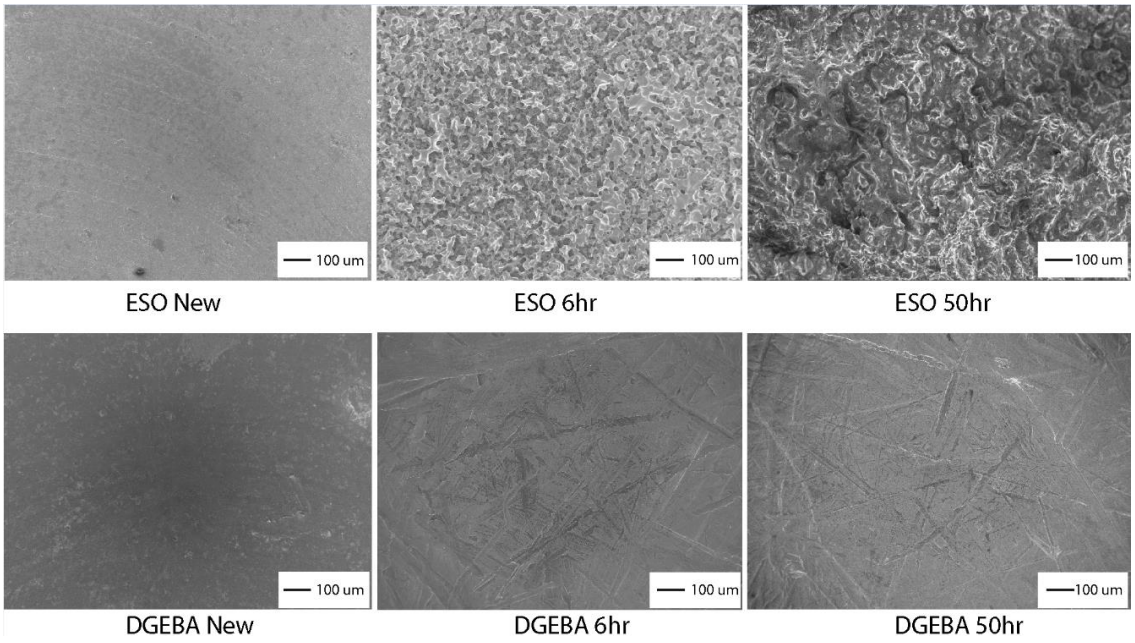

Figure A2.8: SEM images of the surfaces of ESO-based and DGEBA-based epoxy resins, showing surface changes after soaking in a 3wt% NaOH solution at 80 °C for 6 and 50 h.

Analysis of mass spectrometry data obtained from ESO-based epoxy resin degradation products

We assume the epoxy resin degradation proceeds through cleavage of ester groups. The ESO monomer contains ester groups, and the curing reaction between MHHPA and ESO also produces ester groups. Esters groups are therefore dispersed throughout the epoxy network. We considered all possible combinations of fatty acids on the soybean oil triglyceride, and we also considered the presence of either H^+ or Na^+ ions, and the possibility of exchange between H and Na within the molecules. We then assigned the observed mass spectrometry peaks to theoretical epoxy network fragments post-degradation, as outlined below.

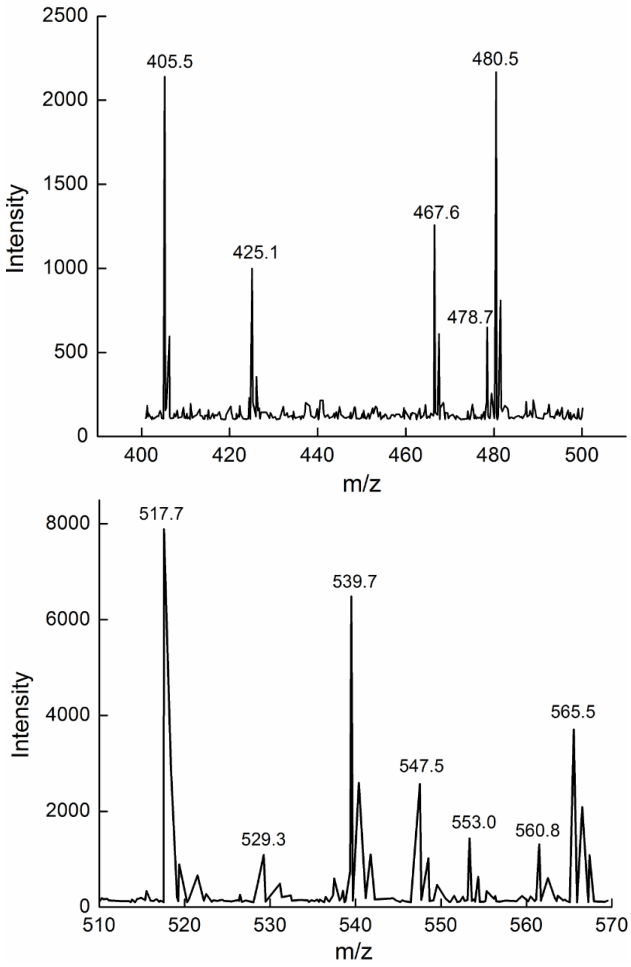
Intensity
m/z
405.5
480.5
467.6
425.1
478.7
517.7
539.7
565.5
547.5
553.0
560.8
529.3

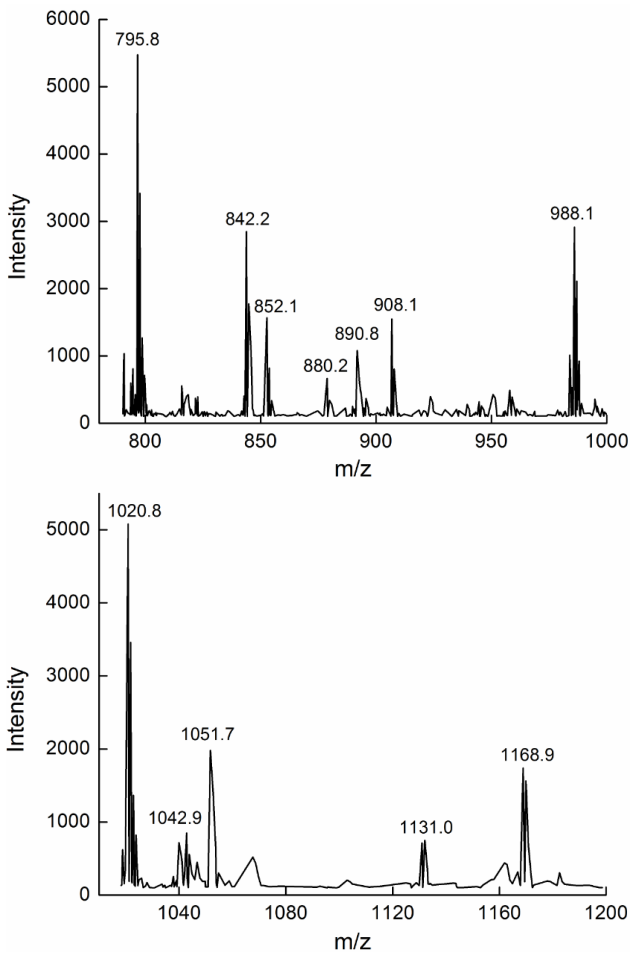

Figure A2.9: Closer view of mass spectra obtained from degradation products of an ESO-based epoxy resin.

Table A2.1: Proposed chemical structures and theoretical molecular weights for peaks detected in mass spectrum).

Code	Chemical Structure	Theoretical Molecular Weight (g/mol)	Observed m/z (g/mol)
1	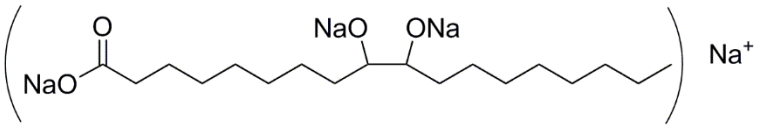	405.4	405.5
2	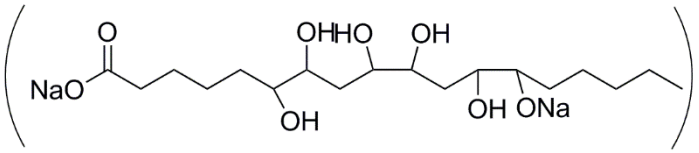	425.5	425.1
3	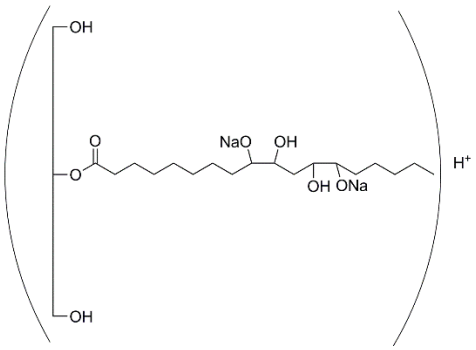	467.5	467.6
4	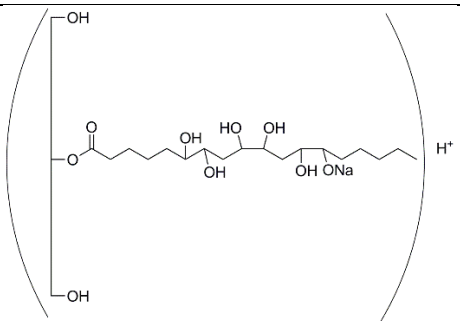	477.8	478.7
5	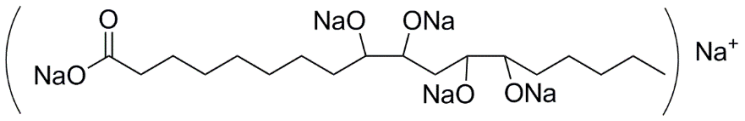	481.3	480.5

Table A2.1 continued

6	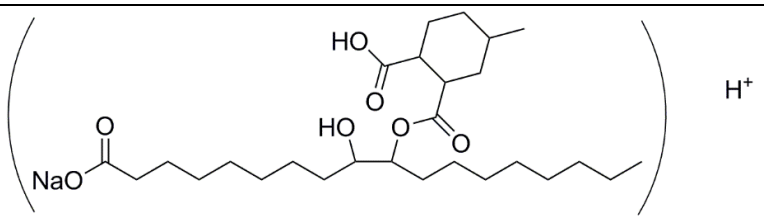	**506.6**	**506.5**
7	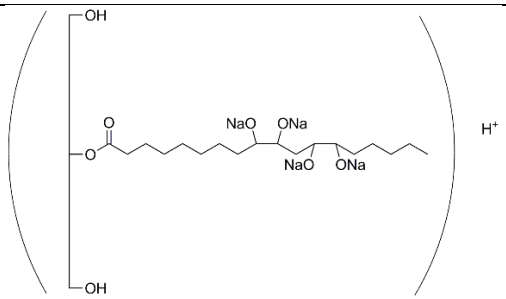	517.5	517.7
8	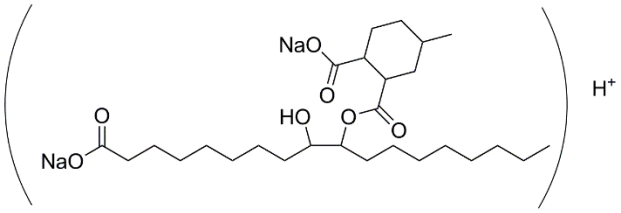	529.8	529.3
9	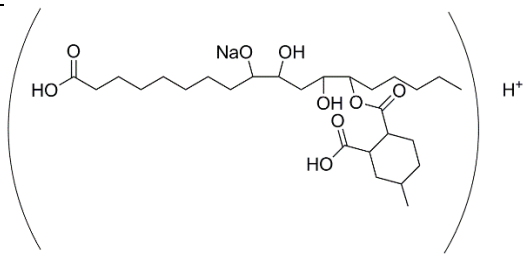	539.7	539.7
10	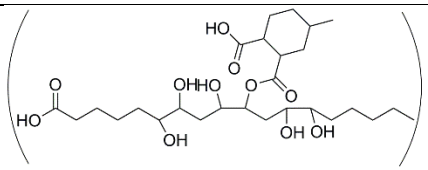	546.9	547.5
11	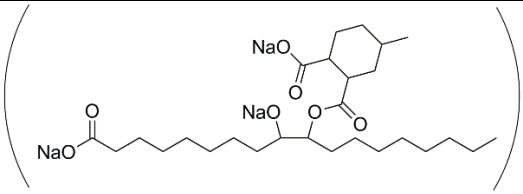	553.2	553.0
12	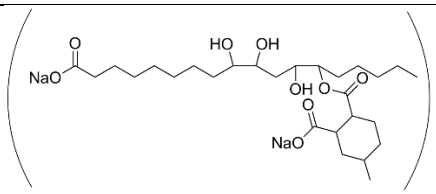	560.7	560.8

Table A2.1 continued

13	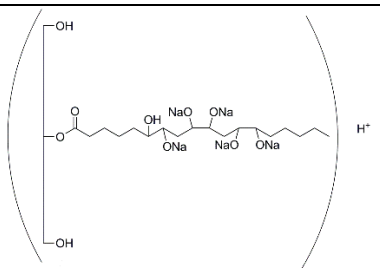	565.7	565.5
14	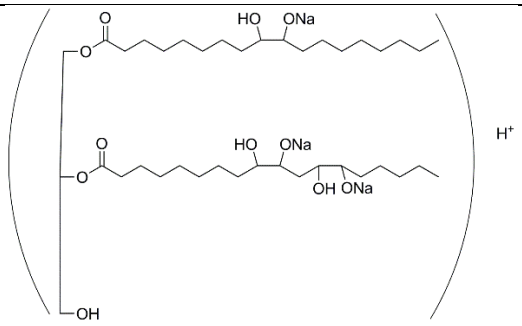	**788.0**	**787.8**
15	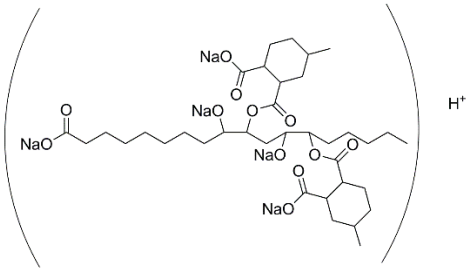	795.9	795.8
16	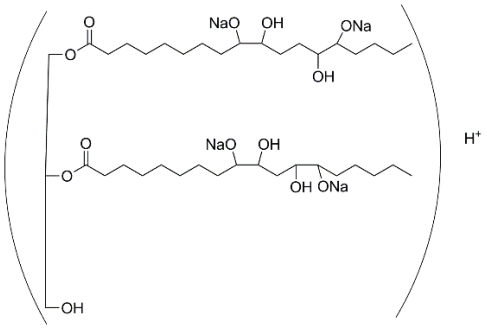	841.9	842.2
17	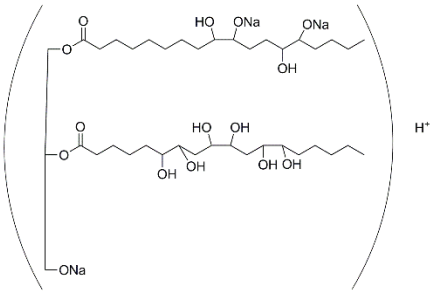	851.6	852.1

Table A2.1 continued

18	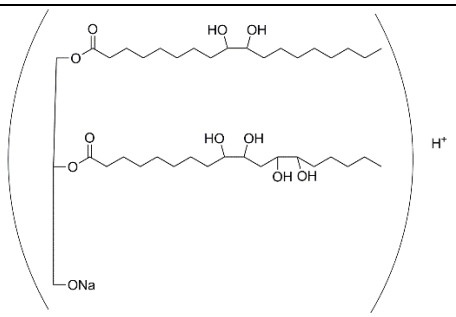	880.6	880.2
19	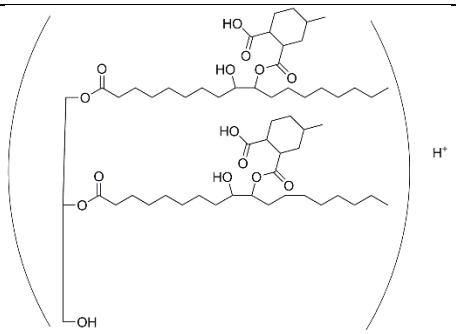	890.5	890.8
20	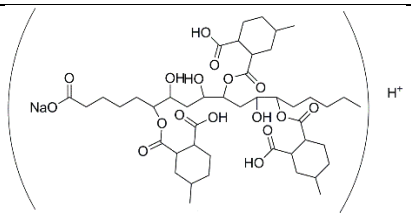	907.9	908.1
21	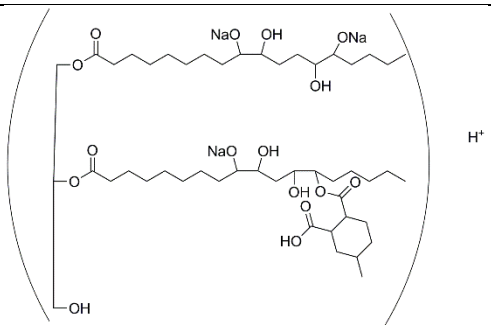	988.3	988.1
22	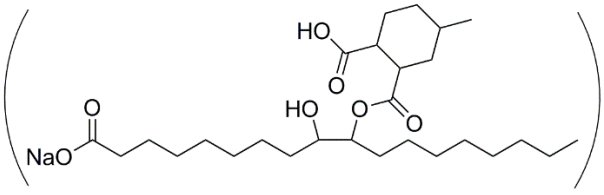 Two-molecule aggregate of structure 6	**1012.0**	**1011.9**

Table A2.1 continued

23	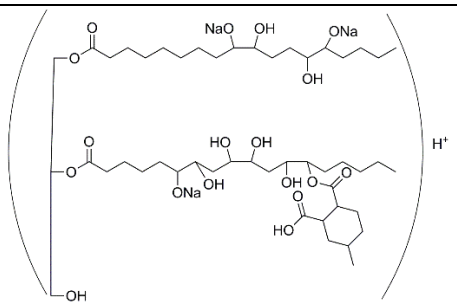	1020.2	1020.8
24	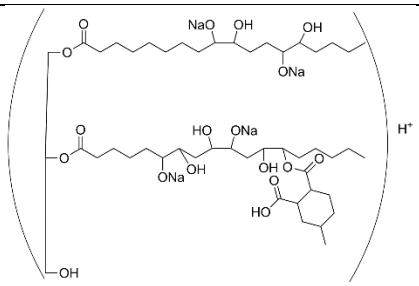	1042.2	1042.9
25	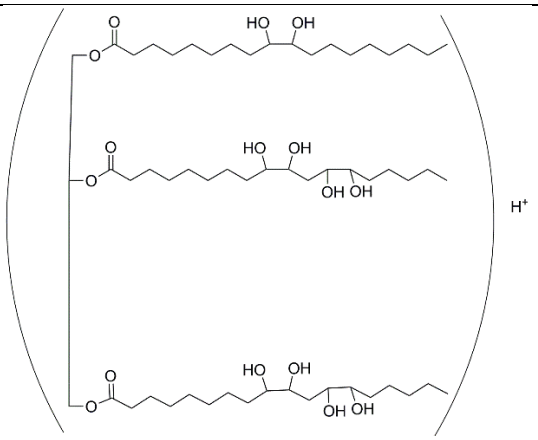	1052.5	1051.7
26	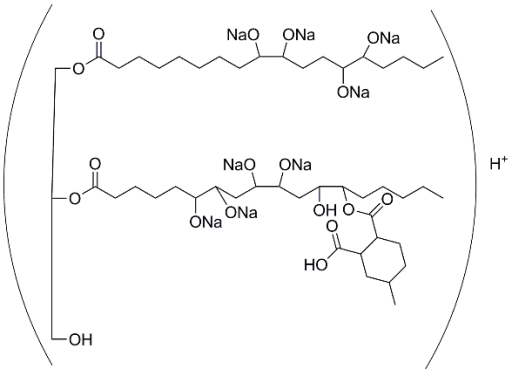	1130.2	1131.0

Table A2.1 continued

27	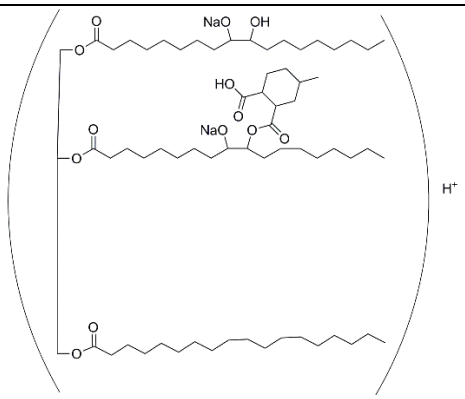	1168.7	1168.9
28	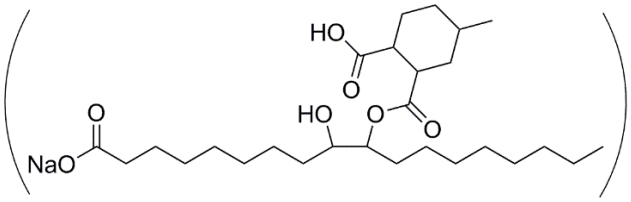 Three-molecule aggregate of structure 6	**1517.5**	**1517.5**

Solid-State Kinetic Models

The general formula for solid-state, heterogeneous kinetics is [158-160]

$$\frac{d\alpha}{dt} = kf(\alpha)$$

Many models have been proposed based on mechanistic assumptions, including nucleation, diffusion, geometrical contraction, and reaction-order models. The choice of a model for solid-state kinetics is based on statistical fits of mathematical models to data, supported by complementary measurements such as scanning electron microscopy, mass spectrometry, etc.

Reaction-order models involve the reaction order in the rate law, and are similar to the rate expressions in homogenous kinetics. We considered first and second-order reaction models.

Diffusion models assumes the rate-limiting step is the diffusion of reactants into reaction sites or products leaving reaction sites.

Geometrical contraction models assume the rate limiting step is the progress of the product layer from the surface to the interior of the specimen, which is related to the sample morphology. We extended the contracting volume model from a cubic specimen, as previously described [159], to a cuboid specimen (i.e., side lengths a, b and c are not equal). The derivation of the model is shown in the next section.

Nucleation models assume the rate-limiting step is the formation and growth of nuclei. However, based on the shape of the curve of the mass fraction remaining versus time, nucleation models were not suitable choices for our degradation data. We therefore did not investigate these further in this study.

All the general formulae of the models are listed as below. We chose to use degradation data obtained from the ESA-based epoxy resin and DGEBA/ESO-based epoxy resin (with 40% ESO) as model samples for probing the best choice of model to fit the data.

Nucleation model: $$f(\alpha) = \alpha(1-\alpha) \quad \text{(A2.1)}$$

3D diffusion model: $$f(\alpha) = \frac{3(1-\alpha)^{2/3}}{2(1-(1-\alpha)^{1/3})} \quad \text{(A2.2)}$$

Contracting volume model: $$f(\alpha) = 3(1-\alpha)^{2/3} \quad \text{(A2.3)}$$

First-order reaction model: $$f(\alpha) = (1-\alpha) \quad \text{(A2.4)}$$

Second-reaction model: $$f(\alpha) = (1-\alpha)^{2} \quad \text{(A2.5)}$$

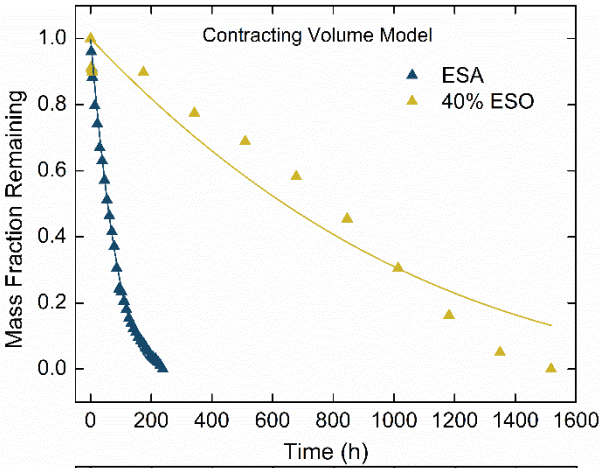
Contracting Volume Model
ESA
40% ESO
Mass Fraction Remaining
Time (h)
0.0
0.2
0.4
0.6
0.8
1.0
0
200
400
600
800
1000
1200
1400
1600

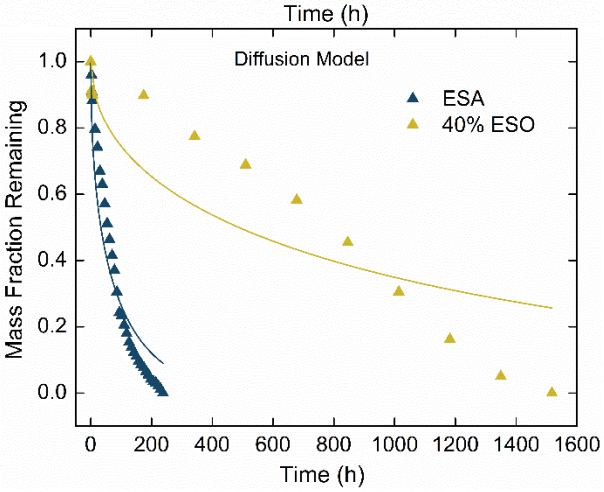
Diffusion Model
ESA
40% ESO
Mass Fraction Remaining
Time (h)
0.0
0.2
0.4
0.6
0.8
1.0
0
200
400
600
800
1000
1200
1400
1600

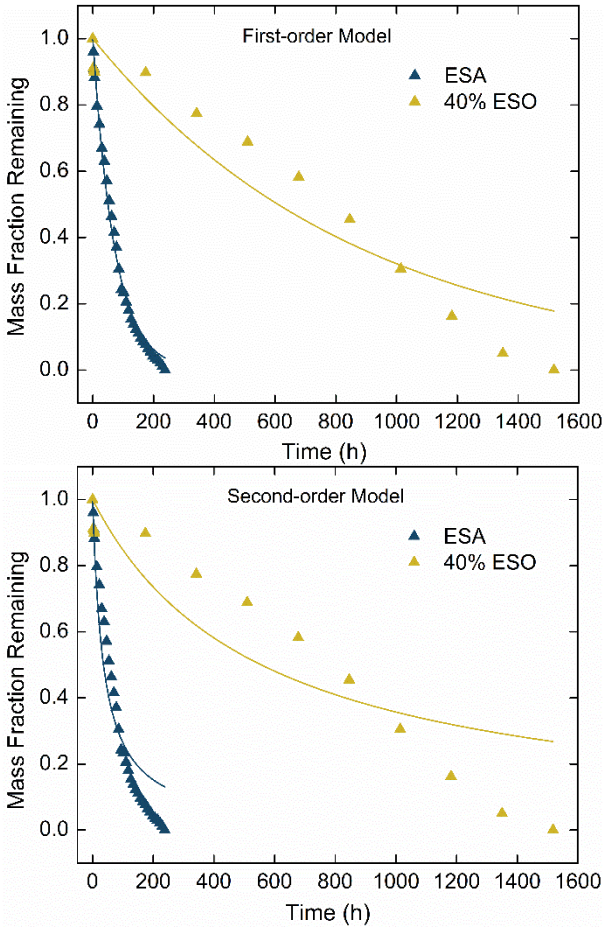

Figure A2.10: Solid-state kinetic models fit to degradation data obtained from ESA and ESO/DGEBA (40% ESO)-based epoxy resins.

Table A2.2: R^2 values obtained during the fit of various solid-state kinetic models to degradation data obtained from epoxy resins.

	ESA	ESO/DGEBA (40% ESO)
Contracting Volume Model	0.997	0.958
First-order Model	0.984	0.905
Second-order Model	0.961	0.883
Diffusion Model	0.928	0.800

Contracting volume model, as applied to a cuboid sample with side lengths a, b and c (a ≠ b ≠ c)

For solid-state kinetic analysis, the conversion fraction (α) can be defined as:

$$\boldsymbol{\alpha = \frac{m_0 - m_t}{m0} = 1 - \frac{m_t}{m_0}} \quad \text{(A2.6)}$$

where m_0 is the initial weight and mt is the weight when time = t.

For a cuboid rectangular sample (side lengths of a, b, c), and assuming 1) k doesn't change over time and 2) the cuboid retains its aspect ratio while undergoing contraction, then

$$\boldsymbol{a_0 - a = kt} \quad \text{(A2.7)}$$

$$\boldsymbol{b_0 - b = \frac{b_0}{a_0} kt} \quad \text{(A2.8)}$$

$$\boldsymbol{c_0 - c = \frac{c_0}{a_0} kt} \quad \text{(A2.9)}$$

where a_0, b_0, c_0 are the initial lengths of the cuboid rectangular sample, a,b,c are the lengths of the cuboid rectangular sample at time = t,

Using the relationship between density and mass, S6 becomes:

$$\boldsymbol{\alpha = 1 - \frac{\rho abc}{\rho a_0 b_0 c_0} = 1 - \frac{abc}{a_0 b_0 c_0}} \quad \text{(A2.10)}$$

Then, substituting A2.10 into A2.7-A2.9:

$$\boldsymbol{\alpha = 1 - \frac{a^3 \frac{b_0 c_0}{a_0^2}}{a_0 b_0 c_0} = 1 - \frac{a^3}{a_0^3}} \quad \text{(A2.11)}$$

$$\boldsymbol{1 - \alpha = \left(\frac{a_0 - kt}{a_0}\right)^3 = (1 - \frac{kt}{a_0})^3} \quad \text{(A2.12)}$$

$$\boldsymbol{1 - (1 - \alpha)^{\frac{1}{3}} = \frac{kt}{a_0}} \quad \text{(A2.13)}$$

A new rate constant is defined as k/a_0:

$$\boldsymbol{1 - (1 - \alpha)^{\frac{1}{3}} = k't} \quad \text{(A2.14)}$$

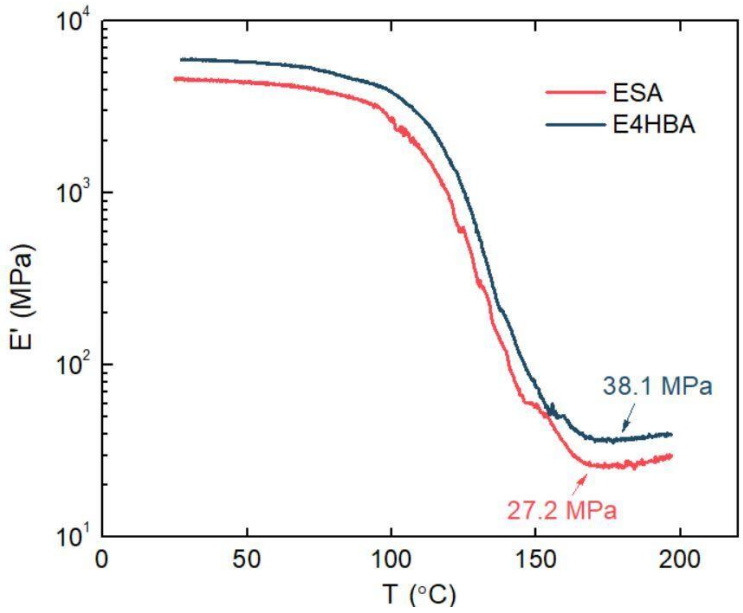

Figure A2.11 Storage modulus (E') of ESA- and E4HBA-based epoxy resins measured by DMA

Appendix 3: Supporting Information for Chapter 5

Degradation Solution Compositions

Table A3.1: Compositions of degradation solutions (total solution: 320 g)

	HCl (g)	H_2O (g)	Acetone (g)	THF (g)	DMF (g)
10 wt% HCl in pure water	32	288	0	0	0
10 wt% HCl in acetone/H_2O	32	68	220	0	0
10 wt% HCl in THF/H_2O	32	68	0	220	0
10 wt% HCl in DMF/H_2O	32	68	0	0	220

Characterization of Epoxidized Vanillic Acid

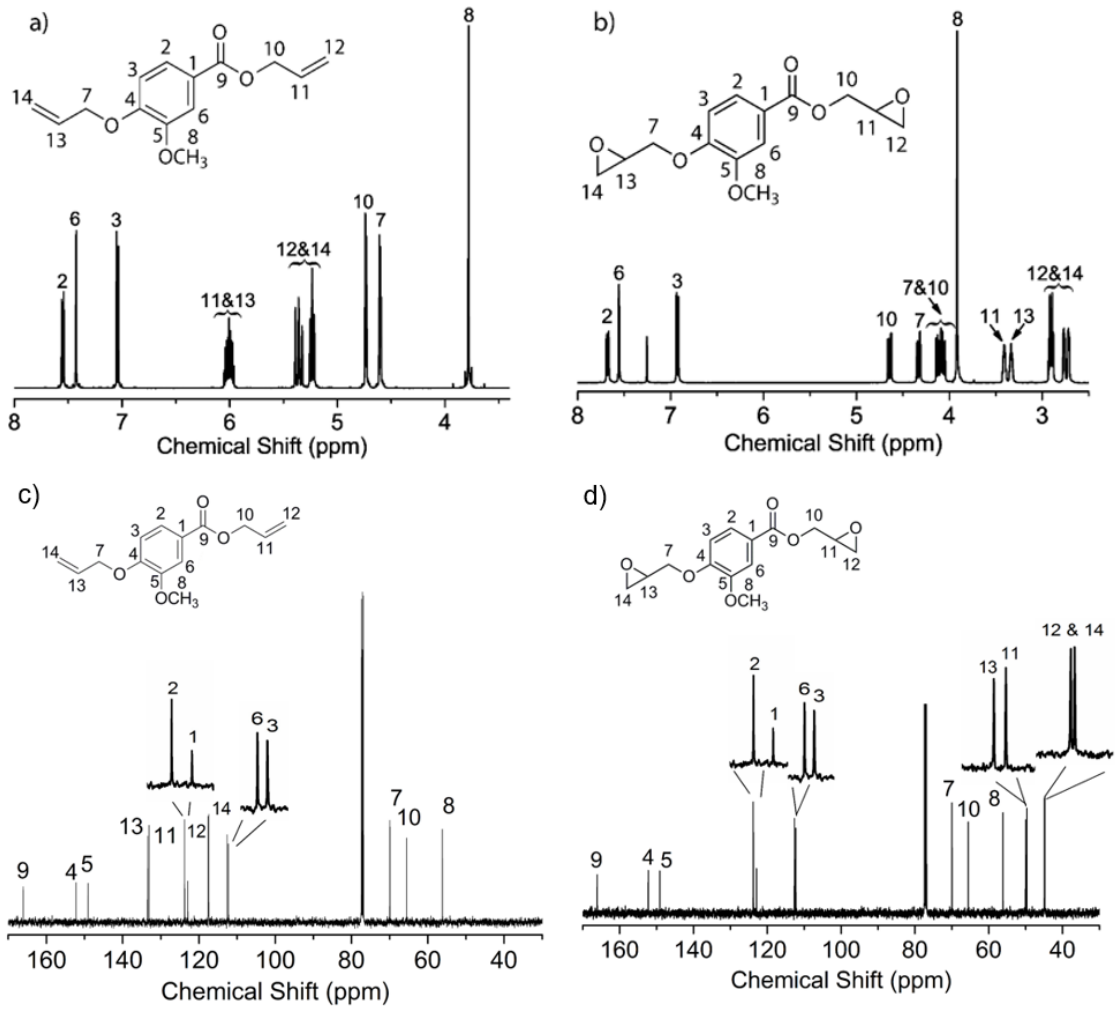

Figure A3.1: ^{1}H NMR data obtained from (a) allylated vanillic acid and (b) epoxidized vanillic acid, and ^{13}C NMR data obtained from (c) allylated vanillic acid and (d) epoxidized vanillic acid.

Calculation of Theoretical Crosslink Density (v_c) and Ester Density (v_{cster}) of Epoxy Resins

v_c is calculated from the theoretical molecular weight of a strand M_c:

$$v_c = \frac{\rho}{M_c} \qquad \text{(eqn. A3.1)}$$

where ρ is the mass density.

We measured the mass density of the EVA- and ESO-based epoxy resins by weighing a specimen of known dimensions (10 mm × 5 mm × 3 mm). The measured densities were: 1.1 ± 0.1 g/cm^3 and 1.01 ± 0.04 g/cm^3 for the EVA- and ESO-based epoxy resins, respectively.

M_c was calculated by considering the chemical structure of a perfect network. We considered the structures of EVA and ESO monomers and the anhydride curing agent (MHHPA) and calculated M_c of EVA and ESO-based epoxy resins.

EVA-Based Epoxy Resin

The general curing reaction for EVA, cured with MHHPA and 1-MI, is shown in Scheme A3.1:

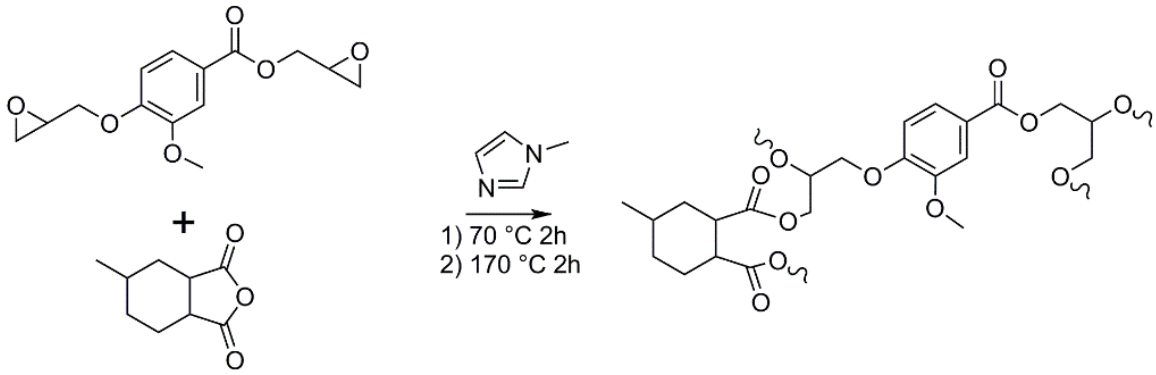

Scheme A3.1: Curing of EVA with MHHPA and 1-MI

We defined a junction to be located at the aromatic ring within the EVA monomer (**Figure A3.2a**). We considered that network strands form in two possible directions: two strands form from the ester linkage in EVA and two strands form from the ether linkage in EVA. Each possibility has the same probability. Thus, there are 4 possible types of strands in the EVA-based epoxy resin network: ether-anhydride-ether (25%, **Figure A3.2b**), ester-anhydride-ester (25%, **Figure A3.2c**), ether-anhydride-ester (25%, **Figure A3.2d**), ester-anhydride-ether (25%, **Figure A3.2d**). We accounted for 25% of the aromatic ring (the junction) when calculating the molecular weight of each strand. The molecular weight of each strand is included in **Figure A3.2**.

M_c for the EVA-based epoxy resin is calculated as below:

$$M_c = \frac{1}{4} * 263 + \frac{1}{4} * 319 + \frac{1}{2} * 291 = 291\ g/mol \quad \text{(eqn. A3.2)}$$

v_c for the EVA-based epoxy resin is calculated as below:

$$v_c = \frac{\rho}{M_c} = \frac{(1.1 \pm 0.1)\ g/cm^3}{291\ g/mol} = 3.8 \times 10^{-3} \pm 0.3 \times 10^{-3}\ mol/cm^3 \quad \text{(eqn. A3.3)}$$

Considering the conversion of the EVA curing reaction (98%, from FTIR):

$$v_c = (3.8 \times 10^{-3} \pm 0.3 \times 10^{-3}) mol/cm^3 * (0.98) = 3.7 \times 10^{-3} \pm 0.3 \times 10^{-3} mol/cm^3 \quad \text{(eqn. A3.4)}$$

where the error on v_c is propagated from the known error on ρ.

v_c measured by DMA is $3.4 \times 10^{-3} \pm 0.3 \times 10^{-3}$ mol/cm^3. The theoretical v_c and measured v_c are therefore within the error on the measurement.

In each strand in the EVA-based epoxy resin (**Figure A3.2**), there are 3 ester groups. Thus, the ester density of the EVA-based epoxy resin is:

$$v_{ester} = (3.4 \times 10^{-3} \pm 0.3 \times 10^{-3}) * 3 = 10.2 \times 10^{-3} \pm 0.9 \times 10^{-3}\ mol/cm^3 \quad \text{(eqn. A3.5)}$$

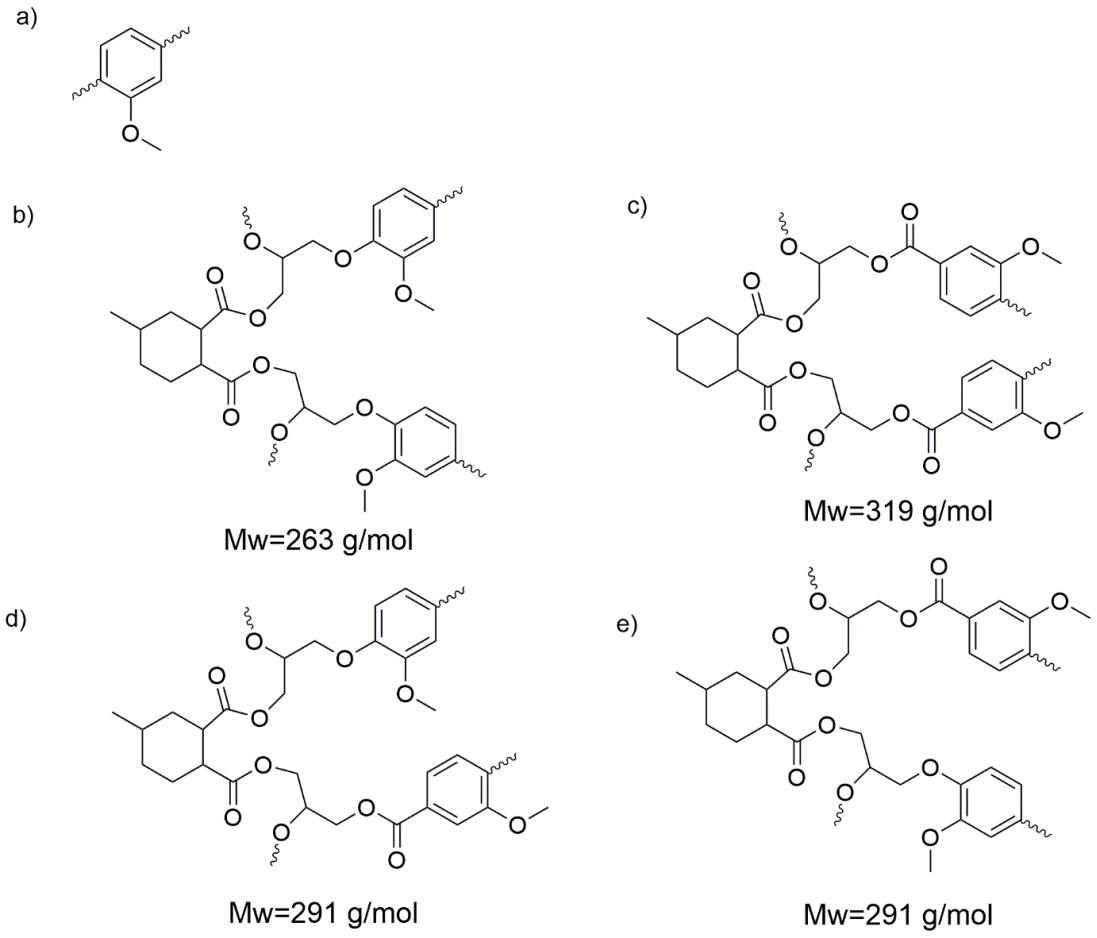

Figure A3.2: Chemical structures of a) junctions and b-e) possible strands in the EVA-based epoxy resin network. Molecular weight (Mw) of each strand is provided.

ESO-Based Epoxy Resin

The general curing reaction for ESO, cured with MHHPA and 1-MI, is shown in Scheme A3.2:

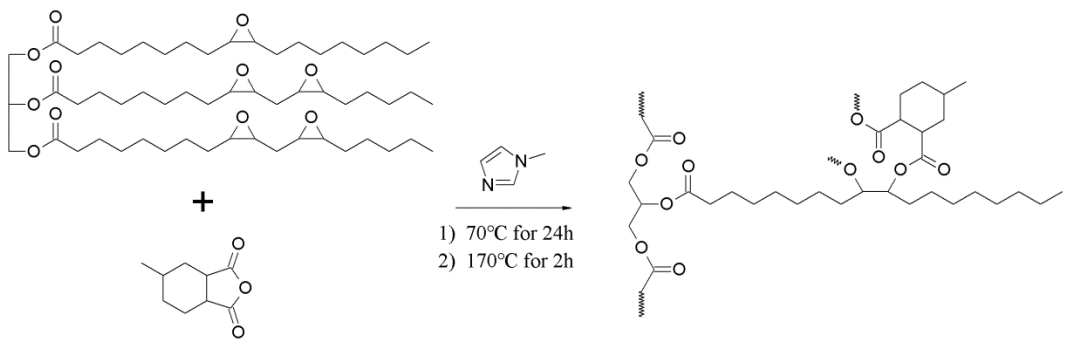

Scheme A3.2: Curing of ESO with MHHPA and 1-MI

ESO contains a distribution of fatty acids: 52% linoleic acid, 26% oleic acid, 7% linolenic acid, 11% palmitic acid and 4% stearic acid. We neglected the presence of palmitic acid and stearic acid, which do not contain double bonds and therefore are not epoxidized when soybean oil is converted to ESO. The presence of palmitic acid and stearic acid strands in the network leads to dangling chains in the network, which do not contribute to the network elasticity. Therefore, the measured v_c is anticipated to be lower than the predicted v_c if we neglect this effect. We normalized the fatty acid composition to only consider linoleic acid, oleic acid and linolenic acid.

We defined a junction as the CH in the middle of the glycerol part of the triglyceride structure of the vegetable oil (**Figure A3.3a**) and identified 6 possible strands in ESO-based epoxy resin: linoleic acid-anhydride-linoleic acid (46.2%, **Figure A3.3b**, linoleic acid-anhydride-oleic acid (36%, **Figure A3.3c**), linoleic acid-anhydride-linolenic acid (7.6%, **Figure A3.3d**), oleic acid-anhydride-oleic acid (7%, **Figure A3.3e**, oleic acid-anhydride-oleic acid (2.9%, **Figure A3.3f**), and linolenic acid to linolenic acid (0.3%, **Figure A3.3g**). We also neglected the end chain after the epoxide group, which does not contribute to the elastic strand in the network. The molecular weight of each strand is included in **Figure A3.3**.

$M_c$for the ESO-based epoxy resin can be calculated as below:

$$M_c = 0.462 * 564 + 0.36 * 606 + 0.076 * 648 + 0.07 * 606 + 0.029 * 648 + 0.003 * 690 = 592\ g/mol$$

(eqn.A3.6)

v_c for the ESO-based epoxy resin can be calculated as below:

$$v_c = \frac{\rho}{M_c} = \frac{1.01 \pm 0.04\ g/cm^3}{592\ g/mol} = 1.71 \times 10^{-3} \pm 0.07 \times 10^{-3} mol/cm^3 \qquad \text{(eqn. A3.7)}$$

Considering the conversion of the EVA curing reaction 79%, from FTIR):

v_c for the ESO-based epoxy resin is:

$$v_c = (1.71 \times 10^{-3} \pm 0.07 \times 10^{-3}) mol/cm^3 * (0.79) = 1.35 \times 10^{-3} \pm 0.06 \times 10^{-3}\ mol/cm^3$$

(eqn. A3.8)

Crosslink density measured by DMA is is $1.4 \times 10^{-3} \pm 0.2 \times 10^{-3}$ mol/cm^3. The theoretical $v_c$and measured v_c are therefore within the error on the measurement.

In each strand in the ESO-based epoxy resin (**Figure A3.3**), there are 4 ester groups. Thus, the ester density of the ESO-based epoxy resin is:

$$v_{ester} = (1.4 \times 10^{-3} \pm 0.2 \times 10^{-3}) * 4 = 5.6 \times 10^{-3} \pm 0.8 \times 10^{-3}\ mol/cm^3$$ (eqn. A3.9)

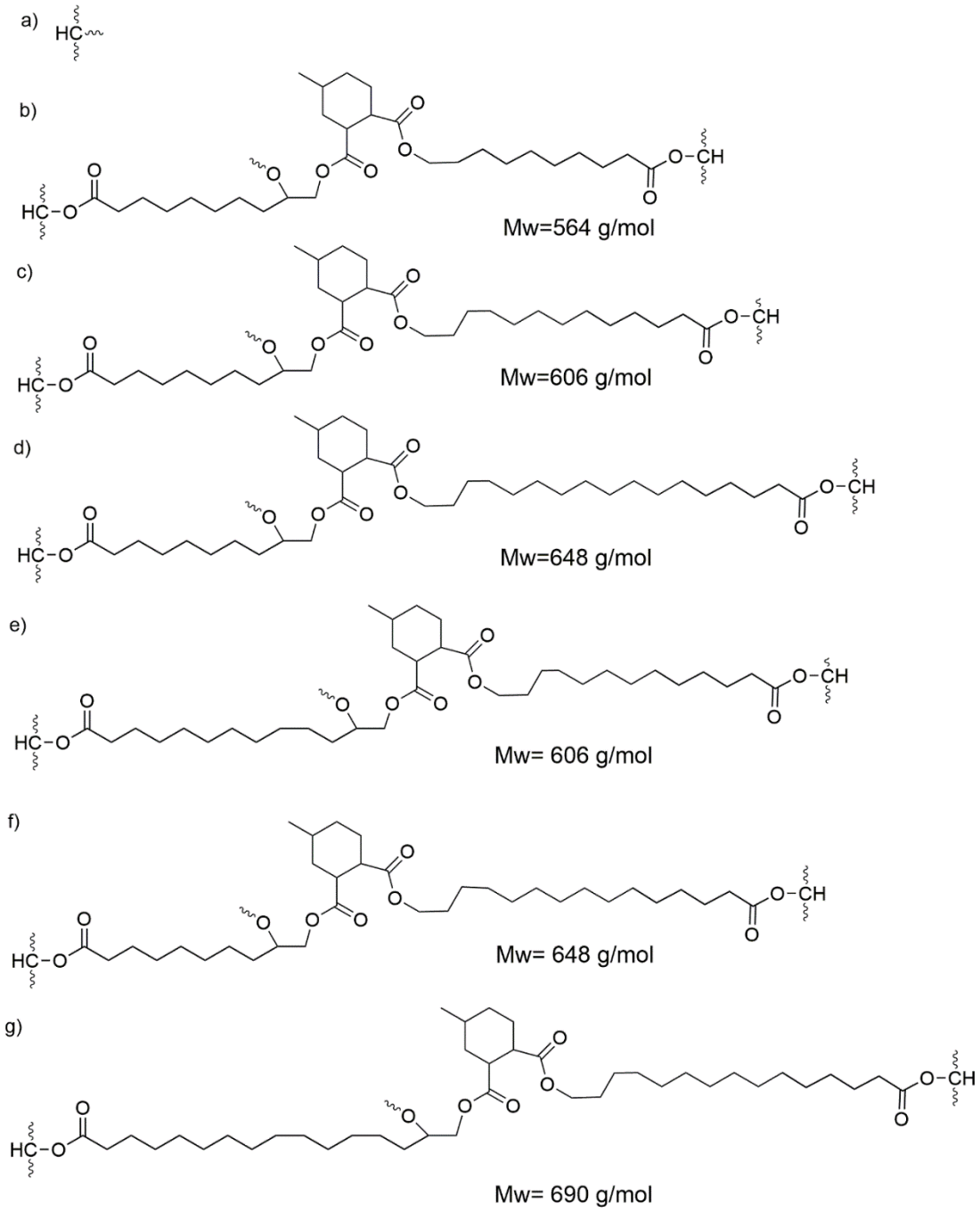

Figure A3.3: Chemical structures of a) junctions and b-e) possible strands in ESO-based epoxy resin network. Molecular weight (Mw) of each strand is provided.

Degradation Data and Solid State Kinetic Model Fitting

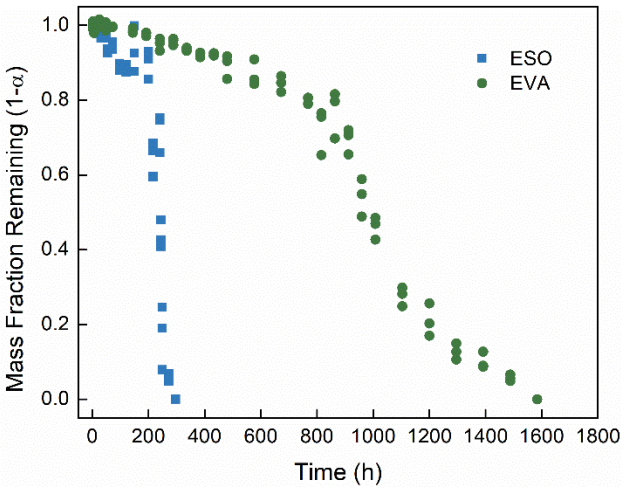

Figure A3.4: Mass fraction remaining of ESO- and EVA-based epoxy resins in 10 wt% HCl aqueous solution at 80 °C. Three independent samples were characterized at each time point and are shown here individually. Averages over the three measurements are provided in Figure 5.3 of the main text.

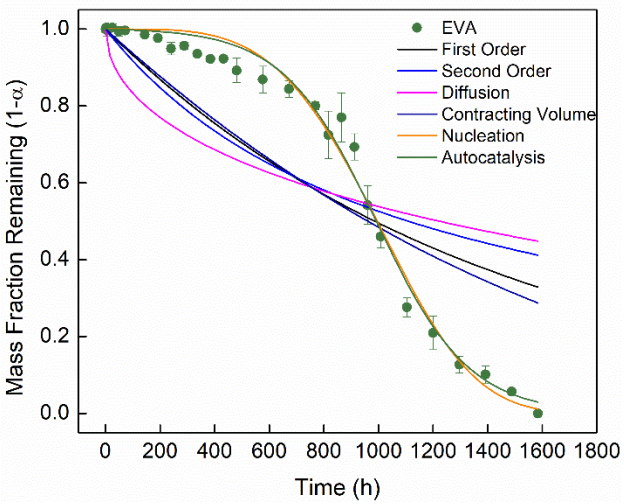

Figure A3.5: Comparison of solid-state kinetic models (first order, second order, a diffusion-based model, the contracting volume and a nucleation model) as well as reaction order model with autocatalysis to fit mass loss data of EVA-based epoxy resins in 10 wt% HCl aqueous solution at 80 °C.

Discussion on Application of Nucleation Model to Degradation Data

Nucleation models describe the transformation of a solid from one phase to another. Nucleation models often include phenomena such as decomposition [161], adsorption [162, 163], hydration, [164] and desolvation [165]. The general form of a nucleation model is described in eqn. A3.10

$$\propto = (kt)^n \qquad \text{(eqn. A3.10)}$$

where $\propto$ is the mass fraction degraded at time t

$$\propto = \frac{m_0 - m}{m_0} \qquad \text{(eqn. A3.11)}$$

and m_0 is the initial mass at t = 0, m is the mass at time t, k is the degradation rate constant, and $n = \beta + \lambda$, where β is the number of successive events that are necessary to form the growth nucleus and λ is the number of growth dimensions. The mass fraction remaining is thus $1-\propto$. The Avrami-Erofeyev models are one class of nucleation models that neglect nuclei ingestion and nuclei coalescence [166]. The models incorporate the extended conversion fraction (α'), which has the relationship with α as:

$$d\alpha' = \frac{d\propto}{1-\propto} \qquad \text{(eqn. A3.12)}$$

After integration, this gives:

$$\propto' = -\ln(1-\propto) \qquad \text{(eqn. A3.13)}$$

Eqn. A3.10 can thus be rearranged to:

$$-\ln(1-\propto) = (kt)^n \qquad \text{(eqn. A3.14)}$$

We fit the degradation data in Figure 5.3 to eqn. A3.14. The resulting fit parameters obtained were k = 3.91x10^{-3} h^{-1} and n = 3.6 for the ESO-based epoxy resin and k =

9.34×10^{-4} h^{-1} and n = 3.7 for the EVA-based epoxy resin (Figure A3.6a). As by definition, n should be an integer, we thus proceeded using n = 4, resulting in eqn. A3.15, in which the only fitting parameter is the degradation rate constant k:

$$-\ln(1-\propto) = (kt)^4 \qquad \text{(eqn. A3.15)}$$

We note that the use of Avrami-Erofeyev models with n = 2 or 3 provided a poorer fit of the model to the data (Figures A3.6b and A3.6c).

The application of the model (eqn. A3.15) to the degradation data obtained in acidic media is shown in Figure A3.7. The degradation behavior is well-predicted by the nucleation model for both ESO- and EVA-based epoxy resins (R^2 was 0.979 and 0.957 for ESO- and EVA-based epoxy resins, respectively). The obtained degradation rate constants (k) for ESO- and EVA-based epoxy resins were 3.98×10^{-3} h^{-1} and 9.38×10^{-4} h^{-1}, respectively. The nucleation model captured the observed sigmoidal mass loss trend with three stages: 1) an initial time period of little mass loss (It takes time for water to penetrate into the matrix and prepare for forming nuclei of the new phase), 2) a time period of rapid mass loss (the nuclei of the new phase keep growing and consuming the old phase), and 3) deceleration at the latest stages of degradation (only little remaining of the old phase). We do note an under-prediction of the mass loss rate at early times by the model in Figure A3.7, which may be due to small part of the cleavage of ester groups at the specimen surface, and may be improved by further modifications to the model.

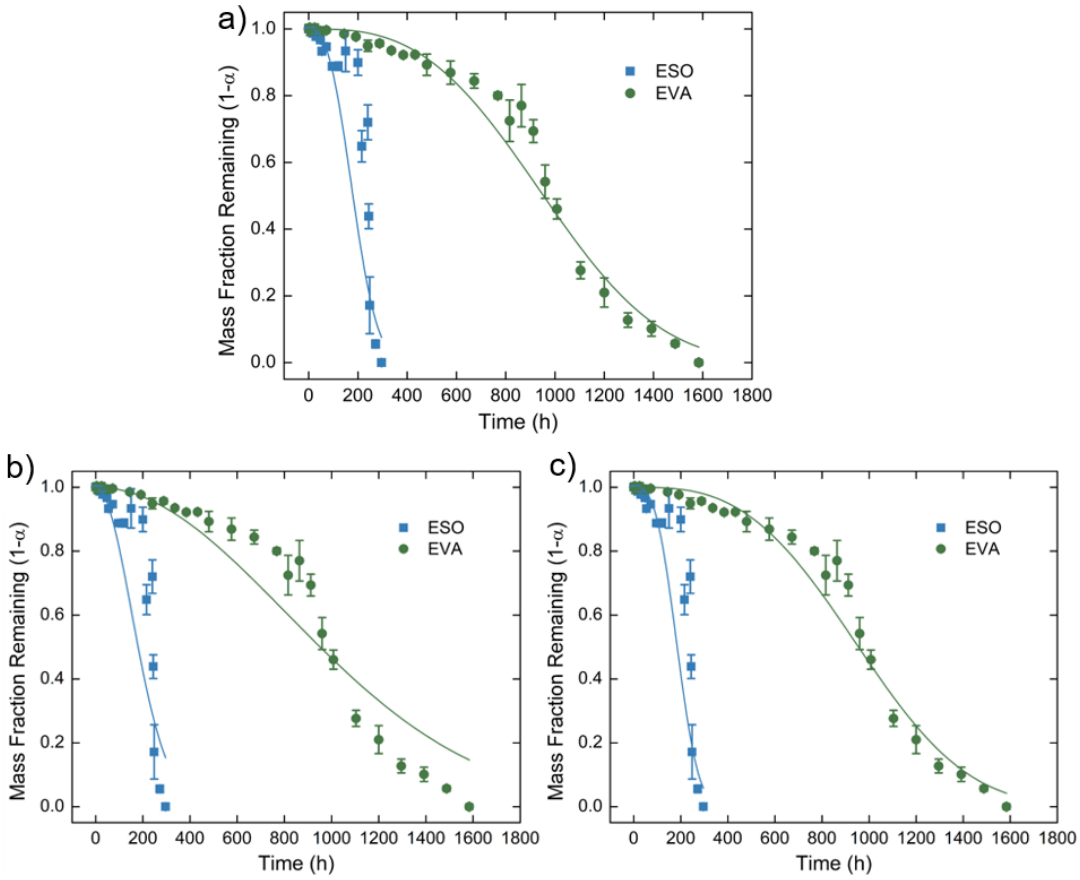

Figure A3.6: (a) Solid curves show fit of the nucleation model (eqn. A3.14) to the data presented in Figure 3 of the main text, in which fitting parameters of both k and n were used. For ESO: k = 4.45x10^{-3} h^{-1} and n = 3.6 (R^2 = 0.962). For EVA: k = 9.34x10^{-4} h^{-1} and n = 3.7 (R^2 = 0.984). (b) (c) Solid curves show fit of the nucleation model (eqn. A3.14) to the data presented in Figure 3 of the main text, in which n was constrained to be b) 2 and c) 3. In b): R^2 = 0.921 and 0.938 for ESO and EVA-based epoxy resins, respectively. In c) R^2 = 0.944 and 0.970 for ESO and EVA-based epoxy resins, respectively. These fits have lower R^2 values than that demonstrated in (a), and thus an n=4 was used in this study.

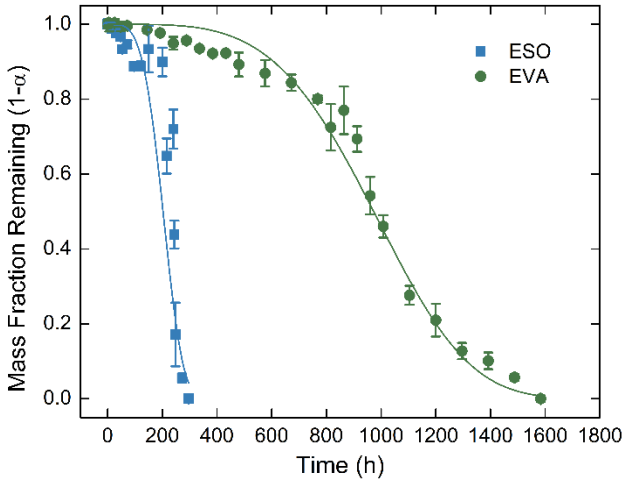

Figure A3.7: Mass fraction remaining $(1-\propto)$ of ESO- and EVA-based epoxy resins in 10 wt% HCl aqueous solution at 80 °C. Averages are shown over three independent measurements with error bars representing the standard deviation. A solid-state nucleation model (eqn. A3.15) was fit to the data (solid curves). The resulting degradation rate constants were k = 3.98x10^{-3} h^{-1} (R^2 = 0.979) and 9.38x10^{-4} h^{-1} (R^2 = 0.957), respectively, for ESO- and EVA-based epoxy resins.

Mass Spectrometry Data and Analysis

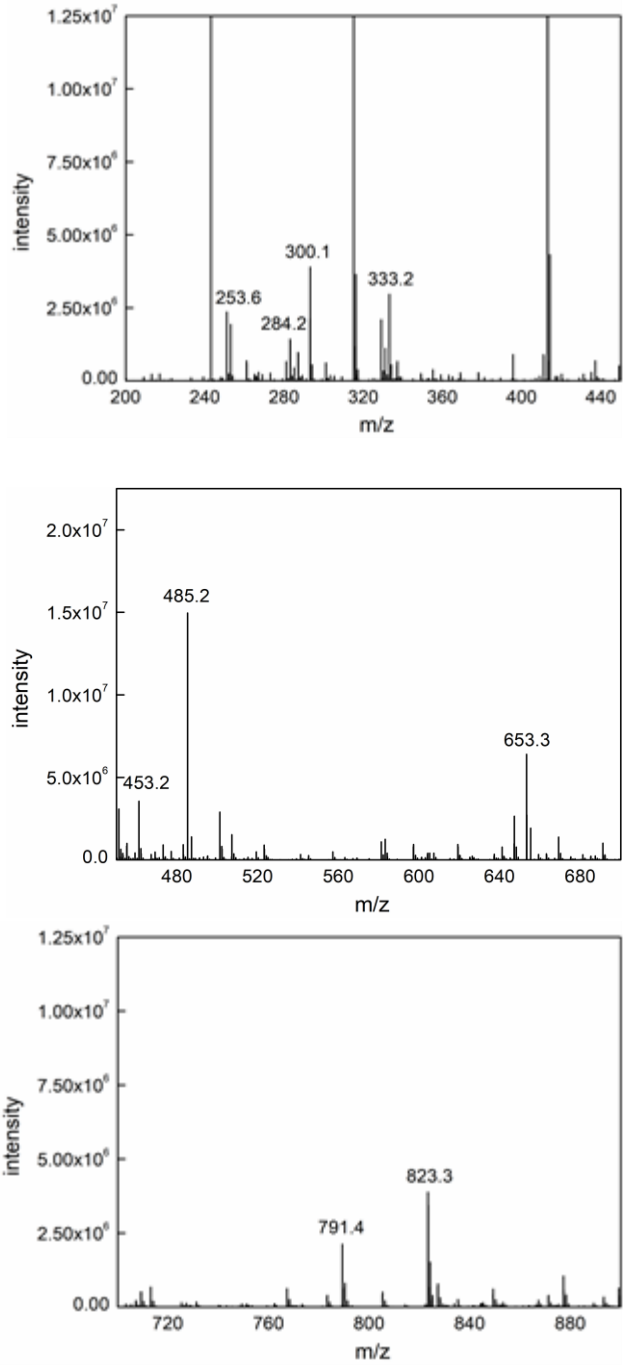

Figure A3.8: Mass spectrum obtained from products of the degradation of the EVA-based epoxy resin in 10 wt% HCl aqueous solution at 80 °C. Proposed chemical structures and theoretical molecular weights for minor peaks observed in the mass spectrum (assignments for major peaks shown in Figure 5.5 of the main text).

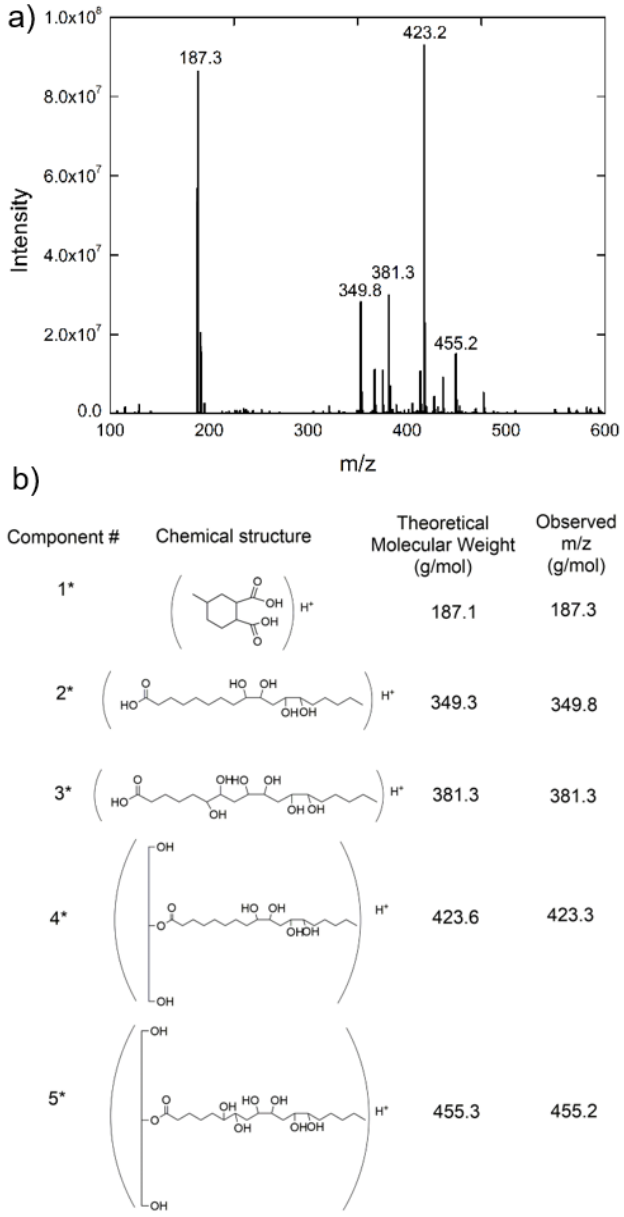

Figure A3.9: Mass spectrum obtained from products of the degradation of the ESO-based epoxy resin in 10 wt% HCl aqueous solution at 80 °C. Proposed chemical structures and theoretical molecular weights for major peaks observed in the mass spectrum (assignments for minor peaks shown in Figure A3.10).

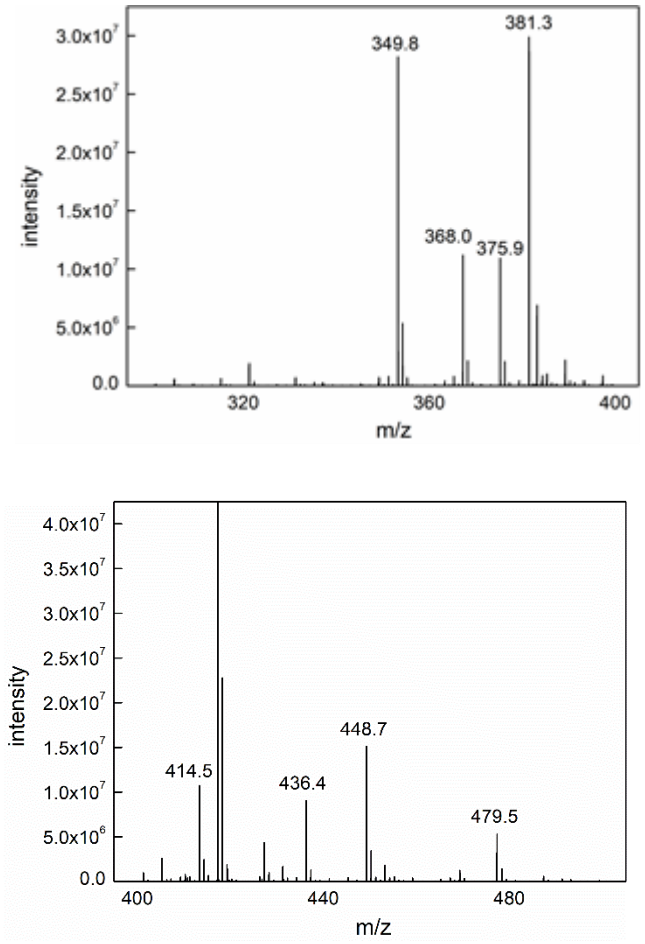

Figure A3.10: Mass spectrum obtained from products of the degradation of the ESO-based epoxy resin in 10 wt% HCl aqueous solution at 80 °C. Proposed chemical structures and theoretical molecular weights for minor peaks observed in the mass spectrum (assignments for major peaks shown in Figure A3.9).

Application of the Nucleation Model to Degradation Data in Various Solvent Systems

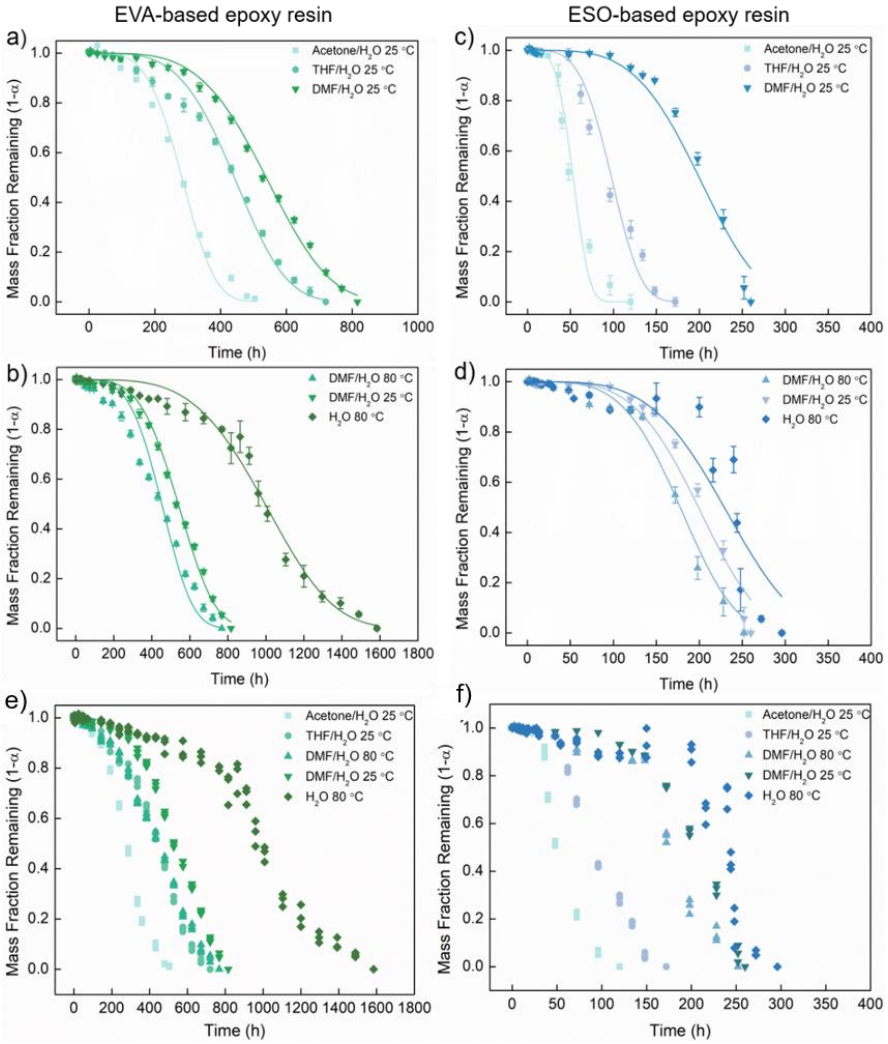

Figure A3.11: Mass fraction remaining $(1-\propto)$ of a) b) EVA-based epoxy resins and c) d) ESO-based epoxy resin in 10 wt% HCl solution using different solvent systems (DMF/H_2O, acetone/H_2O, THF/H_2O, H_2O) and temperatures (25 and 80 °C). Averages are shown over three independent measurements with error bars representing the standard deviation. In some cases, error bars are smaller than the data point. A solid-state nucleation model (eqn. A3.15) was fit to the data (solid curves). In a): k = 3.23x10^{-3} h^{-1} (R^2 = 0.991), 2.07x10^{-3} h^{-1} (R^2 = 0.980), and 1.69x10^{-3} h^{-1} (R^2 = 0.996) for acetone/H_2O 25 °C, THF/H_2O 25 °C and DMF/H_2O 25 °C, respectively. In b): k = 2.02x10^{-3} h^{-1} (R^2 = 0.969), 1.69x10^{-3} h^{-1} (R^2 = 0.996), and 9.38x10^{-4} h^{-1} (R^2 = 0.957) for DMF/H_2O 80 °C, DMF/H_2O 25 °C and H_2O 80 °C, respectively. In c): k = 1.72x10^{-2} h^{-1} (R^2 = 0.949), 9.38x10^{-3} h^{-1} (R^2 = 0.972), and 4.59x10^{-3} h^{-1} (R^2 = 0.964) for acetone/H_2O 25 °C, THF/H_2O 25 °C and DMF/H_2O 25 °C, respectively. In d): k = 5.13x10^{-3} h^{-1} (R^2 = 0.972), 4.59x10^{-3} h^{-1} (R^2 = 0.964), and 3.98x10^{-3} h^{-1} (R^2 = 0.979) for DMF/H_2O 80 °C, DMF/H_2O 25 °C and H_2O 80 °C,

respectively. Extracted rate constants are shown in Table S2. The complete data sets are shown in (e) and (f).

Table A3.2: Degradation rate constant k of EVA- and ESO-based epoxy resins in various solvents obtained from fitting the nucleation model to the mass loss data

Solvent Composition[a]	T (°C)	k (10^{-3} h^{-1}), EVA-based epoxy resin	k (10^{-3} h^{-1}), ESO-based epoxy resin
Acetone/H_2O	25	3.23 ± 0.06	17 ± 2
THF/H_2O	25	2.07 ± 0.03	9.4 ± 0.5
DMF/H_2O	25	1.69 ± 0.02	4.59 ± 0.08
DMF/H_2O	80	2.02 ± 0.03	5.1 ± 0.1
H_2O	80	0.9 ± 0.3	4.0 ± 0.1

[a] 100 g concentrated HCl (32 g HCl and 68 g water) was added to 220 g of the diluting solvent (water, THF, acetone or DMF).

Predictions of Solubility Parameters of Degradation Products

Table A3.3: Hansen Solubility Parameter (δ) of main degradation products of EVA- and ESO-based epoxy resins and pure solvent

	Degradation Product or Solvent	δ_d (MPa$^{1/2}$)	δ_p (MPa$^{1/2}$)	δ_{hb} (MPa$^{1/2}$)	δ (MPa$^{1/2}$)
EVA-Based Epoxy Resin Degradation Products	Component 1	17.2366	1.0144	12.8351	21.5
	Component 2	18.9383	9.0497	24.3313	32.1
	Component 3	19.6322	16.3663	35.2596	43.5
	Component 4	20.0693	8.3405	16.8583	27.5
	Component 5	20.3289	14.1525	30.0653	39.0
	Component 6	21.0835	13.1258	25.1301	35.3
ESO-Based Epoxy Resin Degradation Products	Component 1*	17.2366	1.0144	12.8351	21.5
	Component 2*	17.2700	10.8874	33.3719	39.1
	Component 3*	18.1460	15.5882	47.7881	53.4
	Component 4*	17.8883	16.2806	43.7421	50.0
	Component 5*	17.7031	15.7998	59.3151	63.9
Solvents	Acetone	15.9175	8.3608	5.5765	19.0
	THF	17.5177	6.6407	6.5826	19.9
	DMF	17.7713	13.1447	10.9813	24.7
	Water	15.6	16.0	42.3	47.8

All functional groups are divided into first order groups that comprise the basic molecular structures of the compounds and second order groups defined by conjugation theory.[167]

The dispersion solubility parameter (δ_d), polar solubility parameter (δ_p) and hydrogen bonding solubility parameter (δ_{hb}) are calculated by the following equations:[167]

$$\delta_d = \left(\sum_i N_i C_i + W \sum_j M_j D_j + 17.3231\right) MPa^{0.5} \quad \text{(eqn. A3.16)}$$

$$\delta_p = \left(\sum_i N_i C_i + W \sum_j M_j D_j + 7.3548\right) MPa^{0.5} \quad \text{(eqn. A3.17)}$$

$$\delta_{hb} = \left(\sum_i N_i C_i + W \sum_j M_j D_j + 7.9793\right) MPa^{0.5} \quad \text{(eqn. A3.18)}$$

where C_i is the contribution of the first-order group of type *i* that appears N_i times in the compound and D_j is the contribution of the second-order group of type *j* that appears M_j times in the compound, and δ is calculated as:

$$\delta = \sqrt{\delta_d^2 + \delta_p^2 + \delta_{hb}^2} \quad \text{(eqn. A3.19)}$$

EVA-Based Epoxy Resin

Chemical structures of the degradation products are shown in Figure 5 of the main text. AC refers to an aromatic carbon in the descriptions below.

Component 1:

First-order groups: 1 $-CH_3$, 2 $-COOH$, 3 $-CH$, 3 $-CH_2$

Second-order group: 1 C_6 ring

$$\delta_d = -0.9714 - 2 * 0.2910 + 3 * 0.6450 - 3 * 0.0269 - 0.3874 + 17.3231 = 17.624\ MPa^{0.5} \quad \text{(eqn. A3.20)}$$

$$\delta_p = -1.6448 + 2 * 0.9042 - 3 * 0.6491 - 3 * 0.3045 - 3.6462 + 7.3548 = 1.0144 MPa^{0.5} \quad \text{(eqn. A3.21)}$$

$$\delta_{hb} = -0.7813 + 2 * 3.7391 - 3 * 0.2018 - 3 * 0.4119 + 7.9793 = 12.8351\ MPa^{0.5} \quad \text{(eqn. A3.22)}$$

$$\delta = 21.5\ MPa^{0.5}$$

Component 2:

First order groups: 1 $-OCH_3$, 3 ACH, 3 AC, 2 –OH, 1 –CH, 1 $-OCH_2$, 1 –COOH

Second order groups: 1 ACCOOH, 1 C_6 ring, 1 –CHOH, 1 ACOC

$\delta_d = -0.5828 + 3 * 0.1105 + 3 * 0.8446 - 2 * 0.3462 + 0.6450 + 0.031 - 0.2910 - 0.3874 - 0.2293 + 0.2568 + 17.3231 = 18.9383\ MPa^{0.5}$
(eqn. A3.23)

$\delta_p = 0.1764 - 3 * 0.5305 + 3 * 0.6187 + 2 * 1.1404 + 0.6491 + 0.8826 + 0.9042 - 3.6432 + 0.6349 + 0.8153 + 7.3548 = 9.0497\ MPa^{0.5}$ (eqn. A3.24)

$\delta_{hb} = 0.1460 - 3 * 0.4305 + 3 * 0.0084 + 2 * 7.1908 - 0.2018 - 0.1528 + 3.7391 - 0.9030 + 0.6092 + 7.9793 = 24.3313\ MPa^{0.5}$
(eqn. A3.25)

$\delta = 32.1\ MPa^{0.5}$

Component 3:

First order groups: 1 –OCH_3, 3 ACH, 3 AC, 4 –OH, 2 –CH, 2 –OCH_2, 1 –COO–, 3 –CH_2

Second order groups: 1 ACCOO, 1 C_6 ring, 2 –CHOH, 1 ACOC

$\delta_d = -0.5828 + 3 * 0.1105 + 3 * 0.8446 - 4 * 0.3462 + 2 * 0.6450 + 2 * 0.0310 + 0.2039 - 2 * 0.0269 + 2 * 0.1123 - 0.3874 - 0.1847 + 0.2568 + 17.3231 = 19.6322\ MPa^{0.5}$ (eqn. A3.26)

$\delta_p = 0.1764 - 3 * 0.5305 + 3 * 0.6187 + 4 * 1.1404 + 2 * 0.6491 + 2 * 0.8826 + 3.4637 - 2 * 0.3045 + 2 * 0.2564 - 3.6432 + 0.4059 + 0.8153 + 7.3548 = 16.3663\ MPa^{0.5}$

(eqn. A3.27)

$\delta_{hb} = 0.1460 - 3 * 0.4305 + 3 * 0.0084 + 4 * 7.1908 - 2 * 0.2018 - 2 * 0.1528 + 1.1389 - 2 * 0.4119 - 2 * 0.1928 - 0.1921 + 0.6092 + 7.9793 = 35.2596\ MPa^{0.5}$

(eqn. A3.28)

$\delta = 43.5\ MPa^{0.5}$

Component 4:

First order groups: 1 –OCH_3, 3 ACH, 3 AC, 1 –OH, 4 –CH, 1 –OCH_2, 1 –COO–, 2 –COOH, 1 –CH_3, 4 –CH_2

Second order groups: 1 ACCOOH, 2 C_6 ring, 1 –CHOH, 1 ACOC

$\delta_d = -0.5828 + 3 * 0.1105 + 3 * 0.8446 - 0.3462 + 4 * 0.6450 + 0.0310 - 0.2910 + 0.2039 - 0.9714 - 4 * 0.0269 - 2 * 0.3874 - 0.2293 + 0.1123 + 0.2568 + 17.3231 = 20.0693\ MPa^{0.5}$ (eqn. A3.29)

$$\delta_p = 0.1764 - 3 * 0.5305 + 3 * 0.6187 + 1.1404 + 4 * 0.6491 + 0.8826 + 0.9042 + 3.4637 - 1.6448 - 4 * 0.3045 - 2 * 3.6432 + 0.6349 + 0.2564 + 0.8153 + 7.3548 = 8.3405\ MPa^{0.5}$$

(eqn. A3.30)

$$\delta_{hb} = 0.1460 - 3 * 0.4305 + 3 * 0.0084 + 7.1908 - 4 * 0.2018 - 0.1528 + 3.7391 + 1.1389 - 0.7813 - 4 * 0.4119 + 0.903 - 0.1928 + 0.6092 + 7.9793 = 16.8583\ MPa^{0.5}$$

(eqn. A3.31)

$$\delta = 27.5\ MPa^{0.5}$$

Component 5:

First order groups: 1 –OCH_3, 3 ACH, 3 AC, 3 –OH, 5 –CH, 1 –OCH_2, 2 –COO–, 1 –COOH, 1 –CH_3, 6 –CH_2

Second order groups: 1 ACCOO, 2 C_6 ring, 2 –CHOH, 1 ACOC

$$\delta_d = -0.5828 + 3 * 0.1105 + 3 * 0.8446 - 3 * 0.3462 + 5 * 0.6450 + 0.0310 - 0.2910 + 2 * 0.2039 - 0.9714 - 6 * 0.0269 - 2 * 0.3874 - 0.1847 + 2 * 0.1123 + 0.2568 + 17.3231 = 20.3289\ MPa^{0.5}$$

(eqn. A3.32)

$$\delta_p = 0.1764 - 3 * 0.5305 + 3 * 0.6187 + 3 * 1.1404 + 5 * 0.6491 + 0.8826 + 0.9042 + 2 * 3.4637 - 1.6448 - 6 * 0.3045 - 2 * 3.6432 + 0.4059 + 2 * 0.2564 + 0.8153 + 7.3548 = 14.1525\ MPa^{0.5}$$
(eqn. A3.33)

$$\delta_{hb} = 0.1460 - 3 * 0.4305 + 3 * 0.0084 + 3 * 7.1908 - 5 * 0.2018 - 0.1528 + 3.7391 + 2 * 1.1389 - 0.7813 - 6 * 0.4119 - 0.1921 - 2 * 0.1928 + 0.6092 + 7.9793 = 30.0653\ MPa^{0.5}$$

(eqn. A3.34)

$$\delta = 39.0\ MPa^{0.5}$$

Component 6:

First order groups: 1 –OCH_3, 3 ACH, 3 AC, 2 –OH, 8 –CH, 1 –OCH_2, 3 –COO–, 2 –COOH, 2 –CH_3, 9 –CH_2

Second order groups: 1 ACCOO, 3 C_6 ring, 2 –CHOH, 1 ACOC

$$\delta_d = -0.5828 + 3 * 0.1105 + 3 * 0.8446 - 2 * 0.3462 + 8 * 0.6450 + 0.0310 - 2 * 0.2910 + 3 * 0.2039 - 2 * 0.9714 - 9 * 0.0269 - 3 * 0.3874 - 0.1847 + 2 *$$

$0.1123 + 0.2568 + 17.3231 = 21.0835\ MPa^{0.5}$
(eqn. A3.35)

$\delta_p = 0.1764 - 3 * 0.5305 + 3 * 0.6187 + 2 * 1.1404 + 8 * 0.6491 + 0.8826 + 2 * 0.9042 + 3 * 3.4637 - 2 * 1.6448 - 9 * 0.3045 - 3 * 3.6432 + 0.4059 + 2 * 0.2564 + 0.8153 + 7.3548 = 13.1258\ MPa^{0.5}$
(eqn. A3.36)

$\delta_{hb} = 0.1460 - 3 * 0.4305 + 3 * 0.0084 + 2 * 7.1908 - 8 * 0.2018 - 0.1528 + 2 * 3.7391 + 3 * 1.1389 - 2 * 0.7813 - 9 * 0.4119 - 0.1921 - 2 * 0.1928 + 0.6092 + 7.9793 = 25.1301\ MPa^{0.5}$ (eqn. A3.37)

$\delta = 35.3\ MPa^{0.5}$

Volume fraction based on mass spectrometry intensity:

Component 1: 34.4%

Component 2: 16.8%

Component 3: 15.6%

Component 4: 16.8%

Component 5: 10.9%

Component 6: 5.5%

δ of EVA-based epoxy resin degradation products mixture is:

$\delta = 21.5 * 34.4\% + 32.1 * 16.8\% + 43.5 * 15.6\% + 27.5 * 16.8\% + 39.0 * 10.9\%$

$+35.3 * 5.5\% = 30.4\ MPa^{0.5}$ (eqn. A3.38)

ESO-Based Epoxy Resin

Component 1:*

Component 1* is the same as component 1: $\delta = 21.5\ MPa^{0.5}$

Component 2:*

First order groups: 1 –COOH, 4 –OH, 12 –CH_2, 1 –CH_3, 4 –CH

Second order group: 3 –CHOH

$\delta_d = -0.2910 - 4 * 0.3462 - 12 * 0.0269 - 0.9714 + 4 * 0.6450 + 3 * 0.1123 + 17.3231 = 17.27\ MPa^{0.5}$ (eqn. A3.39)

$\delta_p = 0.9042 + 4 * 1.1404 - 12 * 0.3045 - 1.6448 + 4 * 0.6491 + 3 * 0.2564 + 7.3548 = 10.8874 MPa^{0.5}$
(eqn. A3.40)

$\delta_{hb} = 3.7391 + 4 * 7.1908 - 12 * 0.4119 - 0.7813 - 4 * 0.2018 - 3 * 0.1928 + 7.9793 = 33.3719\ MPa^{0.5}$

(eqn. A3.41)

$\delta = 39.1\ MPa^{0.5}$

Component 3:*

First order groups: 1 –COOH, 6 –OH, 10 $–CH_2$, 1 $–CH_3$, 6 –CH

Second order group: 5 –CHOH

$\delta_d = -0.2910 - 6 * 0.3462 - 10 * 0.0269 - 0.9714 + 6 * 0.6450 + 5 * 0.1123 + 17.3231 = 18.146\ MPa^{0.5}$ (eqn. A3.42)

$\delta_p = 0.9042 + 6 * 1.1404 - 10 * 0.3045 - 1.6448 + 6 * 0.6491 + 5 * 0.2564 + 7.3548 = 15.5882\ MPa^{0.5}$

(eqn. A3.43)

$\delta_{hb} = 3.7391 + 6 * 7.1908 - 10 * 0.4119 - 0.7813 - 6 * 0.2018 - 5 * 0.1928 + 7.9793 = 47.7881\ MPa^{0.5}$

(eqn. A3.44)

$\delta = 53.4\ MPa^{0.5}$

Component 4:*

First order groups: 1 –COO–, 6 –OH, 14 $–CH_2$, 1 $–CH_3$, 5 –CH

Second order group: 5 –CHOH

$\delta_d = 0.2039 - 6 * 0.3462 - 14 * 0.0269 - 0.9714 + 5 * 0.6450 + 5 * 0.1123 + 17.3231 = 17.8883\ MPa^{0.5}$

(eqn. A3.45)

$\delta_p = 3.4637 + 6 * 1.1404 - 14 * 0.3045 - 1.6448 + 5 * 0.6491 + 5 * 0.2564 + 7.3548 = 16.2806\ MPa^{0.5}$

(eqn. A3.46)

$\delta_{hb} = 1.1389 + 6 * 7.1908 - 14 * 0.4119 - 0.7813 - 5 * 0.2018 - 5 * 0.1928 + 7.9793 = 43.7421\ MPa^{0.5}$

(eqn. A3.47)

$\delta = 50.0\ MPa^{0.5}$

Component 5:*

First order groups: 1 –COO–, 8 –OH, 12 $–CH_2$, 1 $–CH_3$, 7 –CH

Second order groups: 1 C_6 ring, 1 –CHOH

$\delta_d = 0.2039 - 8 * 0.3462 - 12 * 0.0269 - 0.9714 + 7 * 0.6450 + 0.1123 - 0.3874 + 17.3231 = 17.7031\ MPa^{0.5}$

(eqn. A3.48)

$\delta_p = 3.4637 + 8 * 1.1404 - 12 * 0.3045 - 1.6448 + 7 * 0.6491 + 0.2564 - 3.6432 + 7.3548 = 15.7998\ MPa^{0.5}$ (eqn. A3.49)

$\delta_{hb} = 1.1389 + 8 * 7.1908 - 12 * 0.4119 - 0.7813 - 7 * 0.2018 - 0.1928 + 7.9793 = 59.3151\ MPa^{0.5}$

(eqn. A3.50)

$\delta = 63.9\ MPa^{0.5}$

Volume fraction based on mass spectrometry intensity:

Component 1*: 34.2%

Component 2*: 11.2%

Component 3*: 12.0%

Component 4*: 36.7%

Component 5*: 5.9%

δ of ESO-based epoxy resin degradation products mixture:

$\delta = 21.5 * 34.2\% + 39.1 * 11.2\% + 53.4 * 12.0\% + 50.0 * 36.7\% + 63.9 * 5.9\% = 40.3\ MPa^{0.5}$ (eqn. A3.51)

Pure Solvents

Acetone:

First-order groups: 1 CH_3CO–, 1 –CH_3

Second-order group: 1 CH_3C=

$\delta_d = -0.3551 - 0.9714 - 0.0785 + 17.3231 = 15.9175\ MPa^{0.5}$ (eqn. A3.52)

$\delta_p = -1.6448 + 2.3192 + 0.3316 + 7.3548 = 8.3608\ MPa^{0.5}$ (eqn. A3.53)

$\delta_{hb} = -0.7813 - 1.3078 + 0.3875 + 7.9793 = 5.5765\ MPa^{0.5}$ (eqn. A3.54)

$\delta = 19.9\ MPa^{0.5}$

THF:

First-order groups: –CH_2O– (cyclic), 3 –CH_2

Second-order group: None

$$\delta_d = 0.2753 - 3 * 0.0269 + 17.3231 = 17.5177\ MPa^{0.5} \quad \text{(eqn. A3.55)}$$

$$\delta_p = 0.1994 - 3 * 0.3045 + 7.3548 = 6.6407\ MPa^{0.5} \quad \text{(eqn. A3.56)}$$

$$\delta_{hb} = -0.1610 - 3 * 0.4119 + 7.9793 = 6.5826\ MPa^{0.5} \quad \text{(eqn. A3.57)}$$

$$\delta = 19.0\ MPa^{0.5}$$

DMF:

First-order group: 1 –CON(CH_3)$_2$

Second-order group: None

$$\delta_d = 0.4482 + 17.3231 = 17.7713\ MPa^{0.5} \quad \text{(eqn. A3.58)}$$

$$\delta_p = 5.7899 + 7.3548 = 13.1447\ MPa^{0.5} \quad \text{(eqn. A3.59)}$$

$$\delta_{hb} = 3.0020 + 7.9793 = 10.9813\ MPa^{0.5} \quad \text{(eqn. A3.60)}$$

$$\delta = 24.7\ MPa^{0.5}$$

Calculation of volume fraction of acetone/H_2O, THF/H_2O and DMF/H_2O:

For 320 g 10 wt% HCl solution (diluted from 32 wt% HCl), there was 32 g HCl, 68 g H_2O and 200 g diluting solvent (acetone, THF or DMF). Densities of acetone, THF, DMF and 32 wt% HCl solution are 0.79 g/ml, 0.89 g/ml, 0.94 g/ml and 1.16 g/ml, respectively.

Volume fraction of acetone in acetone/H_2O solution is:

$$V_{acetone}\% = \frac{\frac{220\ g}{0.79\ g/ml}}{\frac{100\ g}{1.16\ g/ml} + \frac{220\ g}{0.79\ g/ml}} * 100\% = 74.6\% \quad \text{(eqn. A3.61)}$$

$$V_{water}\% = 1 - 74.6\% = 25.4\% \quad \text{(eqn. A3.62)}$$

Similar calculation for THF and DMF volume fractions in THF/H_2O and DMF/H_2O solutions:

$$V_{THF}\% = \frac{\frac{220\ g}{0.89\ g/ml}}{\frac{100\ g}{1.16\ g/ml} + \frac{220\ g}{0.89\ g/ml}} * 100\% = 74.1\% \quad \text{(eqn. A3.63)}$$

$$V_{water}\% = 1 - 74.1\% = 25.9\% \quad \text{(eqn. A3.64)}$$

$$V_{DMF}\% = \frac{\frac{220\ g}{0.94\ g/ml}}{\frac{100\ g}{1.16\ g/ml} + \frac{220\ g}{0.94\ g/ml}} * 100\% = 73.1\% \quad \text{(eqn. A3.65)}$$

$V_{water}\% = 1 - 73.1\% = 26.9\%$ (eqn. A3.66)

δ of a solvent mixture is calculated from the volume fraction of each component:[168]

acetone/H_2O:

$\delta = 19.0 * 0.746 + 47.8 * 0.254 = 26.3\ MPa^{0.5}$ (eqn. A3.67)

THF/H_2O:

$\delta = 19.9 * 0.741 + 47.8 * 0.259 = 27.1\ MPa^{0.5}$ (eqn. A3.68)

DMF/H_2O:

$\delta = 24.7 * 0.731 + 47.8 * 0.269 = 30.9\ MPa^{0.5}$ (eqn. A3.69)

Appendix 4: Supporting Information for Chapter 6

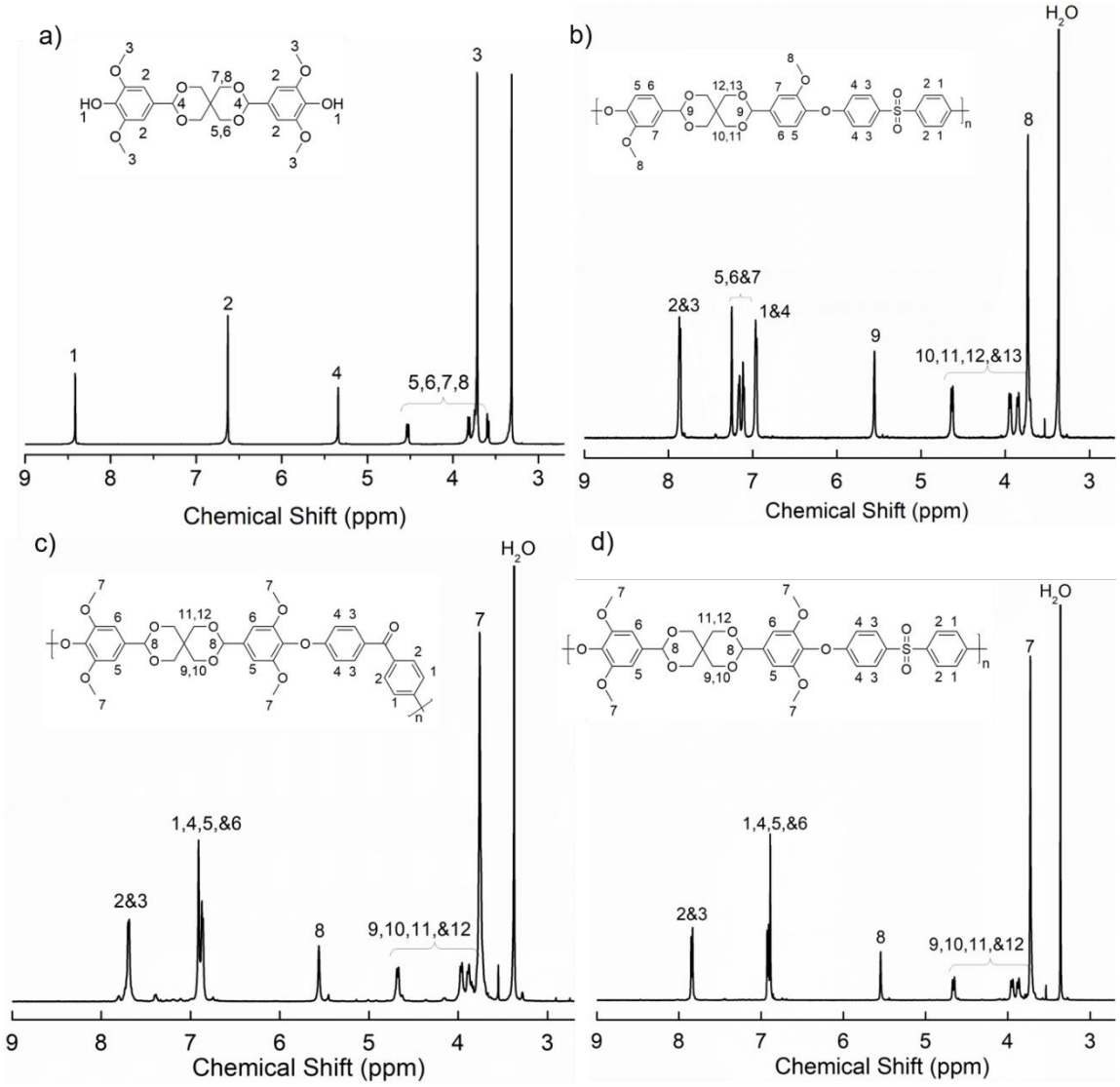

Figure A4.1: ^{1}H NMR of (a) SPA, (b) VPA-DFS, (c) SPA-DFP, and (d) SPA-DFS (in *d*-DMSO).

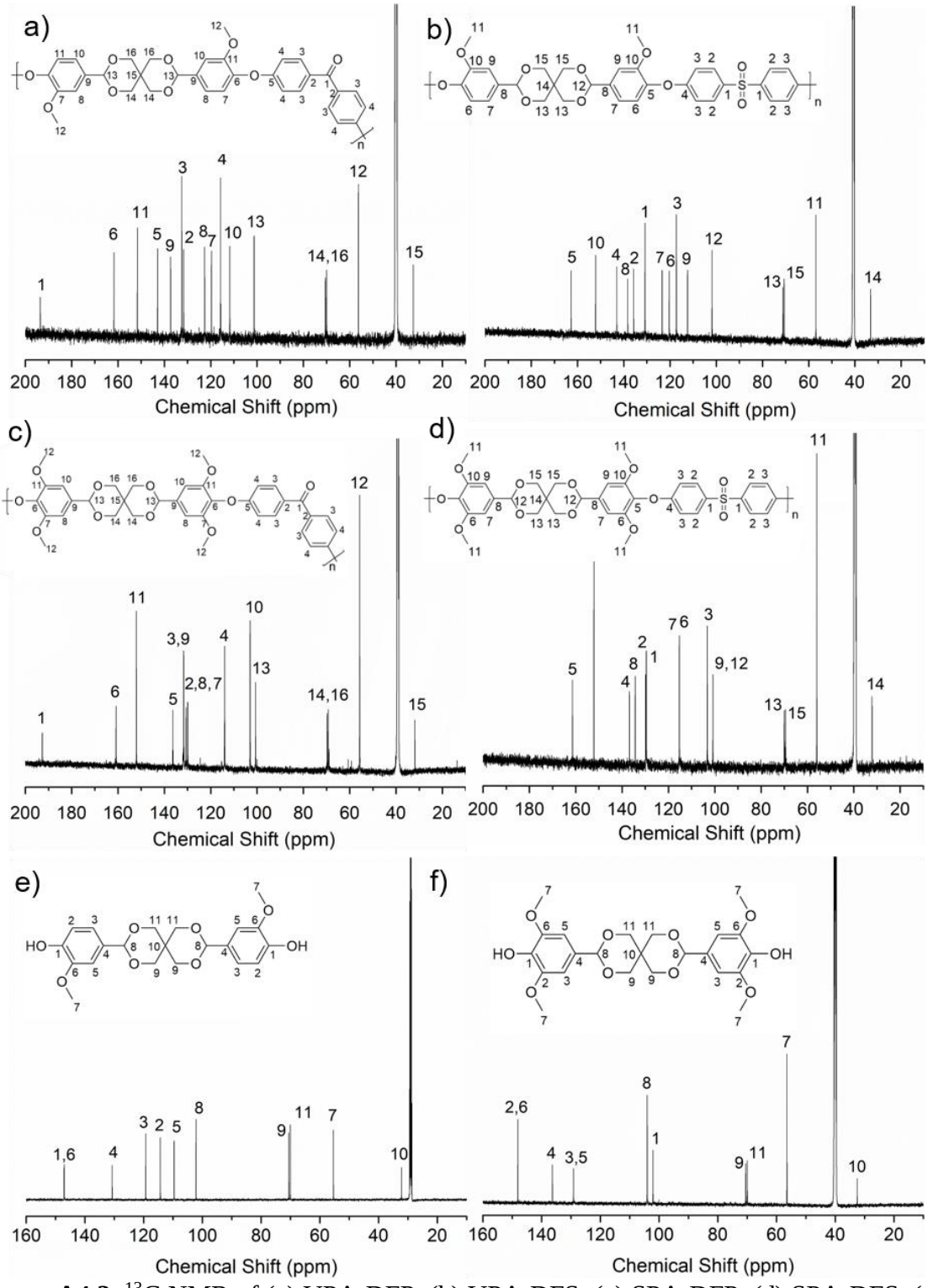

Figure A4.2: ^{13}C NMR of (a) VPA-DFP, (b) VPA-DFS, (c) SPA-DFP, (d) SPA-DFS, (e) VPA, and (f) SPA (in *d*-DMSO).

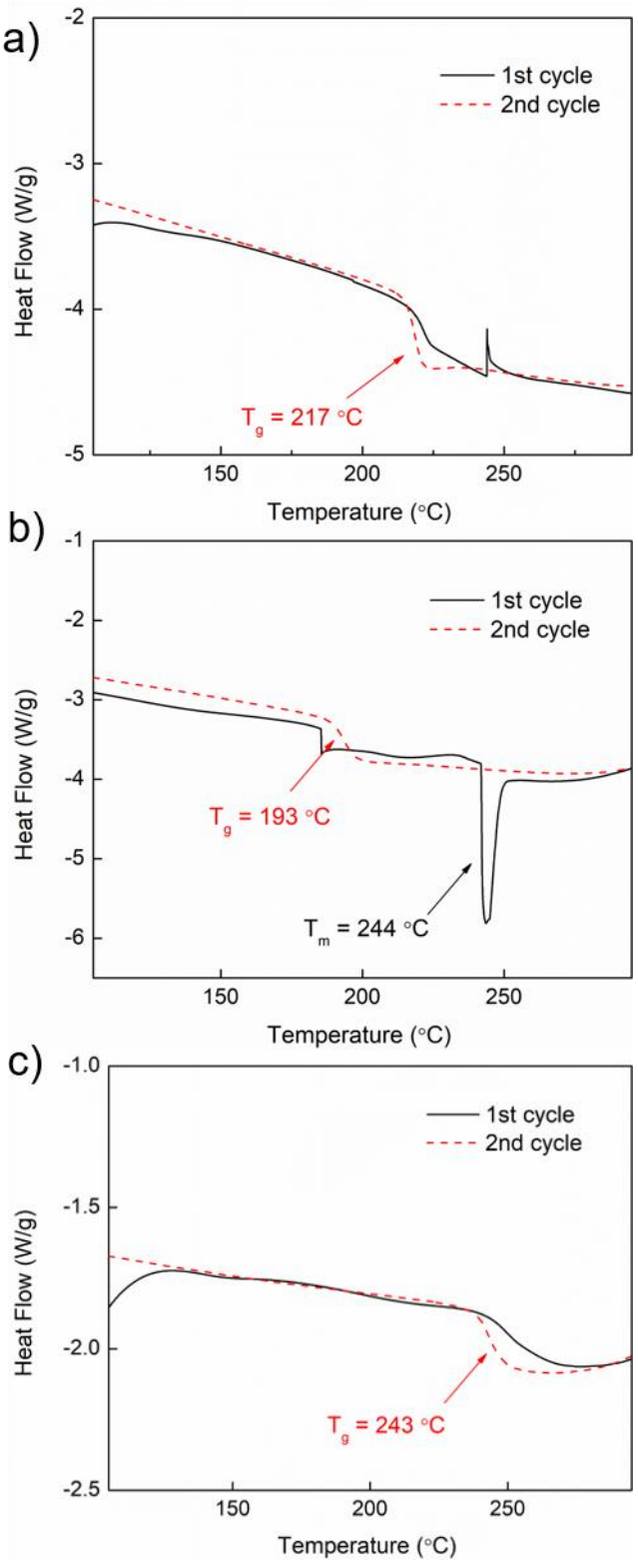

Figure A4.3: Heat flow vs. temperature obtained for (a) VPA-DFS, (b) SPA-DFP and (c) SPA-DFS using DSC.

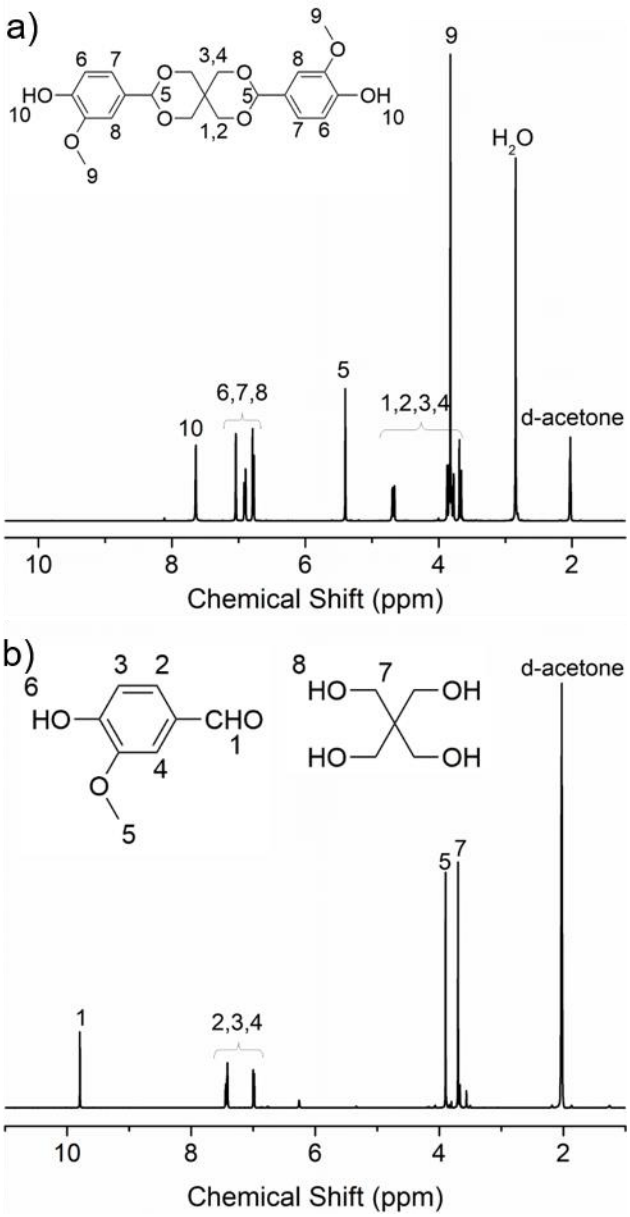

Figure A4.4: ^{1}H NMR data obtained (a) before and (b) after the acid-catalyzed hydrolysis of VPA monomer in *d*-acetone/HCl (pH ~1) at room temperature after 1 h. Degradation experiments were conducted in 0.6 mL *d*-acetone containing 5 µL of 35 wt% aqueous HCl solution.

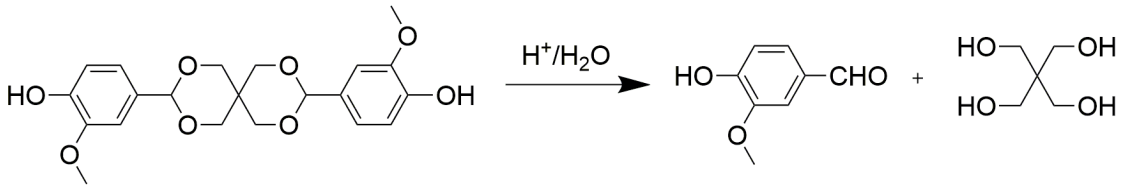

Scheme A4.1: Mechanism of degradation of VPA monomer in acidic acetone.

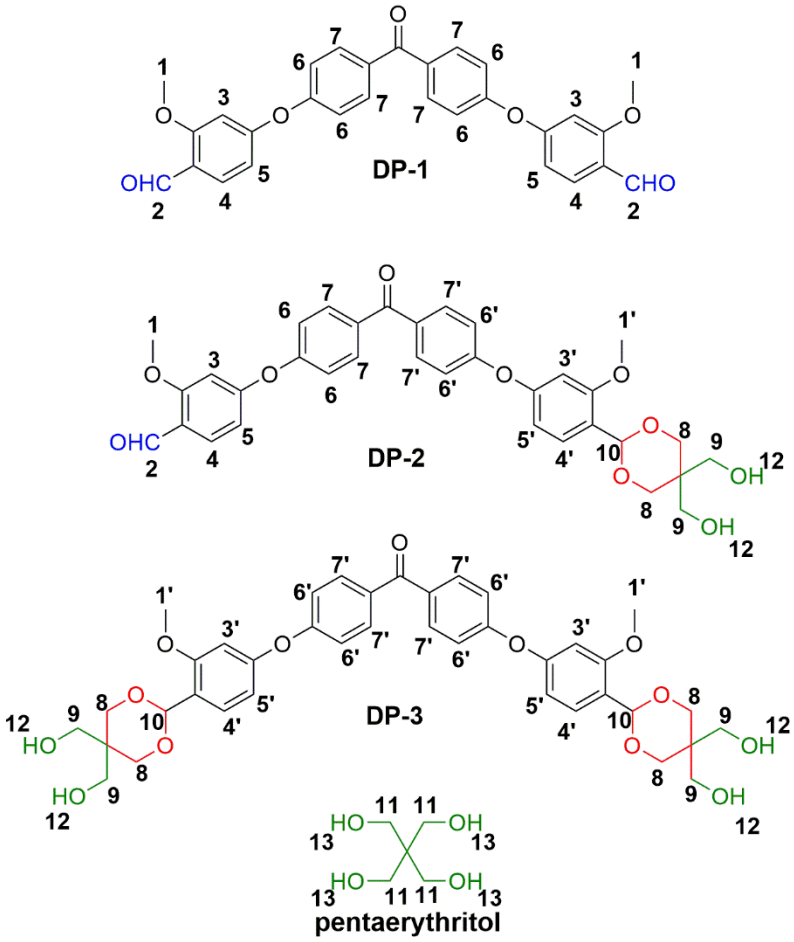

Figure A4.5: Degradation products of VPA-DFP with labeled protons.

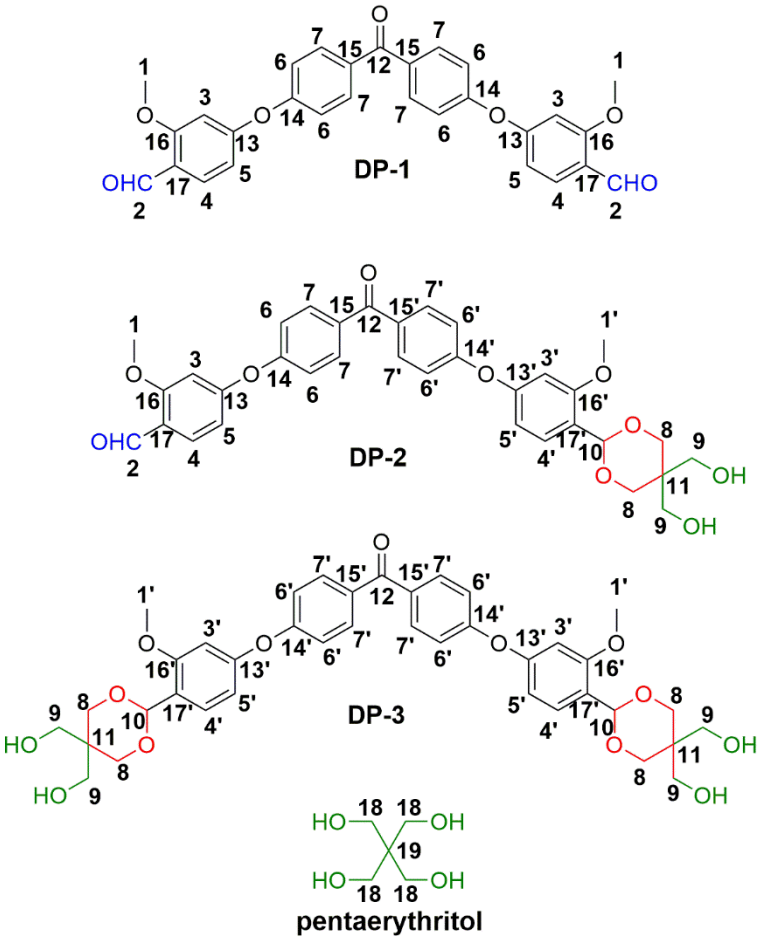

Figure A4.6: Degradation products of VPA-DFP with labeled carbons.

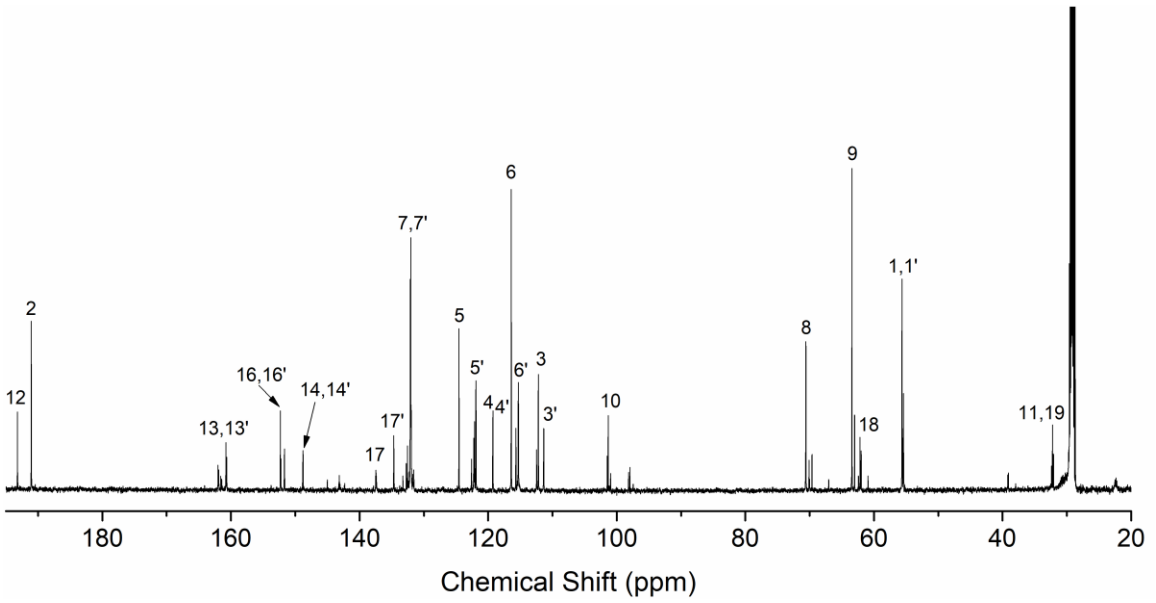

Figure A4.7: ^{13}C NMR of VPA-DFP after 24 h degradation in acidic acetone. Carbon labeling is reference in Figure A4.6. Degradation experiments were conducted in 0.6 mL *d*-acetone containing 5 µL of 35 wt% aqueous HCl solution.

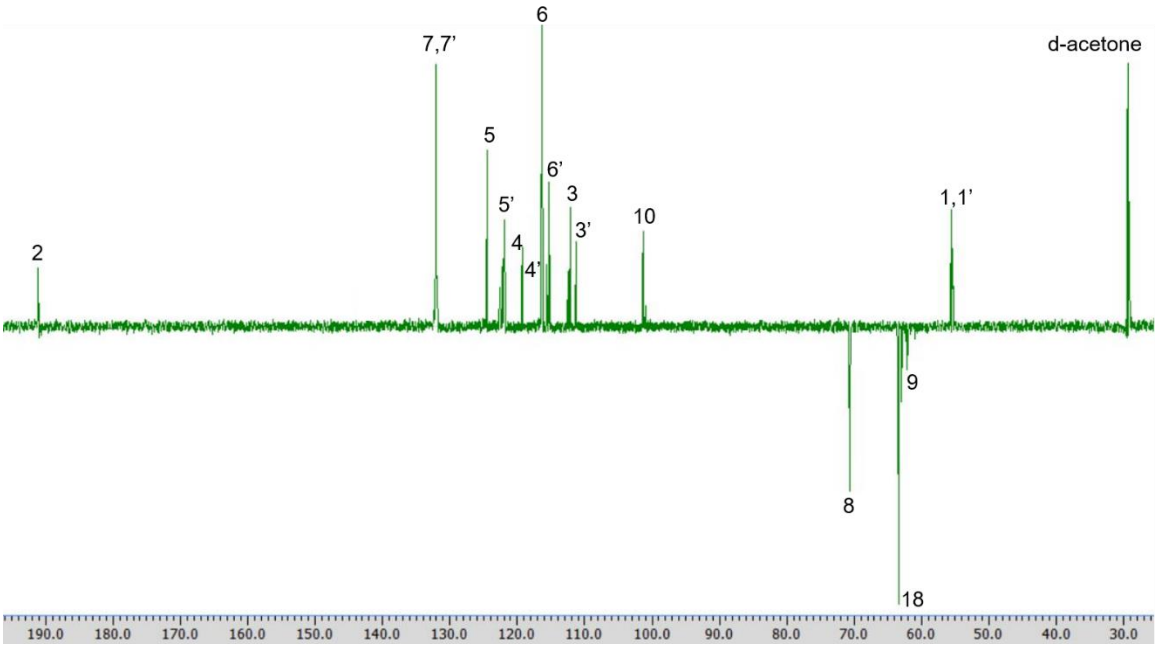

Figure A4.8: DEPT 135 of VPA-DFP after 24 h degradation in acidic acetone. Carbon labeling isreferenced in Figure S6. Degradation experiments were conducted in 0.6 mL *d*-acetone containing 5 µL of 35 wt% aqueous HCl solution.

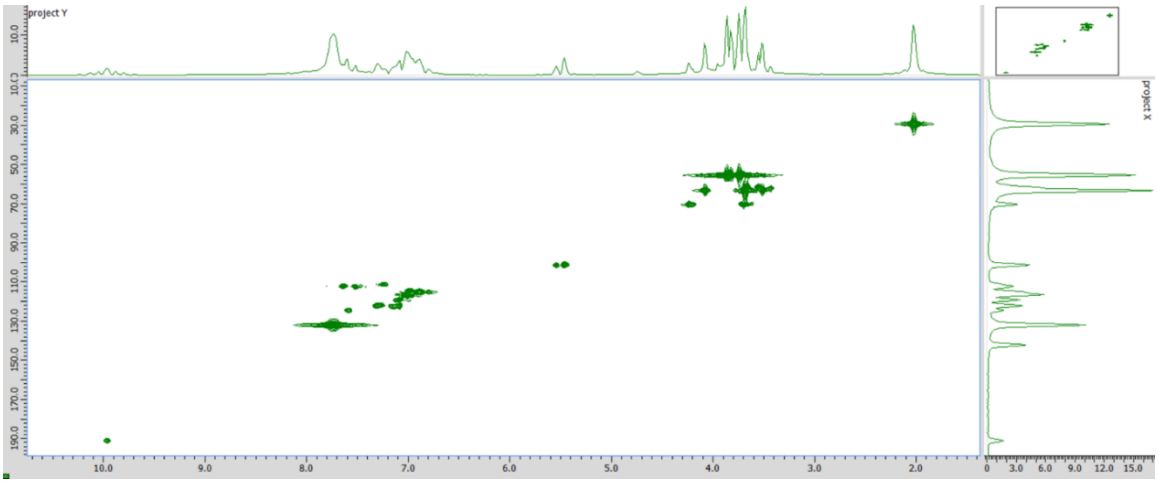

Figure A4.9: HMQC of VPA-DFP after 24 h degradation in acidic acetone. Degradation experiments were conducted in 0.6 mL *d*-acetone containing 5 µL of 35 wt% aqueous HCl solution.

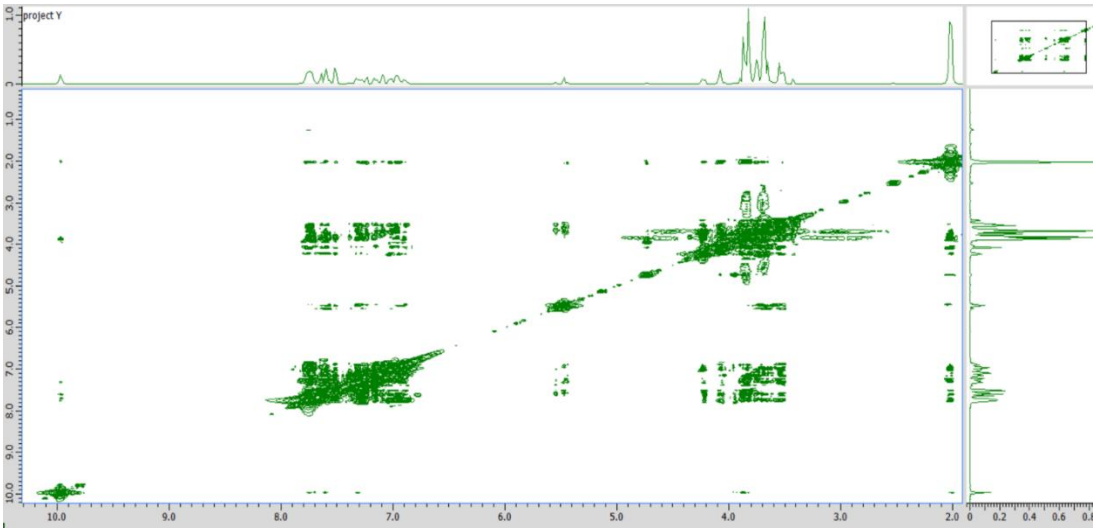

Figure A4.10: COSY of VPA-DFP after 24 h degradation in acidic acetone. Degradation experiments were conducted in 0.6 mL *d*-acetone containing 5 µL of 35 wt% aqueous HCl solution.

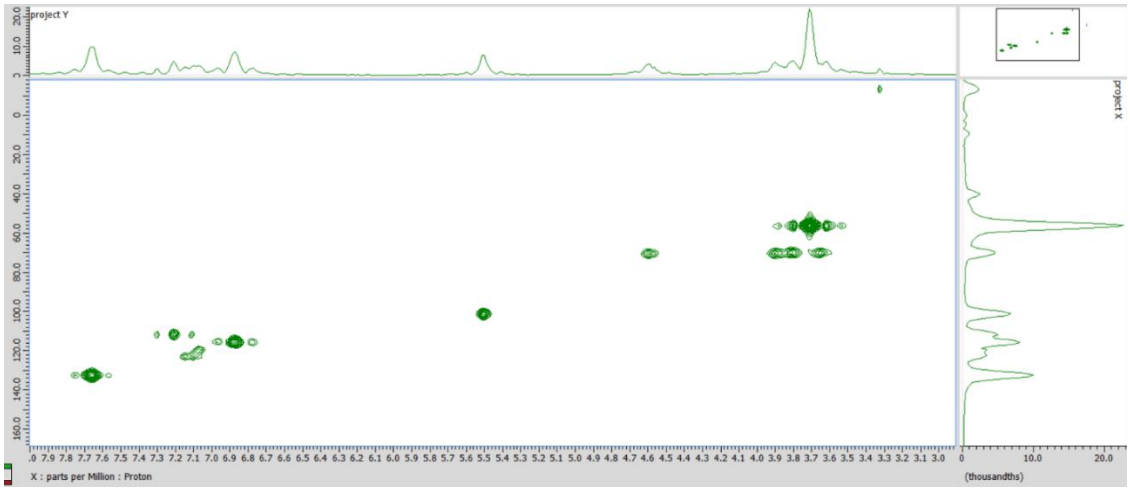

Figure A4.11: HMQC of VPA-DFP prior to degradation.

NMR Peak Assignments Determined through 2D NMR Analyses

We used 2D NMR, including Distortions Enhancement by Polarization Transfer (DEPT 135), Correlated Spectroscopy (COSY), and Heteronuclear Multiple Quantum Coherence (HMQC) (Figures A4.5-A4.11), to assign peaks on the ^{1}H and ^{13}C spectra obtained from VPA-DFP after 24 h of degradation time in acidic acetone, shown in Figures 6.1, 6.5, 6.7, A4.1 and A4.2. The discussion below focuses on the presence of the four degradation products identified in Scheme 6.3: DP-1. DP-2, DP-3, and pentaerythritol. We note that oligomers may be present with the same functional end-groups as DP-1, DP-2, and DP-3. We therefore do not attempt to quantify the concentration of each degradation product, but rather concentrations of each of the relevant functional groups (described in the main text). DEPT experiments are used to distinguish between $-CH_3$, $-CH_2$ and -CH groups: $-CH_3$ and -CH peaks appear as normal, and $-CH_2$ peaks appear inverted. COSY experiments provide correlations when there is spin-spin coupling between neighboring protons. HMQC experiments provide information on coupling between connected protons and carbons.

By combining DEPT (Figure A4.8), HMQC (Figure A4.9) and COSY (Figure A4.10), we can assign the ^{1}H peaks obtained from VPA-DFP after 24 h degradation in acidic acetone (Figure 6.5, with peak labels in Figure 6.5 and A4.5), as well as the ^{13}C data (Figure A4.7, with labels in Figure A4.6). We start with the proton peak at 10.01 ppm in Figure A4.5. From HMQC data, we see a correlation with the carbon peak at 191.1 ppm. We start with the proton peak at 10.01 ppm. From the HMQC data, we see a correlation with the carbon peak at 191.1 ppm. We therefore assigned the peak to the aldehyde group (labeled peak 2).

The peaks at 5.48 and 5.58 ppm belong to the -CH in the acetal structure (peak 10). From HMQC data, we see a correlation with the carbon peak at 102 ppm, and from the DEPT data, we can observe the peak at 102 ppm is either -CH or -CH_3. Since the only expected -CH_3 group is a methoxy group, and would not be anticipated to be located at this ppm value, these results are consistent with the assignment of the proton peak at 5.48 and 5.58 ppm, and the carbon peak at 102 ppm, as the -CH in the acetal structure (peak 10). We note that in the COSY data there are correlations between the peaks at 5.48 and 5.58 ppm with peaks in the aromatic region (6.9-7.8 ppm) as well as the -CH_2 region at 3.5-4.2 ppm (-CH_2 and -OCH_3 peaks). We hypothesize that two -CH peaks (peak 10) are observed due to H-D exchange of the -CH with the deuterated acetone. Both peaks show the same correlations with other protons and carbons in the 2D data.

The peak at 4.7 ppm is assigned to the -OH group (peak 12). Correlations are observed in the COSY data with the -CH_2 peak at around 4-4.2 ppm (peak 9). Additionally, no correlations are observed for the proton at 4.7 ppm to carbons peaks in HMQC, consistent with the assignment of -OH.

We are assigning peaks in the range of 3.5 – 4.2 ppm to -CH_2 and -OCH_3 groups. From the HMQC data, we can see that these peaks are correlated with carbon peaks in the range of 55 – 65 ppm. We can see that there is one positive peak in the DEPT data at 55.2 ppm, indicating this is the -OCH_3 peak (labeled peaks 1, 1'). The others are negative in the DEPT data, indicating -CH_2 peaks. Additionally, we observed correlations in the COSY data between the proton peak at 3.90 ppm and the aldehyde proton peak 2 at 10.01 ppm. Such correlations with the aldehyde peak were not observed for the proton peak at 3.72 ppm. We therefore assign peak 1 at 3.90 ppm and peak 1'at 3.72 ppm. With the help of COSY, peak 10 at 5.5 ppm is correlated with protons in the range of 3.6 - 3.75 ppm, indicating these protons are in close proximity. However, we do not see such correlations between peak 10 at 5.5 ppm and -CH_2 peaks at higher ppm values. As proton 10 is closer in proximity to proton 8 than it is to proton 9, we therefore assign proton 8 to the peaks at 3.6 - 3.75 ppm and proton 9 to the peaks at 4.1 – 4.2 ppm. Peak 11 also does not show correlations with peak 10, and we assign it to proton 11 on pentaerythritol. From the HMQC data, we can see that peak 1 on the ^{1}H spectrum (-OCH_3) is correlated with the peak at 56 ppm on the ^{13}C spectrum. Peak 1' on the ^{1}H spectrum is also correlated with the peak at 56 ppm on the ^{13}C spectrum. Peak 8 on the ^{1}H spectrum is correlated with peak 70 ppm on the ^{13}C spectrum, peak 9 on the ^{1}H spectrum is correlated with peak 63 ppm on the ^{13}C spectrum, and peak 11 on the ^{1}H spectrum is correlated with peak 32 ppm on the ^{13}C spectrum. We thus assigned the peaks in the carbon spectrum in this manner.

Next, we will discuss aromatic peaks in the range of 6.9 – 7.8 ppm in Figure 6.5. Protons 6 and 7 were assigned in the ^{1}H NMR spectrum based on reported data for the DFP monomer.[145] Upon examining HMQC data of both the degradation product mixture

(Figure A4.9) and VPA-DFP prior to degradation (Figure A4.11), we observed correlations between the aromatic proton and carbon peaks: proton 6 at 7.8 ppm is correlated with carbon 6 at 118.2 ppm and carbon 6' at 117.7 ppm, and proton 7 at 6.9 ppm is correlated with carbon 7 at 130.9 ppm and carbon 7' at 130.8 ppm. We now continue to the aromatic protons labeled 3, 4, 5 on DP-1 and DP-2 which are near the aldehyde proton. In the COSY data, we found several spots at 7.3 ppm, 7.6 ppm and 7.7 ppm (which are attributed to protons 3, 4, and 5, though they cannot be distinguished from one another) which are correlated to the aldehyde proton at 10.01 ppm, indicating close proximity. We therefore label these as the aromatic protons located next to the aldehyde group. However, protons 3', 4' and 5' (at 7.0, 7.2, and 7.6 ppm) were not correlated with the aldehyde proton, and instead were correlated with peak 10 (at 5.5 ppm) on the partially hydrolyzed acetal group. Therefore, protons 3', 4' and 5' are the aromatic protons in closest proximity to the partially hydrolyzed acetal group. We observed correlations between the aromatic proton and carbon peaks in HMQC data: protons 3, 4, 5 at 7.3, 7.6, 7.7 ppm are correlated with carbons 3, 4, 5 at 111.3, 119.7 and 124.5 ppm, respectively and carbons 3', 4', 5' at 100.8, 119.6, and 121.9 ppm, respectively. The peaks for carbons 3, 4 and 5 were assigned based on examining reported data of ^{13}C NMR of vanillin,[12] ^{13}C NMR of VPA (Figure A4.2e), ^{13}C NMR of VPA-DFP (Figure 4.2a) and HMQC data of VPA-DFP prior to degradation (Figure A4.11). We also noticed a shift of 3, 4 and 5 to the left of peaks 3', 4' and 5'. We assigned the peak of carbons for 3', 4' and 5' upon considering reported data of ^{13}C NMR of vanillin and ^{13}C NMR data of VPA (Figure A4.2e). As a result, the cleavage of acetal group and formation of aldehyde group would shift the carbons on the neighboring

aromatic rings to the left. We note that all of the assigned aromatic carbon peaks are positive in the DEPT data.

Table A4.1: Molecular weight at the peak maxima[a] (M_p, kg/mol) quantified for each peak observed in GPC data obtained from the acid-catalyzed hydrolysis of VPA-DFP in *d*-acetone/HCl (pH ~ 1) at room temperature. For comparison purposes, the known molecular weight of each small molecule is summarized in **Table A4.2**.

	First Peak (26.8 min): attributed to oligomeric species	Second Peak (27.2 min): attributed to DP-3	Third Peak (27.7 min): attributed to DP-2	Fourth Peak (28.8 min): attributed to DP-1	Fifth Peak (30.1 min): attributed to pentaerythritol
0.5 h	2.9	0.8	0.6	0.5	0.1
1 h	2.7	0.8	0.6	0.5	0.1
3 h	2.7	0.8	0.6	0.4	0.1
6 h	2.7	0.8	0.6	0.4	0.1
10 h	2.7	0.8	0.6	0.4	0.1
24 h	2.7	0.8	0.6	0.4	0.1

[a] Quantified using a calibration curve derived from polystyrene standards

Table A4.2: Molecular weights of degradation products

Degradation Product	Molecular weight (g/mol)
DP-1	482.1
DP-2	600.2
DP-3	718.3
Pentaerythritol	136.1

Hansen Solubility Parameters of Degradation Products and Solvents

All functional groups are divided into first order groups that comprise the basic molecular structures of the compounds and second order groups defined by conjugation theory. The dispersion solubility parameter (δ_d), polar solubility parameter (δ_p) and hydrogen bonding solubility parameter (δ_{hb}) are calculated by the following equations:[167]

$$\delta_d = \left(\sum_i N_i C_i + W \sum_j M_j D_j + 17.3231\right) MPa^{0.5} \quad \text{(eqn. A4.1)}$$

$$\delta_p = \left(\sum_i N_i C_i + W \sum_j M_j D_j + 7.3548\right) MPa^{0.5} \quad \text{(eqn. A4.2)}$$

$$\delta_{hb} = \left(\sum_i N_i C_i + W \sum_j M_j D_j + 7.9793\right) MPa^{0.5} \quad \text{(eqn. A4.3)}$$

where C_i is the contribution of the first-order group of type *i* that appears N_i times in the compound and D_j is the contribution of the second-order group of type *j* that appears M_j times in the compound, and δ is calculated as:

$$\delta = \sqrt{\delta_d^2 + \delta_p^2 + \delta_{hb}^2} \quad \text{(eqn. A4.4)}$$

Degradation Products of VPA-DFP:

Chemical structures of the degradation products are shown in Figure 6.5 of the main text.

AC refers to an aromatic carbon in the descriptions below.

DP-1:

First-order groups: 2 –CHO, 2 –OCH_3, 1 CO, 2 O, 10 AC, 14 ACH

Second-order group: 2 ACHO, 2 ACOAC

$$\delta_d = -0.403 * 2 - 2 * 0.5828 - 0.4343 + 2 * 0.0472 + 10 * 0.8446 + 14 * 0.1105 + 17.3231 = 24.6298\ MPa^{0.5}$$
(eqn. A4.5)

$$\delta_p = 3.4734 * 2 + 2 * 0.1764 + 0.7905 + 2 * 3.3432 + 10 * 0.6187 - 14 * 0.5303 + +7.3548 = 10.4063\ MPa^{0.5} \quad \text{(eqn. A4.6)}$$

$$\delta_{hb} = 0.1687 * 2 + 2 * 0.146 + 1.8147 + 2 * 0.0256 + 10 * 0.0084 - 14 * 0.4305 + 7.9793 = 6.3410\ MPa^{0.5} \quad \text{(eqn. A4.7)}$$

$$\delta = 27.5\ MPa^{0.5}$$

DP-2:

First order groups: 1 –CHO, 2 –OCH_3, 1 CO, 2 O, 10 AC, 14 ACH, 2 –OH, 1 –C, 2 –CH_2, 1 –CH, 2 –OCH_2

Second order groups: 1 ACHO, 2 ACOAC

$$\delta_d = -0.403 - 2 * 0.5828 - 0.4343 + 2 * 0.0472 + 10 * 0.8446 + 14 * 0.1105 - 2 * 0.3462 + 1.2686 - 2 * 0.0269 + 0.645 + 2 * 0.031 + 0.3772 - 2 * 0.5646 + 17.3231 = 18.9383\ MPa^{0.5}$$
(eqn. A4.8)

$\delta_p = 3.4734 + 2 * 0.1764 + 0.7905 + 2 * 3.3432 + 10 * 0.6187 - 14 * 0.5303 + 2 * 1.1404 + 2.0838 - 2 * 0.3045 + 0.6491 + 2 * 0.8826 - 1.811 - 2 * 3.4329 + 7.3548 = 14.9138\ MPa^{0.5}$
(eqn. A4.9)

$\delta_{hb} = 0.1687 + 2 * 0.146 + 1.8147 + 2 * 0.0256 + 10 * 0.0084 - 14 * 0.4305 + 2 * 7.1908 + 0.0866 - 2 * 0.4119 - 0.2018 - 2 * 0.1528 - 1.0096 + 2 * 2.083 + 7.9793 = 20.7\ MPa^{0.5}$
(eqn. A4.10)

$\delta = 36.3\ MPa^{0.5}$

DP-3:

First order groups: 2 $-OCH_3$, 1 CO, 2 O, 10 AC, 14 ACH, 4 –OH, 2 –C, 4 $-CH_2$, 2 –CH, 4 $-OCH_2$

Second order groups: 2 ACOAC

$\delta_d = -2 * 0.5828 - 0.4343 + 2 * 0.0472 + 10 * 0.8446 + 14 * 0.1105 - 4 * 0.3462 + 2 * 1.2686 - 4 * 0.0269 + 2 * 0.645 + 4 * 0.031 - 2 * 0.5646 + 17.3231 = 27.1402\ MPa^{0.5}$
(eqn. A4.11)

$\delta_p = 2 * 0.1764 + 0.7905 + 2 * 3.3432 + 10 * 0.6187 - 14 * 0.5303 + 4 * 1.1404 + 2 * 2.0838 - 4 * 0.3045 + 2 * 0.6491 + 4 * 0.8826 - 2 * 3.4329 + 7.3548 = 19.4213\ MPa^{0.5}$
(eqn. A4.12)

$\delta_{hb} = 2 * 0.146 + 1.8147 + 2 * 0.0256 + 10 * 0.0084 - 14 * 0.4305 + 4 * 7.1908 + 2 * 0.0866 - 4 * 0.4119 - 2 * 0.2018 - 4 * 0.1528 + 2 * 2.083 + 7.9793 = 34.6342\ MPa^{0.5}$
(eqn. A4.13)

$\delta = 48.1\ MPa^{0.5}$

Pentaerythritol:

First-order groups: 4 –OH, 1 –C, 4 $-CH_2$

$\delta_d = 4 * -0.3462 + 1.2686 - 4 * 0.0269 + 17.3231 = 17.0993\ MPa^{0.5}$

(eqn. A4.14)

$\delta_p = 4 * 1.1404 + 2.0838 - 4 * 0.3045 + 7.3548 = 12.7822\ MPa^{0.5}$

(eqn. A4.15)

$\delta_{hb} = 4 * 7.1908 + 0.0866 - 4 * 0.4119 + 7.9793 = 35.1815\ MPa^{0.5}$

(eqn. A4.16)

$\delta = 41.2\ MPa^{0.5}$

Pure Solvents:

Acetone:

First-order groups: 1 CH_3CO–, 1 –CH_3

Second-order group: 1 CH_3C=

$\delta_d = -0.3551 - 0.9714 - 0.0785 + 17.3231 = 15.9175\ MPa^{0.5}$ (eqn. A4.17)

$\delta_p = -1.6448 + 2.3192 + 0.3316 + 7.3548 = 8.3608\ MPa^{0.5}$ (eqn. A4.18)

$\delta_{hb} = -0.7813 - 1.3078 + 0.3875 + 7.9793 = 5.5765\ MPa^{0.5}$ (eqn. A4.19)

$\delta = 19.9\ MPa^{0.5}$

DMSO:

First-order groups: 1 S, 2 –CH_3, 1 O

$\delta_d = 1.4899 - 2 * 0.9714 + 0.0472 + 17.3231 = 16.9174\ MPa^{0.5}$ (eqn. A4.20)

$\delta_p = 9.2072 - 2 * 1.6448 + 3.3432 + 7.3548 = 16.6156\ MPa^{0.5}$ (eqn. A4.21)

$\delta_{hb} = -0.625 - 2 * 0.7813 + 0.0256 + 7.9793 = 5.8173\ MPa^{0.5}$ (eqn. A4.22)

$\delta = 24.4\ MPa^{0.5}$

H_2O:

$\delta = 47.8\ MPa^{0.5}$